Loughborough University

Department of Materials

MICROSTRUCTURAL REJUVENATION IN SINGLE CRYSTAL NI-BASED SUPERALLOYS

By

ZHIQI YAO

A doctoral thesis submitted in partial fulfilment of the requirements for award of Doctor of Philosophy of Loughborough University

May 2014

Supervisors: Prof. Rachel Thomson and Dr. Mark Jepson

Sponsoring Company: E.ON Engineering Ltd.

Industrial Supervisor: Dr. Craig Degnan

ACKNOWLEDGEMENTS

I would like to take this opportunity to express my sincere gratitude to the following people without whom this work would not have been possible:

First, thanks to E.ON Engineering Ltd. for providing samples and support for this project and the Department of Materials for provision of research facilities.

It is a great pleasure to express my sincere gratitude to my supervisors, Prof. Rachel Thomson and Dr Mark Jepson, for supervision throughout the whole of this project. I have benefitted from their advice, assistance and encouragement. I also would like to express my appreciation to Dr. Craig Degnan and Dr. Geoff West for their help and support.

Lastly, my thanks go to my beloved family for their financial support, loving consideration and great confidence in me all through the years.

ABSTRACT

Ni-based superalloys are widely used in aerospace and power generation as gas turbine components due to their excellent high temperature performance. These components are subjected to a combination of elevated temperature, high stress and aggressive environments during service, which can cause significant degradation of the materials. This microstructural and chemical degradation deteriorates the mechanical properties such as tensile strength and creep resistance, which can lead to failure in the components and reduce their service life. When a superalloy power plant gas turbine component reaches the end of its predicted life, the user typically has two options: replace the component or attempt to extend its remaining life. Replacement not only requires expensive materials but also adds to the maintenance and operational costs of the turbine, which has made the life extension of components a financially viable alternative. Rejuvenation heat treatments are designed and used to recover some extra life for expensive Ni-based components by restoring the pre-service microstructure, and hence mechanical properties, ready for the component's extended life.

In this research, the microstructural evolution of the Ni-based superalloy CMSX-4 ,including the change in gamma prime morphology, size and distribution has been examined in detail using field emission gun scanning electron microscopy (FEGSEM) and transmission electron microscopy (TEM) after high temperature degradation and rejuvenation heat treatments. The microstructures have been correlated to the observed mechanical properties of the material to assess the effectiveness of the heat treatment procedures, and their effect on the subsequent performance. It is shown that there are significant differences in the rafting behaviour, the size of the 'channels' between the gamma prime particles, and the size of the tertiary gamma prime particles. Results from this research will provide greater understanding of the suitability of rejuvenation heat treatments and

their role in the extension of component life in power plant applications.

Chemical segregation investigations were carried out to investigate the cause of reduced mechanical properties of the rejuvenated sample after high temperature degradation compared to an as-received sample after the same degradation procedure. The results indicate that although the microstructure of the as-received and rejuvenated samples was similar, the chemical segregation was more pronounced in the rejuvenated samples, suggesting that chemical segregation from partitioning of the elements during rejuvenation was not completely eliminated. Later a few modified rejuvenation trials were carried out to solve the chemical segregation problem. However, the creep test results suggest that the chemical segregation has no significant influence on the mechanical properties under the test conditions used.

An application of rejuvenation heat treatment on an ex-service industrial gas turbine blade was carried out to study the feasibility of the rejuvenation heat treatment on large complex components. The results show a good agreement with the bar specimen taken in the laboratory work. However, care must be taken during handling of large industrial ex-service blades, since small mechanical stress whilst at high temperature may cause permanent damage to the blade. The overall aim of this research is to provide greater understanding of the suitability of rejuvenation heat treatments and their role in the extension of component life in power plant applications.

CONTENTS

CHAPTER 1

INTRODUCTION

1.1 Project Background

Ni-based superalloys were developed for use in aircraft and land-based turbine engine components in the 1950s. As Ni-based superalloys provide excellent creep strength and corrosion resistance at elevated temperature, they have since become the major material used for this application. The demand for high temperatures driven by an increasing need for high operating temperature and efficiency dictates the use of single crystal superalloys, such as CMSX-4, developed by Cannon Muskegon Corporation, for use in gas turbines since the late 1980s. CMSX-4 is a rhenium containing single crystal superalloy capable of long-term operation at temperatures up to 1100°C [1, 2]. CMSX-4 is widely used in gas turbine components for power generation, such as turbine blades. These components are subjected to aggressive environments in service consisting of a combination of elevated temperature and high stress, which inevitably causes various changes in the material. This microstructural deterioration can lead to a degradation of mechanical properties such as creep and fatigue resistance during service and finally can lead to failure in the components. The service lives of components are limited by the occurrence of creep, fatigue and corrosion which are worsened by this microstructural degradation [3–5]. When a superalloy power plant gas turbine component reaches the end of its predicted life, the user typically has two options: replace the component or attempt to extend its life through the application of heat treatments. The high cost of replacement parts drives people to consider the application of economical

methods for the extension of the service life of these components, which has made the life extension of components worth considering.

The repair of industrial gas turbine components has developed into a significant after-sales market over the last 20 years [6]. Before that, the majority of turbines were overhauled and components were replaced rather than repaired. Rejuvenation heat treatments were developed and played an important role in the repair and service life extension of turbine engine components, saving significant amounts of money for industrial gas turbine operators. Rejuvenation is designed to restore the microstructure (and, hence mechanical properties) to a condition that is equivalent to that before service exposure, to recover some extra life for the expensive single crystal Ni-based superalloy components [6]. Traditionally, the refurbishment of the gas turbine blades involves stripping the component of its thermal barrier and bond coating, roughening of the surface via grit blasting and then recoating. The recoating process involves a thermal treatment, which is usually carried out at around 1140°C for 6 hours. It is claimed that this low temperature refurbishment is sufficient to rejuvenate a rafted (or partially rafted) CMSX-4 substrate back to its originally manufactured condition [7]. In this research, the efficiency of rejuvenation heat treatments for CMSX-4 has been examined and a new high temperature rejuvenation heat treatment procedure has been designed and compared with a low temperature refurbishment. Following the application of rejuvenation heat treatments, samples have been further “degraded” under conditions representative of the service environments. Microstructural investigation of these samples was carried out using scanning electron microscopy (SEM) and transmission electron microscopy (TEM), combined with energy dispersive X-ray (EDX) for chemical analysis to establish fully understanding of microstructural evolution of CMSX-4 after different heat treated conditions.

1.2 Aims and Objectives

In the case of the CMSX-4 used in power plant applications, the predicted lifetime is primarily governed by the degradation of the microstructure through the coarsening and rafting of the gamma prime particles [5]. Therefore, to understand changes in the size, morphology and distribution of the gamma prime particles during these rejuvenation heat treatments becomes very important. However, at present, limited information is available in the open literature about the effect that these types of heat treatments on the integrity of the components. In this study, microstructural characterisation and mechanical performance of CMSX-4 after different heat treatments were investigated to gain a fundamental understanding of the microstructural evolution of CMSX-4 during high temperature degradation and rejuvenation, combined with changes in its mechanical properties. The aims of this research are as follows:

1. To determine the relationship between the microstructure, heat treatment and mechanical properties;
2. To examine the effectiveness of different rejuvenation treatments through the microstructural characterisation and mechanical test results;
3. To establish the underlying mechanisms for fast degradation rate of rejuvenated samples;
4. To Study the feasibility of rejuvenation on an ex-service industrial turbine blade.

A literature review focusing on the microstructural evolution of the CMSX-4 during degradation and rejuvenation, combined with some current rejuvenation procedures is presented in Chapter 2. Chapter 3 describes the details of the materials used in this research and reviews the experimental procedure and techniques used throughout of this research. Thermodynamic equilibrium

calculation predictions and observation of the general microstructure of CMSX-4 at different temperatures are presented in Chapter 4 to give a brief introduction of the microstructures of CMSX-4. The changes in tensile and creep properties after different heat treatments are presented in Chapter 5 and 6, and further connected with microstructural characterisation, to study the effect of the heat treatments on microstructural degradation and recovery. Detailed chemical segregation analysis was carried out on differently heat treated CMSX-4 samples and is presented in Chapter 7, to study the influence of the chemical segregation on the mechanical performance of the materials. Later a number of rejuvenation trials were applied in an attempt to modify the current rejuvenation practices, results of which are presented and discussed in Chapter 7. Finally an ex-service blade was rejuvenated at high temperature and studied using dimensional and microstructural investigation to study the feasibility of rejuvenations for ex-service blade components. The conclusions drawn from this research are presented in Chapter 9, together with a few suggestions of the possible research for its future development and further work.

CHAPTER 2

LITERATURE REVIEW

2.1 Introduction

Ni-based superalloys are usually employed for aeronautical and industrial applications, because they exhibit superior high temperature mechanical strength and hot corrosion resistance compared to conventional alloys. Owing to these attractive properties, Ni-based superalloys are suitable for high temperature critical components such as turbine blades and vanes in modern aircraft engines and power plants. The demand for high operating temperature drives the use of single crystal Ni-based superalloys, such as CMSX-4, which has excellent high temperature performance and reasonable price [1–3]. Microstructural degradation of these superalloys occurs when they are subjected to a combination of elevated temperature and stress during service. An understanding of the microstructural revolution of these single crystal superalloys will help us to develop a suitable rejuvenation heat treatment for these materials to recover some extra life of the components.

In this literature review, some important issues are considered. Firstly, the development of the superalloys is reviewed. Then the major phases of Ni-based superalloys are introduced, with the effects of chemical composition. Moreover, as a major part of this literature review the changes of microstructure and mechanical properties during the service are discussed in detail. Finally, a general introduction of CMSX-4 and coatings are presented, which are followed the some important considerations of rejuvenation heat treatment.

2.2 Historical Review of Ni-based Superalloy

The term “superalloys” is used to describe a wide range of high temperature materials which combine high strength and corrosion resistance at temperature above 650°C. The major classes of superalloys are based on iron, cobalt and nickel, and each is designed for specific applications [1–5]. Ni-based superalloys, for example, are widely used in aircraft and land-based gas turbine engines. These superalloys are employed in the hottest portions of the turbines, under large continuous stress. This is because they can retain most of their strength even after long exposure times at elevated temperature [1-5]. Rapid developments in high temperature materials for the use in aerospace technologies occurred as a direct result of the onset of World War II. This was closely followed by the requirements of the industrial gas turbines, which demanded strength and long service life at high temperatures plus the additional reliability and economic feasibility. The demand of the high efficiency increases the operating temperature of the gas turbine engine, which drives the development of the Ni-based superalloy.

The first Ni-based superalloys, Ni-20wt% Cr alloys, were developed in Great Britain in 1941[2]. Since then, rapid developments in high temperature materials for the use in aerospace has occurred and the performance of materials has improved dramatically, especially in operating temperature. This is because a higher temperature results in improvements to the efficiency of the engine and therefore lower fuel burn[1]. The main superalloys developed in the last 60 years and their operating temperatures are shown in Figure 2.1. There are four types of Ni-based superalloys since it was developed, which are wrought, conventionally cast, directionally solidified and single crystal followed in the time sequence of development [1, 4, 5, 9, 10].

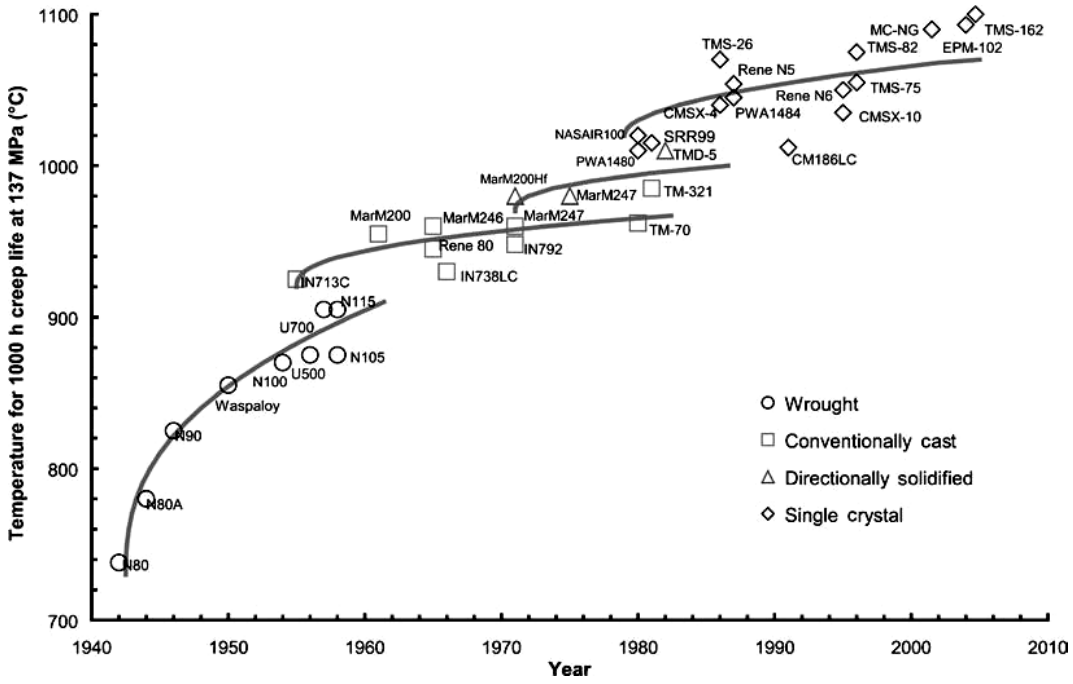

Figure 2.1. Evolution of the high-temperature capability of the superalloys over a 60 year period since their emergence in the 1940s [1].

2.2.1 Wrought

The wrought alloys were very popular in 1940s and 1950s, and were developed for use in aircraft turbine engines. The wrought alloys have excellent high-temperature tensile strength and creep resistance at 650°C, but this decreases sharply at 900°C. The poor strength and oxidation resistance at elevated temperature limits the applications of these materials. Even though, significant amounts of chromium and cobalt were added for solid solution strengthening, the strength of materials at high temperature is still weak due to the low volume fraction of gamma prime precipitates (γ'), the volume fraction of which determines the high temperature capability [5]. The details of this phase will be discussed in microstructure section.

2.2.2 Conventionally cast

The wrought alloys reached their limitation in the late 1950s. Further increase in the high temperature strength of these alloys was unlikely and difficulties were encountered when forging and machining complex components, such as blade [1]. Attention was moved to cast alloys, which increase the operating temperature by increasing γ' volume fractions. Moreover, the cast alloys also perform better in creep resistance and corrosion resistance. In addition, with the help of vacuum casting technologies, the quality and cleanness of alloys increased dramatically. For some applications, such as blades, cast is preferred due to its complex shape and design. However, poor mechanical performance, such as creep and fatigue, limit its further application. Since failures are preferential formed at transverse grain boundaries, which is a consequence of the equiaxed grain structures, see Figure 2.2a. The limitation of the microstructure and mechanical properties is the barrier for the development of the conventionally cast.

2.2.3 Directionally solidified

A significant improvement in performance of superalloys is attributed to the use of a directionally solidified casting process. It is found that the creep strength and ductility of superalloys are improved dramatically by using directionally solidified casting, which were developed in 1970s [2, 9]. This is because a columnar grain structure (Figure 2.2b) is produced, which removes the transverse grain boundaries and aligns the grains parallel to the blade axis and the applied stress [5, 10]. With this structure, the materials can afford more strength compared with equiaxed structure. However, the grain boundaries are still weak points of materials and they limit the application of this processing.

2.2.4 Single crystal

The single crystal alloys were developed from the directional solidification casting processes, which the single grain grows to encompass the entire part during solidification. Further improvement is achieved by complete removal of grain boundaries. In single crystal alloys, see Figure 2.2c, the grain boundaries are eliminated together with grain boundary strengthening elements such as carbon, nitrogen and zirconium, since they are no longer necessary. The absence of these elements increases melting point and provides improved flexibility in alloy composition and heat treatment [1, 5, 11]. With the help of removal grain boundaries, the even higher creep strength and thermal mechanical fatigue properties were achieved. The number of single crystal alloys has increased dramatically since the first single crystal - PWA 1480 was developed in 1970s [1]. Up to today, there are five generations of single crystal superalloys. The typical single crystal superalloys for each generation with their nominal compositions are shown in Table 2.1.

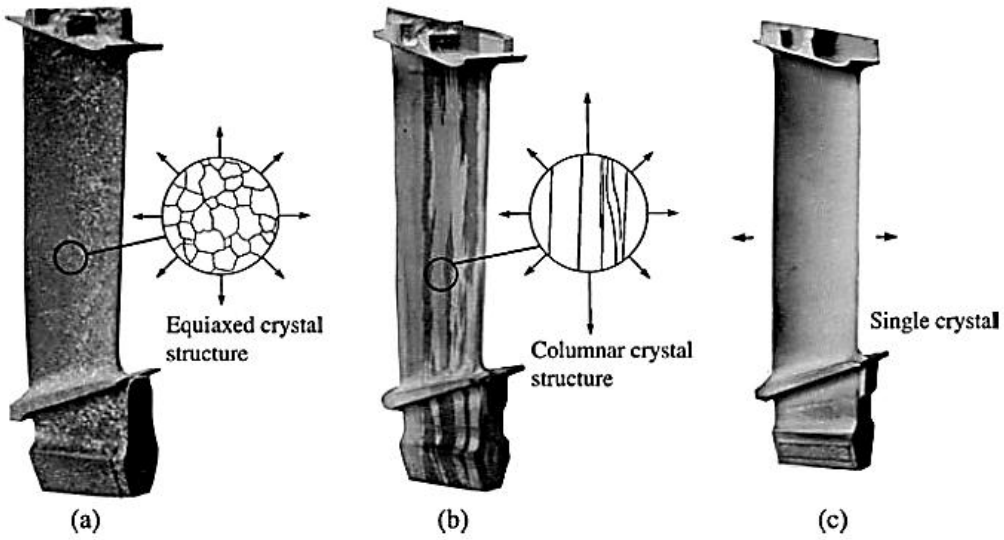

Figure 2 2. The different casted turbine blades in the (a) equiaxed, (b) columnar and (c) single-crystal form [1].

Table 2.1 The generations of single crystal superalloys and their nominal compositions (wt.%) [12-17]

	Cr	Co	Mo	W	Al	Ti	Nb	Ta	Re	Hf	Ru
1st Generation											
PWA1480	10.0	5.0	--	4.0	5.0	1.5	--	12.0	--	--	--
CMSX-2	8.0	5.0	0.6	8.0	5.6	1.0	--	6.0	--	--	--
2nd Generation											
CMSX4	6.5	9.6	0.60	6.4	5.6	1.0		6.5	3.0	0.1	--
PWA1484	5.0	10.0	2.0	6.0	5.6	--	--	9.0	3.0	0.1	--
Rene N5	7.0	8.0	2.0	5.0	6.2	--	--	7.0	3.0	0.2	--
3rd Generation											
CMSX10K	2.0	3.0	0.4	5.0	8.0			5.7	6.0	0.03	--
Rene N6	4.2	12.5	1.4	6.0	7.2		0.1	5.75	6.0	0.15	--
4th Generation											
MC-NG	2.0	3.0	0.4	5.0	5.7	0.2	--	5.0	4.0	0.15	4.0
TMS-138	3.2	5.8	2.9	5.8	5.8	--	--	5.6	5.0	0.10	2.0
5th Generation											
TMS-173	3.0	5.6	2.8	5.6	5.6	--	--	5.6	6.9	0.10	5.0
TMS-196	4.6	5.6	2.4	5.0	5.6	--	--	5.6	6.4	0.10	5.0
	Cr	**Co**	**Mo**	**W**	**Al**	**Ti**	**Nb**	**Ta**	**Re**	**Hf**	**Ru**

However, high cost is a big issue for these materials. The price of a modern

single crystal turbine blade is an order of magnitude greater than a directionally solidified one. This is not only because of the high cost of rare elements, such as Re and Ru, but more the high degree of technological sophistication required to produce a single crystal component [1, 4, 7]. The demand for high efficiency of gas turbine engines leads to continuously development of single crystal superalloys. Moreover, the longer service life reduces the frequency of the shutdown of the power plant and maintenance [1-5].

2.3 The Microstructures of Ni-Based Superalloy

The microstructures of Ni-based superalloys can be very complex and each phase has different effects on the mechanical properties. Generally, there are four major types of phases present in Ni-based superalloys, which can be summarised as the gamma phase (γ), the gamma prime precipitate (γ′), carbides and nitrides and Topologically Close-Packed (TCP) phases [1-5].

2.3.1 The gamma phase (γ)

The basic microstructure of any Ni-based superalloy consists of a gamma (γ) matrix. The γ phase is a face-centred-cubic (FCC) Ni-based austenitic phase (Figure 2.3a), which usually contains a high percentage of solid-solution elements such as Co, Cr, Mo and W [3, 18]. The γ phase is favoured by most gas turbine designers due to its excellent stability even at severe temperature for a long exposure times. This is important since any phase transformations, either during thermal cycling or operating will cause a reduction of high temperature properties and may lead to a failure of the components [1-5,18].

2.3.2 The gamma prime phase (γ′)

The primary strengthening phase in Ni-based superalloys is $Ni_3(Al,Ti)$, which is called the gamma prime precipitate (γ′). It is an ordered $L1_2$ crystal structure (Figure 2.3b), which is very close to γ structure, but with nickel atoms at the centres of faces and aluminium or titanium atoms at the cube corners [3, 5,19,20]. For single crystal Ni-based superalloys, the excellent mechanical properties at elevated temperature were contributed by containing high volume fraction of γ′ within the alloy [22]. The strength of most metals decreases as the temperature is increased, simply because assistance from thermal activation makes it easier for dislocations to surmount obstacles. However, nickel based superalloys containing γ′, which essentially is an intermetallic compound and particularly resistant to temperature. The similar lattice parameter of γ and γ′ and coherent, caused formation of anti-phase boundary, which makes dislocations in the γ nevertheless find it difficult to penetrate γ′, partly because the γ′ is an atomically ordered phase. The order interferes with dislocation motion and hence strengthens the alloy [3, 4-6].

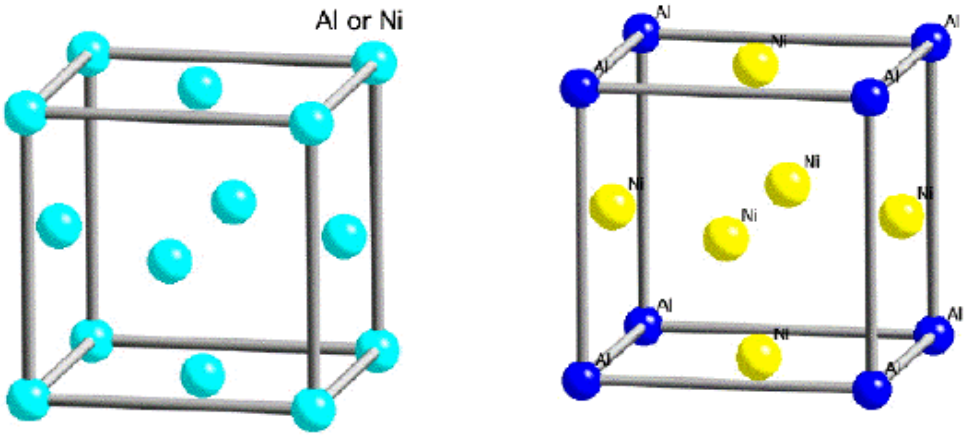

(a)FCC **(b) $L1_2$**

Figure 2.3. The crystal structure of γ and γ′ in Ni-based superalloy [3].

Figure 2.3 indicates that the $L1_2$ structure is similar to FCC structure. The close match in matrix lattice parameter leads to coherent interface between γ/γ′ when the precipitate size is small. The properties of the Ni-based superalloys are very dependent on the coherency of γ/γ′ interface. This is favoured by small values of the lattice misfit, δ, defined according to

$$\delta = \frac{2(a_{\gamma'} - a_{\gamma})}{a_{\gamma'} + a_{\gamma}} \quad (2.1)\ [19, 21–23]$$

Where $a_{\gamma'}$ and a_{γ} are the lattice parameter of the γ' phase and γ phase.

The degree of lattice misfit or mismatch between the γ and γ′ phase determines the morphology of the γ′ phase. For small values of lattice misfit (0-0.2%), the γ′ particles are spherical. As the misfit increases to 0.5-1.0%, the morphology of γ′ turns into cuboidal, finally it changes into plates or rafts at misfit greater than 1.25% [19- 22]. According to the literature [19- 22], for single crystal Ni-based superalloy, the cuboidal γ′ maintains its maximum performance of the alloy at high temperature exposure, with reasonable lattice coherency of γ and γ′. That is why most of the single crystal superalloys show uniform distribution of cuboidal γ′ within the microstructure before service exposure.

2.3.3 Carbides and nitrides

Carbides and nitrides can form within the microstructure of a superalloy with minor additions of carbon, nitrides, zirconium and hafnium. It is believed that carbides and nitrides have beneficial effects on rupture strength and creep properties at high temperature. This is because they prefer to form at grain boundaries, where they inhibit grain-boundary sliding and permit stress relaxation [12, 25–30]. This strengthening is utilised with both conventionally

cast and directionally solidified components. However, carbides influence ductility and chemical stability of the matrix via the removal of reacting elements. Moreover, the presence of carbides and nitrides tends to lower the solidus of the alloy, which limits the maximum heat treatment temperature and operating temperature of materials [1-6, 24]. Therefore, the amount of the carbon and nitrogen add into superalloy is tolerance by accurate design and controlled processing.

There are various carbides and the types of carbide are very dependent on the alloy composition and the processing conditions employed. The most common carbides and nitrides are MC, M_6C and $M_{23}C_6$ where M stands for a metal atom such as Cr, Mo, Ta and Ti [24, 26-28], with FCC structures. MC carbides (shown in Figure 2.4), usually take a coarse random cuboidal or script morphology and precipitate at high temperature, but they begin to decompose and form 'lower' carbides such as $M_{23}C_6$ and M_6C. M_6C carbides form at about 980°C, while $M_{23}C_6$ carbides precipitate at lower temperatures—around 750°C. Both M_6C and $M_{23}C_6$ carbides are usually found to form at grain boundaries, which enhances the grain boundary strength of materials [11, 26-28]. The $M_{23}C_6$ carbides tend to form in abundance within alloys that contain high amounts of Cr [11]. M_6C carbides form at 815-980°C in rare circumstances in Widmanstätten intragranular morphology [11]. This carbide is similar to $M_{23}C_6$ but is usually formed when there is a substantial concentration of Mo or W in the alloy. This stability at higher temperatures makes it beneficial as a grain boundary precipitate which can control the grain size within wrought and cast alloys.

Nitrogen is usually present in Ni-based superalloys within the range of 50-500 ppm. Nitrides form as TiN or HfN with FCC structure at the grain boundaries as MN, which block the onset of grain boundary tearing under creep rupture stress,

resulting in increased creep strength [25-30]. However, since the amount of nitrogen is so tiny, the influence of the nitrides on the mechanical properties is not as pronounced as carbides.

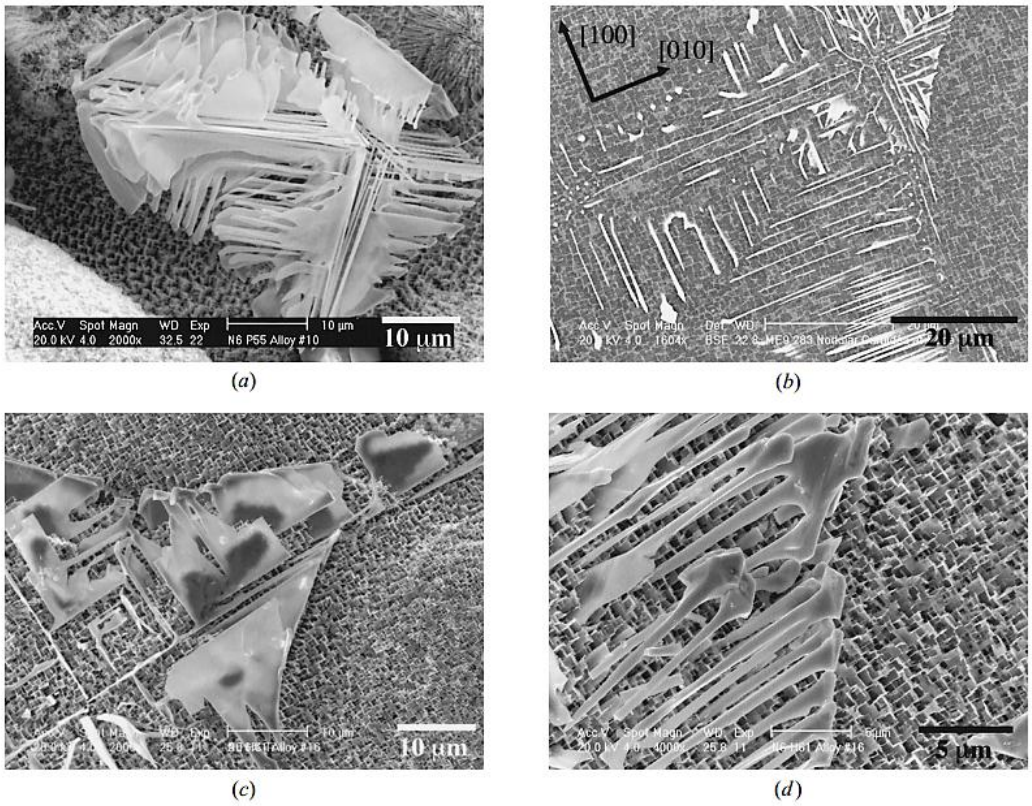

Figure 2.4. Example of MC carbide with different morphology formed in an experimental Ni-based single crystal superalloy [13] .

2.3.4 Topologically close packed phases

Topologically Close-Packed (TCP) phases are intermetallic compounds that generally form in service after long times at elevated temperatures due to the high concentrations of refractory elements such as W, Re, Mo, and Ta [1-3, 12, 33–37]. The name TCP comes from the structure of the phase, which has close-packed atoms in layers separated by relatively large inter-atomic distances, which looks like “basket weave” morphologies, see Figure 2.5. Due to this 'topological' structure, these phases are called Topologically Close-Packed

Phases and the formation of these phases can result in a deterioration of the mechanical properties, especially creep [12, 33–37]. The structure and composition of TCP phases are relatively complex and hard to distinguish by the normal SEM analysis. However, the common TCP phases, such as σ, P, μ and R, have distinct crystallographic structures, which can be easily distinguish by TEM diffraction. Table 2.2 is the summary of the TCP phases with their crystallographic structures and lattice parameters [32]. TCP phases are undesirable brittle phases, which can form either during the heat treatment or more commonly during service. The presence of TCP phases is detrimental for materials, as the precipitate and grow of TCP phase deplete the surrounding matrix of refractory solid solution strengthening elements, consequently weakening the matrix. Moreover, the TCP phases can de-laminate in the fracture zone and it is frequently associated with formation of voids, which potentially leads failure of the materials [12, 33-37]. Therefore, the amount of TCP phases should be reduced as much as possible in service.

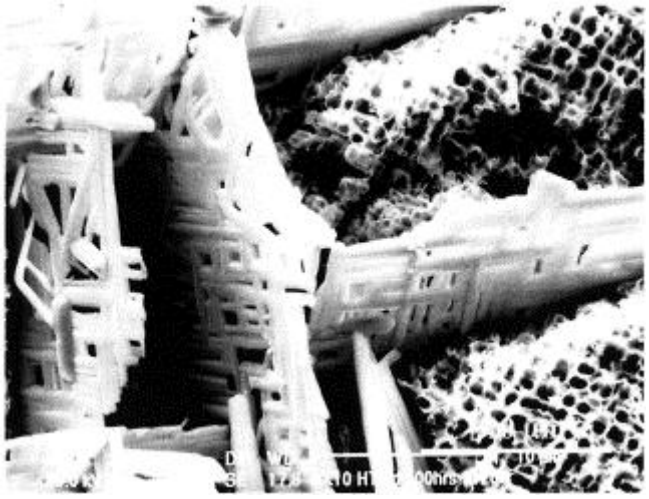

Figure 2.5. SEM image of deep-etched TCP platelets from alloy SX-2 revealing the characteristic “basket weave” pattern [11].

Table 2.2 Crystallography and lattice parameter of the TCP phases [36]

TCP phase	System	Lattice Parameter(Å)	*α*
σ	Tetragonal	a_0= b_0=9.12, C_0=4.72	90°
P	Orthorhombic	a_0= 16.90, b_0=4.71, C_0=9.04	90°
μ	Rhombohedral	a_0= b_0=4.73, C_0=25.54	120°
R	Rhombohedral	a_0= b_0=10.93, C_0=19.34	120°

2.4 Change of the Microstructure during High Temperature Exposure

Microstructure changes can occur during heat treatment or more commonly during service. The changes in morphology, size and distribution of constituent phases can affect the mechanical properties of the alloy and are dependent on the thermal exposure conditions and the applied stress. Knowledge of how the phases evolve with temperature and time is required for the realistic estimation of service life within components in order to avoid premature failures during service. In this section, microstructural evolutions of γ/γ′ and carbides in Ni-based superalloys under different conditions have been reviewed.

2.4.1 Microstructural evolution of γ/γ′

As it is the main strengthening phases at high temperature, microstructural change of the γ/γ′ precipitates is one of most important aspects in Ni-based superalloys, and can directly affects the mechanical properties of materials. In this section, two important changes (coarsening and rafting) of γ′ phase were reviewed, to provide a good understanding of the microstructural changes of Ni-based superalloy at elevated temperature

2.4.1.1 Coarsening

Coarsening refers to the mechanism by which there is an increase in average particle size at constant volume fraction [33–37]. Figure 2.6 is schematic showing the formation of γ′ platelets due to coarsening. The γ′ particles are observed to increase in size with increase in temperature and change their morphology. The initially cuboidal precipitates can group together, forming chain and block-like structures, which have a tendency to coalesce. These grouped precipitates can orientate in a specific direction depending on the degree of anisotropy such as residual chemical gradients resulting from segregation [10, 20, 40-42].

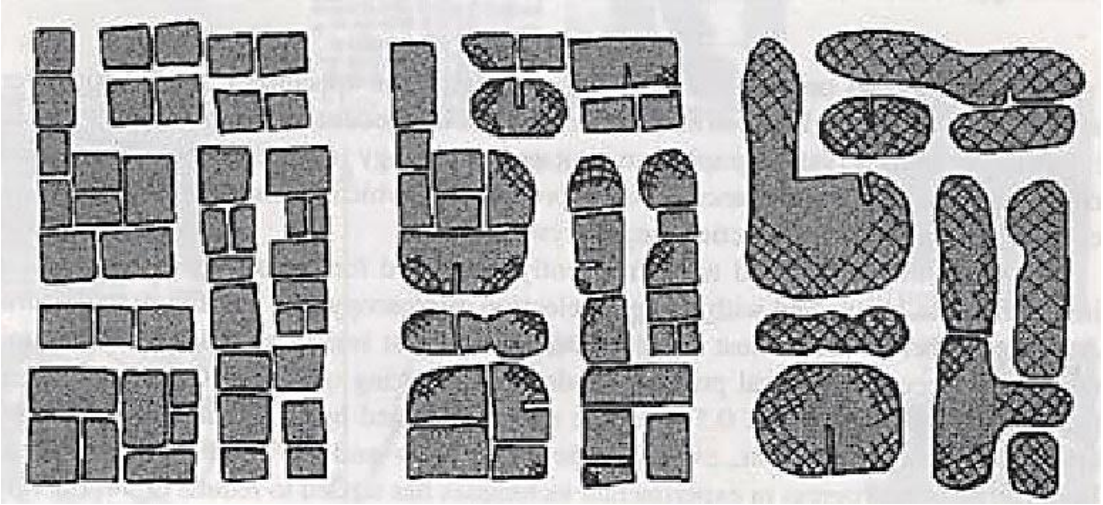

Figure 2.6. Schematic illustration of the coarsening and formation of the γ' platelets [5].

When Ni-based superalloys undergone continuous cooling from solution heat treatment, a few γ′ particles have been precipitated, with several morphology changes as they grow, as illustrated in Figure 2.7. The coarsening behaviour of the γ′ particles can be seen and the morphology of the precipitates is significantly changed [5, 37–39]. The morphology of γ′ precipitates are changed by the following sequence:

Sphere → cube → octocube →octodendrite → dendrite

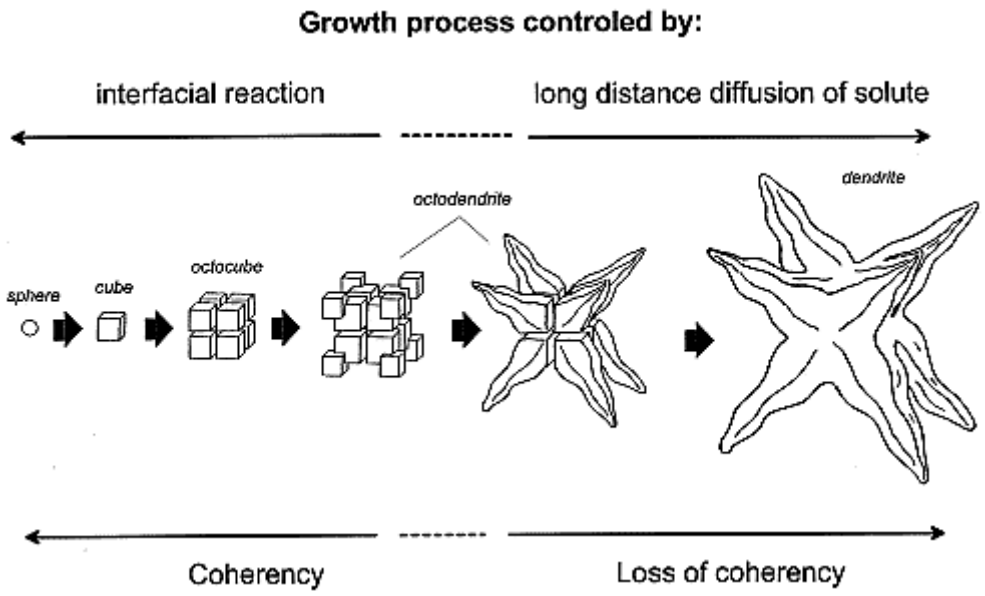

Figure 2.7. Schematic diagram showing the evolution of γ' morphology during continuous cooling [23]

In the absence of applied stress, the driving force for the morphology changes is the minimisation of the interfacial and elastic energy. In Figure 2.7, when the precipitate is very small (less than 200 nm), the interfacial energy is prominent, which leads to a spherical γ′ due to minimisation of the interfacial energy. As the precipitate grows, up to a few micrometres, the elastic energy dominates and cuboidal morphology is preferred. The octocube structure is formed by the splitting of a single precipitate. It is believed that the elastic energy associated with the octocubic morphology is lower than the one associated with the cuboidal morphology [5, 37-40]. Further growth leads to the formation of a γ′ octo-dendrite, which largely reduces the coherency of the γ/γ′ [22, 23]. This process is controlled by the diffusion of the solute. With coarsening of the dendrites, the diffusion distance of solute increases, which reduces the growth rate of dendrite and finally forms a stable dendrite in alloys. In Ni-based superalloys, the evolution of γ′ morphology and distribution during the cooling is strongly affected by elastic distortions associated with the γ/γ' misfit [22, 23]. A decrease in interfacial energy can be achieved by reducing the γ/γ′ lattice misfit, which in turn

increases its coherency. For a low growth rate of the γ′ precipitates, a coherent γ/γ′ interface and low lattice misfit is required, as defined by equation 3.1 [19, 21-23]. The majority of the single crystal nickel based superalloys have a negative lattice misfit, meaning that the lattice constant of the γ' phase is smaller than that of the γ phase. However, the misfit is seen to vary with temperature due to different thermal expansion coefficient of the γ and γ′. The microstructural changes that occur for the reduction of the total interfacial energy are the decrease in area of the various interfaces. This is achieved by precipitate coarsening, morphology changes of the precipitates and interactions of phase and grain boundaries [1, 2, 22, 26].

For spherical γ′ precipitates, the particle coarsening is the result of an exchange of solute atoms between the precipitates and the matrix. In other word, it is diffusion controlled process [4]. As a consequence of coarsening, larger particles will tend to grow at the expense of smaller ones, which is known as Ostwald ripening [40–44]. The growth mechanism of spherical γ′ precipitates is shown in the following equation:

$$(\bar{\gamma})^3 - (\bar{\gamma}_0)^3 = Kt \tag{2.1}$$

Where $\bar{\gamma}$ and $\bar{\gamma}_0$ are the average particle radius at time t and 0, respectively. The coarsening rate coefficient K is very depends on the materials, temperature and diffusion rate [20-22]. An example of this theory is shown in Figure 2.8, where the radius of the spherical γ′ precipitates has liner relationship with time.

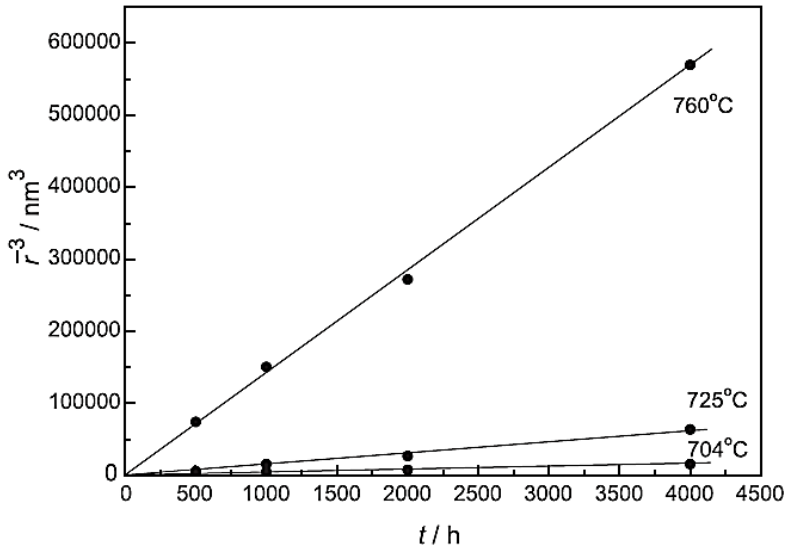

Figure 2.8. Coarsening rates of the γ′ precipitates in the designed new Ni-based superalloy at different temperatures [18].

2.4.1.2 Rafting

Directional coarsening of γ′ precipitates is observed after high temperature exposure and under an externally applied stress and is commonly referred as “rafting” [45–48]. Due to the combined influence of stress and temperature, the cuboidal γ′ precipitates coalesce to form rafted γ′ morphologies as illustrated in Figure 2.9. Rafting occurs in all single crystal Ni-based superalloys but is commonly generated under an applied stress [48][53][54]. This is because when stress is applied, there is a large elastic energy introduced along the stress direction, which forces the rafts to develop perpendicular or parallel to the direction of applied stress [49–51]. The specific direction of orientation of the raft depends on the direction of the applied stress with respect of the crystal structure, and on the sign of the lattice misfit between γ/γ′ [19, 21-23]. Generally, the orientation of a raft is perpendicular to the tensile stress direction and parallel to the compressive stress direction [45-49]. Figure 2.9 illustrates the relationship between the orientations of the γ′ rafting and applied stress.

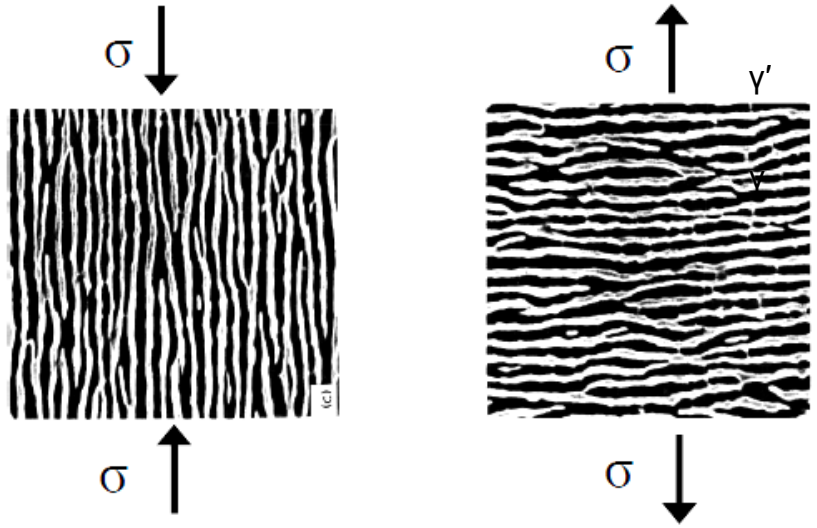

Figure 2.9. Typical SEM image showing the rafting of γ′ in the single crystal Ni-based superalloys under different directions of applied stress [49].

The degree of rafting is not usually uniform throughout components such as gas turbine blades, as it depends on the gradient of both temperature and stress as a function of time. During service, the response to stress across gas turbine blades is not uniform, therefore, difference in temperature and stress are experienced over the surface of the aerofoil, therefore, resulting in variations in rafting direction. However, generally, the rafting of the γ′ precipitates is orientated perpendicular to the blade axis, as it is along this axis the centrifugal stresses act. With this in mind it is possible to assess the remaining life of a component by the development and growth of rafting, including morphology and size, which are dependent on the time of stress applied at elevated temperatures [45-49].

Most Ni-based superalloys are precipitation hardened by a dispersion of fine γ′ particles. The mechanical properties of an alloy are strongly dependent on the size and distribution of the γ′ precipitates. The rafting rate of γ′ is very dependent on the stress, temperature and time. Basically, the rafting rate is increased by the increasing stress, temperature and time. This is because the rafting is a

diffusion controlled process, the higher stress and temperature results a higher diffusion rate and hence, faster rafting [31, 32]. Time is an important factor for the γ′ precipitate evolution. Figure 2.10 illustrates the relationship between the degree of rafting and time [32]. The size and morphology changes with times under the creep test. A uniform distribution of cuboidal γ′ particles with a size ~ 0.5 μm is observed before the creep test. The γ′ particles remain their cuboidal structure after 150 hours, but they tend to from small rafts after 280 hours. After that, the length of γ′ rafts increase but their width decrease with increasing time, which in other order is that degree of rafting has increased with increasing time. The degraded microstructures with well-developed rafts are observed after 1000 hours with long γ′ rafts and wider γ channels. The presence of the wider γ channels in the microstructure which affects the movement of the dislocations, later affect the mechanical properties of materials [31-32].

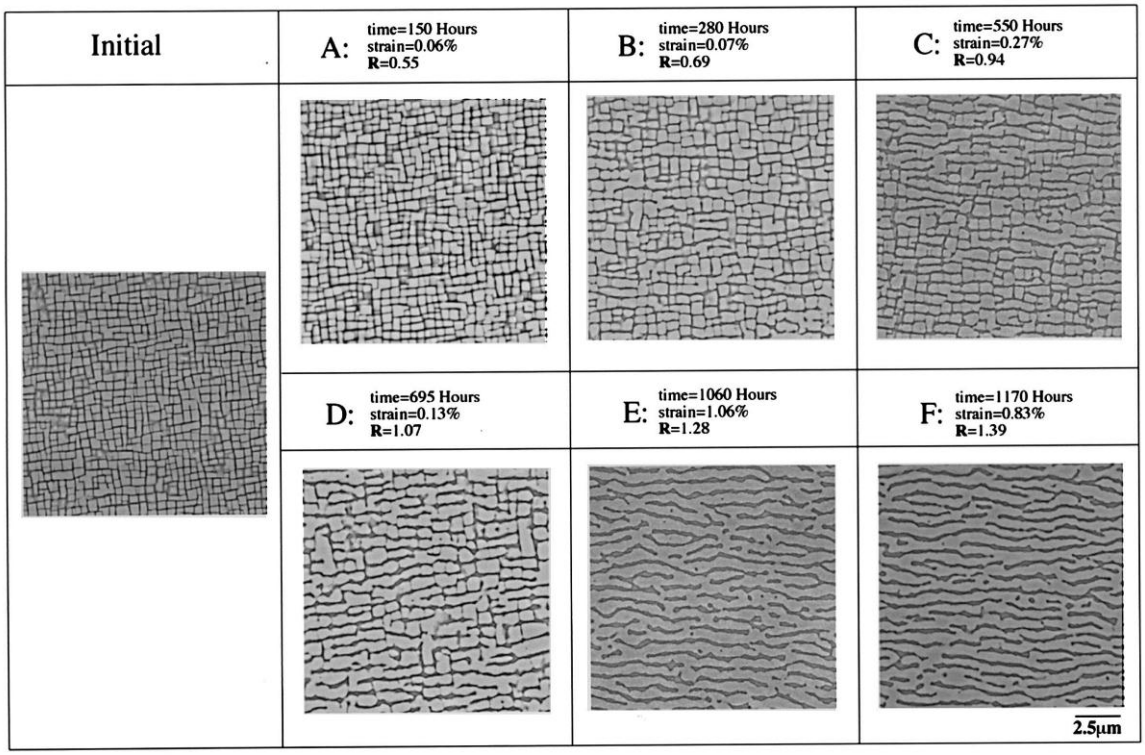

Figure 2.10. The rafting behaviour of γ′ at different time during creep test at 185 MPa and 950°C for 150, 280, 550, 695, 1060 and 1170 h. The microstructure of CMSX-4 in the pre-crept condition is also shown for comparison [32].

2.4.2 Microstructure evolution of carbides

In Ni-based superalloys, about 0.05-0.2 wt.% carbon is added to combine with refractory elements such as Mo, W and Re to form carbides [24-28]. The carbides have beneficial effects on the rupture strength and creep properties. However, the types of carbides change in different heat conditions [24, 25, 29]. Therefore, it is very important to understand the changes in carbides and carbide reactions during cooling. Chemical composition and temperature are two key factors affecting these changes.

MC, $M_{23}C_6$ and M_6C are the three most common carbides in Ni-based superalloys. The M in MC is mainly composed of Ta, Ti and Hf at higher temperature. When temperature reduces, MC begins to decompose to form M_6C and $M_{23}C_6$. M_6C has a cubic structure and forms at higher temperatures (815–980°C). The reaction is shown as follows:

$$MC+\gamma \rightarrow M_6C+\gamma'$$

M_6C carbides tend to form at W and Mo rich regions and they usually prefer to precipitate on grain boundaries, which has been confirmed through EDX analysis [2, 12, 25-29]. Since M_6C carbides are more stable at higher temperature, M6C is more beneficial as a grain boundary precipitate to control grain size of polycrystalline superalloys. $M_{23}C_6$ is similar to M_6C but it more likely to be found at Cr rich regions and they form during lower temperature (around 760°C) heat treatments or service. The reaction is shown as follows:

$$MC+\gamma \rightarrow M_{23}C_6+\gamma'$$

Both $M_{23}C_6$ and M_6C prefer to precipitate on the grain boundaries, which have significant effects on alloy properties. Their critical location at grain boundaries increases rupture strength by inhibition of grain boundary sliding [2, 24].

From early research of Ni-based single crystal superalloy, there is no carbon or little carbon in the composition, which means no or few carbides within the microstructure. Because the removal of the grain boundary makes these carbides become unnecessary. However, later research points out that for modern Ni-based single crystal alloys, the addition of carbon has beneficial effects to the superalloys, which reduces the extent of segregation for refractory elements by forming of carbides instead of TCP phases [28, 29, 31-33]. For recently developed Ni-based superalloy, high level of mechanical properties is achieved due to the large contents of refractory elements such as Mo, W and Re. However, the excessive amount of these elements promotes the formation of TCP phases, which were shown to have deleterious effects on the mechanical properties. This problem has been solved by reintroduction of carbon in the single crystal alloys.

2.5 Change of Mechanical Properties during High Temperature Exposure

Since the mechanical properties and microstructure of Ni-based superalloys are linked, the microstructural degradation during service and, in particular, the rafting and coarsening of γ′ precipitates, can significantly affect the mechanical properties of the materials. Creep behaviours as one of the most important life-limiting factors, the change during high temperature exposures require detailed investigation.

2.5.1 Creep behaviour

The size and distribution of γ′ precipitates have significant influence on the creep properties of materials. The high level of creep strength of superalloys is mainly

due to the presence of fine and well distributed γ′ precipitates in the matrix [38, 41, 52–55]. The reduction of creep resistance during service results from microstructural degradation such as rafting of γ′ precipitates and the formation of TCP phases and creep cavitation [45, 58, 60–67]. Figure 2.11 shows the evolution of the γ-γ′ microstructure in CMSX-4 during creep at 1100°C and 120 MPa, and Figure 2.12 shows the relationship between the channel width and time [53, 54].

(1). The rafting direction of γ′ precipitates is perpendicular to the creep stress and the degree of rafting increased with increasing time.

(2). Under this testing condition, the evolution of the γ-γ′ microstructure results in an initially cuboidal structure to a plate-like structure. Moreover, the channel width between these γ′ particles increases with time.

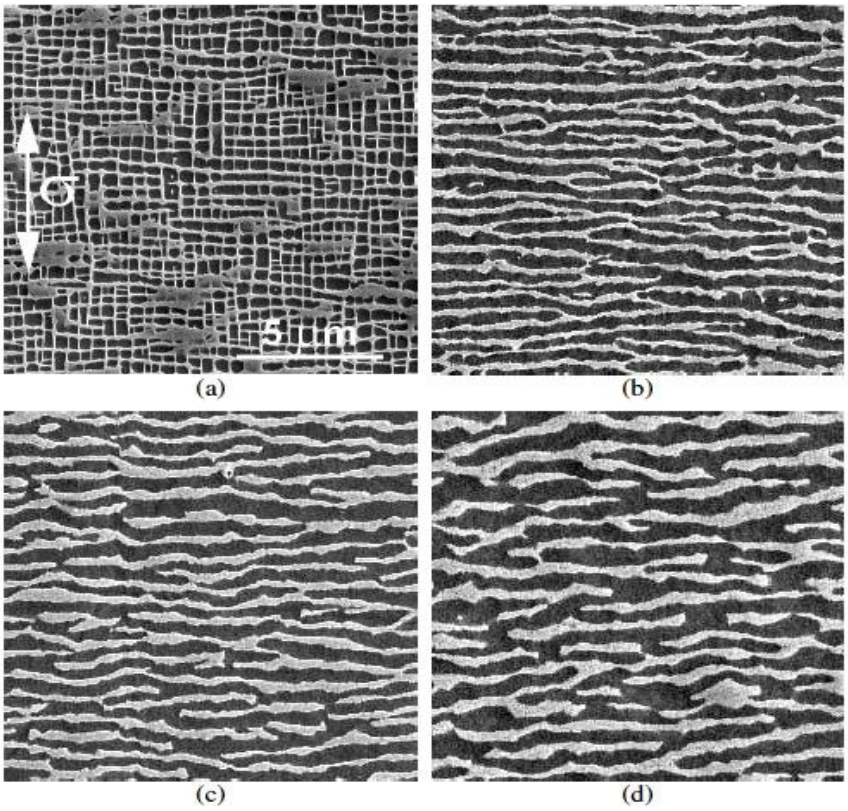

Figure 2.11. Evolution of the γ-γ′ microstructure in CMSX-4 during creep at 1100 and 120 MPa (Image taken in the secondary dendrite arms). (a) 4h primary creep; (b) 25h, transition primary to steady creep; (c) 150h, middle of steady creep; (d)393h, rupture, far from the rupture surface [34].

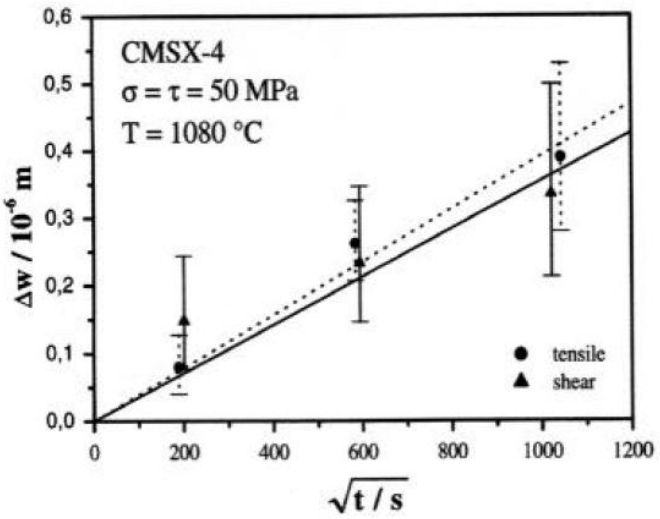

Figure 2.12. Change of channel widths with time under uniaxial and shear creep test conditions [29].

As the primary strengthening phase, the size, morphology and spacing of γ′ precipitates are very important to the mechanical performance of a component. In Figure 2.11, at the very beginning of the creep test, the γ′ is cuboidal with a small spacing, or in other word called, γ channel width. And it is believed that the presence of the well distributed cuboidal maintain the maximum mechanical properties of the materials. With continuous degradation, γ/γ′ microstructure changes during creep test: γ′ gradually coarsening and rafts form after directional coarsening, which later become irregular. With this continuous degradation, the γ channel width becomes larger. The critical value for the channel width for rafts formation, Wc, is three times of the cuboidal channel width. Rafting and increasing of γ channel width cause a reduction of the creep resistance and later leads failure of materials [47, 57, 63–69].

In some case of pre-heat treatment, there are two kinds of γ′ precipitates: the secondary γ′ precipitates, which are cuboidal with a size of ~ 0.5 μm, with tertiary γ′ precipitates, which are spheroidal with a diameter around 50 nm, are located

in the channels between the secondary precipitates [59, 60, 68–70]. When the size and spacing of secondary γ′ precipitates is small, dislocations move through the precipitates by shearing or cutting. The small spacing and presence of tertiary γ′ precipitates largely inhibit the movement of dislocations. This structure improves the creep properties of materials by providing effective barriers to prevent dislocation gliding and climbing around γ′ precipitates, see Figure 2.13 [79]. The rafting of secondary γ′ precipitates increases their size and spacing, which makes the channel wide enough for dislocation to glide. In addition, the coarsening of secondary precipitates is contributed to at the expense of tertiary γ′ precipitates. These changes make it much easier for the dislocation to pass through and finally lead to a decrease in creep properties [60, 68-70].

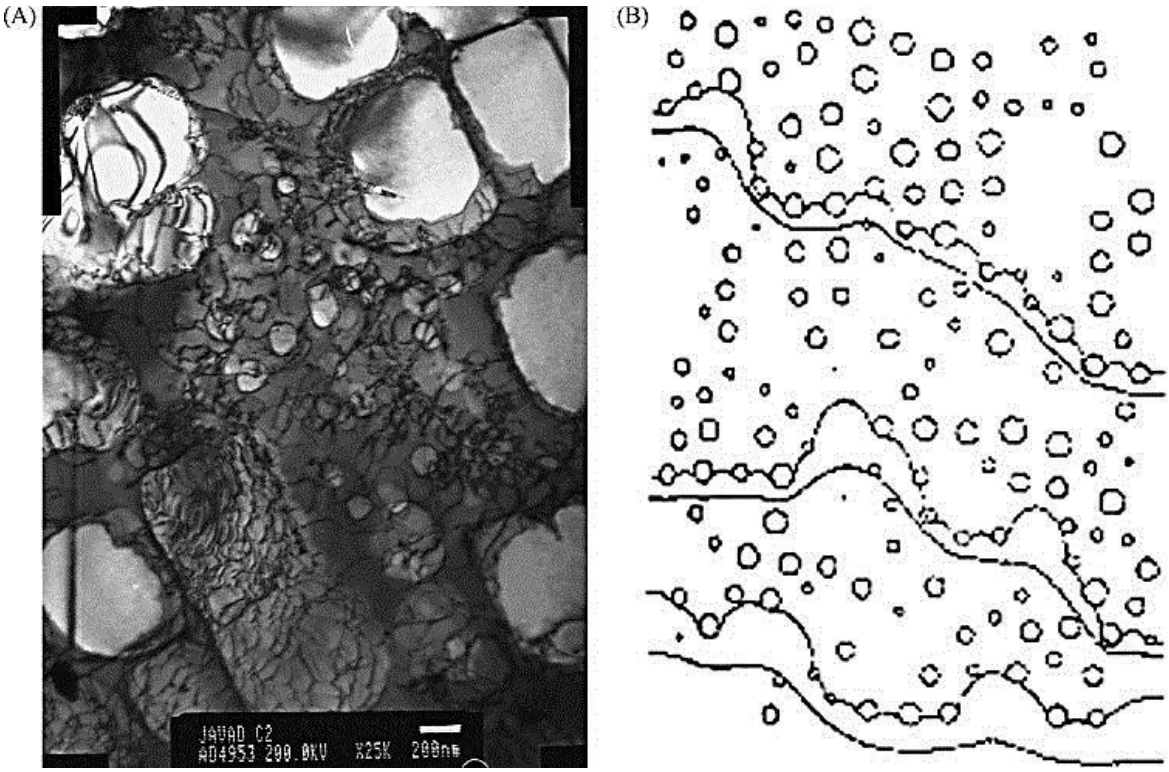

Figure 2.13. TEM microstructure during creep at 871 °C under a stress of 290 MPa after 0.5% creep strain, (a) dislocation glide and climb and (b) dislocation pair movements in superalloy containing ordered particles (schematically) [64][80].

2.5.2 Cavities and cracks

The formation of creep cavitation is another important reason for the loss of creep properties. During service, cavities are initialled and associated with some defects such as casting porosity and topologically close-packed (TCP) phases, see Figure 2.14. These isolated cavities can grow due to stress directed vacancy flow, especially at high temperature because this is a diffusion-controlled process. The growth and coalescence of cavities along the grain boundaries produces cracks, which finally leads to creep fracture [81]. For single crystal Ni-based superalloy, the linkage of the isolated cavities forms orientated cavities and micro-crack, which leads crack growth and propagation into the material, results a final failure to the material. Therefore, a reduction of these defects as much as possible has beneficial effects on the creep properties.

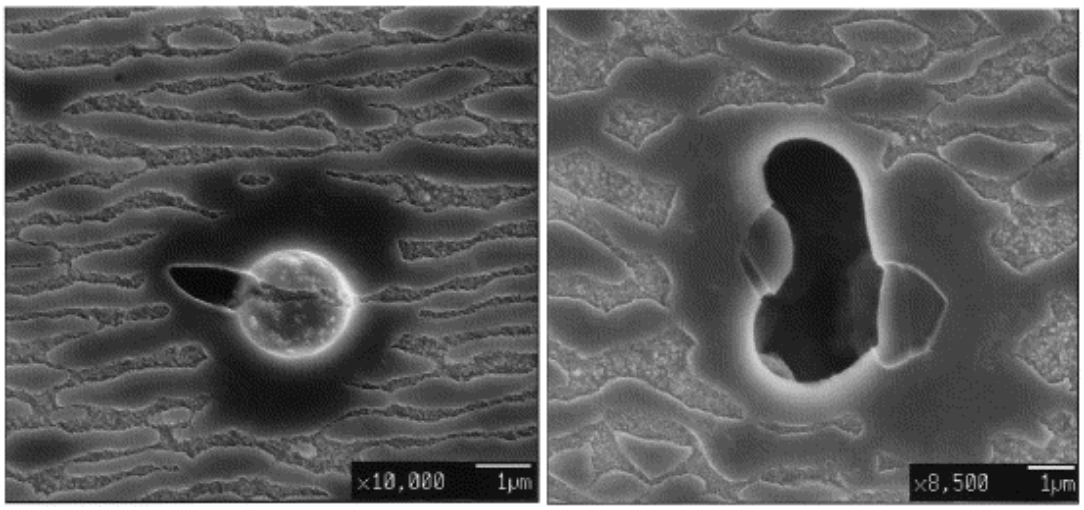

Figure 2.14. SEM images illustrating creep cavitation associated with casting pores (left) and topologically close-packed (TCP) phases (right) [39].

Crack is another important factor to determine the life of the materials. Commonly, the crack life of material can be divided into three stages[9]:

- Crack initiation or crack nucleation
- Crack propagation
- Failure

As describe above, the crack is initialled with defects inside the material, such as cavities, TCP phases and porosity. Once the crack is formed, it will link the nearby cracks to form macro-cracks, or it grows into the material by crack propagation. For Ni-base superalloy, the crack propagation is always along the weak phase. During creep, the cracks initial and propagate easily along the γ channels, which lead final failure to the sample [76–80]. Figure 2.15 shows some example of the crack initiation of the CMSX-4 superalloy during the fatigue test [79–84]. Once the crack is formed, it grows quick and very difficult to eliminate, since it is permanent damage and cannot recovery from conventional refurbishment [83]. Therefore, reduce the amount of the casting porosity and TCP phase will help enhance the life of the material by reducing or delay the crack formation.

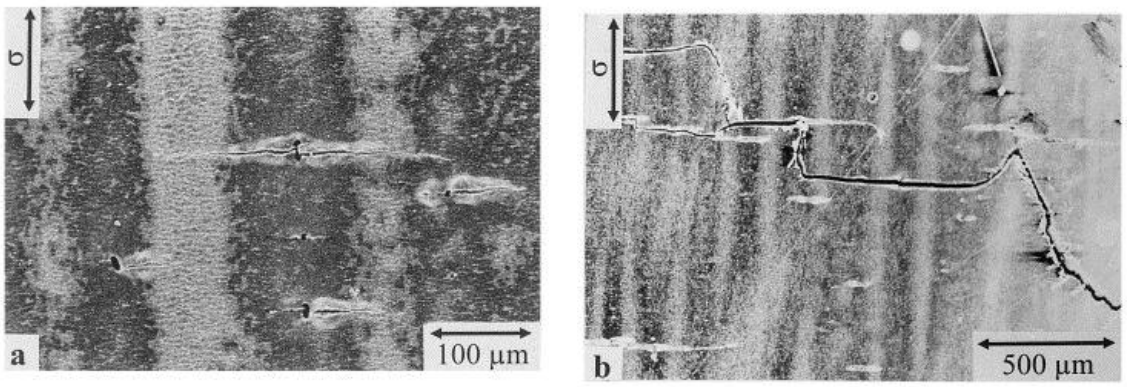

Figure 2.15 Crack initiation at the surface of specimens of the alloy CMSX-4 after fatigue at T=1050°C, Δεt=0.9%. (a) Singular cracks at a surface casting porosity; (b) crack formation at the surface through linking-up of short cracks [85].

Once the crack forms, it will grow very fast. Research studies show that in Ni-based superalloys, whether the cracks propagate in the γ or in the γ-γ′ interface is very strongly influenced by the γ-γ′ morphology [77–81]. Figure 2.16 gives an overall view of the fatal crack propagation observed in the alloy CMSX-4 during fatigue test [79]. The cracks are perpendicular to the stress direction in the specimen with cuboidal γ′-particles and with γ/γ′-rafts perpendicular to the stress axis. This suggests that the crack is able to propagate along the γ channels between γ′ particles, especially for the specimen with γ/γ′-rafts perpendicular to the stress axis, in which the extended γ channels encourage the crack propagation. Thus for these two microstructures, once a crack is formed, it can propagate very fast. However, for the specimen with γ/γ′-rafts parallel to the stress axis, the crack propagation obliquely to the stress axis in the γ phase. The γ′ particles lie perpendicular to the crack path and act as an obstacle to delay the crack propagation in the early stage, which extends the fatigue life of the specimen. Later, the crack deviates in the direction of the γ/γ to avoid cutting γ′ particles. This is because cutting of the γ′ particles by dislocations would require the formation of a high energy anti-phase boundary [85]. The detail of cyclic life of CMSX-4 specimens with three different kinds of γ/γ′-morphology is shown in Figure 2.17.

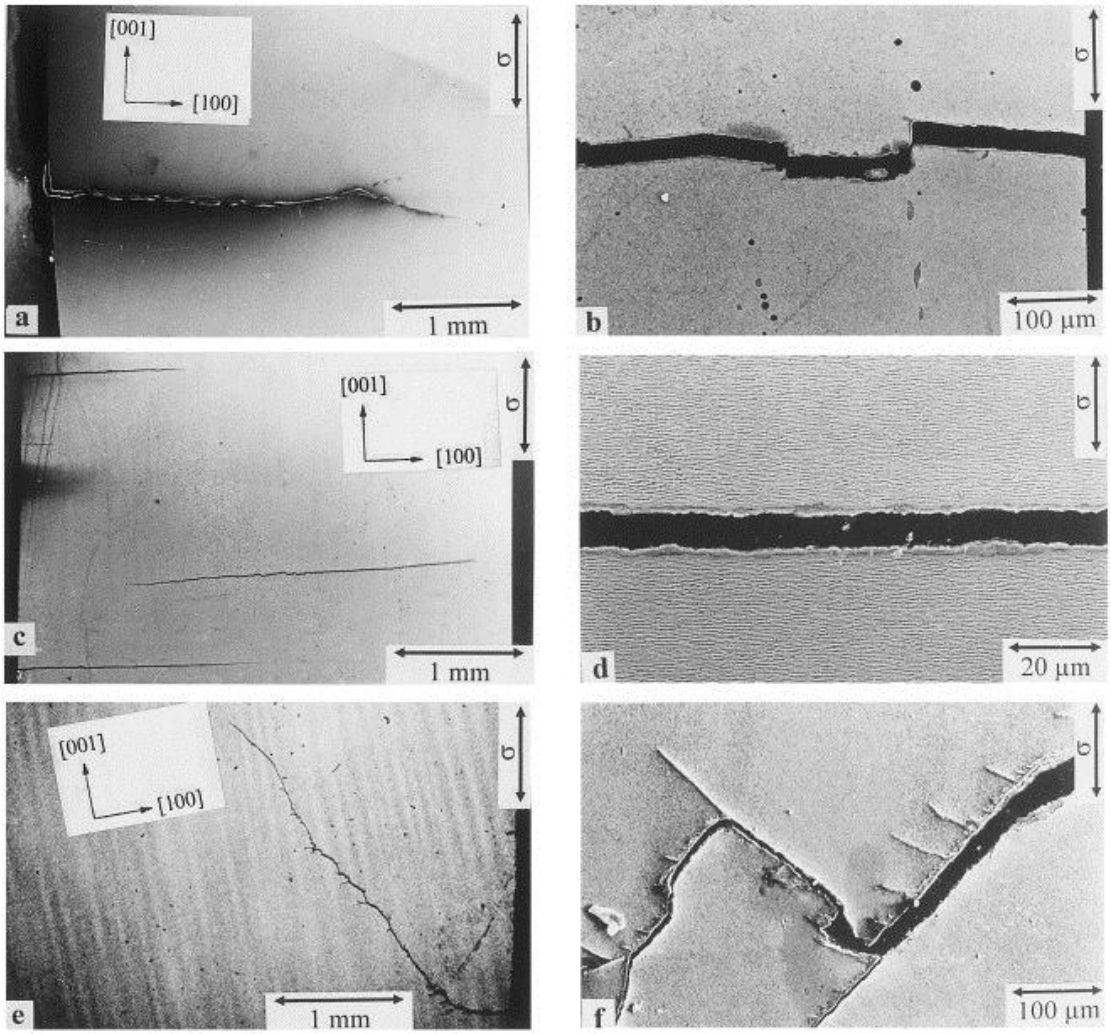

Figure 2.16 Fatigue crack propagation in the alloy CMSX-4 after fatigue at 1050°C, Δεt=0.9%. (010)-section parallel to [001]. (a, b) A specimen with cuboidal γ′-particles; (c, d) a specimen with γ/γ′-rafts perpendicular to the stress axis; (e, f) a specimen with γ/γ′-rafts parallel to the stress axis [79].

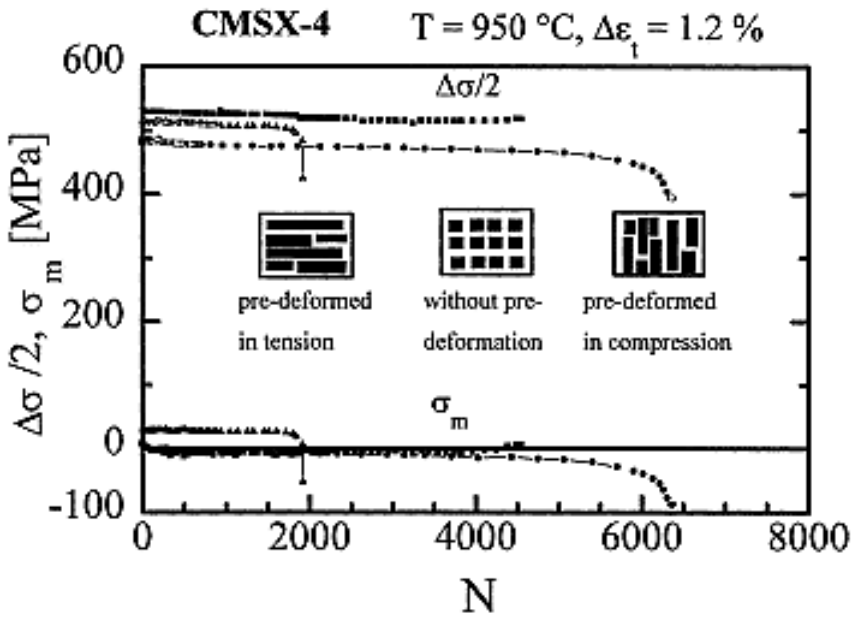

Figure 2.17. Cyclic deformation curves of CMSX-4 specimens with three different kinds of γ/γ′-morphology. The three initial γ/γ′-morphologies are indicated schematically. T=950°C, Δεt=1.2% [79].

2.5.3 Larson-Miller parameter

Since the creep behaviour is very important in determining the life of the material, therefore, there are a few way to predict creep life of the material, one of the most common technique is Larson-Miller parameter, which can be described by the following equation:

$$LM = T[logt_r + C] \quad (2.3)$$ [1, 81–84]

Where T is the temperature in kelvin temperature scale, t_r is the stress-rupture time in hours, C is the constant usually to be about 20, independent of the material.

When creep tests for various combination of stress and temperature, are carried out, the relationship between the temperature, time and creep life can be

determined by using Larson-Miller parameter diagram. Figure 2.18 is the typical diagram about the relationship between Larson-Miller parameter and applied stress. For example, the performance of the SRR99, CMSX-4 and RR300 are compared, which were 1st, 2nd and 3rd generation of single crystal Ni-based superalloy. For the same applied stress and temperature, we can found the Larson-Miller parameter was shift towards the right as the creep life has arisen due to increased creep resistance by designed from metallurgist [1]. For the same Larson-Miller parameter, the creep time massive decreased if the applied temperature is higher. Therefore, a long reality creep life of materials can be predicted by using a higher temperature but shorter creep time in laboratory, which save massive time and cost for the testing. Figure 2.19 is another example from E.ON literature data of the stress rupture test conducted on virgin CMSX-4 superalloy, where the creep life of the material under different applied stress and temperature were shown as follow functions. Based on this Larson-Miller diagram, the predicted creep life for the selected stress-rupture test conditions (red dot), under 425MPa at 900°C, is about 250 hours, which has a good agreement with practical creep test time (257 hours) [7]. Therefore, Larson-Miller parameter is very useful tool for the life prediction of the Ni-based superalloy.

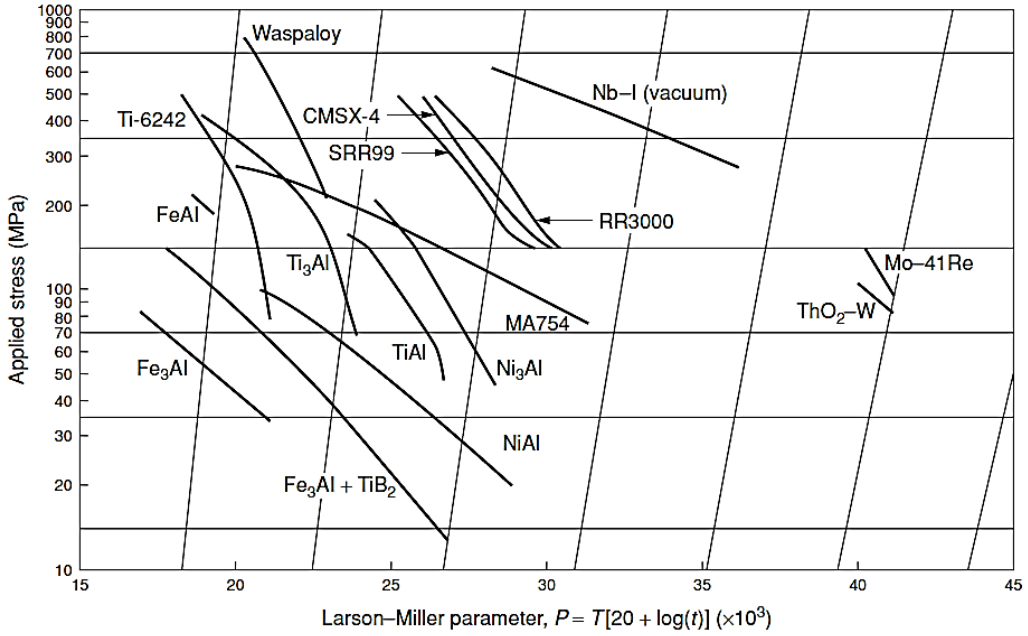

Figure 2.18. The example of the Larson miller parameter used for the life prediction of the different type of Ni-based superalloy for the power plant application [1].

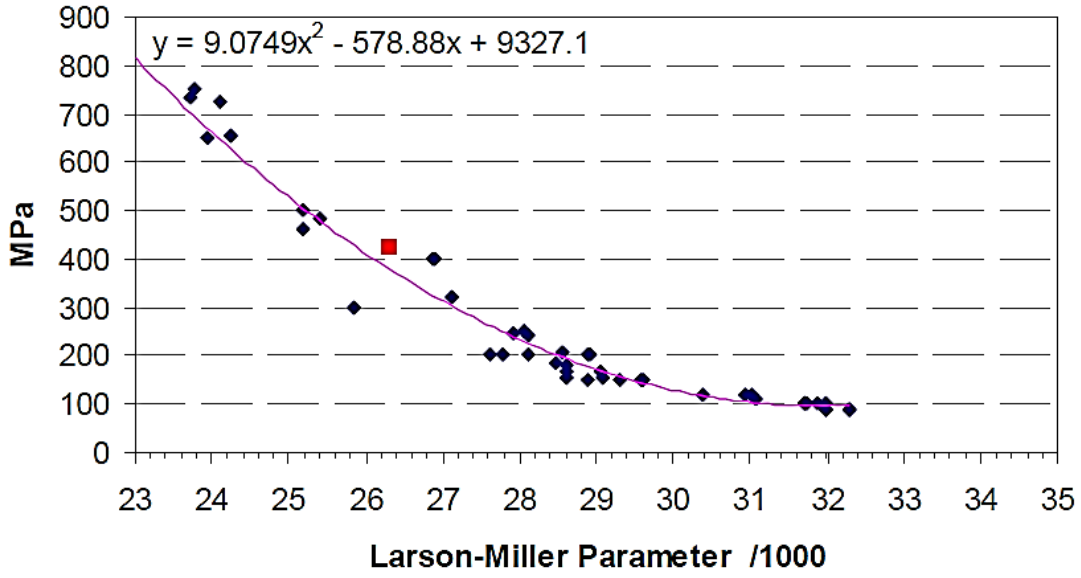

Figure 2.19. Literature date of the stress rupture test conducted on virgin CMSX-4 superalloy, the red dot is E.ON stress-rupture test condition [7].

2.6 CMSX-4

The increasing demand for higher efficiency and performance of the gas turbine engine has led designers to seek higher performance materials. The problem has been solved through the use of single crystal Ni-based superalloys. CMSX-4 is widely used as turbine aerofoil materials in jet engines and industrial gas turbines to increase the turbine inlet gas temperatures and improve fuel efficiency and performance with a lower life cycle costs. This superalloy was developed by Cannon Muskegon Corporation for the use of solar turbines in the late 1980s. CMSX-4 is a second-generation single crystal Ni-based superalloy and it can be operated at temperature up to 1163°C [96]. It provides excellent creep and fatigue strength at elevated temperature with improved oxidation and corrosion resistance. The excellent properties of this material are achieved by the balance of chemical composition. Table 2.3 shows the typical chemical composition for CMSX-4 [97].

Table 2.3 The typical chemical composition for CMSX-4 [96]

	Al	C	Co	Cr	Fe	Mo	Ni	Re	Si	Ta	Ti	W
Wt.%	5.6	0.006	10	6.5	0.15	0.6	60.5	3.0	0.04	6.5	1.0	6.4

As the second generation of Ni-based single crystal superalloy, CMSX-4 contains about 3 wt.% rhenium (Re), and other refractory elements such as tungsten (W) tantalum (Ta) and molybdenum (Mo). Excellent high temperature strength, creep properties, long term stability is due to the addition of these elements, by enhance γ phase at elevated temperature. However, adding these elements increases the density and cost of the materials, since the rare earth elements are very expensive. Moreover, the presence of high amount of these

elements can promote the formation of TCP phases, which are detrimental for the mechanical properties when material is exposed at high temperature [1,4,93-96].

CMSX-4 contains about 70% volume fraction of γ′ in alloy. The high volume fraction of γ′ results from the high concentration of Al and Ti added in the materials. No carbon or very little carbon is another interesting feature. The reason for that is the removal of the grain boundary makes these grain boundary strengthers become unnecessary [4, 96-97]. The solution temperature has increased by removing of these boundary strengthers phases and elements. The solution heat treatment window is quite narrow for fully dissolve γ′ and eutectic γ′ and γ-γ′ solutioning without incipient melting. Since this superalloy is often used with thermal barrier coatings, therefore, lanthanum (La) and yttrium (Y) have added in ppm level for enhanced bare oxidation resistance and thermal barrier coating adherence [99].

2.7 Coatings

The demand of high efficiency of gas turbine leads higher operating temperature, which increases the needs of high temperature materials. However, the aggressive working environment in aircraft and industrial gas-turbine engines, cause the metal dissolution, oxidation and corrosion, results potential damaging and limits the life of the Ni-based superalloy. Thermal barrier coatings (TBCs) were used to provide protective coatings against high temperature, oxidation and corrosion of gas turbine components [88, 95–102]. TBCs has lower thermal conductivity to provide thermal insulation to the substrate or metallic component from the hot gas stream in gas-turbine engines used for aircraft propulsion and

power generation [99-102]. The use of TBCs (100 to 500 μm in thickness), along with internal cooling of the underlying superalloy component, provide major reductions in the surface temperature (100°C to 300°C) of the superalloy, which leads the operating temperature above the melting temperature of superalloy, results a higher efficiency and performance [95-102]. Extensive use of TBCs on superalloy substrates is evident within gas turbine engines such as combustors, blades and vanes. These components operate within a highly aggressive environment due to increased inlet gas temperature.

Thermal barrier coated components consist four layers, each have their different physical, thermal and mechanical properties and functions. The typical TBC structure is illustrated in Figure 2.20. where the structure are substrate, bond coating, thermally grown oxide (TGO), and the ceramic top-coat [102].

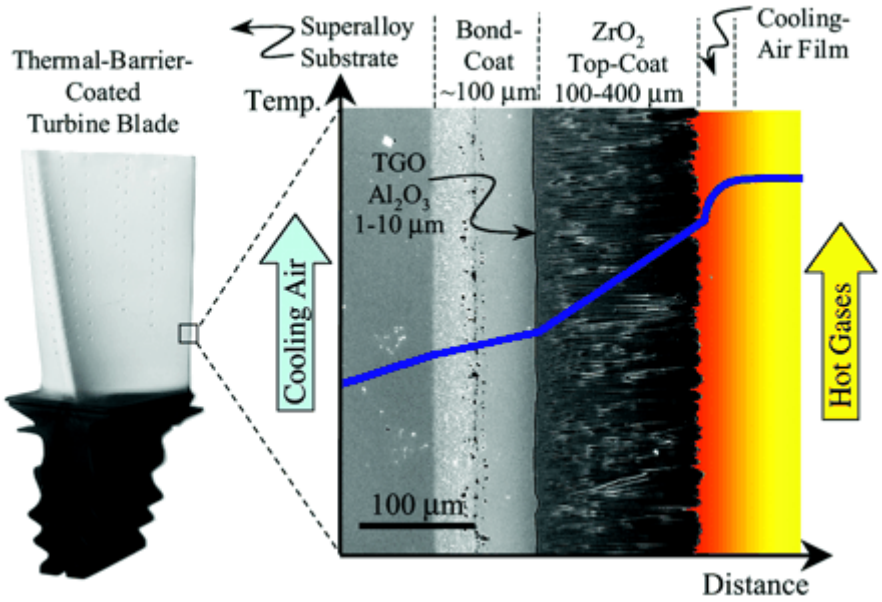

Figure 2.20. Cross-sectional scanning electron image (SEM) of an electron-beam physical-vapour deposited (EB-PVD) TBC, showing substrate, bond coating, TGO and ceramic top coating [102].

Substrate: typical is Ni-based superalloy for the industrial gas turbine engine, which was casted in polycrystalline or single crystal form.

Bond coating and TGO: the bond coating is oxidation resistant metallic coating, which is about 75-100 μm in thickness. It typical made of NiCrAlY or NiCoCrAlY alloy deposited on top of the substrate by physical-vapour deposition (PVD) or plasma-spray. The bond coating not only provides excellent oxidation and corrosion resistance, but also gives a good adherence for the coatings. During the service, the bond coating oxidised and formed the third layer called thermally grown oxide (TGO), which is about 1 to 10 μm. The presence of this layer stops the diffusion of oxygen from the working environment and protects the bond coat. Once this layer disappears, the coating will fail very fast. That is one of the most common failures of the TBCs.

Ceramic top-coat: this layer is typical made of Y_2O_3-stabilized ZrO_2 (YSZ), which provides excellent thermal insulation and corrosion resistance.

MCrAlY overlayer coatings

There are two main types of bond coatings, which are diffusion coatings and overlay coatings. The diffusion coating is more often used in aerospace application, while overlay coatings is more common in land-based industrial gas turbine engine [95, 97, 102]. One of the most recent advanced overlayer coating is the MCrAlY coating[96, 102–108]. The major element retarding oxidation and corrosion of a coating is Al and Cr. The presence of small amount of Y, Si and Hf can enhance oxide scale adhesion and decreases oxidation rates [103-108].

The major microstructures of coating are β and γ, depending on the composition and temperature. The presence of γ increases the ductility of coating and thereby improves the thermal fatigue resistance. β is always described as an

aluminium reservoir and the coating life is often measured by depletion of β. This is because high temperature expose in service causes Al depletion, which was not only due to diffusion of Al from coating to substrate, but also due to formation of TGO [97-102,105]. In practical, the coating is often failure earlier before β is fully depletion. This is because the formation of TCP phases, carbides, voids and porosity cause oxidation, corrosion and spall of the TBCs [91].

2.8 Refurbish Treatment

Ni-based superalloys are widely used as blades in gas turbines for the power generation application. The blades work at temperatures up to 1150°C under high stress in an aggressive environment [1-4]. With a long-term exposure at such aggressive operating conditions, the service lives of components are limited by creep, mechanical fatigue and corrosion due to microstructural degradation [81-85, 109, 110]. The high cost of the replacement components has tended to lead to the use of reconditioned components, which can extend their service lives by appropriate refurbishments [90, 109–112]. The rejuvenation as one of the most common refurbishment is welcomed in industry. Rejuvenation heat treatment usually preformed at temperature above the γ′ solvus temperature and is capable of regenerating a microstructure to something close resembling that of the alloy before service exposure [109, 113–115].

2.8.1 Rejuvenation

Generally, the rejuvenation of Ni-based superalloys involves two types of heat treatments: solution heat treatment and ageing. The solution heat treatment is used to dissolve the degraded γ′, γ-γ′ eutectic, TCP phases and carbides

resulted from the service or high temperature exposure. The ageing heat treatment, typically at 870°C, is applied to precipitate additional γ′ and other phases such as carbides and nitrides on grain boundaries, which strengthens the material [4, 7, 109, 113-115].

2.8.1.1 Solution heat treatment

High temperature exposure in service causes a few microstructure degradations, which have three main effects:

1. Coarsening and rafting of γ′ precipitates: the size, spacing and degree of rating of γ′ precipitates increased and cause a mechanical properties reduction.
2. Increased chemical segregation: the chemical segregation between dendritic and interdendritc region has increased due to different diffusion rate of elements after high temperature exposure.
3. Formation of the secondary phases: the presence of refectory elements such as W, Re and Ta promotes the formation of the secondary phases, such as TCP phases, which can prove detrimental and significantly reduce the mechanical properties of materials [4,7,16].

In order to reduce or eliminate these degradation effects, solution heat treatment was applied, which usually holding at temperature above the γ′ solvus temperature and are capable of dissolving degraded structure and regenerating a microstructure to something close resembling that of the alloy before service exposure. It should be noted that the temperature of solution heat treatment should be well controlled. It must be high enough to dissolve the interdendritic particles and precipitates (above the γ′ solvus), but not too high to melt the materials (below the incipient melting temperature). Commonly, a solution heat

treatment “window” is used to identify the temperature range of treatment. The typical CMSX-4 solution heat treatment window is 1280-1340°C [72, 118, 119]. For single crystal materials, the elimination of the grain boundaries allows the removal of grain boundary strengtheners such as carbon, boron and zirconium, which increases the melting temperature and homogenises the structure prior to ageing [119].

In order to fully reduce chemical segregation, the solution heat treatment usually involves several steps. Table 2.4 shows a standard solution heat treatment for CMSX-4, which comprises seven-step solution heat treatment [119]. The reason for this sequence is that the low temperature steps were used to remove carbides, TCP phases and other phases. While the γ′ particles are dissolved at a medium temperature, whereas chemical segregation is much more difficult to dissolve, which requires a higher temperature and much longer processing time [4]. Take CMSX-10 for example, the γ′ and the eutectic γ/γ′ are completely dissolved at approximately 1340°C, while the chemical segregations will not dissolve until the temperature reaches 1360°C [6,14]. It needs an extremely long time to eliminate all the chemical segregations. The residual segregations of W and Re in the dendrite cores will lead to an unstable microstructure and possibly the formation of TCP phases [14]. The temperature of solution heat treatment at each step is gradually increased due to the increasing of incipient melting temperature, which is contributed by homogenisation [4].

Table 2.4 The typical solution heat treatment cycle for CMSX-4 Ni-based single crystal superalloy [119]

Alloy	Refractory Metal Content	Solution Heat Treatment
CMSX-4	**W+Re+Mo+Ta (wt.%) 16.4**	1276°C for 2 h → 1287°C for 2 h → 1296°C for 3 h → 1304°C for 3 h → 1315°C for 2 h → 1321°C for 2 h → 1324°C for 2 h/GFQ*

*GFQ – Gas (Argon or Helium) Furnace Quench.

2.8.1.2 Ageing

The ageing process is carried out at a lower temperature but a longer time compared with solution heat treatment. The typical ageing process for single crystal Ni-based alloys is holding at 850-1100°C for 4-16 h [6, 38, 120]. The detail of the heat treatment condition is sensitive to the mechanical properties required. Usually, there are two ageing treatments. A higher temperature treatment, sometimes called a precipitation treatment, which is used to optimise the mechanical properties by producing suitable size of γ′ precipitates [4, 19]. Another aging treatment is carried out at a lower temperature to precipitate additional γ′ particles and other phases such as carbides and nitrides, this treatment sometimes called stabilisation treatment [4, 10].

2.8.2 Restoration of microstructure

The primary microstructural degradations resulting from long term thermal exposures at elevated temperature are: the formation of cavities and voids, coarsening or rafting of γ′ particles; changes in grain boundary carbides and the formation of topologically close packed (TCP) phases[111, 115–117, 121]. Most

of these changes are reversible and numerous studies have demonstrated the possibility of the restoration of the blade microstructure and properties after service. The implementation of the rejuvenation procedures, such as an appropriate solution heat treatment has proven to be able to restore even severely overaged microstructure and alloy properties to a practically “as-new” condition [115-119]. However, the second life of this “as-new” condition sample has not been studied yet, and the recovery of the microstructure is not fully understood. In this section, the restoration of microstructure after rejuvenation is reviewed.

1. Grain boundary cavities

It is well known that the creep fracture usually occurs due to the formation and coalescence of grain boundary cavities. This is more common when there is a stress applied on it [75, 122–124]. A rejuvenation heat treatment eliminates or reduces grain boundary cavities in two ways: firstly, it inhibits the further growth of creep cavitation. Secondly, it removes the cavitation completely by means of a sintering heat treatment. However, the recovery of the grain boundary cavities is very dependent on the cavities size. It only works when the cavities are small. Therefore, the rejuvenation heat treatment must be carried before significant failure occurs [119]. For CMSX-4 superalloys, although there is no grain boundaries, creep cavities may form and has the same effects as grain boundary cavities. Therefore, understanding the grain boundary cavities is also very important for CMSX-4 superalloys.

2. Gamma prime

The coarsening of γ′ precipitates is one of the most important life limiting factors for the single crystal Ni-based superalloys. This is because when the particles are small and well distributed, the dislocations find it difficult to shear between

the γ′ particles. The coarsening of γ′ precipitates or rafting increases the widths of the channels between the precipitates, which makes the dislocations much easier to move across them [4, 60-65]. The formation of dislocation networks finally leads to failure of the components. The common rejuvenation heat treatment has a complete solution heat treatment and re-precipitation procedure, by which it dissolves the coarse γ′ precipitates and redistributes the precipitates in a similar manner to the original microstructures [65].

3. Carbides

Carbides have either a beneficial or a deleterious effect on the mechanical properties. The beneficial effect is that $M_{23}C_6$ and M_6C grain boundary carbides pin the grain boundaries, which prevent the grain boundary sliding and increase creep properties [32]. While the formation of continuous MC carbide film along the grain boundary has detrimental effects on the creep properties. Rejuvenation heat treatment leads to the dissolution of the continuous carbides, which is good for the creep properties. However, the rejuvenation heat treatment also dissolves the carbides on the grain boundaries, which may results in a reduction of the creep properties [119]. Therefore, the effect of rejuvenation for the carbides is unpredictable and is also dependent on the exact type and amount of the carbides present [25-27].

4. TCP phases

Embrittling TCP phases such as σ, μ and P, can form during service exposure for CMSX-4 depends on the composition and temperature. As described in earlier portions, the presence of these phases is deleterious for the materials [30-35]. The aim of the rejuvenation is to remove or eliminate the amount of TCP phases in the alloy. During a rejuvenation heat treatment, the TCP phases can be dissolved into solution. However, the elemental segregation resulting from the

prolonged exposure at high temperature may lead to these phases reprecipitating very rapidly once parts are returned to service [30].

2.8.3 Considerations for rejuvenation procedures

The rejuvenation heat treatment must be tailored because it is very dependent on the type of alloy, the stage of damage and the cost of repairs [119]. Temperature is one of the most important factors for the rejuvenation heat treatment. Usually it is performed at a temperature above the γ′ solvus temperature to regenerate a microstructure close to the original state, but not too high to melt the alloy [115-119]. The rejuvenation temperature for directional solidification alloy is much lower than the single crystal superalloy, since the later one has removed additions of grain boundary elements and the solution temperature increased significantly. The rejuvenation treatment is only capable to recovery the microstructure and mechanical properties of Ni-based superalloy, but it is not suitable for thermal barrier coatings. Therefore, for some serviced components, such as blade with thermal barrier coatings. TBCs have been stripped off before the rejuvenation was applied. Another limitation of rejuvenation is that it can only be used to recovery the components with non-permanent damage obtained, such as cracks. Once the crack formed, the rejuvenation cannot recovery that and it will grow and propagation into the components very quickly. Finally, applying the rejuvenation procedures at the optimum stage in service is also very important. The rejuvenation procedures must be applied early enough to prevent irreparable damages but late enough to give a cost-effective benefit. Usually, it is applied at the end of the secondary or early in the tertiary stage creep [109, 112-115,119].

2.9 Summary

This chapter has reviewed the history of superalloys, illustrating the major developments in alloy composition and processing techniques. Major phases and their microstructure evolutions during heat treatment and service exposure conditions have been well discussed, especially for γ, γ′ and TCP phases. The mechanical properties under different service conditions, such as creep, are well reviewed combined with microstructural changes. The detail of CMSX-4 and typical thermal barrier coatings has also been reviewed. Finally, the details of CMSX-4 and rejuvenation issues have also been reviewed.

CHAPTER 3

EXPERIMENTAL PROCEDURES

3.1 Introduction

This research programme focused on microstructural evolution during high temperature degradation and rejuvenation, combined with mechanical tests. For this purpose, a number of heat treatments and experimental techniques were used. In this chapter, details of the materials, heat treatments, mechanical tests and microstructural analysis methodologies used in this project are presented. A variety of experimental techniques have been used for microstructural characterisation of CMSX-4 single crystal superalloy after high temperature degradation and the subsequent application of a number of different rejuvenation heat treatments. The analysis of these samples has focused on the distribution, size and morphology of gamma (γ) and gamma prime (γ′) particles. Techniques used for those analyses include field emission gun scanning electron microscopy (FEGSEM), energy dispersive X-ray (EDX) spectroscopy, and focused ion beam (FIB), together with ion milling to produce samples for high resolution analysis in the transmission electron microscopy (TEM).

3.2 Materials

The CMSX-4 single crystal specimens were provided by E.ON Engineering Ltd. All of the specimens were cast in the <001> direction following a standard casting procedure and standard solution heat treatment. There were two types

morphology of materials, which were bars and blade. The mechanical test bars, such as tensile and creep tested specimens were provided by E.ON and a few virgin bars were also provided for rejuvenation trials in the later stages of the work. An ex-service blade was also examined in this research. A typical chemical composition of the CMSX-4 alloy used in the investigation is given in Table 3.1.

Table 3.1. The chemical composition for CMSX-4 used in this project

Elements	Al	C	Co	Cr	Fe	Mo	Re	Hf	Ta	Ti	W	Ni
Wt.%	5.7	0.0022	9.6	6.28	0.06	0.6	2.95	0.09	6.49	1.0	6.43	Bal*

***** Bal=balance

3.3 Heat Treatment

A heat treatment programme was carried out to enable systematic analysis of the microstructural evolution of the CMSX-4 samples during rafting and rejuvenation. The heat treatment programme included rafting, high temperature rejuvenation and low temperature refurbishment. The detail of each heat treatment is shown in Table 3.2 and all of them were carried at no applied stress conditions. Rafting is a degradation treatment, which included holding the samples at 1050°C for 1000 hours to generate a microstructure similar to the samples after long-term service exposure [7]. A high temperature rejuvenation heat treatment was developed based on that of the manufacturer but a using higher solutionising temperature, followed by two steps of ageing. Lower temperature refurbishment treatment is used in industry, which was believed can restore the rafted microstructure back to the pre-service conditions [7].

For all mechanical tests, the samples were categorised into five groups as shown in Table 3.3. S1 is the virgin sample, after casting and standard solution

heat treatment; it had no other heat treatment applied, which is the baseline for all heat treated samples. The remaining samples had undergone a rafting (degradation) treatment, followed by other treatments. S2 was only rafted and was used to examine the microstructure after degradation. S3 was rafted and then rejuvenated using a high temperature rejuvenation heat treatment. These samples were used to examine the effects of the high temperature rejuvenation treatment (solution and ageing) on the microstructure. S4 had undergone rafting, rejuvenation and an additional rafting heat treatment, and was used to compare to S2 and to evaluate the rejuvenation process. S5 had experienced a lower temperature refurbishment heat treatment after rafting, which included a hold at 1140°C for 6 hours and 871°C for 20 hours. For the ex-service blade, the operating temperature of the gas turbine engine was assumed to be about 1000°C, and allowing for the temperature difference of the coatings, the operating temperature seen by the substrate was about 850-950°C. The blade was in service for 24,063 hours, after which the coatings were believed to have been stripped off and a rejuvenation heat treatment was applied.

Table 3.2 The details of the heat treatments applied to the CMSX-4 samples

Rafting	**High Temperature Rejuvenation**		**Low Temperature Refurbishment**
	Solution Heat Treatment	**Two Step Ageing**	
Holding at 1050°C for 1000 h	1283°C for 2 h 1285°C for 2 h 1301°C for 2 h 1309°C for 2 h 1318°C for 2 h 1321°C for 2 h 1323°C for 2 h Air Cool to RT	➢ 1140°C for 6 h Air cool to RT ➢ 871°C for 20 h Air cool to RT	➢ 1140°C for 6 h Furnace cool to RT ➢ 871°C for 20 h Air cool to RT

Table 3.3 The CMSX-4 samples with their heat treatment conditions

Samples		Heat Treatments
Tensile	S1	As Received
	S2	Rafted
	S3	Rafted + HT Rejuvenation
	S4	Rafted + HT Rejuvenation + Rafted
	S5	Rafted + LT Refurbishment
Short Term Creep	S1	As Received
	S2	Rafted
	S3	Rafted + HT Rejuvenation
	S4	Rafted + HT Rejuvenation + Rafted
Long Term Creep	S1	As Received
	S2	Rafted
	S3	Rafted + HT Rejuvenation
	S4	Rafted + HT Rejuvenation + Rafted
Long Term Creep		Modified Rejuvenation Trials (see Chapter 7)
Blade		In service for 24,063 hours + HT Rejuvenation

3.4 Mechanical Testing

In order to examine the effects of the heat treatments on mechanical properties, mechanical testing was employed to provide comparative data on the CMSX-4 single crystal superalloy. The tests included: tensile, short and long term creep tests. The details of the procedures and test conditions utilised are given in the following sections.

3.4.1 Tensile testing

Tensile testing was performed in accordance with ASTM E8/E8M on a servo-mechanical test frame at room temperature using a strain rate of 0.7mm/min [127]. The specimens were in the form of bars measuring 100 mm in length and 14 mm in diameter with two threaded heads. The gauge length had a diameter of 10 mm. The tensile specimen used is shown in Figure 3.1. Due to concerns over the notch-sensitivity of the single crystal material, specimen extension was measured via cross-head displacement, rather than a contact extensometer.

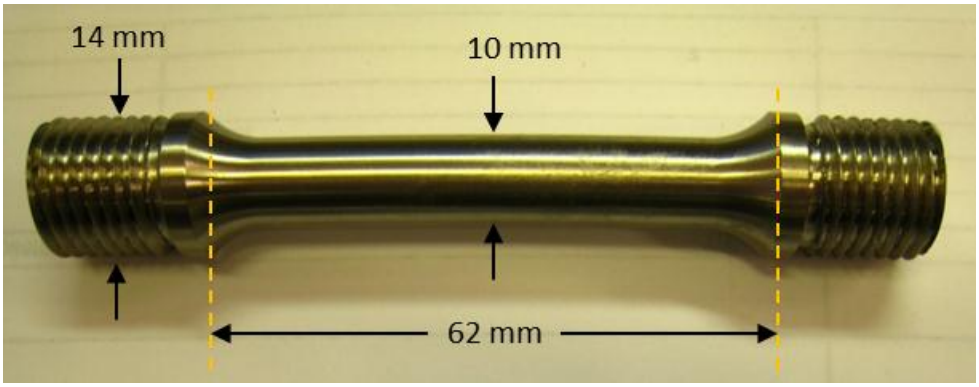

Figure 3.1. The details of the CMSX-4 tensile specimen used in the project

3.4.2 Short term creep testing

Short term creep or creep rupture tests were performed using static weight creep machines in accordance with ASTM E139 [128]. Tests were conducted at a temperature of 900°C under a stress of 425 MPa. These conditions were selected on the basis of results from a literature survey of similar tests conducted on virgin CMSX-4, shown in Figure 3.2. Based on the time frame of the project, the tests for the as-received CMSX-4 were designed to last in the region of 200 to 300 hours [7]. The specimens were in the form of bars measuring 20 mm in

length and 10 mm in diameter with two heads, with the gauge length having a 5 mm diameter. A schematic diagram of the creep rupture specimens used is shown in Figure 3.3

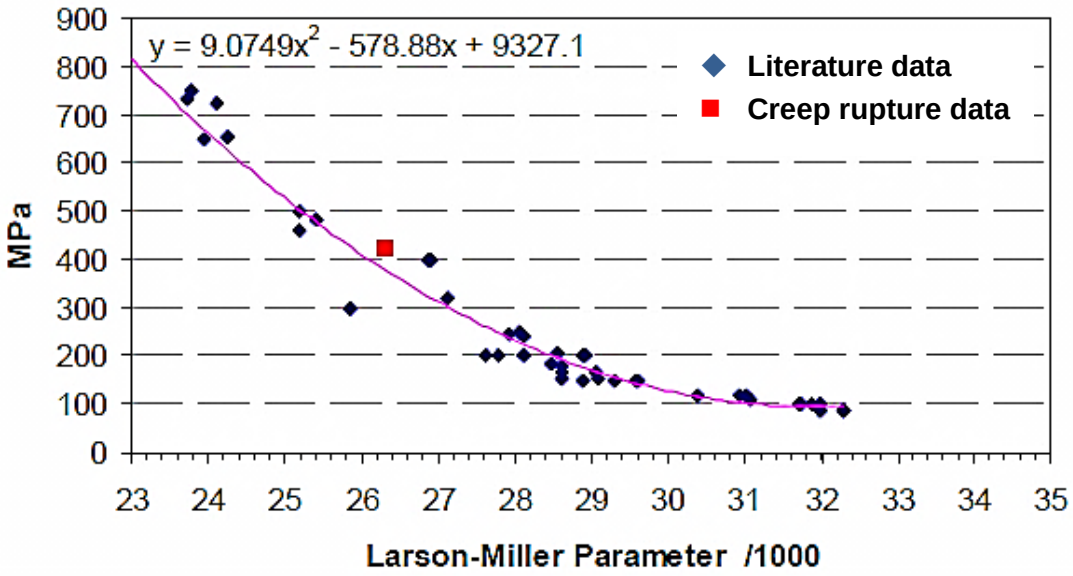

Figure 3.2. Set data of short term creep tests conducted on virgin CMSX-4. The creep rupture test conditions were selected based on these data [7].

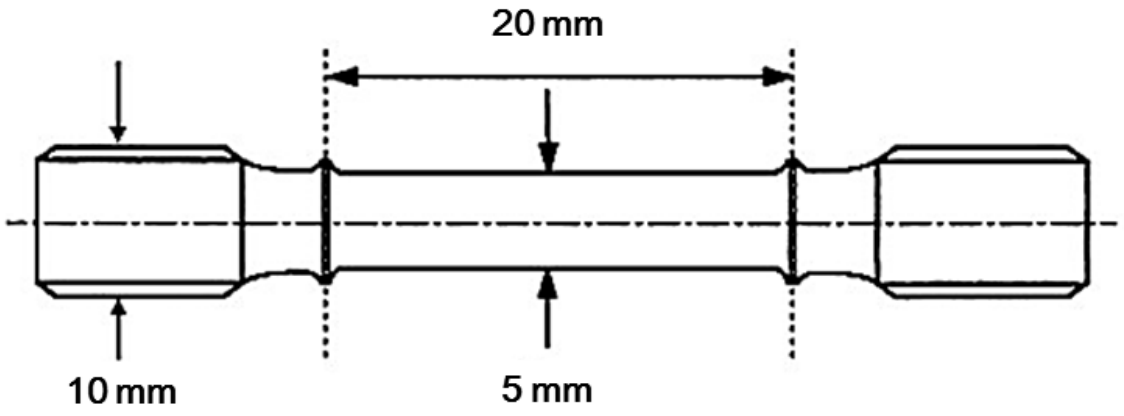

Figure 3.3. Schematic diagram illustrating the size of the CMSX-4 short term creep specimen.

3.4.3 Long term creep testing

Long term creep tests were performed at a temperature of 982°C and a stress of 167 MPa. These test conditions were based on the creep test performed by Svoboda and Lukas [123] based on an as-received sample which failed around 1000 hours, a time short enough to perform tests within the required timeframe but long enough to be a meaningful indicator of longer term creep behaviour. Therefore, this creep testing was called long term creep to distinguish it from the creep rupture test, but it was not exactly the “long term” creep testing performed in industry. The single crystal CMSX-4 long term creep test specimens were in the form of bars measuring 25 mm in length and 12 mm in diameter with two heads, with the gauge length having a 6 mm diameter at the middle shown in Figure 3.4

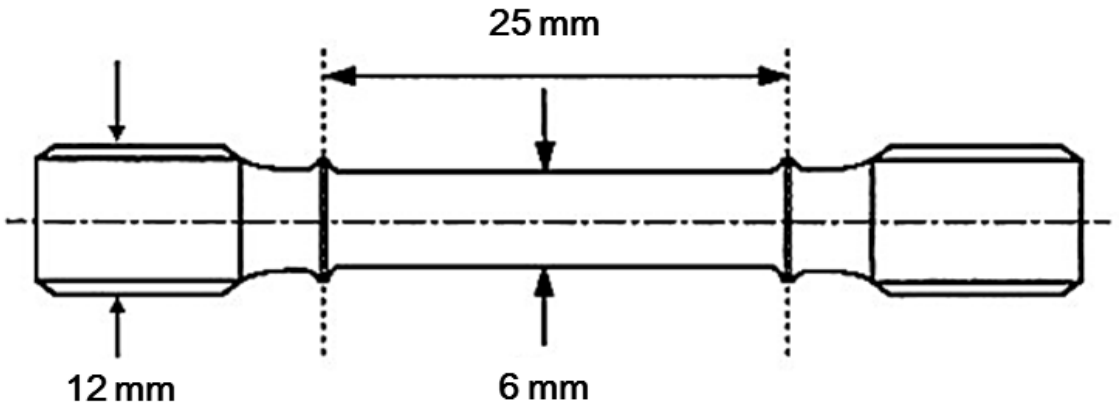

Figure 3.4. Schematic diagram illustrating the details of the CMSX-4 long term creep specimen used in the project.

3.5 Metallographic Preparation of Samples

The primary object of the metallographic preparation was to reveal the microstructure of the specimen for investigation by using the different microscopies. Due to their size difference, the mechanical tests bars and an ex-service blade were prepared in different ways.

3.5.1 Mechanical test bar specimens

For examination of the microstructure of the differently heat treated specimens, all the specimens were cut using a Struers Accutom-5 circular saw to a suitable size to be mounted. The head portions were cut off and mounted in conductive Bakelite. Longitudinal cross-portions of the gauge lengths were produced and were mounted in conductive Bakelite to examine the microstructure at different positions towards the fracture face. A schematic diagram of how the tensile specimens were cut is shown in Figure 3.5.

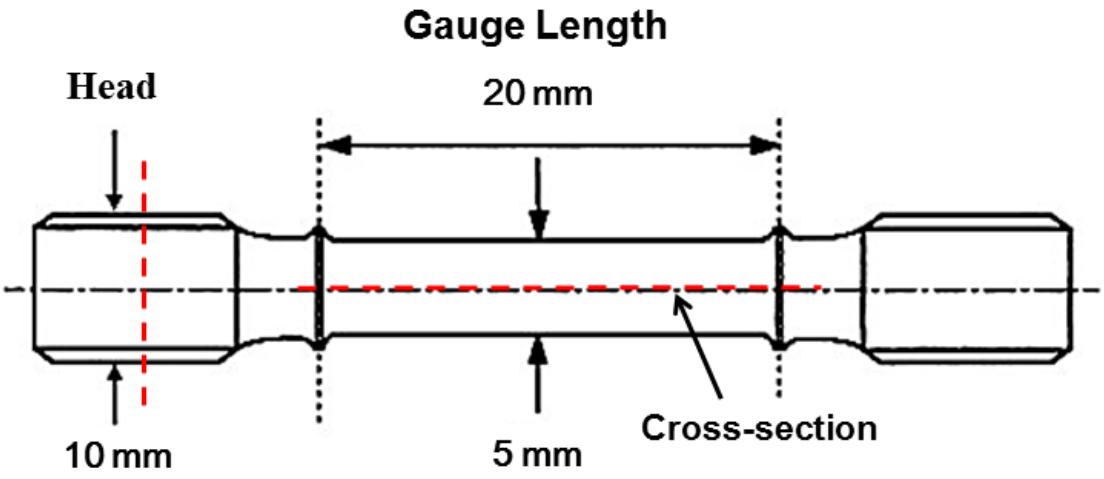

Figure 3.5. Schematic diagram illustrating where the heads and gauge lengths portions were come from the tensile and creep specimens

3.5.2 An ex-service blade

The ex-service blade was from Alstom's EX GT26 advanced gas turbine for power plant applications. The substrate of the blade was CMSX-4 single crystal Ni-based superalloy. Thermal barrier coatings (TBCs) with a MCrAlY bond coating were used and replaced during its service life. The blade was in service for 24,063 hours, after which TBCs were stripped off, followed by high temperature rejuvenation to restore the microstructure back to the virgin conditions. The focus of this project is analysing the distribution, size and morphology of gamma (γ) and gamma prime (γ′) particles during service and rejuvenation. Therefore the microstructure changes of coating were little discussed in this study.

In order to examine the effects of the heat treatment on the microstructure in different regions, the blade was cross-sectioned from 1/3, 1/2, 2/3 of the aerofoil height of the blade, which were called section 2, 4 and 6 respectively, see Figure 3.6. Each section was cut into a number of parts, where the detail of the distribution, size and morphology of gamma (γ) and gamma prime (γ′) particles was examined. The microstructures obtained from different parts and portions were compared in both horizontal and vertical to further confirm the effects of the high temperature rejuvenation on the microstructure restoration in different places.

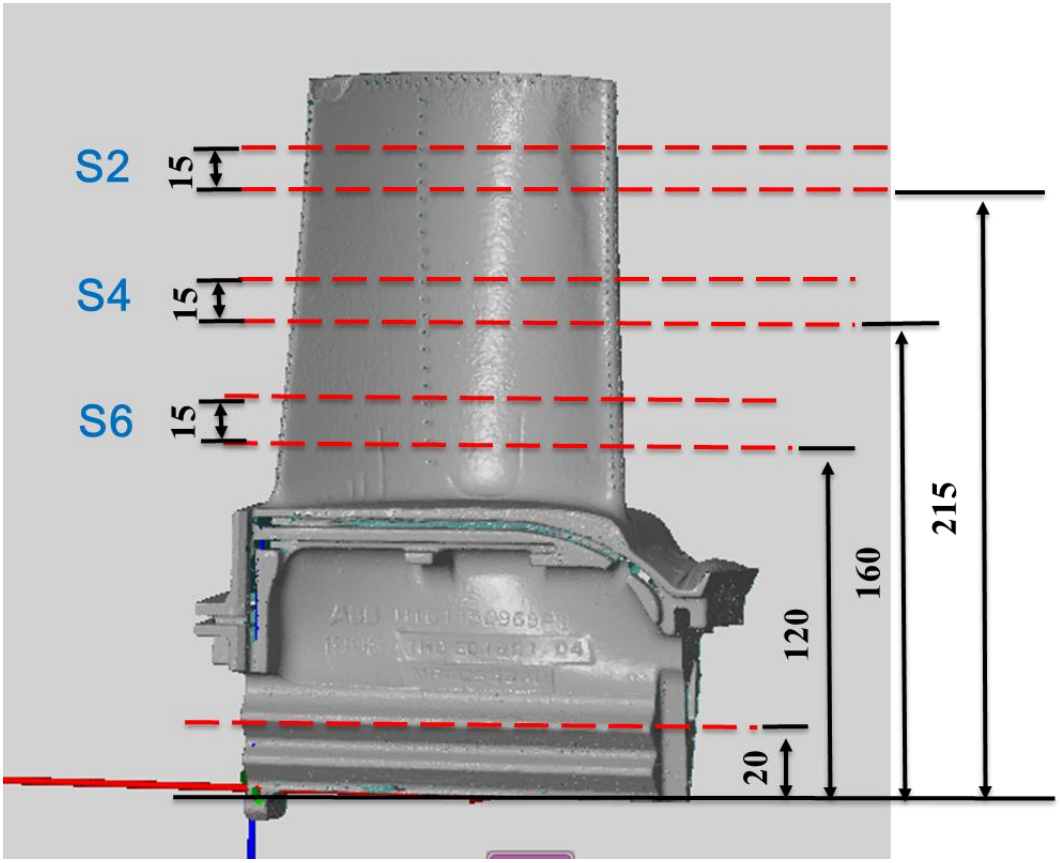

Figure 3.6. Schematic diagram of a service run turbine blade, showing the cut positions from which cross-portions were extracted and the area examined across the aerofoil surface.

3.5.3 Polishing and etching

After cutting and mounting, the specimens were ground on successively finer grades of silicon carbide paper from 220, 600 and 1200 grit to eliminate deep scratches. Then the specimens were polished using 6 μm, 3 μm and 1 μm diamond polishing suspensions. Finally the polished metallographic specimens were electrolytically-etched in 10% orthophosphoric acid, which is 1g ammonium sulphate powder and 1 g citric acid powder in 100 ml water. Etching was carried out by submerging the sample into the etching solution in the centre of a beaker. A positive terminal was connected to a stainless steel needle, which acts as the

anode. The cathode was connected to a stainless steel mesh. A potential of 10 V was applied whilst the needle was placed at the edge of the samples, and the stainless steel mesh was placed into the electrolyte near to (but not touching) the sample. The sample surface was etched for 30 seconds. This etchant promotes the dissolution of the γ phase within the materials, whilst leaving the γ′ particles in relief. After that, the specimens were rinsed with clean water to remove the chemicals followed by rinsing in methanol and drying in a stream of warm air.

3.6 Scanning Electron Microscopy (SEM)

The majority of the microstructural characterisation was carried out using a Leo 1530VP field emission gun scanning electron microscopy (FEGSEM) to obtain sizes, morphology and distributions of γ and γ′ particles. The FEGSEM was operated at voltages of 10-20 kV and at a working distance between 3-16 mm, depending on the detector used, i.e. an Everhart-Thornley detector (ETD) or an in-lens detector. The ETD was used for lower magnification images; while the in-lens detector was used to obtain higher resolution images. Different magnifications were used to obtain details of area fractions and size of γ′ particles and γ channel widths. The difference in position between ETD and the in-lens detector is shown in Figure 3.77. ETD is the most commonly used secondary electron detector. Its position is away from the optic axis of the instrument. This detector is very efficient at detecting secondary electrons because of the use of a positively biased grid, which attracts the lower energy secondary electrons [129]. However, the large working distance leads to a low image resolution. To achieve the best resolution, short working distances are required. For an In-lens detector, the detector is placed inside of the final lens of

the microscope, which makes a short working distance possible. However, at short working distances the ETD has a reduced signal in most systems because the path to the detector is obstructed by the pole piece. Therefore, for an In-lens detector, the high resolution can be achieved by expense of the amount of the secondary electrons detected.

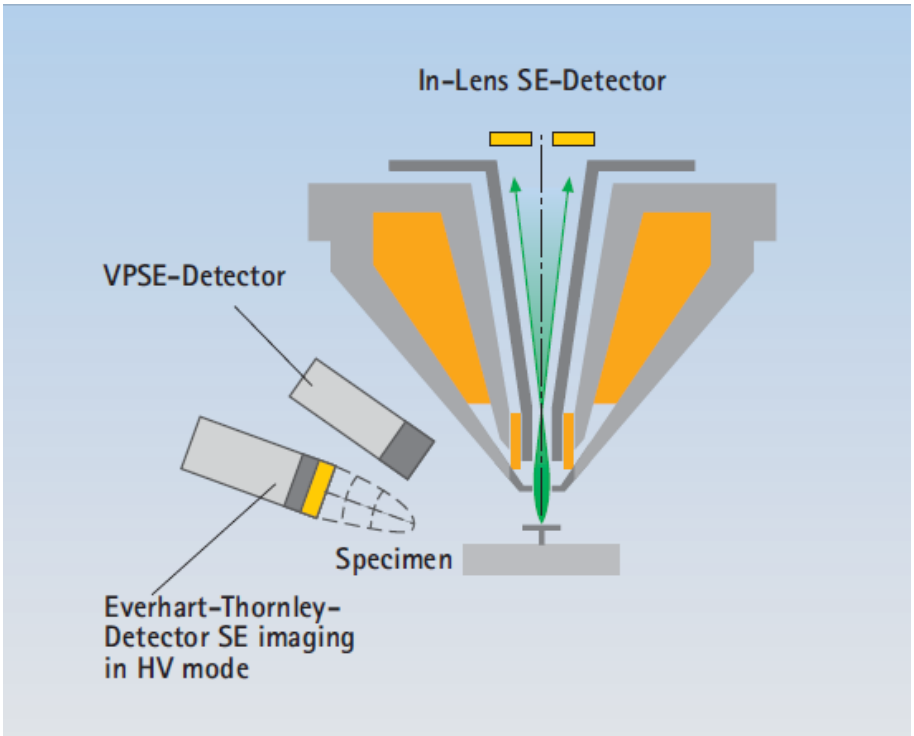

Figure 3.7. Schematic diagram illustrating the principle of secondary electron signal detection with the high efficiency In-lens detector and the lateral detector in the sample chamber [129].

SEM Images were collected by either in secondary electron (SE) or backscatter (BSD) modes. Secondary electrons have low energies, usually less than 50 ev. Therefore these detected electrons are created relatively near the surface of the sample, making them sensitive to topography. Backscattered electrons interact with sample atoms and are significantly scattered by them. Higher atomic mass atoms have a greater probability of producing an elastic collision because of their greater size. Consequently, the number of backscattered electrons (BSE)

reaching a BSE detector is proportional to the atomic number of the sample. Therefore, the BSE signal is very sensitive to the atomic number of the elements. The higher the atomic number, the stronger the signal emitted, resulting in a brighter appearance. The backscattered electrons have greater energies (>50 eV) than that of the secondary electrons. The high energy of these electrons allows them to escape from within a greater depth of the sample. The depth is related to the interaction volume, which is illustrated in Figure 3.8. When an electron beam bombards a sample, the interaction volume can extend to depth of a few micro meters, as shown in Figure 3.8. The size of the volume depends on the atomic number of the material and the energy of the incident electron beam. Basically, the larger atomic number and the lower energy of the incident beam the smaller interaction volume [129].

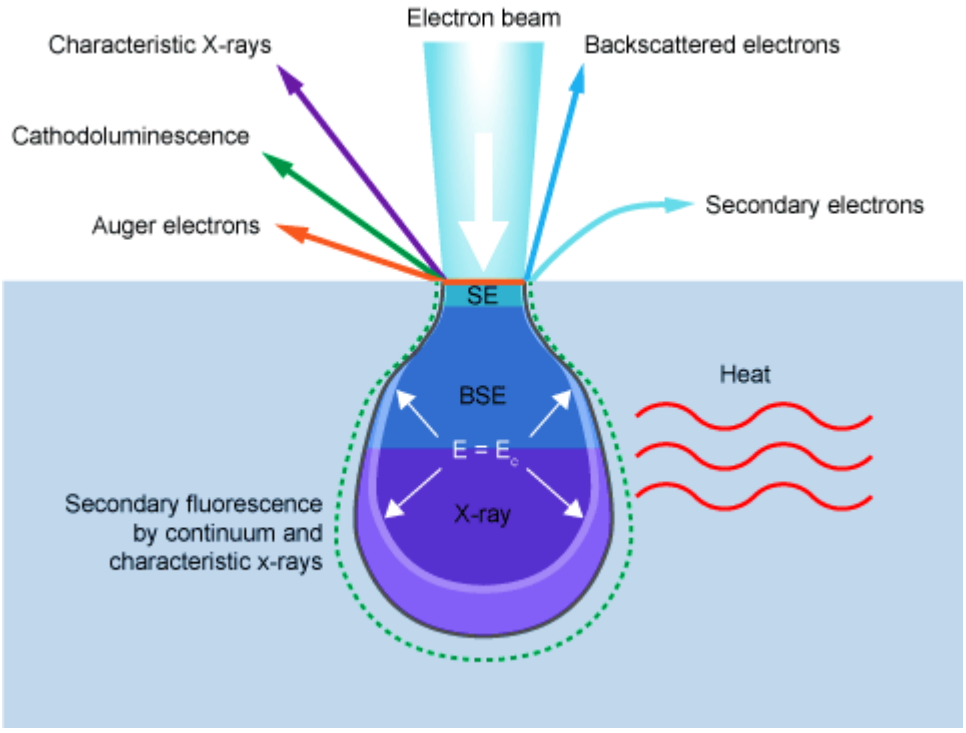

Figure 3.8. Schematic diagram illustrating the interaction volume for different electron-specimen interactions [129].

3.7 Microstructural Analysis of SEM Images

After the SEM images were taken, further microstructural analyses such as the area fraction of secondary γ′ particles, γ channel width and rafting parameter were required. The procedures of these analyses are illustrated in detail as follows.

3.7.1 Area fractions of secondary γ′ particles

The excellent mechanical behaviour of CMSX-4 at high temperature is contributed to by the high volume fraction of γ′ particles [5]. Therefore, quantification of the volume fraction of γ′ phases is very important. However, it is very difficult to experimentally measure the volume fraction. In this project, the area fraction was introduced and represented as volume fraction. The 20kX magnification SEM images were used to obtain quantitative measurements of area fractions of secondary γ′ via the image analysis software – Image J. Using this software, suitable contrast and brightness settings were applied to the images to distinguish the secondary γ′ particles and channels. After that, the images were thresholded to give a different “colour” to the secondary γ′ particles and channels. A schematic diagram of threshold processing is shown in Figure 3.9. The black colour represents secondary γ′ whereas the white colour represents the channels. Finally, an area measurement of the black colour was carried out by the software and the area fraction of γ′ was obtained. In some cases, the presence of tertiary γ′ precipitates in the channels (shown in Figure 3.10) causes a problem in the threshold processing. The software gives the same colour and contrast to secondary and tertiary γ′ precipitates, both of which were counted in the area fraction measurement, results a higher area fraction in the analysis. Therefore, for this situation, manual tracing was applied using

Photoshop software before threshold processing. Tracing of the channels ignores the tertiary γ′ precipitates in the channels, which makes the measurement of secondary γ′ particles more accurate. Figure 3.10 is a schematic diagram of manual tracing for area fraction measurements.

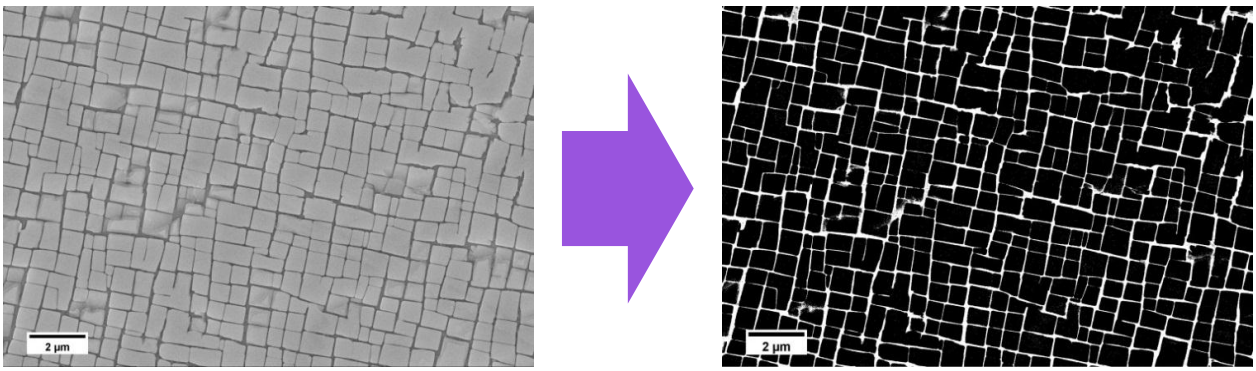

Figure 3.9. Schematic diagram illustrating the threshold processing of the images for area fraction measurement of secondary phases within the CMSX-4 tensile specimen.

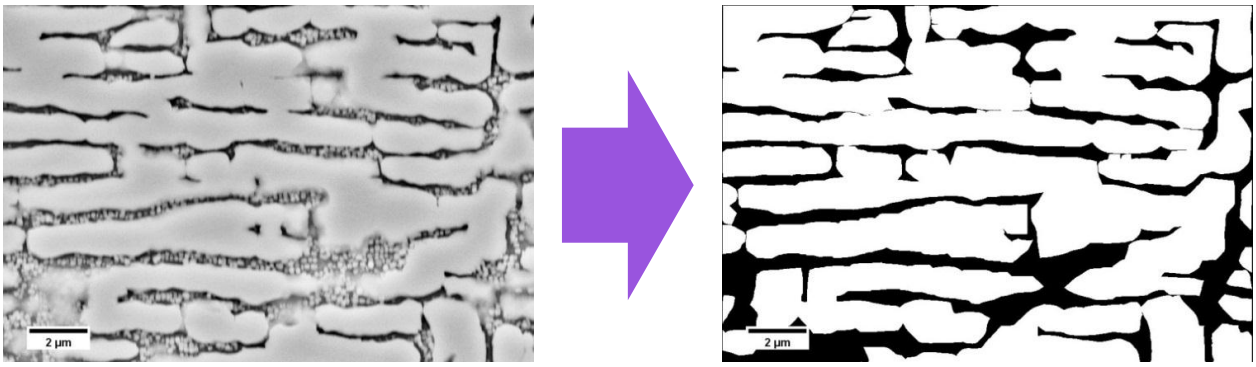

Figure 3.10. Schematic diagram illustrating the manual tracing of channels for area fraction measurement of CMSX-4 tensile specimen.

3.7.2 Channel width measurement and rafting parameter

Channel width is another important factor for the microstructure of CMSX-4. In order to obtain these data, a piece of 20 X 20 grids paper was placed on the top of 20kX magnification images. The direction of the grids was positioned parallel to the direction of the rafts. The channel widths of all channels intercepting each line of the grid were measured manually. Both the channel widths of the parallel and perpendicular direction of the rafts were measured, as shown in Figure 3.11. In some cases, the channel width of parallel and perpendicular directions is significantly different, which indicates a large difference in degree of rafting. In order to define the degree of rafting, a rafting parameter was introduced by Ignat et al [130]. The rafting parameter, R, is defined as:

$$\mathrm{R} = \frac{2L^2}{4LT} = \frac{L}{2T} \qquad [3.1]$$

Where L is the length of rafts and T is the thickness of rafts. The larger value of rafting parameter suggests the materials has more continues rafts within the microstructure, which provides less barrier effect on dislocation motion and leads to a poor mechanical properties. Therefore, rafting parameter is very useful tool to measure degree of rafting and hence linked with mechanical performance of the materials.

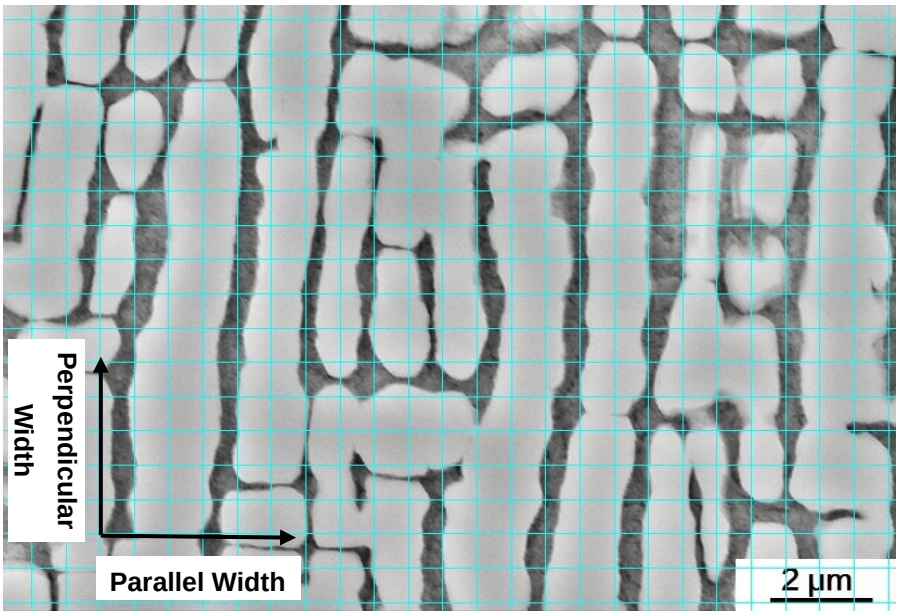

Figure 3.11. A schematic illustration of the orientation of the perpendicular and parallel channel widths for the measurement of the γ channels.

3.8 Transmission Electron Microscopy (TEM)

Transmission electron microscopy (TEM) is a technique that uses a high energy electron beam transmitted through a very thin sample to image and analyse the microstructural features and crystallographic data of materials with atomic scale resolution [133, 134]. A Jeol JEM-2000FX TEM operating at an accelerating voltage of 200 kV was used in the bright field image mode and diffraction mode to obtain the internal microstructure and crystal structure. In bright field mode, the brighter areas of the image show regions where the electrons have transmitted through the sample without significant deflection and the darker areas are produced when large amount of electrons have been deflected. For diffraction, the crystal structure can be obtained from the diffraction patterns, which can be used for further confirmation of the crystallographic data. TEM sample preparation is very important to obtain good TEM results. In this project, the TEM samples were prepared by ion milling and a focused ion beam (FIB).

3.8.1 Sample preparation via ion milling

Thin 3 mm diameter discs were cut and mechanically ground to 100 μm using from 220 to 2400 grit silicon carbide papers. After thinning, these were ion milled to electron transparency using a Leica EM RES 101 ion milling system. For ion milling, a two-step ion milling procedure was used: 2 h of Ar ion milling with an inclination angle of 7°, 3.0 mA current at 8 kV acceleration voltage followed by a second step with a 2.0 mA beam current at 5 kV acceleration voltages for 20 h.

3.8.2 Sample preparation via focused ion beam

Samples were prepared for TEM directly from the bulk samples using focused ion beam (FIB) milling in an FEI Nova Nano-Lab 600 dual beam (FEGSEM/FIB) system. [133]. The FIB system uses a focused beam of gallium ions for imaging, milling and deposition of the surface of a sample. The dual beam system combines a FIB and a FEGSEM column whereby the ion beam can be used for milling and the electron beam for imaging. This system has an advantage over more traditional techniques, such as electro polishing and carbon replicas, of being able to extract specific areas or particles for analysis [133].

In this project, an important application of FIB in preparing TEM specimen was applied, which is called the “TEM lift-out” technique [134]. This technique was used to provide site specific electron transparent cross sections measuring ~ 10 X 5 μm. The area of interest and size of the specimen are defined by the user. Firstly, a suitable sized protective platinum layer was deposited onto the surface of the specimen using an in-situ gas injection system to prevent implantation and damage from the Ga ion beam over the location of the specimen to be extracted, see Figure 3.12a. Secondly, a stepped trench was milled on both sides of the

area of interest by using a high current Ga ion beam, followed by a cleaning cross-section procedure using a lower current ion beam, shown in Figure 3.12b. After that a U shaped cut (Figure 3.12c) was made underneath which results in the sample being attached by one small ligament on the side. Later, an Ominiprobe was inserted and the sample was welded using platinum deposition, allowing the sample to be cut away from the bulk sample. The sample was lifted out and welded onto TEM grids by careful control of the Ominiprobe and platinum needle, see Figure 3.12d&e. Finally, thinning was carried out by using FIB milling using progressively smaller current from 1nA, 0.5 nA and 0.3 nA with inclination angles of 1.5 ^{o} to the plane of the specimen, shown in Figure 3.12f. This reduces the sample thickness to approximately 200 nm, ready for examination in the TEM.

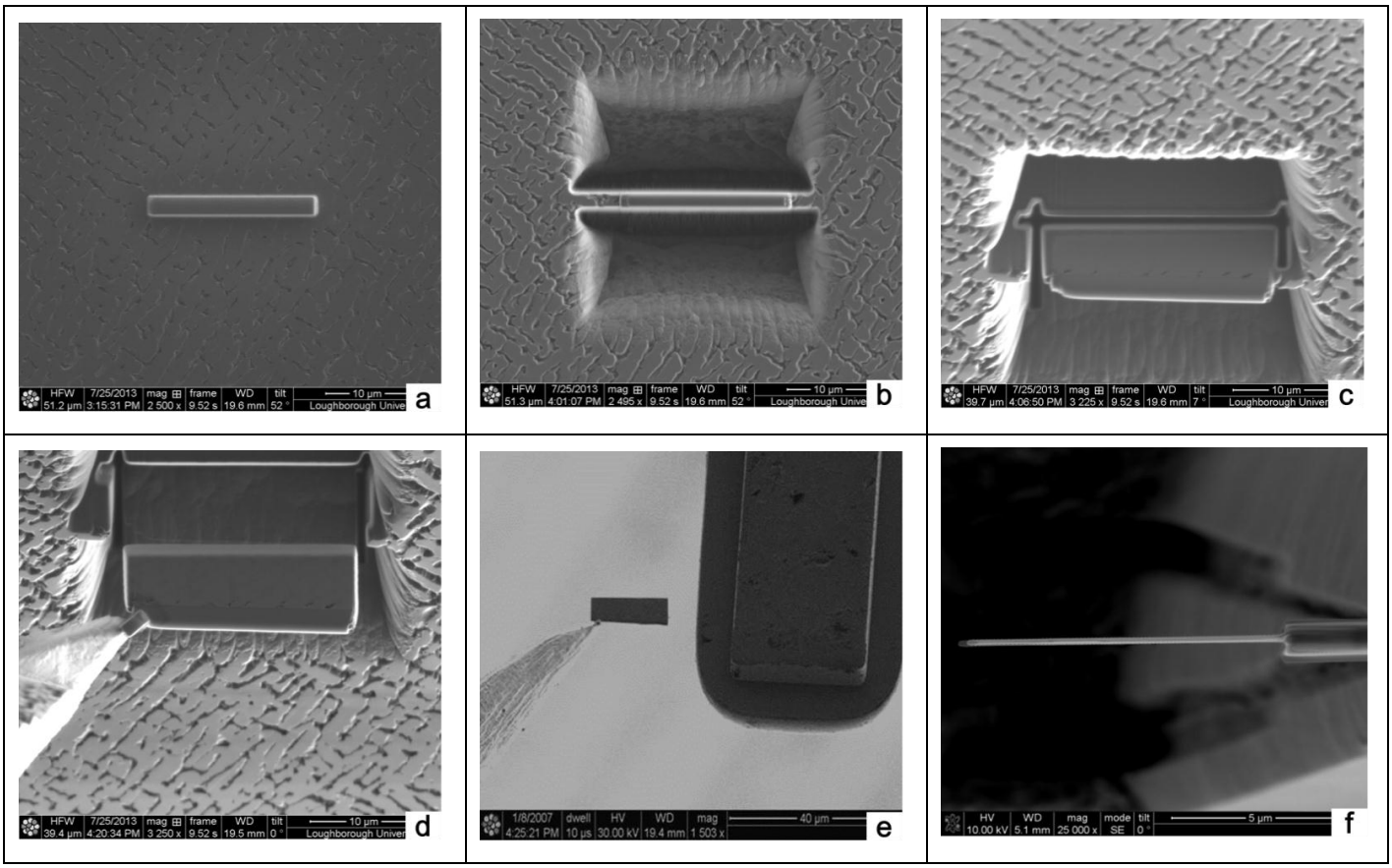

Figure 3.12. Images illustrating the major steps involved in FIB lift-out technique: (a) platinum deposition; (b) stepped trenches milling; (c) U-shaped cut; (d) lift out of specimen; (e) attachment of specimen; (f) finally thinning of specimen to required thickness.

3.8.3 Analysis of diffraction patterns

TEM was also used for collecting crystallographic data of the specimens. When an incident electron beam is directed on to a very thin sample, some of the electrons pass through without interaction while others are scattered due to interactions with lattice planes within the specimen. The scattered electrons create ordered spots or rings known as a diffraction pattern on the viewing screen. With this information, the crystallographic data can be obtained. Diffraction patterns provide structural details related to the specimen's phase, orientation and defect morphology. TEM diffraction pattern (for structural characterisation) combined with energy dispersive X-ray (for chemical characterisation) is commonly used for identifying the phases present in the specimen.

When an electron incident beam is on a thin specimen, electrons are reflected and diffracted following Bragg's law, as stated below and shown in Figure 3.13

$$n\lambda = 2d \sin\theta \qquad [3.2]$$

where n is an integer, for most cases n is 1. λ is the wavelength of the incident radiation. d is the spacing between the atomic lattice plane, and θ is the angle between the incident beam and the scattering planes.

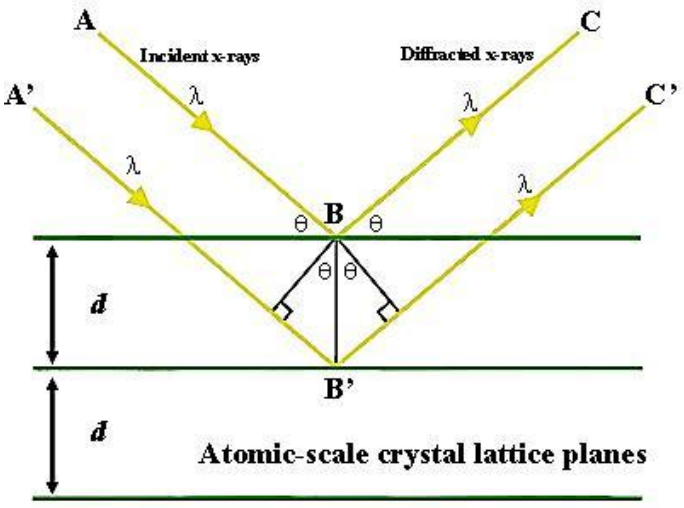

Figure 3.13. Diffraction of electron waves from atomic planes illustrating the Bragg's law.

Simple geometry is used to relate the distance between the spots on diffraction patterns to the values for lattice spacing (d) within a crystal structure. The distance between the specimen and the phosphor screen is known as camera length (L). The radius (R) of the diffraction pattern from the centre spot is measured. For small angles of θ, tan2θ=sin2θ=2sinθ, Therefore;

$$\frac{R}{L} = 2\sin\theta \qquad [3.3]$$

Combining with Bragg's Law, the equation can be simplified to the following equation:

$$Rd = \lambda L = \text{camera constant} \qquad [3.4]$$

where R is the radius of diffraction rings on the photographic screen, λ is wavelength of incident beam, L is camera length. For the same microscope the L and λ is constant, so this value is also called camera constant.

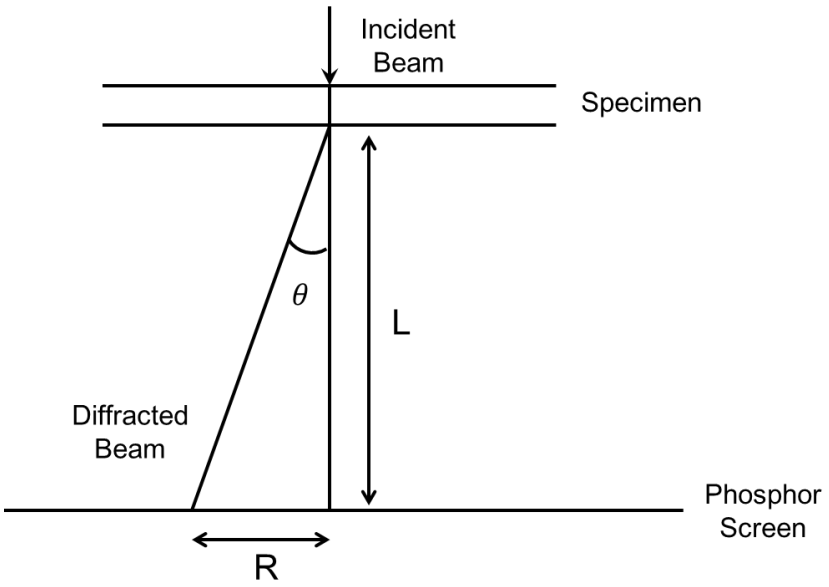

Figure 3.14. Schematic diagram of the geometry related to diffraction pattern formation and its relationship to Bragg's law.

According to the above equations, for cubic structure, the lattice spacing (d) can be easily calculated using the radius (R) of diffraction pattern. For cubic system, the relationship between the lattice spacing (d) and lattice parameter (a) is shown as below:

$$\mathrm{d} = \frac{\mathrm{a}}{\sqrt{\mathrm{h}^2 + \mathrm{k}^2 + \mathrm{l}^2}} \qquad [3.5]$$

where the (h, k, l) is called the Miller index for plane, which was used for determination of the crystal directions [131]. For typical face-centred cubic (FCC) and body-centred cubic (BCC) structures, the lattice parameters are confirmed by comparing with the standard diffraction pattern in literature [131]. However, for some complex crystal structures, such as Tetragonal and Rhombohedral, it is difficult to find the standard diffraction patterns. In this case, for determination of the phases, there are three steps required:

1. Three closest radiuses (R1, R2 and R3) near the centre spot, and angles between these three spots are measured.
2. No matter known the crystal structure or not, the ratios of each other and angles were input into the software program Practical Crystallography version 1.6 developed by H.K.D.H. Bhadeshia. Use this program determines any possible matches to the relevant lattice spacing (d) and miller indices. But knowing the crystal structure will help to narrow down the possibility for the matches.
3. The lattice parameter (a, b and c) were calculated and compared with literature data.

For Ni-based superalloys, the γ matrix and γ′ are cubic structure, which can be easily determined by comparison to a standard pattern. For complex Topologically Closed Packed (TCP) Phases, their typical crystal structures and lattice parameters are shown in Table 3.4 [35-38].

Table 3.4. Some typical TCP phases and their lattice parameter [35-38]

Phase	Crystal Structure	Lattice Parameters	α(°)
σ	Tetragonal	a=b=9.12 Å c=4.72 Å	90
μ	Rhombohedral	a=b=4.73 Å c=2.54 Å	120
P	Orthorhombic	a=17.2 Å b=4.86 Å c=9.2 Å	90
R	Rhombohedral	a=b=10.93 Å c=19.34 Å	120

3.9 Energy Dispersive X-ray (EDX) Analysis

Energy dispersive X-ray (EDX) analysis was used both in the FEGSEM and TEM to investigate and help identify particles and phases by determining their chemical composition. When the sample is bombarded by an electron beam, electrons are excited from inner shells. A resulting electron vacancy is filled by an electron dropping down from a higher shell, and an x-ray is emitted to release the energy difference. These energy differences are unique and linked to the elements, which is used to identify the elements in the samples [131, 137]. The EDX systems in FEGSEM and TEM are different, because of the size of sample and associated interaction volume. For FEGSEM, the bulk sample is used and a large number of x-rays can be collected since a large volume fraction is present, which generates strong signals. However, this can cause a large background or noise, which reduces the accuracy of measurement. For TEM, very thin sample was used, consequently the number of x-rays emitted is much lower, but less background is generated, which gives a more accurate measurement. However, there are a few limitations in EDX analysis:

1. Overlap of different energy peaks can occur, which affects the quantification of elements. This problem mainly arose with the heavier elements such as W, Ta, Re and Hf. Peak identification was undertaken manually to remove this problem.
2. EDX has a limitation in detecting light elements such as carbon, boron and oxygen. This problem can be solved by using Electron Energy Loss Spectroscopy (EELS) system, which was designed and more sensitive technique for light elements.
3. The lateral resolution or minimum size of particles which can be analysed is approximately 0.5 μm in FEGSEM. Hence it is not suitable to use EDX for the analysis of particles size less than 0.5 μm.

3.10 Thermodynamic Equilibrium Calculations

Thermodynamic equilibrium calculations have been extensively used to predict the amount and chemical composition of the phases in a component as a function of temperature and compositions. The calculation can reduce the effort required to determine phases and their amounts in equilibrium conditions in a multicomponent system. The main approach for this project is: firstly predict the equilibrium phases and compositions of Ni-based superalloy during the long term tests or service conditions. Secondly, make comparison of the experimental determination of the phases present and their compositions.

Thermodynamic equilibrium calculations were carried out using MTDATA. The MTDATA software, developed and maintained by the National Physical Laboratory (NPL), provides a facility for retrieving thermodynamic data from databases, compiling data sets for the elements of interest, and assessing these data; calculating equilibrium phase diagrams in multicomponent system [138, 139]. In this study, the commercial chemical compositions of CMSX-4 and rejuvenation temperatures were input into the system. The calculation was carried out using MTDATA with a set of thermodynamic databases for Ni-based superalloy, Ni-DATA. The Ni-DATA contains the relevant thermodynamic coefficients, possible phases and their compositions. In this database, it includes the following elements and phases, which was shown in Table 3.5.

Table 3.5 The composition and phases present in Ni-DATA

Composition														
Ni	Al	Co	Cr	Fe	Hf	Mo	Nb	Re	Ta	Ti	W	Zr	B	C	N
Phases														
Liquid			γ′			γ			Ni_3Al				Ni_3Nb	
γ″			η			Ni_4Mo			δ-NiMo				α(Cr, Mo, W)	
Laves			σ			μ			R phase				P phase	
M(C,N)			$M_{23}(B,C)C_6$			M_6C			$M_7(B,C)_3$				M_2N	
M_3B			M3B2			Cr_3B_3			TiB_2					

In this software, the allowed compositions and phases can be determined by the user. For CMSX-4, according to the composition and temperature, the elements and phases listed above can be selected based on literature, rather than selected all phases present in the database, which will accurate and accelerate the calculations. However, the thermodynamic equilibrium calculations have their limitations. It can only be used for equilibrium conditions, or long term conditions at the selected temperature. Therefore, it will not be suitable for short term heat treatment and testing.

3.11 Summary

This chapter has presented and discussed the various techniques used in the detailed microstructural investigation of different heat treated CMSX-4 samples. Thermodynamic equilibrium calculations have been used in order to predict the amount and chemical composition of the phases present or will occur within the material as a function of temperature. The main investigation was carried out on FEGSEM and TEM, combined with the EDX to examine the microstructural evolution of CMSX-4 samples during different heat treated conditions.

CHAPTER 4

GENERAL MICROSTRUCTURE AND THERMODYNAMIC MODELLING OF CMSX-4

4.1 Introduction

In this chapter, the phases and their amounts present within CMSX-4 after different heat treatments were predicted by thermodynamic equilibrium calculations and followed by experimental examination using field emission gun scanning electron microscopy (FEGSEM) and transmission electron microscopy (TEM). The general microstructural features obtained from bar specimens, such as uniformly distributed γ′ and γ in as-received conditions, rafted γ/γ′ structure after long isothermal ageing times, chain like γ′ particles, TCP phases and cast pores have been thoroughly investigated and discussed, and combined with the chemical analysis carried out using energy dispersive x-ray spectroscopy (EDX).

4.2 Thermodynamic Equilibrium Calculations

Thermodynamic equilibrium calculations have been carried out using commercial software MTDATA, in conjunction with a Ni-based database as described in Chapter 3. The calculations have been performed based on the chemical composition given in Table 3.1, with a simulated temperature range of 600 to 1400°C. In all the calculations, no phases were excluded. The calculations were used to predict phases and their amount present in CMSX-4 after different heat treatments. Figure 4.1 shows the results of these calculations

under thermodynamic equilibrium conditions from 600 to 1400°C using the composition shown in Table 3.1. Seven phases were predicted in the temperature range from the composition, which are: liquid, γ, γ′, carbides (MX and $M_{23}C_6$), and TCP phases (σ and μ).

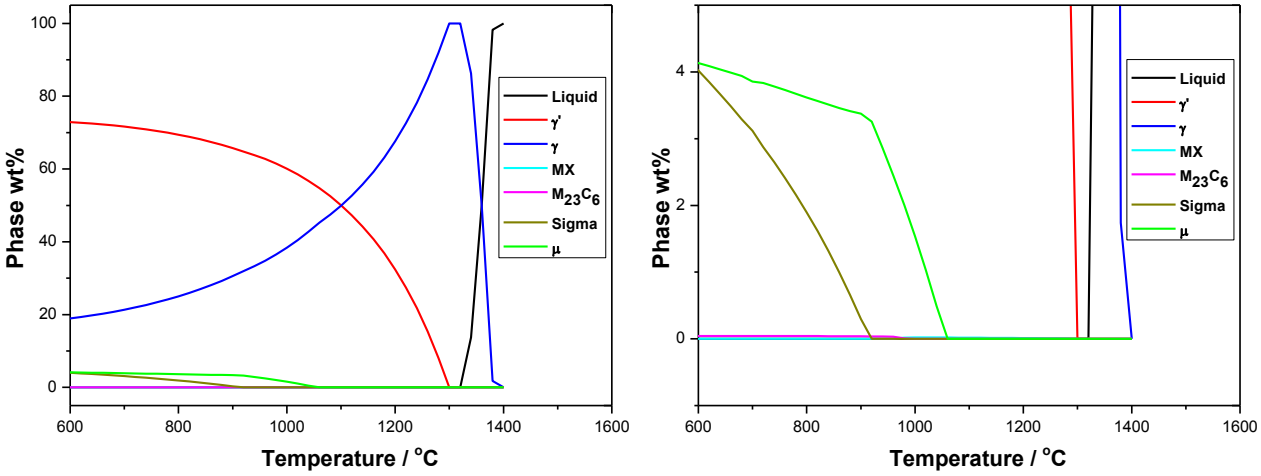

Figure 4.1. Predicted thermodynamic equilibrium quantities of the phases present in standard CMSX-4 as function of temperature, showing (a) full scale, and (b) expanded scale.

As shown in Figure 4.1(a), the main phases predicted in the microstructure are γ and γ′, with a relatively low weight percentage (wt.%) of TCP phases and very small amount of carbides. The thermodynamic calculations indicate that both the γ and γ′ are predominately Ni based. γ′ appears to reach its maximum value of approximately 73 wt.% at 600°C, when on the other hand γ is at its minimum, ~ 19 wt.%. However, the γ and γ′ show opposite trends when temperature increases; the γ′ content decreases, while the fraction of γ increases with rising temperature. The γ′ phase along with other phases is completely dissolved when the temperature reaches 1300°C, only leaving γ which is at its maximum. This temperature is called the γ′ solvus temperature. When the temperature increases to 1340°C (solidus temperature), γ starts to form liquid and it is

completely liquid when the temperature reaches 1380°C, which is known as the liquidus temperature. According to the literature, the incipient melting temperature is about 1327°C. Therefore, the solution heat treatment window for CMSX-4 is from 1300°C to 1327°C [5, 123]. The temperature must be high enough to take rafted γ′ phases into solution, but sufficiently low to avoid incipient melting. That is the reason that the solution temperature applied during the high temperature rejuvenation was chosen to range from 1300°C to 1323°C.

Figure 4.1(b) is an expanded scale of thermodynamic equilibrium calculations, showing the details of the carbides and TCP phases present in the microstructure. The calculations predicted the existence of MX and $M_{23}C_6$ carbides within the CMSX-4. However, the carbides in this composition are predicted at a level of less than 0.1%, which are about 0.023 and 0.043 wt.% respectively, due to the alloy containing only 0.0022 wt.% carbon. $M_{23}C_6$ is the thermodynamically stable carbide when the temperature is below 980°C, with a maximum of ~0.043 wt.%. Above this temperature, the MC phase is predicted to be stable up to a temperature of 1400°C, and reaches a maximum of 0.023 wt.%. Due to the very low amount of carbides predicted for CMSX-4, it can be assumed that virtually no carbides will be present within the actual alloy.

TCP phases are also predicted in the calculations, shown in Figure 4.1 (b). The σ phase is predicted to have a concentration about 4 wt.% at 600°C but is only thermodynamically stable below the temperature of 900°C. The μ phase will not disappear until the temperature reaches 1060°C. Considering the heat treatment applied, most rafting treatment was carried out 1050°C, which suggests that μ phase is likely to exist, since σ phase has been dissolved at that temperature. The details of the relevant temperatures and phase amounts are shown in Table 4.1 and Table 4.2.

Table 4.1 Summary of the most relevant temperatures for CMSX-4 from prediction

Name	Temperature / °C
Liquidus Temperature	1380
Solidus Temperature	1340
Incipient Melting Temperature	1327
γ′ Solvus Temperature	1300
Solution Heat Treatment Window	1300-1327
MC Stability Range	<1400
$M_{23}C_6$ Stability Range	<980
σ Stability Range	<900
μ Stability Range	<1060

Table 4.2 The maximum amount of phases present in CMSX-4 from prediction

Phase	Amount / wt.%	Temperature / °C
γ′	73	600
γ	100	1300
MC	0.023	1020
$M_{23}C_6$	0.043	600
σ	4.02	600
μ	4.13	600

Figures 4.2(a) and (b) show the weight percentage of elements a function of temperature in γ and γ′, carbides and TCP phases. Ni is the major constituent of both the γ′ and γ phases. In the γ′ phase, all the other alloying elements are present in a minor amount up to 10 wt.%. Al and Ti, as the main elements in the γ′, are expected to be a higher concentration compared to the rest the elements,

whilst in the γ phase, other elements such as, Co and Cr are also dominating the composition. The γ phase contains a greater amount of Co and Cr, 23.1 wt.% and 17.8 wt.% respectively at 600°C. The Cr and Co content within the γ phase is predicted to decease with temperature, leading to a corresponding increase in Ni content.

Figures 4.2(c) and (d) are related to MC and $M_{23}C_6$ carbides, where MC is predicted to be rich Ta and Hf. As the temperature increases, the Ta content increases but Hf decreases. At 1050°C, the composition of MC contains approximately 55 wt.% Ta, 34 wt.% Hf, 7 wt.% C and small amounts of Ti and Re. $M_{23}C_6$ is a Cr and Re rich particle, containing ~75 wt.% Cr, 14 wt.% Re and a small amount of Co and Ni. The Cr dominates the composition in $M_{23}C_6$ but it decreases with increasing temperature, resulting in an increase of other elements. However, the carbide content predicted in this CMSX-4 bar specimen is very small. Therefore the influence of these particles on the microstructure and mechanical performance can be ignored.

Figures 4.2(e) and (f) show the composition of alloying elements in the TCP phase throughout the selected temperature range. The TCP phases predicted in CMSX-4 are σ and μ phases. The σ phase is Re, Cr and Mo rich particle, which is only thermodynamically stable at temperatures below 900°C. According to the heat treatment conditions, the main TCP phase which is predicted to be present in the tensile and creep specimen after testing is μ phase, which is W and Re rich. The concentration of W and Re increased with increasing temperature. At 1050°C, it has a content of W and Re is about 40 wt.% and 30 wt.% respectively. These data can be used for comparison of EDX analysis in the future experimental examinations.

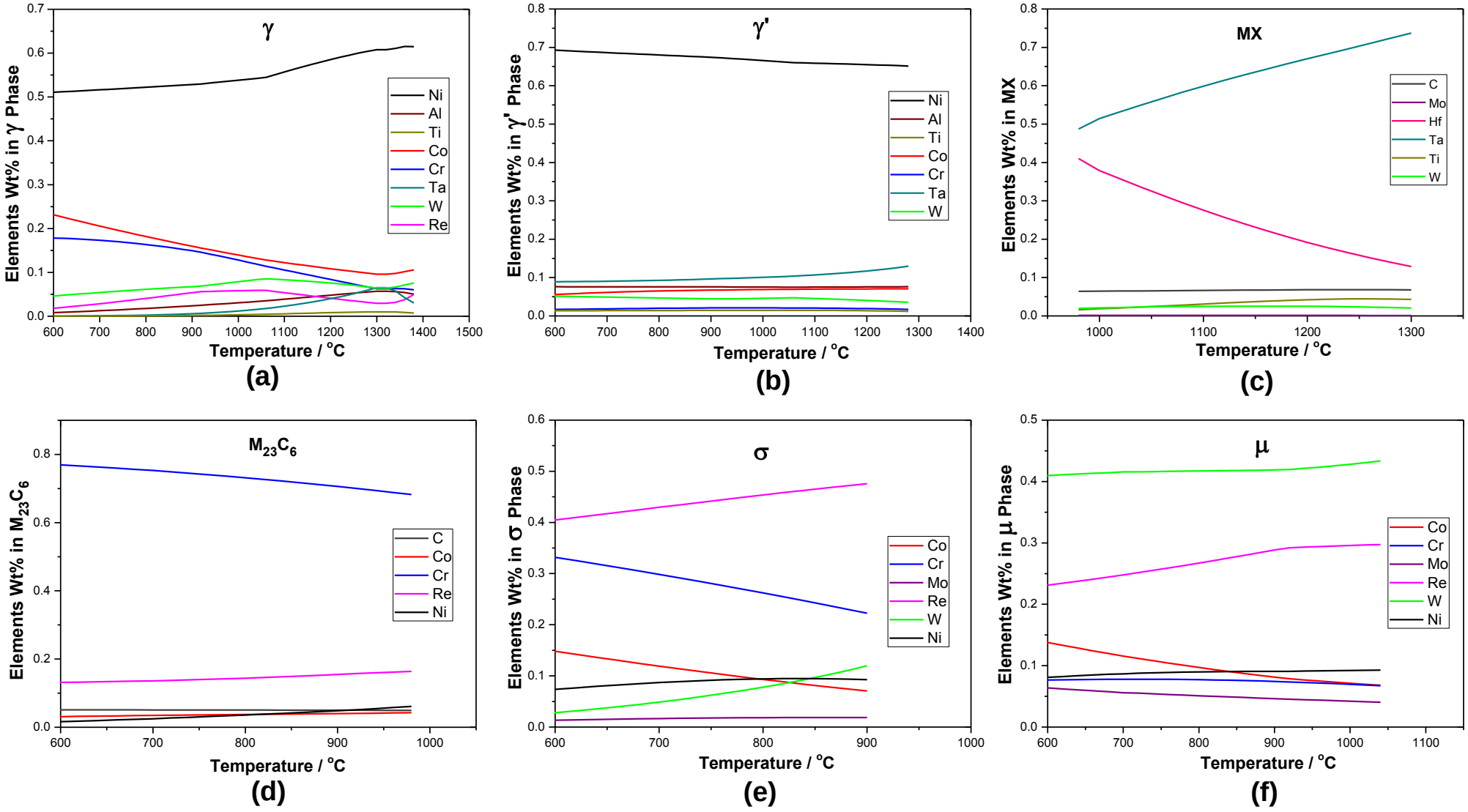

Figure 4.2. Thermodynamic equilibrium calculations results showing the wt.% of elements as function of temperature in CMSX-4, (a) γ, (b) γ′, (c) MX, (d) $M_{23}C_6$, (e) σ, and (f) μ.

4.3 General Microstructure of CMSX-4 Superalloys

This section presents the general microstructure of the CMSX-4 before and after degradation and rejuvenation. The general microstructural features obtained from the bar specimens, such as well distributed cuboidal γ′ in the as-received condition, rafted γ/γ′ structure after degradation, chain like γ′ particles, TCP phases and cast pores were investigated and are discussed in this section.

4.3.1 As-Received CMSX-4

The main constituents of Ni-based superalloys are gamma (γ) and gamma-prime (γ′). It is the γ′ phase which is largely responsible for the high temperature strength of the material and its incredible resistance to creep deformation. The main matrix is γ phase, which is a solid solution with a face-centred cubic crystal structure. γ′ phase is an intermetallic precipitate with a close face-centred cubic crystal structure, where the nickel atoms are at the face-centres and the aluminium or titanium atoms at the cube corners. This atomic arrangement has the chemical formula Ni_3Al, Ni_3Ti or $Ni_3(Al,Ti)$. Since both of the phases are a cubic structure with similar chemical composition, the lattice mismatch between γ and γ′ phases is very small, typically about 0.1%. The good coherence of these two phases is another reason for excellent mechanical properties [3].

The as-received sample has not experience any heat treatment, therefore, the microstructure of the CMSX-4 in as-received condition is the base line for this research, which is shown in Figure 4.3. γ′ particles were uniformly distributed throughout the whole sample, with a size ranging from ~0.5 to 1.0 μm. Most γ′ particles displayed a regular cuboidal morphology to maintain excellent mechanical performance. The gap or channel between the γ′ particles was very small, less than 100 nm. There were no coarse γ′ (γ′ eutectics) particles or carbides detected within

this alloy, although thermodynamic equilibrium calculations discussed reported in Section 4.2 did indicate an expected presence of carbides. However, these carbides were in a very small amount, less than 0.1 wt. % and virtually had no influence on mechanical properties.

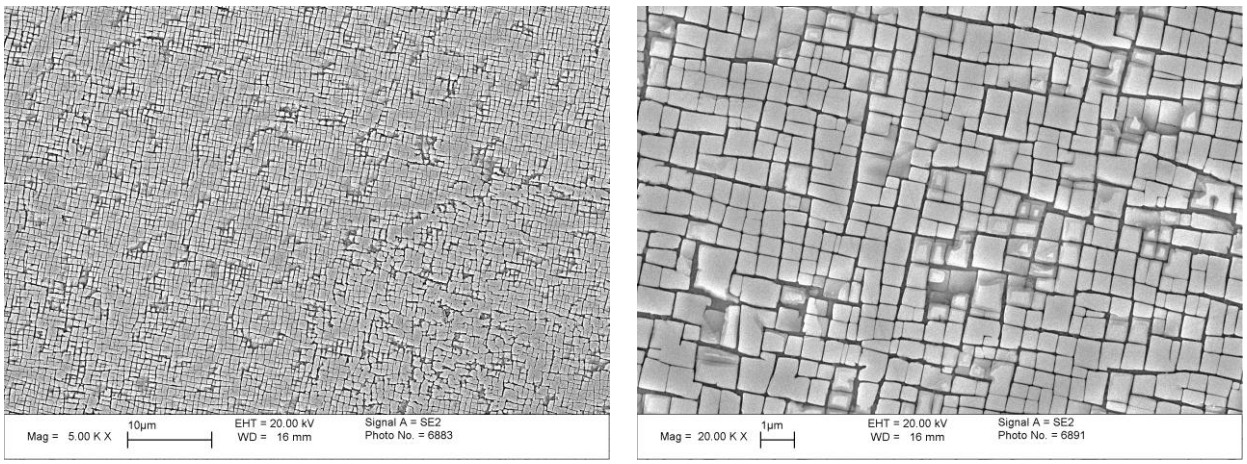

(a) Low Mag **(b) High Mag**

Figure 4.3. SEM images showing microstructure of standard CMSX-4 in the as-received condition. The right is the higher magnification of the same area showing γ and γ′.

In order to evaluate the thermodynamic prediction, chemical analysis was carried out on the main phases observed within the alloy by using FEGSEM combined with EDX. The results of such investigation provided quantitative information on the chemical compositions and can be used for comparison of the predicted values. The chemical analysis and predicted results are shown in Table 4.3. Table 4.3 shows that the γ′ particles contain mainly Ni with smaller amounts of Ta, Al and Co, approximately 9.3(±0.9), 7.5(±0.2) and 6.9(±0.5) wt.% respectively. These values are very close to the range predicted by the thermodynamic equilibrium calculations for Ta (8.8-13wt.%), Al(7.6-7.7wt.%) and Co(3.8-7.1wt.%). The predicted and experimentally determined compositions have a good agreement. The etchant used throughout this project promotes the removal of γ phases, leaving γ′ phases in the microstructure. Therefore the chemical analysis on γ was not applied in this study.

Table 4.3 Chemical analysis of γ′ phase in CMSX-4 / wt%

Elements	Ni	Al	Cr	Co	Ta	W	Re
γ′ predicted	65.1 - 70.9	7.6 - 7.7	1.7 - 2.1	3.8 - 7.1	8.8 - 13.0	3.5 - 5.8	0 - 0.5
γ′ EDX	63.4 - 65.6	7.3 - 7.6	2.4 - 3.1	6.4 - 7.4	8.4 – 10.2	4.6 - 6.7	0.1 - 0.8

4.3.2 Rafted CMSX-4

After isothermal ageing at 1050°C for 1000 hours, the microstructure of CMSX-4 has been degraded. Figure 4.4 shows the microstructure of CMSX-4 after long term exposure at high temperature, where cuboidal secondary γ′ particles were coalesced together in directions to forms plate known as ”rafts”, with increased average size (5-10 μm). This directional coarsening of γ′ particles is often observed after high temperature exposure under applied stress, which is commonly, referred to as “rafting”. In the isothermally aged condition, without any stress, directional coarsening or rafting is caused by residual chemical gradients and stress present in the alloys [21]. In Figure 4.4, most secondary γ′ particles were directionally coarsened to form rafts, but in some regions, see lower right corner of Figure 4.4a, cuboidal secondary γ′ particles were present with only slight rounding of the edges. The size of these cuboidal γ′ particles is the same as those in the as-received condition. However, in later microstructural analysis, such as area fraction of secondary γ′ particles and γ channel width measurement, both rafted and cuboidal γ′ particles were included into the analysis, giving representative results.

As a consequence of rafting, the corridor or channel between these secondary γ′ particles becomes larger, which makes it easier for dislocations to pass through [5]. For this reason, the channel widths have been measured throughout this research. Inside the channels, small spherical γ′ particles with various sizes were observed.

In order to distinguish between the large cuboidal and rafted secondary γ′ particles, these small spherical particles are referred to as tertiary γ′ precipitates. The presence of tertiary γ′ precipitates is at the expense of the secondary ones. It is reported that these particles have second phase hardening effect on the material, which can act as boundaries to block the movement of dislocations [5]. However, the majority of the strength still results from the small γ channels. Tertiary γ′ precipitates as another important microstructural feature were also investigated in this project.

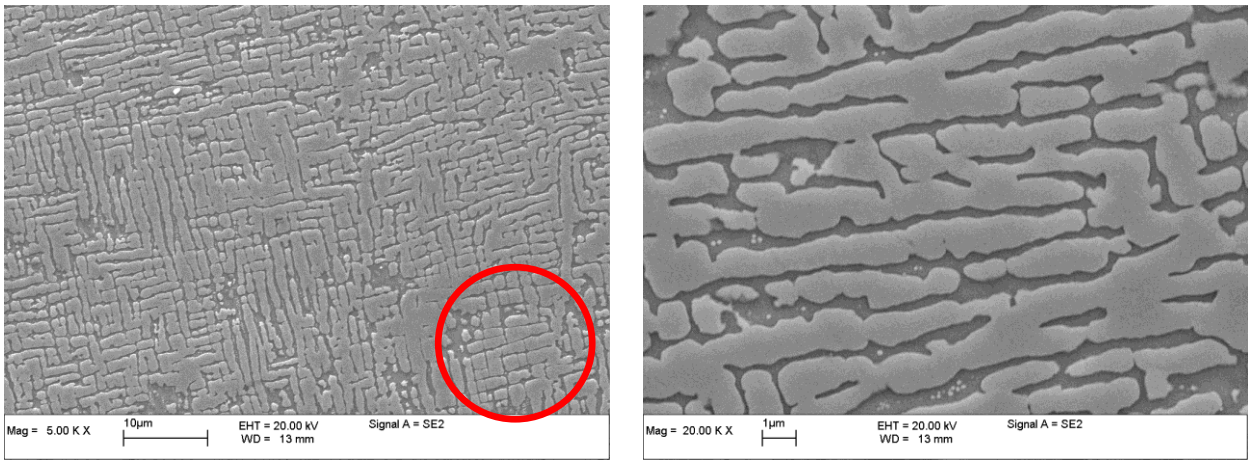

(a) Low Mag **(b) High Mag**

Figure 4.4. SEM images showing microstructure of standard CMSX-4 in rafted conditions. The right is the higher magnification of the same area showing γ channel and tertiary γ′ precipitates.

4.3.2.1 "Chain like" Gamma Prime (γ′)

In some regions, there are very small amount of γ′ particles coalesce to form aligned structures, or chain like γ′ particles, which disrupt the γ matrix. Figure 4.5(a) shows the typical chain like γ′ particles in the microstructure of CMSX-4 superalloy in as-received conditions, where a continuous curved line of cuboidal γ′ particles are observed throughout the microstructure. The chemical analysis shows that the chemical composition of the chain like γ′ particles is the same as normal cuboidal γ′ particles. It has been reported that these microstructural features were often

observed after high temperature solution heat treatments and could result from highly localised melting at planar defects or more likely from the different precipitation conditions at such defects upon cooling [1]. It has been suggested that these microstructural features are low angle gain boundaries. However, they are not apparently associated with any detrimental effects on the microstructure or mechanical properties [5].

These microstructural features are more often to be found when the sample has undergone isothermal ageing at 1050°C for 1000 hours, see Figure 4.5(b). This is because under that conditions, diffusion is fast and γ′ particles are more easily coalesced to form rafts. In some cases, the raft formed as a long continuous curve or chain, but no harmful effect has been identified [5]. It has been reported that the coalescence of the γ′ particles can be induced by residual chemical gradient resulting from segregation [5], which will be discussed in more detail in the chemical segregation chapter.

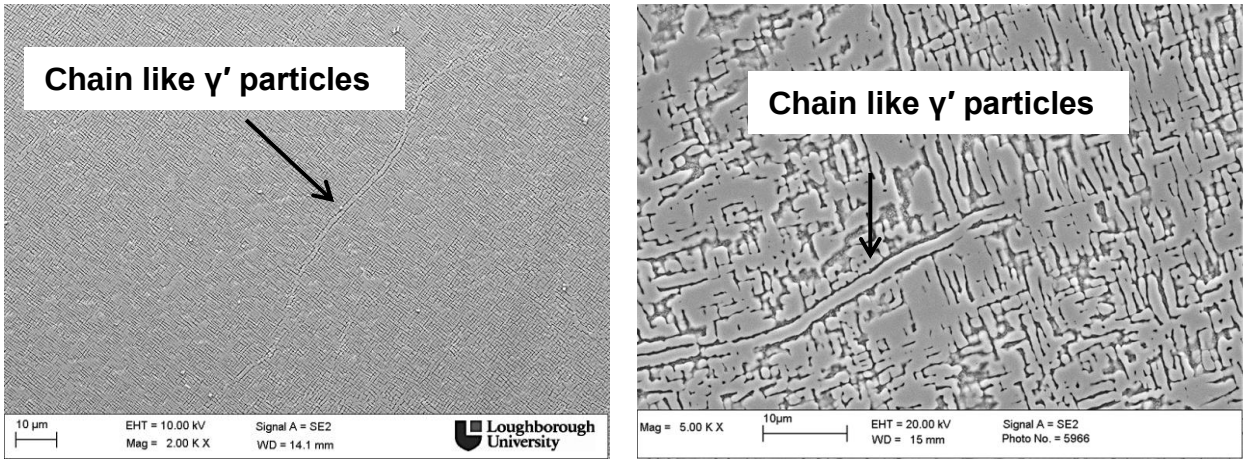

(a) As-Received **(b) Rafted**

Figure 4.5. SEM images showing microstructure of standard CMSX-4 in (a) as-received conditions, (b) rafted, which is isothermal ageing 1050°C for 1000 hours, showing chain like γ′ particles.

4.3.2.2 TCP phases

After isothermal ageing at 1050°C for 1000 hours, clusters of blocky and needle like precipitates were observed within the alloy shown in Figure 4.6. These particles are very bright in backscatter detector (BSD) mode, which indicates they contain heavy elements. The chemical analysis obtained from the FEGSEM shows that these precipitates contain a large amount of Re and W, ranging from 21-26 wt.% and 26-37 wt.% respectively. The morphology and the high content of Re and W suggests that these precipitates are TCP phases. The thermodynamic equilibrium calculations show at 1050°C, the TCP phase present within this alloy is μ phase. However, the thermodynamic calculated μ phase at 1050°C contains Re and W with approximately 30 wt.% and 43 wt.%. The difference between the experimental results and predicted data is on the Ni content. The chemical analysis results obtained from FEGSEM contain a large content of Ni, ~25 wt.%, compared to predicted value which is only about 9.3 wt.%. The large content of Ni present in this chemical analysis brings down the wt.% of Re and W. The reason for this difference is that the EDX in FEGSEM has interaction volume effects, where underneath γ/γ′ phases are also detected and analysed, resulting in a large content of Ni. The full chemical composition of these TCP phases both experimentally determined and from thermodynamic predictions is shown in Table. 4.4.

In order to eliminate the γ phase's effects in interaction volume, the EDX was applied using TEM, which was carried out on a very thin sample, ~200 nm, which was prepared by using FIB lift out technique. The small size of the sample massively reduces the interaction volume and gives a more accurate chemical analysis results. The full TEM EDX result is shown in Table 4.4. The TEM chemical analysis results show that the TCP phase contains 28 wt.% Re and 37 wt.% W, which is consistent with the thermodynamically predicted data (±10 wt.%). The morphology and chemical composition have a good agreement of the μ phases. These precipitates were further identified as μ phases by using a combination of

TEM images and selected area fraction diffraction patterns. The typical TEM images and diffraction pattern of these precipitates are shown in Figure 4.7, where the lattice parameters obtained from the μ phases were a_o=4.72Å, c_o=25.6Å. The obtained lattice parameters were very close to the literature data (a_o=4.75Å c_o=25.67Å), where μ phase is a rhombohedral crystal structure. The patterns and lattice parameters have a good agreement with the μ phase in the literature [35-38].

Table 4.4. Thermodynamic calculations and EDX analyses in the SEM and TEM / wt%

Element	Ni	Cr	Co	Ta	W	Re
Predicted	9.3	6.7	6.8	3.6	43.4	29.7
FEGSEM	23.5 - 26.8	7.9 – 9.4	8.1 - 9.9	2.63 -2.75	26.2 - 36.8	21.6 - 25.7
TEM	6.7 - 7.0	9.4 - 9.8	9.3 - 9.7	5.0 - 6.5	38.4 - 39.6	25.9 - 28.0

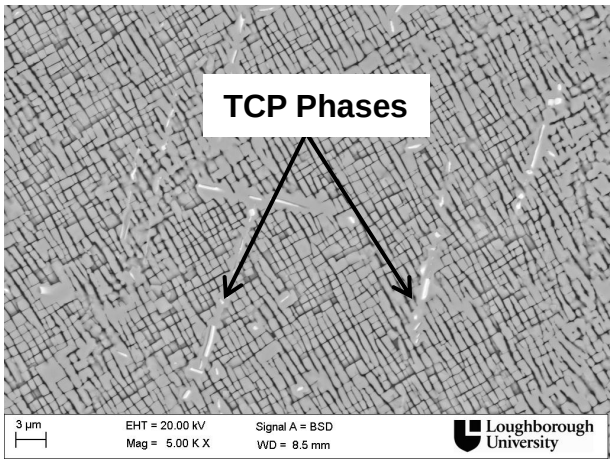

(a) Need like

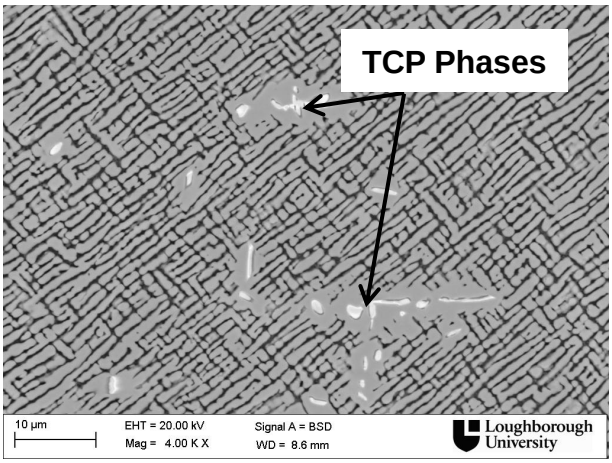

(b) Cluster

Figure 4.6. SEM images of CMSX-4 superalloy, showing the (a) needle like and (b) cluster TCP phases present within the microstructure.

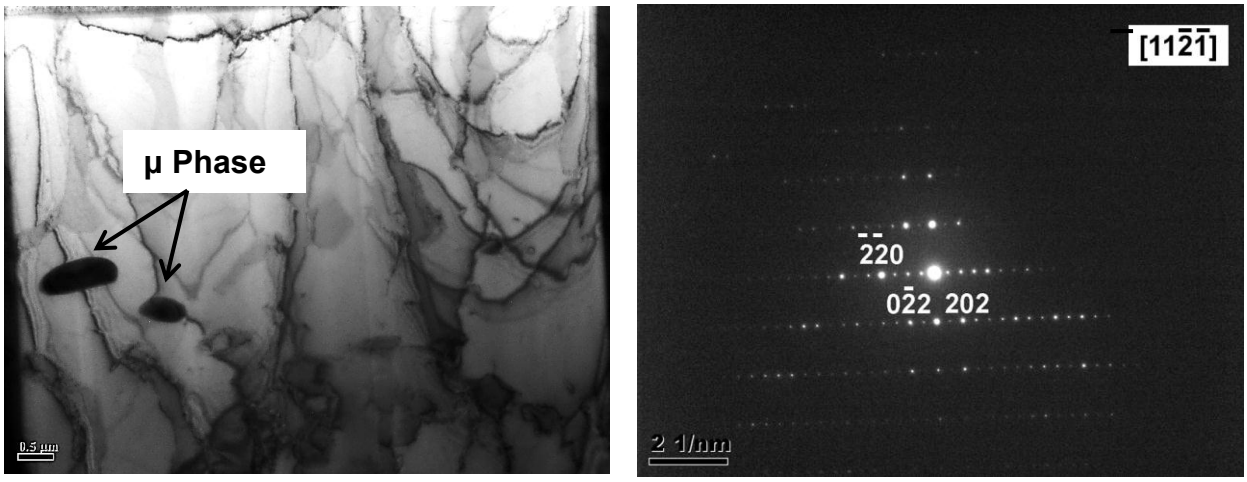

(a) Bright Field **(b) Diffraction Pattern**

Figure 4.7. TEM images of TCP phases, showing (a) bright field of μ phases and (b) selected area of the diffraction pattern.

4.3.2.3 Cast Pores

Another interesting thing observed in the SEM images were casting pores, which are shown in Figure 4.8. Most pores are generally spherical with a diameter of 5-20 μm, although some irregularly shaped pores were observed as well. In order to observe the detail of the pores, a 3D reconstruction image of casting pores was taken by using Alicona Mex 3D software, which is shown in Figure 4.9. The casting pore exhibits valleys and hills in the depth direction with a depth of ~4 μm. The casting pores are present in all samples, which may be caused by the casting during processing.

The size and volume of porosity are two important issues for the cast components. Large cast pores are potentially harmful in the cast components. Sometimes, creep cavities are associated particularly with the well-aligned big size casting pores, leading to failures of the component during its service. However, the cast or gas pores present in these bar specimens are very small, mostly less than 10 μm. These small sizes of the pores will not cause a significant influence on the

mechanical properties. Since the porosity volume obtained from these bar specimens was much smaller than it is acceptable value (0.1%), the volume of porosity is not expect to affect the mechanical performance of these bar specimens in later research.

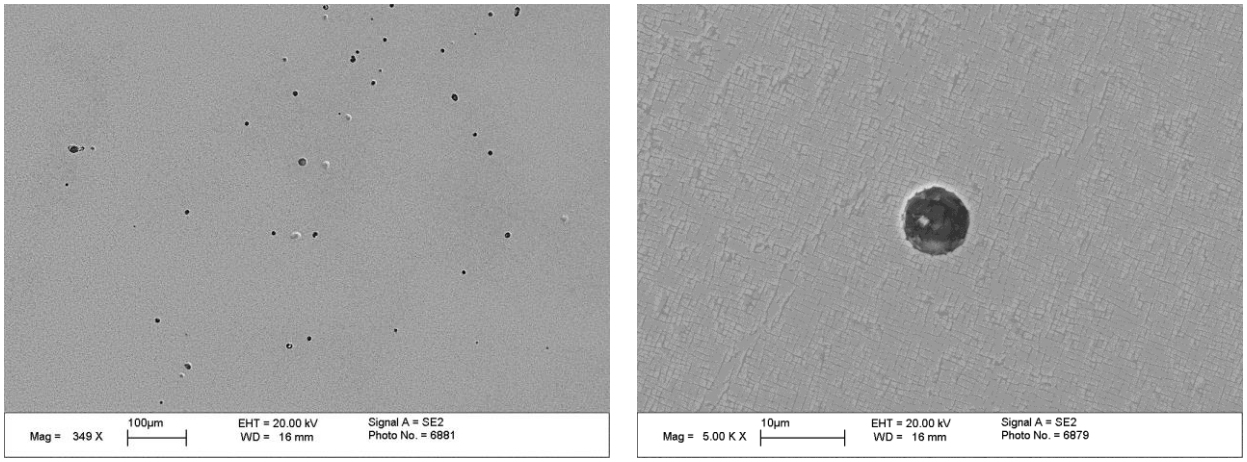

(a) Low Mag **(b) High Mag**

Figure 4.8. SEM images of the cast pores of CMSX-4, (a) low magnification showing the distribution of cast pores, (b) high magnification showing size of the cast pores.

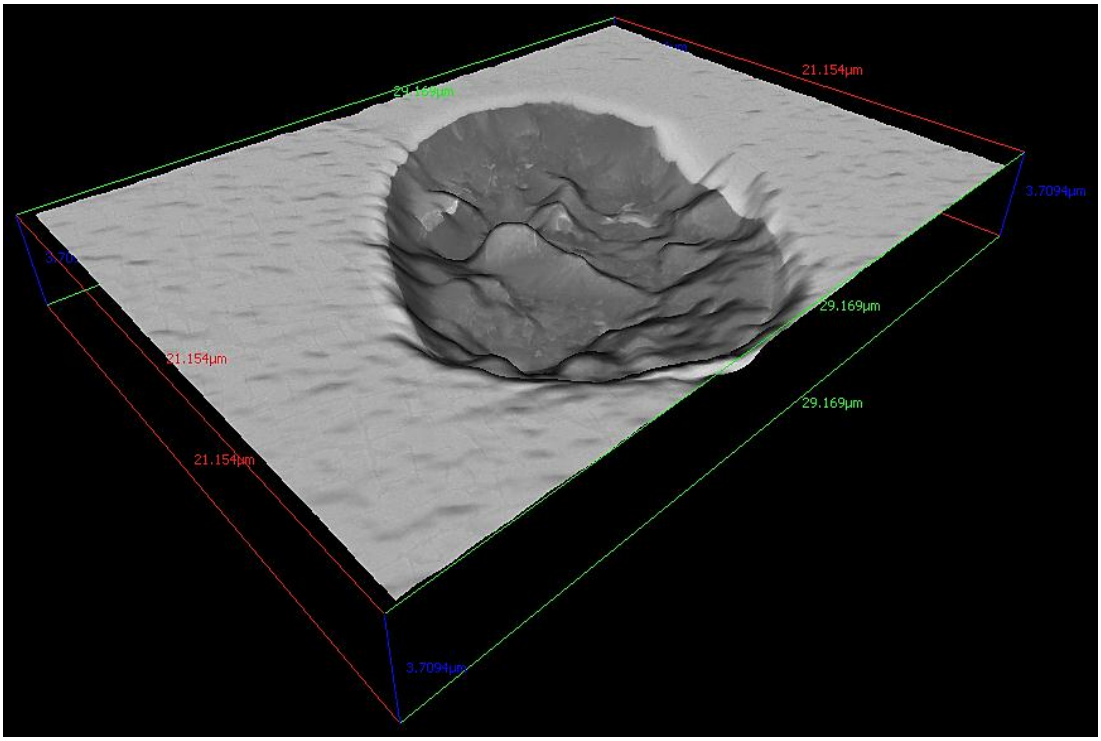

Figure 4.9. 3D image of a casting pore by using MEX software.

4.4 Summary

This chapter has presented and discussed the results of thermodynamic equilibrium calculations and the general microstructural investigation carried out on the standard CMSX-4 in the as-received and degradation conditions. Thermodynamic equilibrium calculations were carried out to predict the amount and chemical composition of the phases occurring at the equilibrium conditions as a function of temperature, ranging from 600 to 1400°C. The general microstructure obtained in the CMSX-4 in as-received conditions, such as uniformly distributed cuboidal γ′, rafted γ/γ′ after degradation, chain like γ′, TCP and cast pores are examined to give a brief introduction of the microstructure of CMSX-4. The thermodynamic calculation predictions have a good agreement with the experimental determination. The chemical analysis of γ′ particles and TCP phases was in close agreement with thermodynamic calculation. However, the focus of this project is on the microstructure evolution of γ and γ′ before and after degradation and rejuvenation combined with their effects on the mechanical performance, which will be discussed in the following chapters.

CHAPTER 5

TENSILE TESTS AND MICROSTRUCTURAL ANALYSIS

5.1 Introduction

In this chapter, the results of tensile testing after different heat treatments, together with microstructural analysis will be presented and discussed. The microstructural evolution of γ′ size and distribution in the Ni-based superalloy CMSX4 after degradation and rejuvenation has been examined. The relationship between mechanical behaviour, heat treatment and microstructure are studied. Experimental techniques used in the study include field emission gun scanning electron microscopy (FEGSEM) and transmission electron microscopy (TEM).

5.2 Tensile Test Data

The tensile test results and curves obtained from the five differently heat treated specimens are shown in Table 5.1 and Figure 5.1 respectively. S1 and S3 (as received and HT Rejuvenation) performed similarly in the tensile test but S3 showed a reduced ductility compared to S1 with an extension of 8.5 mm compared with 12.2 mm. S1 demonstrated a yield strength of 874 MPa and a ultimate tensile strength (UTS) of 921 MPa, whilst the measured values of the yield strength (also UTS) of the rejuvenated sample, S3, was slightly higher at 900 MPa. The high temperature degraded samples (S2 and S4) exhibited considerably lower yield strength and UTS, but demonstrated increased levels of

ductility. Sample S5 has the lowest tensile strength of the five samples. The yield strength and UTS were much lower than sample S3, in which the high temperature rejuvenation had been applied.

Table 5.1 Tensile test results for the five different samples

Sample No.	Heat Treatments	Yield Strength (MPa)	UTS (MPa)	Elongation (%)
S 1	As-received	874	921	19.6
S 2	Rafted	724	832	22.7
S 3	Rafted + HT Rejuvenation	900	900	13.7
S 4	Rafted + HT Rejuvenation +Rafted	728	792	31.9
S 5	Rafted + LT Refurbishment	698	698	24.7

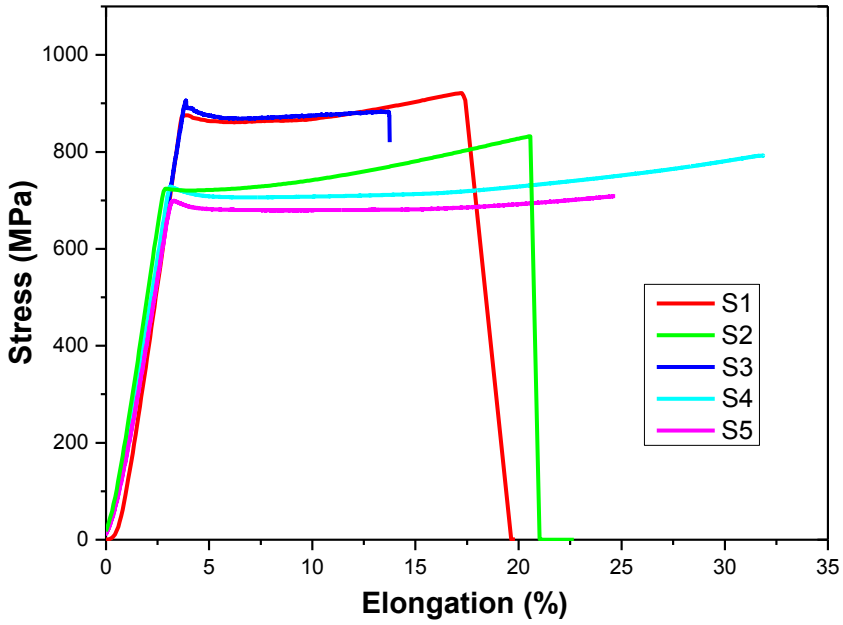

Figure 5.1. Tensile test results of CMSX-4 samples after five different heat treatment conditions: (a) S1. as received, (b) S2. rafted, (c) S3. rafted + HT rejuvenation, (d) S4. rafted + HT rejuvenation+ rafted, and (e) S5. rafted + LT refurbishment.

5.3 SEM Microstructural Examination

In this section the results of the SEM microstructural investigation of the five heat treated samples will be presented and discussed. The results obtained can be used for microstructural analyses such as the area fraction of secondary γ′ particles, γ channel width and rafting parameter. The aim of this investigation was to evaluate the performance of the rejuvenation, combined with the examination of their tensile behaviour. However, more importantly the intention was to find the relationship between mechanical property, microstructure and heat treatments. In order to individually investigate the influence of isothermal ageing and external stress, the heads and gauge lengths portions of each sample were examined respectively.

5.3.1 Heads

Figure 5.2 and Figure 5.3 show the microstructure of the head portions of the CMSX-4 samples after the five different heat treatments. The head portions have not experienced any stress during test, the microstructures of which are representative of isothermal ageing only, rather than the application of the external stress. S1 and S3 exhibited a uniform distribution of the secondary (cuboidal) γ′, with a size of ~0.5 μm. S2, S4 and S5 had a rafted microstructure with an increased size of secondary γ′ particles. The gaps between the secondary γ′ particles or γ channels were broader. Tertiary γ′ precipitates in the γ channels between the large γ′ particles were found in all samples except S1. The size of the tertiary γ′ varied, especially in S2, where both very large (>100 nm) and fine (<20 nm) tertiary γ′ precipitates were found. It is believed the presence of a large amount of tertiary γ′ precipitates in the channels affected the mechanical behaviours since it has second phases hardening effect on materials,

which provides some obstacles for dislocation motion [5, 6].

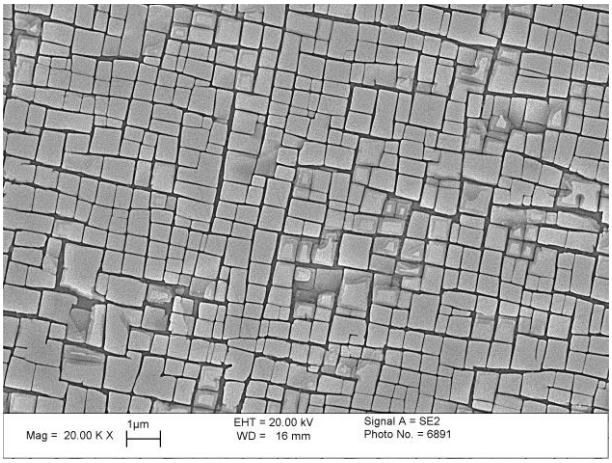

(a) S1. As Received

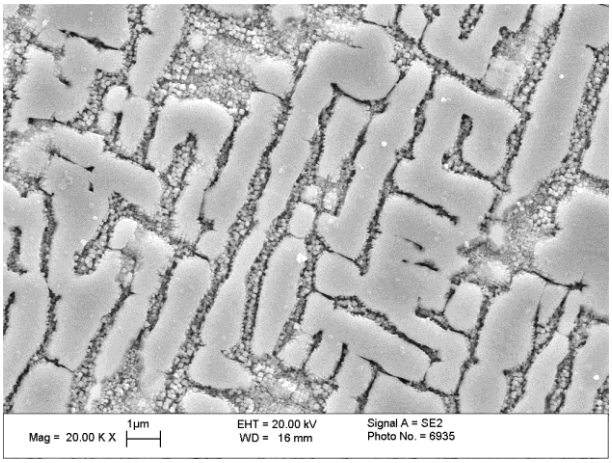

(b) S2. Rafted

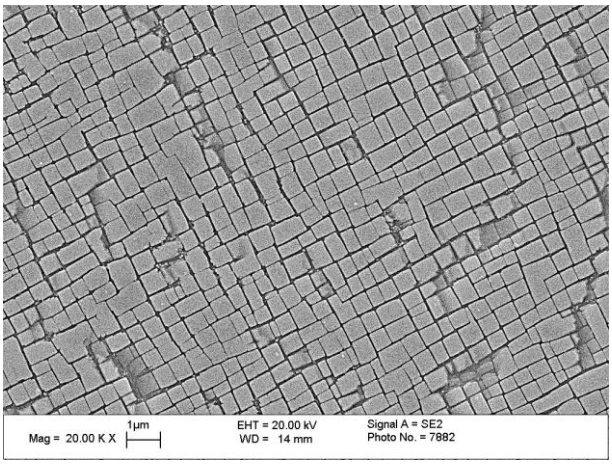

(c) S3. Rafted + HT Rejuvenation

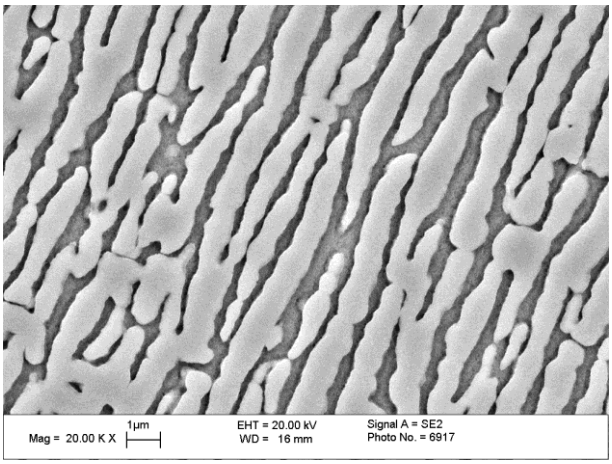

(d) S4. Rafted + HT Rejuvenation+ Rafted

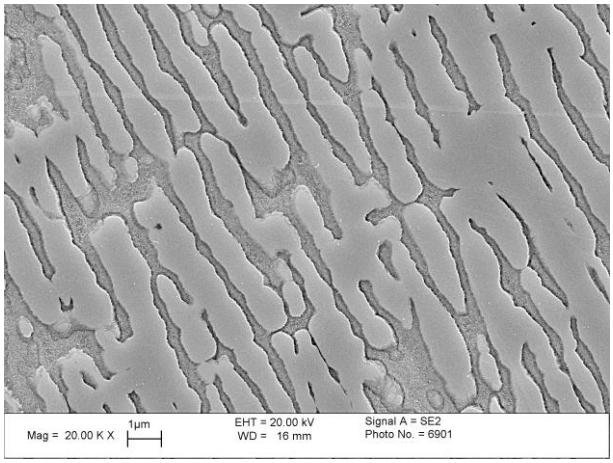

(e) S5. Rafted + LT Refurbishment

Figure 5 2. Low magnification SEM images of the head portions of the tensile samples after five different heat treatment conditions, showing distribution and morphology of γ/γ′.

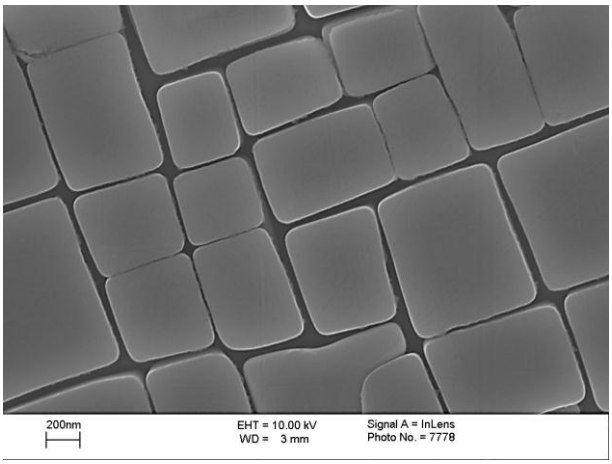

(a) S1. As Received

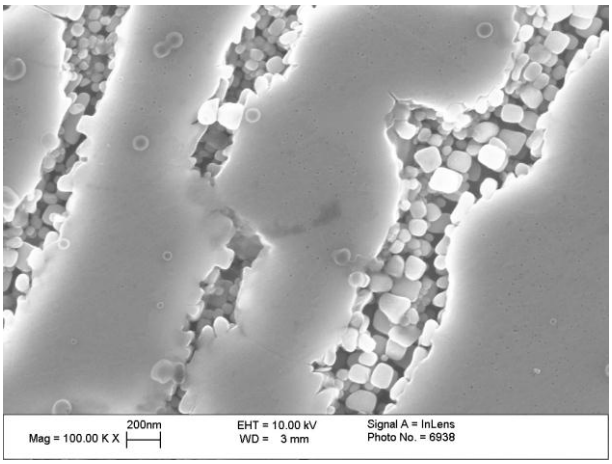

(b) S2. Rafted

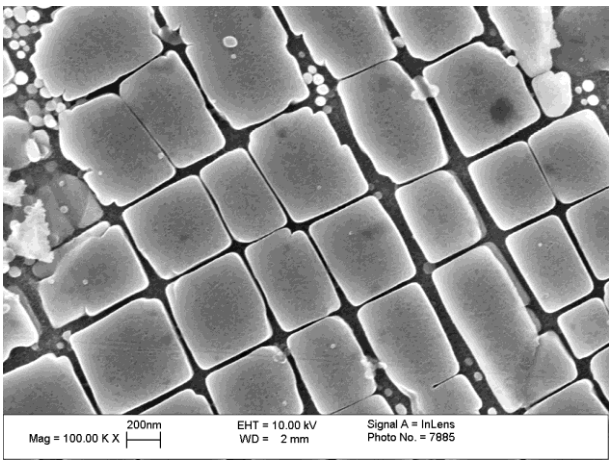

(c) S3. Rafted + HT Rejuvenation

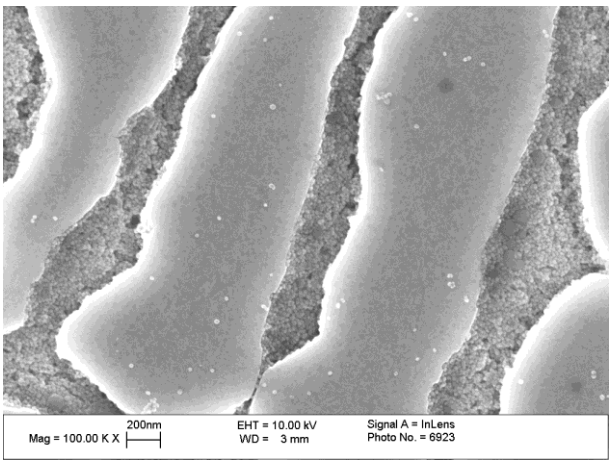

(d) S4. Rafted + HT Rejuvenation+ Rafted

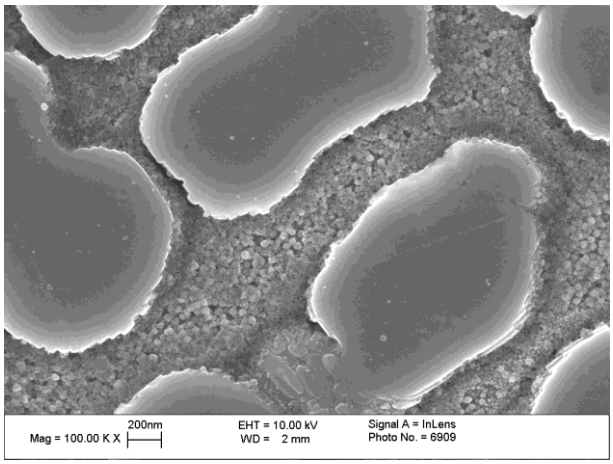

(e) S5. Rafted + LT Refurbishment

Figure 5.3. High magnification SEM images of the head portions of the tensile samples after five different heat treatment conditions, showing γ channels and tertiary γ′ precipitates.

5.3.2 Gauge lengths

In order to examine the effects of the external stress on the microstructure, the gauge lengths of the tensile specimens were also examined. According to the images taken from various positions along the gauge length, it was found that the microstructure at a position some distance from the fracture face was similar to that seen in the head portions. Therefore, in this section only the microstructure no more than 100 μm away from the fracture will be discussed.

The microstructure of gauge length portions of the tensile specimens is shown in Figure 5.4 and Figure 5.5. The microstructure of the gauge length was very similar to the microstructure of the corresponding head portions. Some distortion of the cuboidal γ′ particles was observed in S1 and S3, which is likely to have been caused by the elongation of the microstructure due to the applied stress. The microstructures of S2, S4 and S5 show no significant differences when compared to the images of the corresponding head portions in Figure 5.2. This is because the room temperature tensile was a very quick mechanical test, compared with creep and fatigue testing. The external tensile stress has little or small effect on the microstructure, resulting in a similar microstructure in heads and gauge lengths.

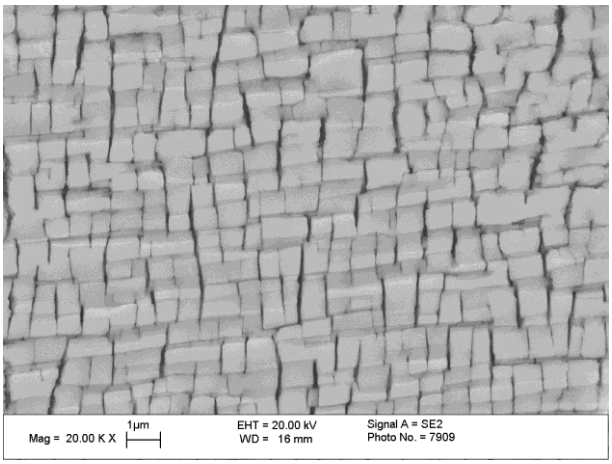

(a) S1. As Received

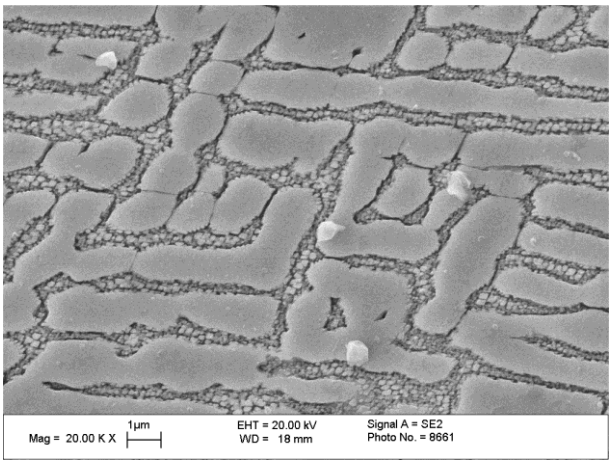

(b) S2. Rafted

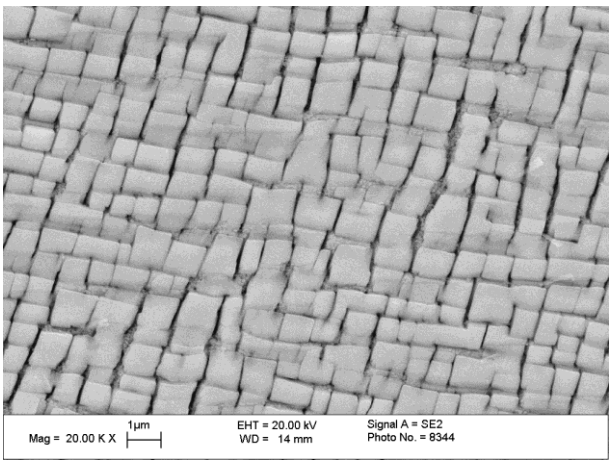

(c) S3. Rafted + HT Rejuvenation

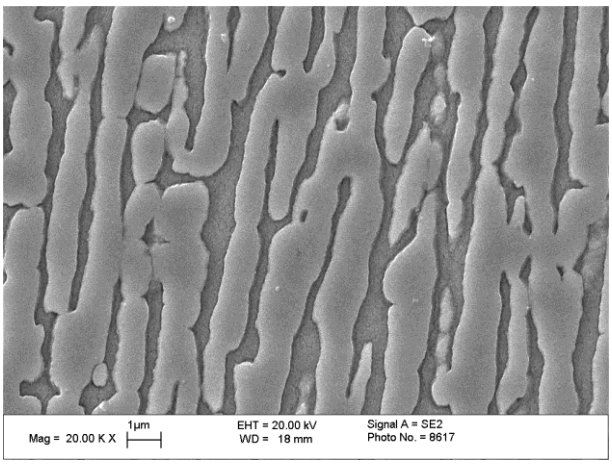

(d) S4. Rafted + HT Rejuvenation+ Rafted

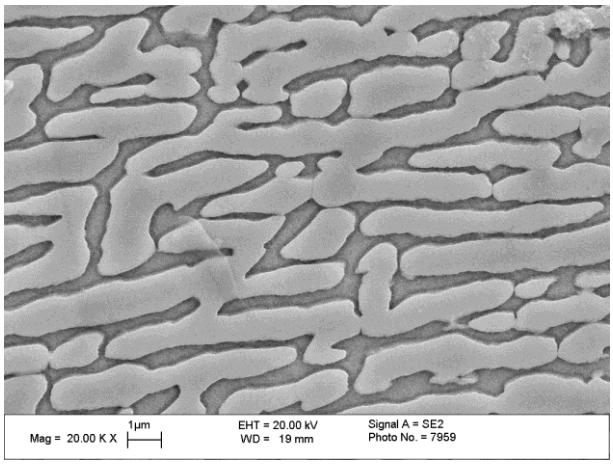

(e) S5. Rafted + LT Refurbishment

Figure 5.4. Low magnification SEM images of the gauge length portions of the tensile samples after five different heat treatment conditions, showing distribution and morphology of γ/γ′.

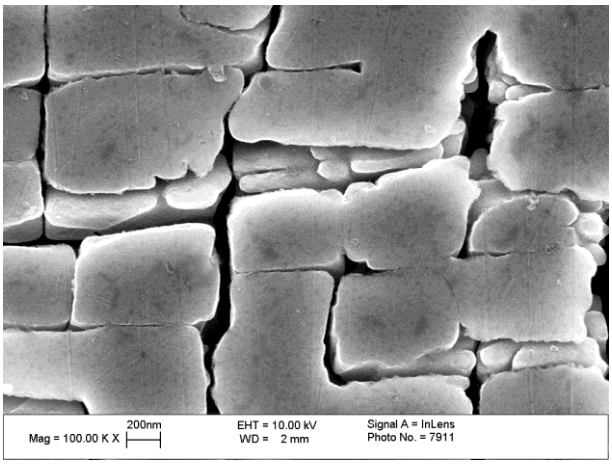

(a) S1. As Received

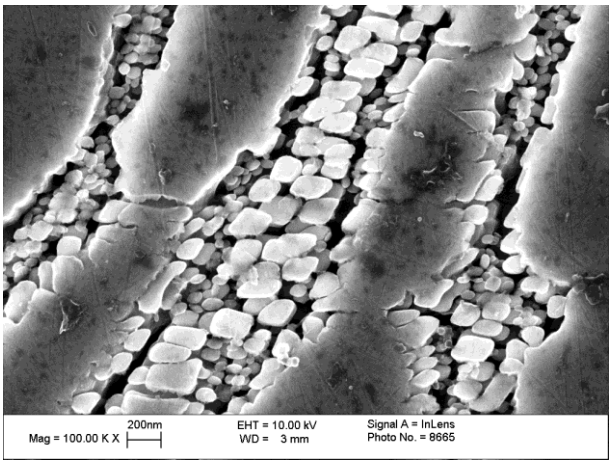

(b) S2. Rafted

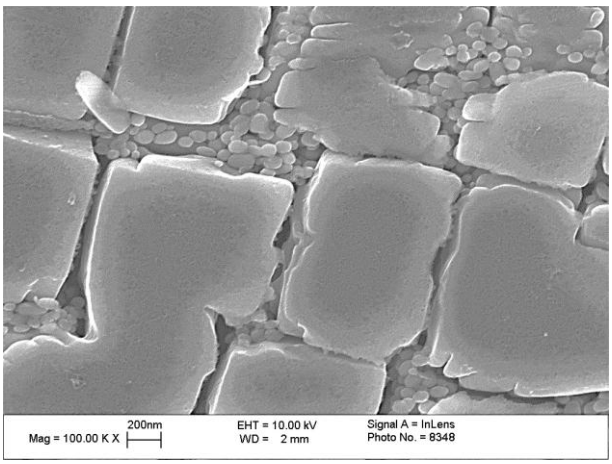

(c) S3. Rafted + HT Rejuvenation

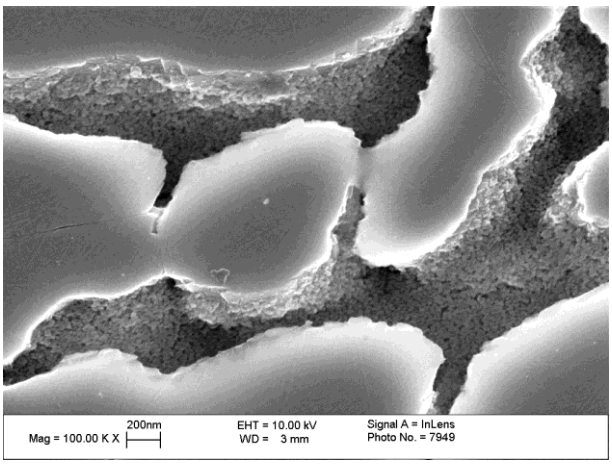

(d) S4. Rafted + HT Rejuvenation+ Rafted

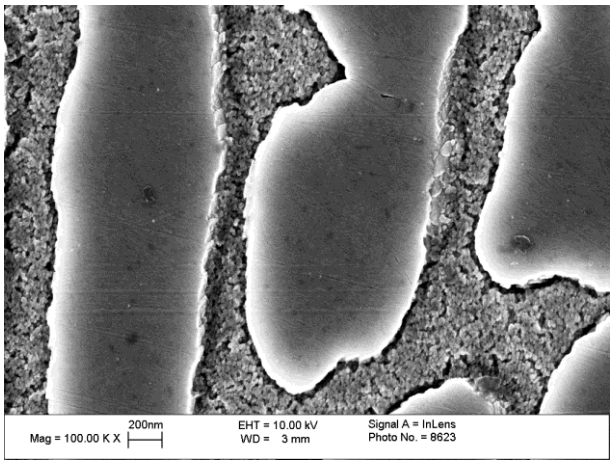

(e) S5. Rafted + LT Refurbishment

Figure 5.5. High magnification SEM images of the gauge length portions of the tensile samples after five different heat treatment conditions, showing γ channels and tertiary γ′ precipitates.

5.4 Quantification of Area Fraction of Secondary γ′, γ Channel Widths and Rafting Parameter

In order to quantify the microstructural features of CMSX-4 after the different heat treatments, image analysis was carried out to quantify the area fraction of secondary γ′, γ channel widths and rafting parameter using image analysis software. Figure 5.6 illustrates the overall results of the area fraction of secondary γ′ particles for both the heads and gauge lengths, followed by the channel width measurements and rafting parameter, shown in Table 5.2, Table 5.3 and Figure 5.7 respectively.

In single crystal nickel-based superalloys, the high level of rupture strength and creep resistance results from the high volume fraction of γ′ contained within the alloy [1-5]. In this study, the area fraction of γ′ has been used as an approximation of volume fraction, which is reasonable given the similar densities of γ and γ′. The area fraction of secondary γ′ particles for both heads and gauge length of the five different samples are shown in Figure 5.6. For all five samples, the area fraction of the gauge length is slightly higher than the heads. This may be due to the distortion of secondary γ′ particles due to tensile testing, which makes the particles beneath the top layers visible, which are subsequently counted in the area fraction measurement. However, the area fraction of the heads and gauge lengths show the same trend, which suggests that the relationship between area fraction of secondary γ′ particles and tensile stress is still valid for the gauge length. According to both the tensile test results and the area fraction measurements, the yield and ultimate tensile strength increases with the area fraction of secondary γ′ particles. Although the rafted sample (S2) has the lowest area fraction of secondary γ′ particles, 0.684, it should be noted that there are a large number of tertiary γ′ precipitates in the channels. Moreover,

the size of these precipitates is quite large (100-200 nm). The presence of these large tertiary γ′ precipitates in the channel will affect the movement of dislocations, which improves the yield and ultimate strength but reduces the ductility [5].

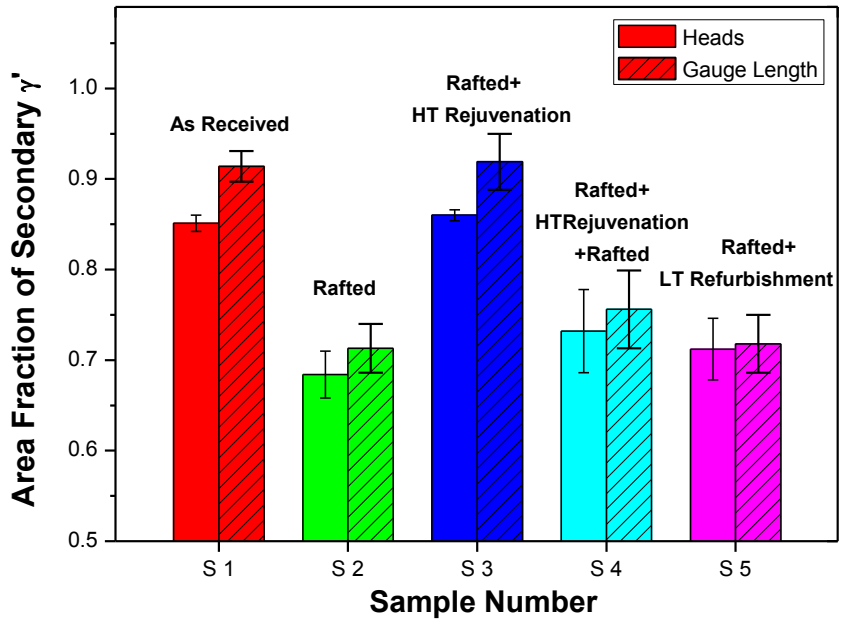

Figure 5.6. The area fractions of secondary γ′ particles from the five different heat treatment conditions for both the heads and gauge lengths of the tensile specimens.

In order to quantify any influence of the γ channel widths on mechanical properties, these were measured in both the perpendicular (⊥) and parallel (//) directions with respect to the <001> orientation and are given in Table 5.2 and Figure 5.7. A schematic illustration of the orientation is shown in Figure 5.8. The channel widths between the secondary γ′ precipitates in the as-received and high temperature rejuvenated samples are very small (~60 nm), whilst those in the degraded structures are much larger (~300 nm). The small channels of the as-received and rejuvenated samples lead to higher yield and ultimate strengths in the tensile test. In CMSX-4, the movement of dislocations are governed by the

spacing of the secondary γ′ particles [5]. When the spacing is small, the dislocation has to move across the precipitates by shearing or cutting. The dislocation movement is thus impeded, leading to an increase in the applied stress and hence improved mechanical properties. When the spacing is larger, as in the rafted structure, dislocations can move by glide or climb, which is a process which requires less stress and results in poorer mechanical performance [5-10].

Table 5.2 γ Channel widths of the five different heat treated samples

Sample No	Heat Treatments	γ Channel Width (nm)			
		Heads		Gauge Lengths	
		//	⊥	//	⊥
S 1	As-received	67±13	58±11	63±13	59±15
S 2	Rafted	293±55	255±50	280±53	250±42
S 3	Rafted + HT Rejuvenation	60±13	59±10	58±19	54±17
S 4	Rafted + HT Rejuvenation + Rafted	270±64	116±35	242±81	99±31
S 5	Rafted + LT Refurbishment	298±95	127±45	257±84	101±37

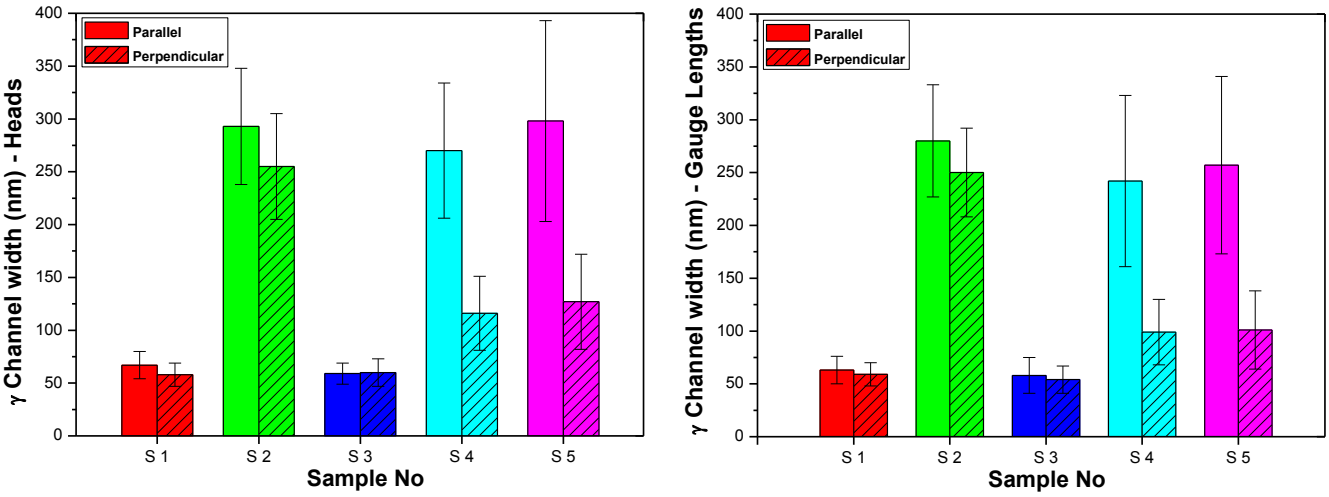

(a) Head Portions **(b) Gauge Length Portions**

Figure 5.7. Channel width measurements of the channels between the secondary γ′ particles of both (a) heads and (b) gauge lengths for the five different heat treated samples measured in parallel and perpendicular directions using image analysis.

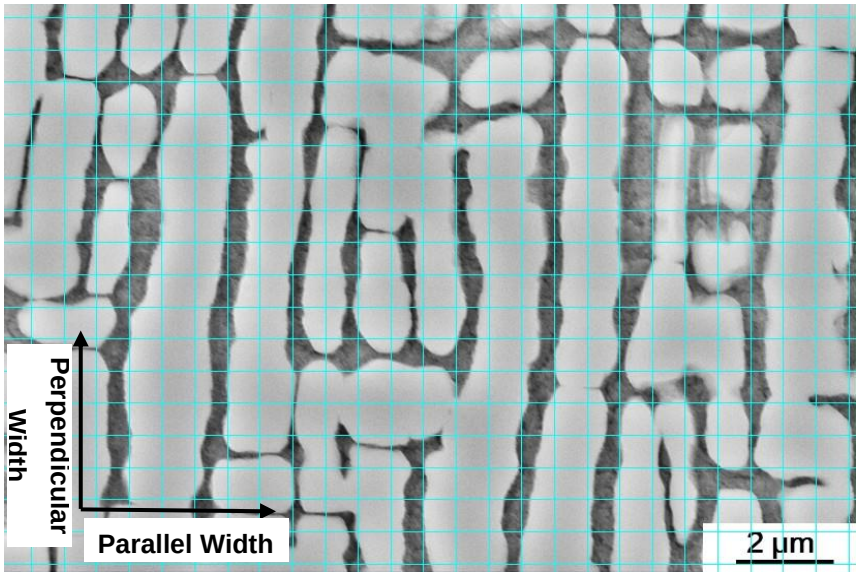

Figure 5.8. A schematic illustration of the orientation of the perpendicular and parallel channel widths for the measurement of the γ channels.

Table 5.3 Rafting Parameter of the five different heat treated samples

Sample No	Heat Treatments	Heads	Gauge Lengths
S 1	As-received	0.56	0.59
S 2	Rafted	1.64	1.72
S 3	Rafted + HT Rejuvenation	0.55	0.57
S 4	Rafted + HT Rejuvenation + Rafted	2.65	2.78
S 5	Rafted + LT Refurbishment	2.15	2.23

Although the average parallel γ channel width of S2 (293 nm in head and 280 in gauge length) and S4 (270 nm in head and 242 nm in gauge length) show no significant difference, the channel widths in the perpendicular direction are substantially different. S2 has an average width of 255 nm (head) in the perpendicular direction, whilst S4 was only 116 nm (head). The difference in channel width indicates that the degrees of rafting are different in these samples.

In order to define the degree of rafting, a rafting parameter R was used, where R=L/2T (L is the length of rafts and T is the thickness) [130]. For a cuboidal γ′ particle a rafting parameter of 0.5 would be expected. As shown in Table 5.3, the rafting parameter of S1and S3 is very small, around 0.5, because the length and thickness values are the same. However, for rafted samples, rafting results in a very large length but small thickness value, which leads to a greater rafting parameter. The rafting parameter for S4 is much larger than S2, which confirms the observation that S4 has a more continuous rafted microstructure. With these continuous broader channels, dislocations can move more easily through the structure, which consequently leads to a reduction in tensile strength. Rafting increases the size and spacing of the secondary γ′ precipitates, this in turn makes the γ channels broader and causes a reduction in the measured area fraction of secondary γ′ particles. Moreover, it was observed that the long-term degradation process precipitated large amounts of fine, spherical tertiary γ′ precipitates within the channels with a size range from 20 to 200 nm. The tensile strength data and the morphology of the rafted samples are in good agreement with previous work [9-11].

After an initial rafting treatment, two samples had undergone two different rejuvenation heat treatments: high temperature rejuvenation (solution and ageing) and low temperature refurbishment (holding 1140 °C for 6 hours). According to the SEM images, the microstructure of the high temperature rejuvenation sample, S3, shows the same distribution, size and morphology as the as-received sample. The remnants of the fine γ′ precipitates in the channels indicate that the rejuvenation heat treatment failed to take all of the fine inter-channel precipitates back into solution, which were also found in the rafted + rejuvenated + rafted sample (S4). This may because the rejuvenation heat treatment is too short to dissolve all the tertiary γ′ precipitates in channels.

However, the microstructure of the low temperature refurbished sample (S5) shows a further degradation of an already rafted structure. The bigger difference of γ channel width in parallel and perpendicular directions and a larger rafting parameter indicate that S5 has a more continuous rafted microstructure. With these continuous broader channels, the dislocations can move easily and unhindered through the structure, which consequently leads to a reduction in tensile properties. Moreover, the low temperature refurbishment process appears to dissolve the larger tertiary γ′ in the channels, which can be advantageous as a barrier to prevent the movement of dislocations. The lower yield and UTS obtained in the tensile test may be partly attributable to the absence of these particles.

In order to evaluate how the high temperature rejuvenation performed in recovering the microstructure and mechanical properties, the high temperature rejuvenated sample had then undergone subsequent rafting treatment, which was S4. The microstructure of S4 showed a similar size of secondary γ′ particles but with a greater extent of rafting compared with S2. This is might because any segregation presence within the microstructure from the first degradation was not recovered and has been enhanced by the second rafting treatment [10], resulting a higher degree of rafting within the microstructure. A substantial difference of the channel width in the parallel and perpendicular directions was also observed in S4, again indicating that a more continuous rafted microstructure was obtained, with an accompanying reduction in mechanical properties.

Microstructural examination confirmed that under the tensile test conditions used here, the evolution of the γ′ size and γ channel widths, and the precipitates of γ′ show a good agreement with the tensile results. In addition, the similarity of the

heads and gauge lengths indicates the external stress has no significant influence on the microstructure during the tensile test compared with heat treatments. The results suggest that the high temperature rejuvenation is an effective heat treatment for rafted (or partially rafted) CMSX-4 materials, and appears to be significantly better than a low temperature refurbishment. Furthermore, applying a refurbishment which does not fully dissolve the γ′, like low temperature refurbishment, is in fact detrimental, rather than beneficial.

5.5 TEM Microstructural Examination

This section will present and discuss the results of the TEM microstructural investigation of CMSX-4 samples. During sample preparation, etching may dissolve or remove the tertiary γ′ precipitates in the channels, which will affect the SEM investigation. In this case, ion milling or FIB lift-out prepared TEM samples were used to further examine the presence of the tertiary γ′ precipitates and their effects on dislocations within the material. Figure 5.9 shows TEM images of the gauge length of CMSX-4 tensile specimen after the five different heat treatment conditions. The TEM results were consistent with SEM investigations. S1 and S3 have well distributed cuboidal secondary γ ′ particles (<1μm), with a channel width of less than 100 nm. Tertiary γ′ precipitates were found in samples S2, S3, S4 and S5, all except S1, which could act as barriers to block the movement of dislocations. For S2, which has undergone a single rafting process, the tertiary γ′ precipitates are relatively large at ~100-200 nm, whereas those formed in S4 are considerably smaller (~20 nm). Dislocations were also observed in S2, S4 and S5, where they were mainly present in the γ channels, especially near the edge of the secondary γ′ particles. These results are consistent with earlier research [11-14]. A small number of tertiary γ′

precipitates were found in S3, in good agreement with the SEM results.

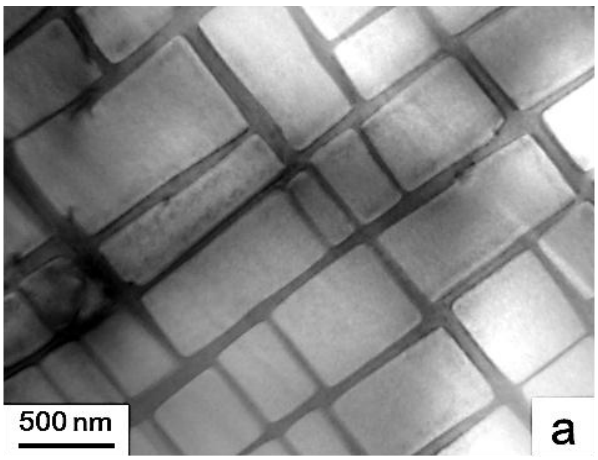

(a) S1. As Received

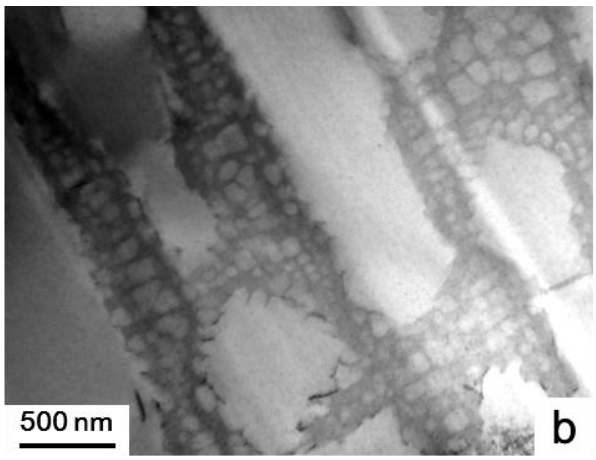

(b) S2. Rafted

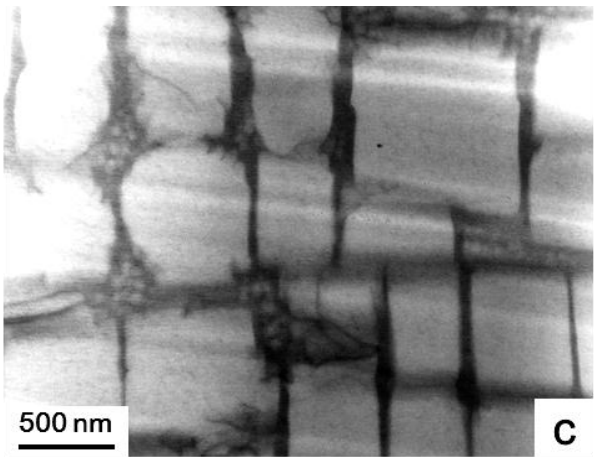

(c) S3. Rafted + HT Rejuvenation

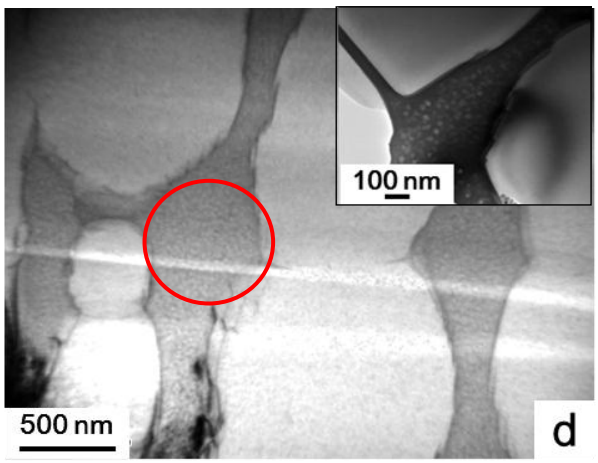

(d) S4. Rafted + HT Rejuvenation+ Rafted

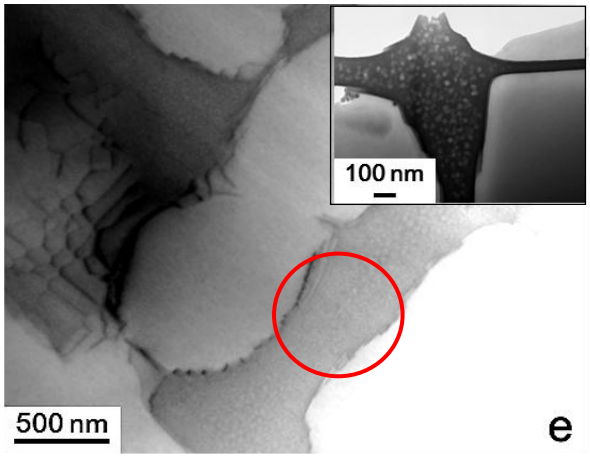

(e) S5. Rafted + LT Refurbishment

Figure 5.9. TEM images of the gauge length of tensile tested samples after five different heat treated conditions, showing distribution and morphology of γ/γ′.

5.6 Summary

The microstructural evolution and tensile behaviour of differently heat treated CMSX-4 samples have been examined. The microstructural evolution of these five samples can be illustrated by the schematic diagrams, see Figure 5.10. The resulting tensile properties developed in CMSX-4 in its various states of degradation, result from changes in the area fraction of secondary γ′ particles, γ channel width and precipitation of tertiary γ′ in the channels. The microstructure of the rejuvenated sample shows the same γ′ distribution, size and morphology as the as-received sample, which is consistent with the tensile test results. These microstructures indicate that the rejuvenation procedure restores the microstructure of a previously rafted sample to a microstructure which is apparently equivalent to the as-received structure. Refurbishment practices involving relatively short term thermal treatment at 1140°C do not appear to be helpful in rejuvenating the microstructure of CMSX-4 and, in fact, care must be taken to ensure that process does not further degrade the materials. The tensile test results show that, whilst the mechanical properties of degraded CMSX-4 are restored using the rejuvenation heat treatment, importantly these are subject to more rapid decline than those of its as-received equivalent during further subsequent degradation treatment.

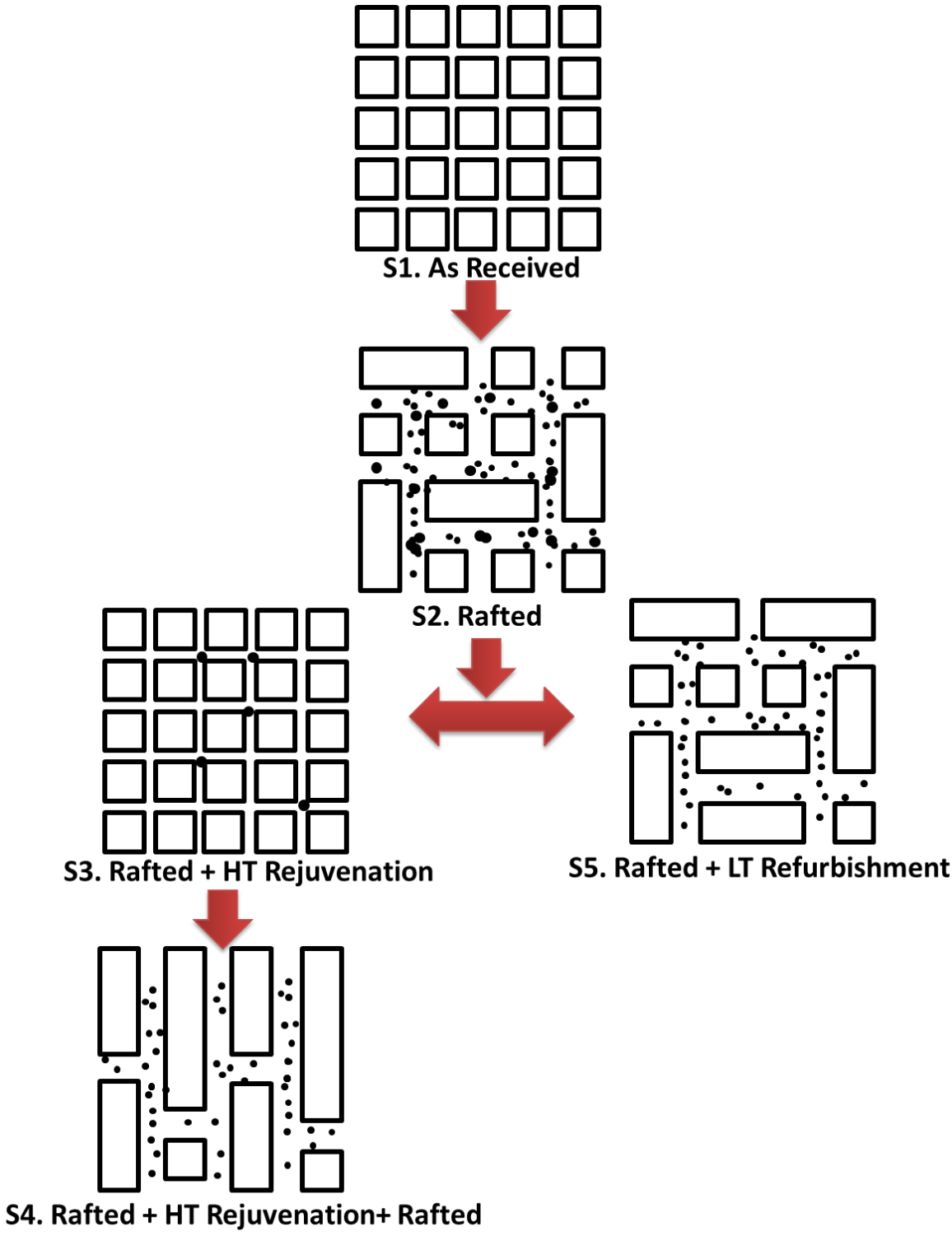

Figure 5.10. Schematic diagrams of the microstructural evolution after five different heat treatment conditions.

CHAPTER 6

CREEP TESTS AND MICROSTRUCTURAL ANALYSIS

6.1 Introduction

The high cost of modern Ni-based superalloys and the shortage of the critical constituent elements have led to an increased interest in extending the service life of the turbine engine components. Creep resistance is the one of the most important mechanical properties which plays a very important role in the service life of the components. In this chapter, two types of creep test (short and long term) have been carried out on samples before and after high temperature degradation and rejuvenation. The results of these creep tests together with microstructural analysis, such as area fraction of secondary γ′, γ channel width and rafting parameter will be presented and discussed. The evolution of γ′ morphology, size and distribution in the Ni-based superalloy CMSX4 during degradation and rejuvenation has been examined as well as the relationship between mechanical behaviour, heat treatment and microstructure. Experimental techniques used in the study include field emission gun scanning electron microscopy (FEGSEM) and transmission electron microscopy (TEM).

6.2 Short Term Creep

There were two types of creep test applied in this project and according to the time to rupture, they can be considered as short term creep tests and long term creep tests. For short term creep tests, four samples after different heat treatments were tested at 900°C with a stress of 425 MPa. These conditions were selected on the basis of results from a literature survey of similar tests conducted on virgin CMSX-4 [7]. Based on these data, the test on as-received CMSX-4 was designed to last in the region of 200 to 300 hours. These short creep tests were accelerated by using high stress, but it provides a meaningful indication of the long term creep behaviour. Table 6.1 and Figure 6.1 show short term creep results and curves respectively. S1 and S3 showed a much longer creep rupture life with more strain compared with degraded samples at 900°C and 425 MPa. S1 illustrated a rupture life of 257 hours with a strain of 7.6%, which is consistent with that reported in the literature for virgin CMSX-4 with a crystal orientation along the <001> axis [1, 12, 39], whilst the measured creep life for S3 (331 hours) is about 30% longer than S1 but with less strain (6.7%). After high temperature degradation, S2 and S4, the samples not only exhibited much shorter creep lives of 77 and 53 hours respectively, but also experienced lower strains of 5.5% and 4.5% respectively. Since S4 had undergone two high temperature degradation treatments, the considerable reduction in creep performance is as expected. Minimum creep rates are another important factor shown in Table 6.1. Minimum creep rate is the minimum gradient of the creep curve, usually taken at the secondary creep stage. In Figure 6.1, S1 and S3 showed a much lower gradient when compared to the degraded samples, which lead a much smaller minimum creep rate obtained in these samples.

Table 6.1 Short term creep results of four different heat treated samples

Sample No	Heat Treatments	Time to Rupture (hour)	Strain (%)	Minimum Creep Rate ($Hour^{-1}$)
S 1	As Received	257	7.6	$4.8X10^{-5}$
S 2	Rafted	76	5.5	$1.2X10^{-4}$
S 3	Rafted + HT Rejuvenation	331	6.7	$2.7X10^{-5}$
S 4	Rafted + HT Rejuvenation + Rafted	53	4.5	$1.2X10^{-4}$

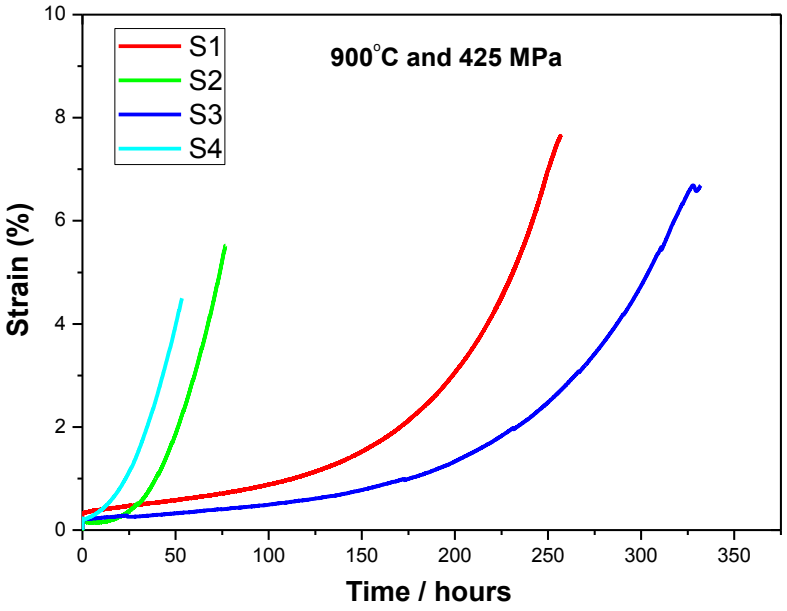

Figure 6.1. Short term creep curves of CMSX-4 samples after four different heat treated conditions: (a) S1. as received, (b) S2. rafted, (c) S3. rafted + HT Rejuvenation, and (d) S4. rafted + HT rejuvenation+ rafted.

6.2.1 SEM microstructural examination

In this section, the results of the SEM microstructural investigation will be presented and discussed. The obtained results can be used for microstructural analysis such as area fraction of secondary γ′ particles, γ channel width and

rafting parameter. The aim of this investigation was to evaluate the performance of the rejuvenation heat treatments applied, combined with an examination of material's creep behaviour.

6.2.1.1 Heads

Figure 6.2 shows the microstructure of the head portions of the short term creep samples. Since head portions experienced no applied stress, the microstructure of which is representative as isothermal ageing at 900°C. S1 and S3 samples exhibited an even distribution of cuboidal secondary γ′ particles with a size of 0.5 to 1.0 μm. However, unlike the tensile tested sample, due to the high temperature exposure, the microstructure was further degraded. This is proven by the presence of coarsened γ′ with rounded edges and broader γ channels within the microstructure. In S1, although the majority of the γ′ particles remain cuboidal, the edge is not as sharp as those observed in the tensile tested samples, see Figure 5.2. Moreover, a number of coarsened γ′ (2-3 μm) and wider γ channels (60-80 nm) were also observed, which results from the high temperature exposure during the tests. The microstructure of S3 was more degraded than S1. In S3 both γ′ rafts and coarsened γ′ particles were observed with much widened channels (>100 nm) between the secondary γ′ particles. These microstructural differences indicate that the rejuvenated sample (S3) degraded faster than the as-received sample (S1) during the high temperature exposure during these creep tests. S2 and S4 had a rafted microstructure, the majority of which is directional coarsen γ′ particles (γ′ rafts) within much broader γ channels. The rafts are short with random orientation in S2, but are much longer in S4 and most of them are aligned in the same orientation. This microstructure indicates that S4 contains a larger degree of rafting within the microstructure than S2. This is because S4 had undergone two degradation

treatments, which caused more degradation within the microstructure. Figure 6.3 displays the high magnification images showing γ channels and tertiary γ′ precipitates of the samples. Rafted samples (S2 and S4) have much larger γ channels in both the parallel and perpendicular directions. The increased width of the γ channels makes dislocations easy to move. Tertiary γ′ precipitates with various sizes were found in all samples except S1. This is because the formation of tertiary γ′ precipitates was from degradation, but the as-received sample has not experienced any heat treatment.

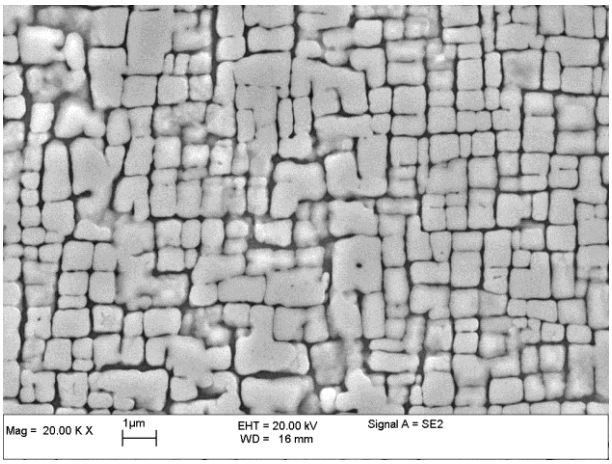

(a) S1. As Received

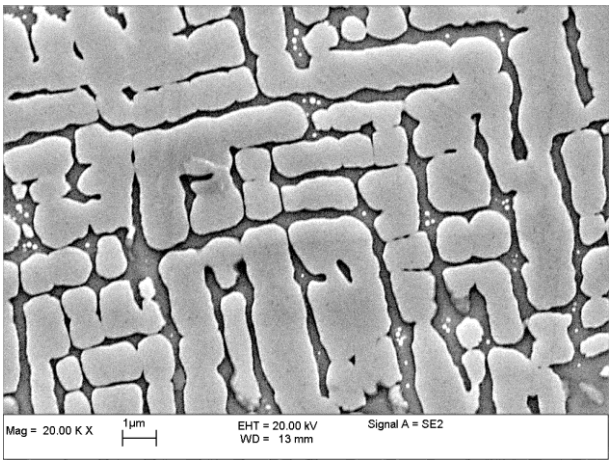

(b) S2. Rafted

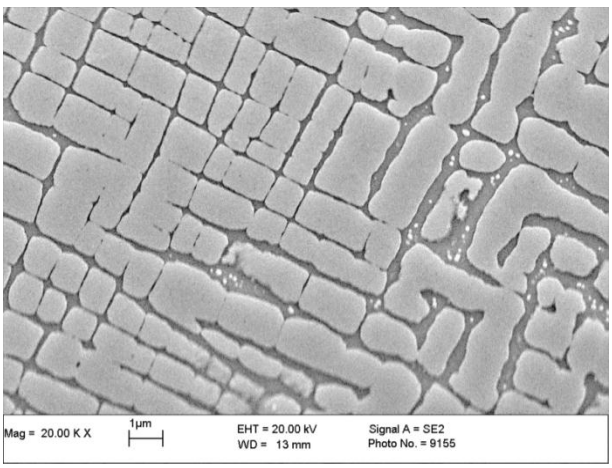

(c) S3. Rafted + HT Rejuvenation

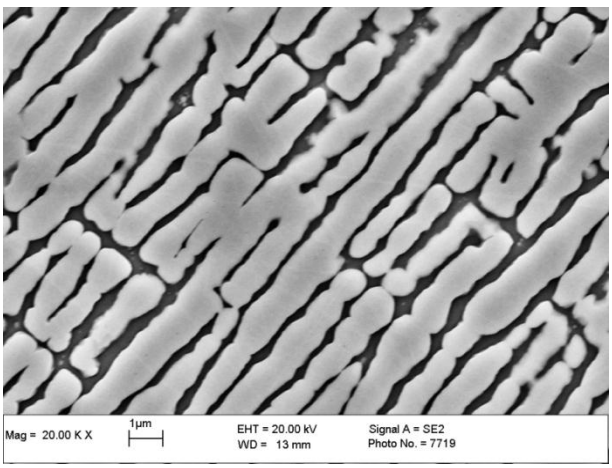

(d) S4. Rafted + HT Rejuvenation+ Rafted

Figure 6.2. The low magnification SEM images of the head portions of the short term creep samples after four different heat treatment conditions, showing distribution and morphology of γ/γ′.

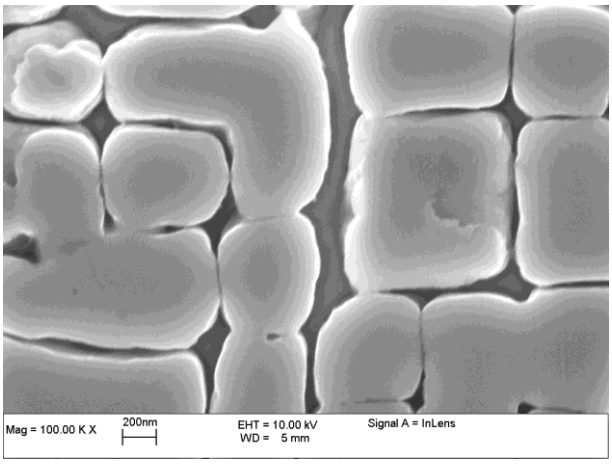

(a) S1. As Received

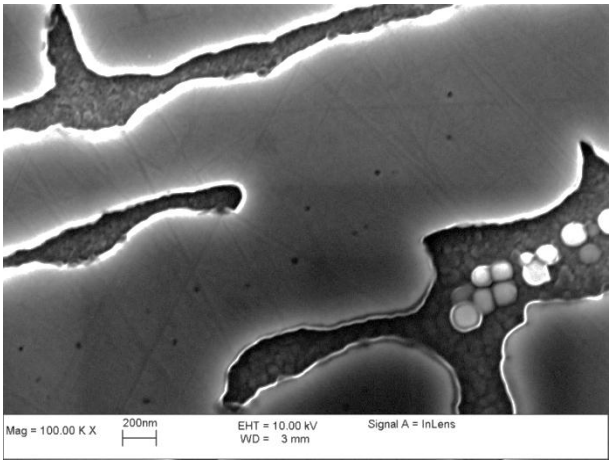

(b) S2. Rafted

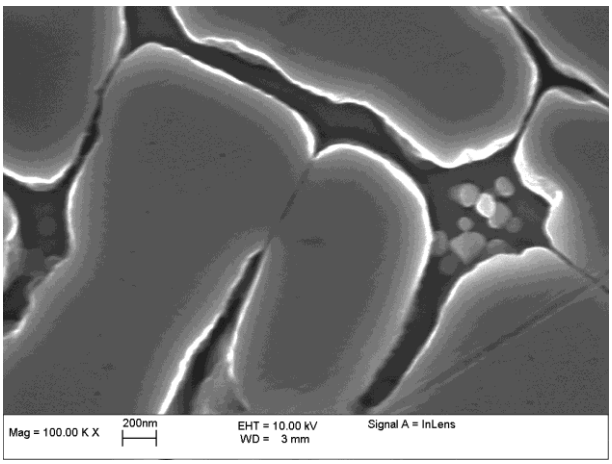

(c) S3. Rafted + HT Rejuvenation

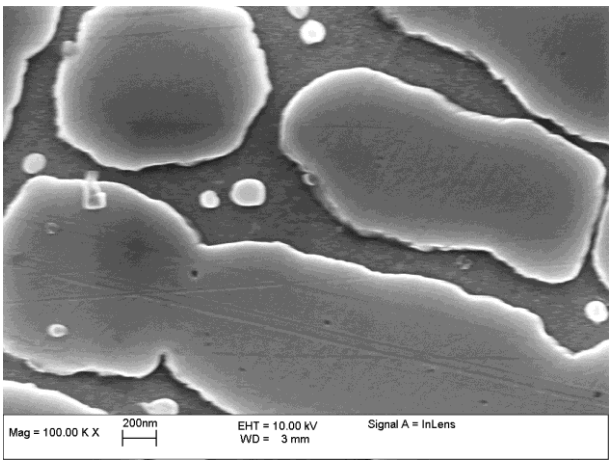

(d) S4. Rafted + HT Rejuvenation+ Rafted

Figure 6.3. The high magnification SEM images of the head portions of the short term creep samples after four different heat treatment conditions, showing γ channels and tertiary γ′ precipitates.

6.2.1.2 Gauge Lengths

In order to investigate the effects of the applied creep stress on the microstructure, SEM examinations of the gauge length portions of short term creep samples were carried out. For each sample, SEM images taken from various positions along the gauge length were similar and followed the same trends. Therefore, in this section only the microstructure no more than 100 μm from the fracture will be presented and discussed.

Figure 6.4 shows the microstructure of the gauge length portions of short term creep samples after four different heat treated conditions. With applied stress, most of the microstructure was rafted or orientated perpendicular to the stress direction, where applied stress was in up and down direction, which has a good agreement with literatures [51-57]. The microstructures of S1 and S3 in the gauge length portions are very different compared to the head portions. This is because long time exposure at stress conditions promotes coarsening and rafting of the γ′ particles. Although the majority of the secondary γ′ particles observed in S1 and S3 are still close to cuboidal, the size of secondary γ′ in S3 has significantly increased, which has double the size of head portions. The microstructure of S3 is more degraded than S1 after long term exposure at high temperature, since more coarsened γ′ particles and short γ′ rafts were observed with wider γ channels in S3. The rafting structure is more pronounced in S2 and S4. The majority of them are γ′ rafts with much wider γ channels. The rafts in S4 have much larger extent compared with S2. The extension of rafts increases the length of γ′ particles, but reduces their thickness, which expands the γ channels and causes a reduction of the mechanical performance. However, the microstructure of head and gauge length portions for the degraded samples show no significant differences when compared to the corresponding head portions in Figure 6.4. This is because the test time for these two samples is 50-70 hours, which is too short to produce significant microstructural differences.

Figure 6.5 displays the high magnification images showing γ channels and tertiary γ′ precipitates of the samples. Gauge length portions have a more degraded structure, such as rafts and coarsened γ′, which increases the size of γ channels. Tertiary γ′ precipitates were observed in all the samples except S1, which is consistent with head portions.

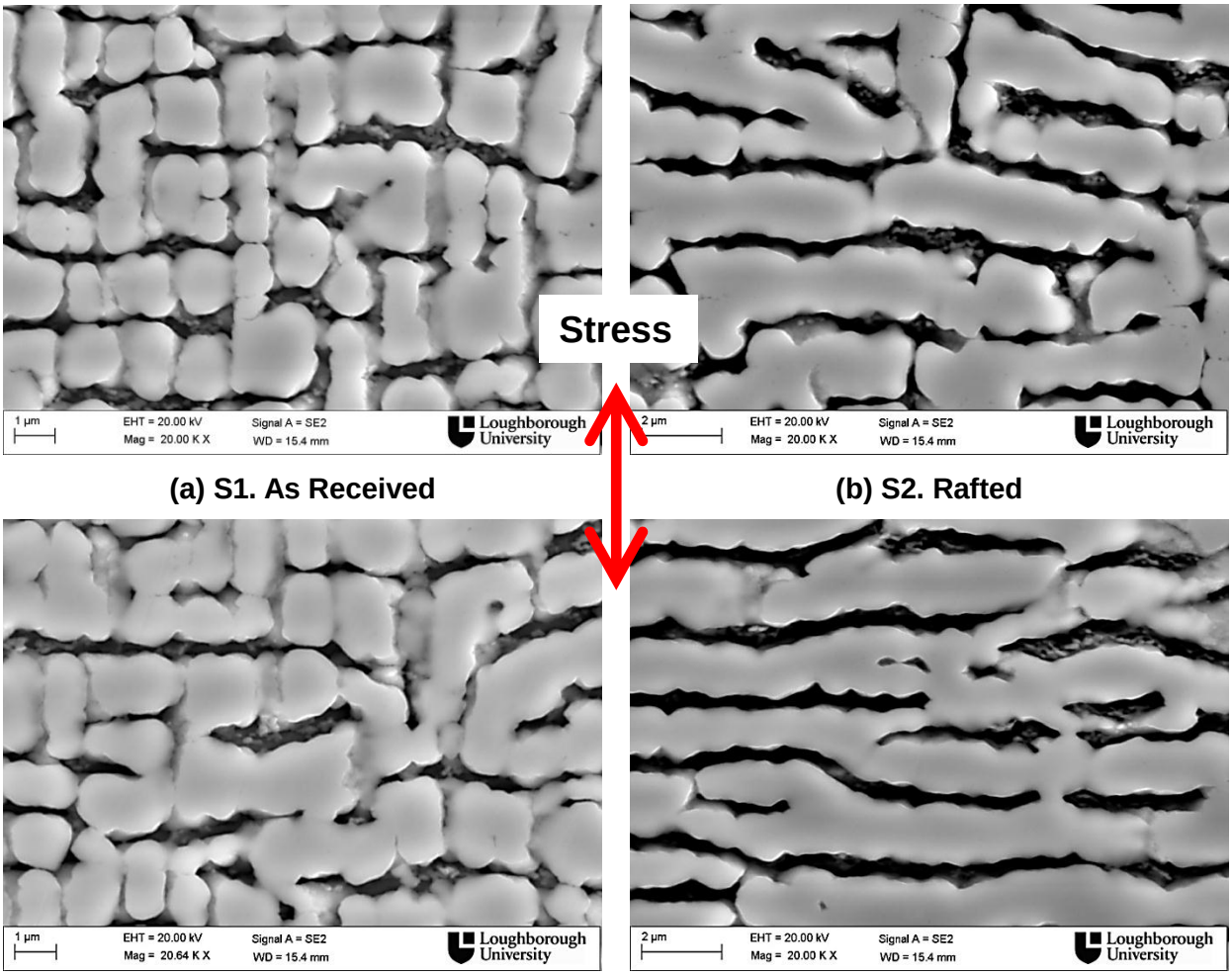

(a) S1. As Received **(b) S2. Rafted**

(c) S3. Rafted + HT Rejuvenation **(d) S4. Rafted + HT Rejuvenation+ Rafted**

Figure 6.4. The low magnification SEM images of the gauge length portions of the short term creep samples after four different heat treatment conditions, showing distribution and morphology of γ/γ′.

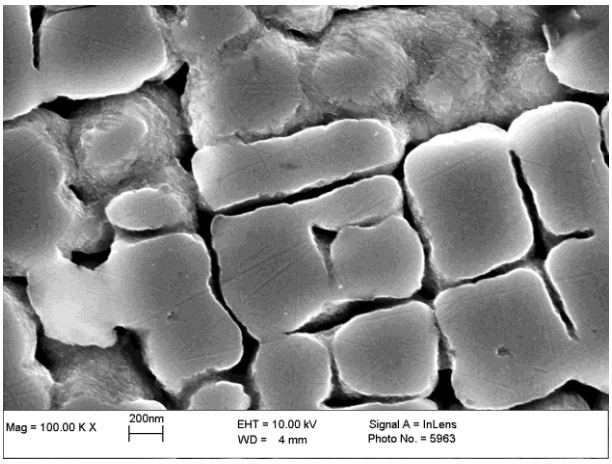

(a) S1. As Received

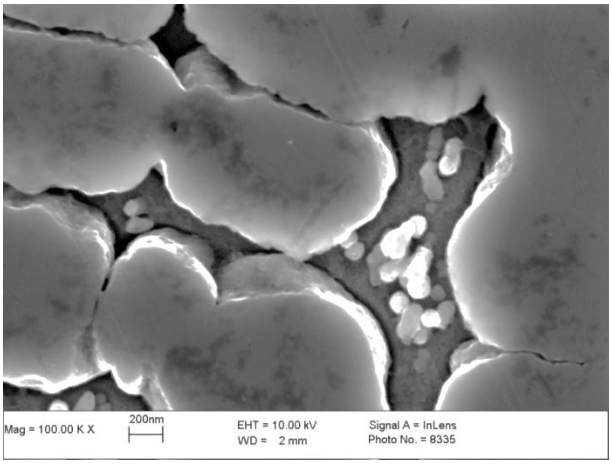

(b) S2. Rafted

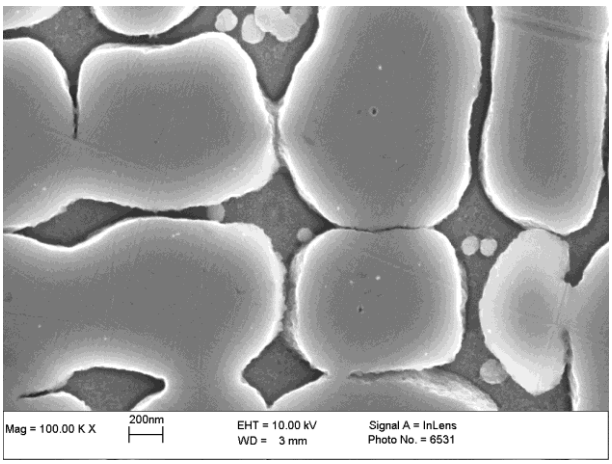

(c) S3. Rafted + HT Rejuvenation

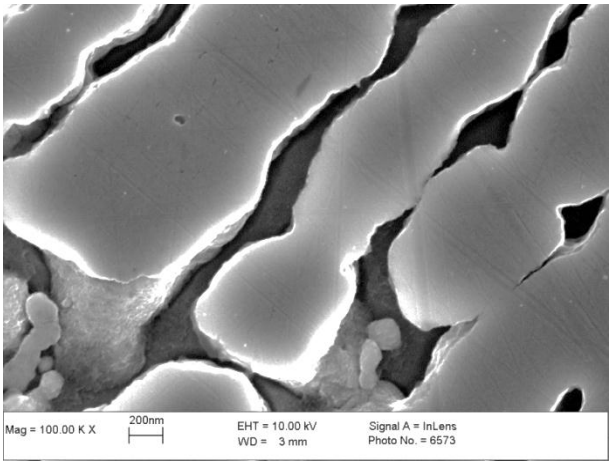

(d) S4. Rafted + HT Rejuvenation+ Rafted

Figure 6.5. The high magnification SEM images of the gauge length portions of the short term creep samples after four different heat treatment conditions, showing γ channels and tertiary γ′ precipitates.

6.2.2 Quantification of area fraction of secondary γ′, γ channel widths and rafting parameter

In order to further examine the microstructure described in the previous section, image analysis was carried out to quantify the area fraction of secondary γ′ particles, γ channel widths and rafting parameter using image analysis software.

Figure 6.6 illustrates the results of area fractions of secondary γ′ particles for both the heads and gauge lengths of the short creep tested samples. The area fractions of head portions are slightly higher than gauge lengths. This is because the γ′ precipitates' coarsening and rafting were accelerated by the applied stress, since it is both a diffusion and strain controlled process. However, the area fraction of heads and gauge lengths show the same trend. Therefore, the area fraction of the head portions are considered to be representative of both head and gauge length portions in the later comparison. According to the short term creep curves and area fraction measurements, creep life increased with the area fraction of secondary γ′ particles. This is because of the fact that the excellent high temperature performance of CMSX-4 is due to the presence of a high volume fraction of γ′. The area fraction of S1 and S3 are very similar but much higher than the degraded samples (S2 and S4). The longer creep rupture life of S3 is contributed by the presence of the tertiary γ′ precipitates in the channels, which impede the movement of dislocations and provides second phase strengthening of superalloy [55-57]. Although the area fraction of γ′ in S4 is a litter higher than S2, it has a more continuous rafted structure, shown in Figure 6.4, which in other words, the degree of rafting is much larger in S4. Moreover, the rafts' orientations in S4 are more aligned in one direction rather than random. With that structure, the dislocations can glide or pass through the structure along the γ channels in the rafting directions.

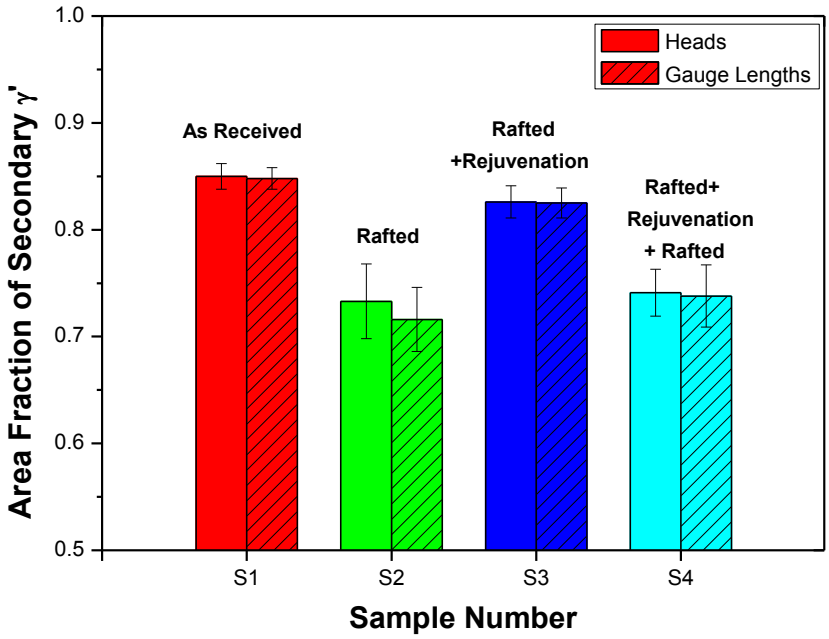

Figure 6.6. The area fractions of secondary γ′ particles from the four different heat treatment conditions for both heads and gauge lengths of the short term creep specimen

Table 6.2 and Figure 6.7 show the γ channel width measurements for each of the samples. The channels of the gauge lengths portions are slightly wider than the head portions due to exposure to stressed conditions, which helps γ′ rafting by increasing its length but reducing thickness. However, trends for these four samples for heads and gauge lengths are the same, therefore, to simplify comparison, only the channel widths in heads sections are compared. Similar to the tensile tested samples, channel widths of the as-received (S1) and rejuvenated (S3) samples are much smaller than the rafted samples, although their sizes have increased from 60 nm for the tensile tested samples to 90-120 nm for the short term creep tested samples. The most significant difference between the tensile and short term creep tested samples is that the channels in S3 are much wider (124 nm) in later ones. This significant increase of γ channel width indicates that rejuvenated sample (S3) degraded faster than the

as-received (S1) sample under this short term creep test condition. This is because the rejuvenation heat treatment has not completely restored the sample to the as-received condition and any residual segregation, stress and misfit between γ/γ′ resulting from the previous degradation may accelerate the rafting rate, since it is a stress-assisted diffusion controlled process [49-57,72]. However, these channels still remain very small, which is less than critical channel width (180 nm). The small channel width is another contributory factor for the long creep rupture life of the as-received and rejuvenated samples. The formation of the anti-phase boundary of γ′ makes cutting γ′ particles more difficult, which requires higher stress and energy [4, 55-57]. The dislocation movement is thus impeded by smaller γ channels and leads to a higher creep resistance. When the spacing is larger, as in the rafted structure, dislocations can move by gliding through γ, which requires less stress and results in poorer mechanical performance. The channel widths of the degraded samples (S2 and S4) are much larger, 200-300 nm. The degradation not only promotes the directional coarsening of γ′ but also increases the gap between γ′ rafts. The microstructure of S4 shows a greater extent of rafting than the sample which had received only one rafting treatment (S2). It is possible that any segregation effects present within the microstructure have been enhanced by the second rafting treatment. A substantial difference in rafting direction was also observed, again indicating that a more continuous rafted microstructure was obtained, with an accompanying reduction in mechanical properties.

The rafting parameter is used to quantify the degree of rafting in superalloys, the results of which is shown in Table 6.3. The rafting parameter shows a good agreement with creep curves. The creep rupture life decreases with increasing rafting parameter. For S1 and S3, an even distribution of cuboidal γ′ precipitates with a few rafts results in a small rafting parameter and a long creep rupture life.

This is because cuboidal γ′ provides the maximum mechanical performance of superalloys, due to fact that the cuboidal morphology provides an excellent barrier effect for the dislocation movements in all the directions. While with an increasing extent of rafting, the length of the γ′ particles increases but has an associated decrease in thickness, which leads to a greater rafting parameter value. The rafting parameter of S4 is much larger than S2, which confirms the observation that S4 has a more continuously rafted microstructure. With these continuous broader channels, dislocations can move more easily through this structure, which consequently leads to a reduction in creep life.

Table 6.2 γ channel width measurements of the four different treated samples

Sample No	Heat Treatments	γ Channel Width (nm)			
		Heads		Gauge Lengths	
		//	⊥	//	⊥
S 1	As-received	92±13	87±16	93±14	82±17
S 2	Rafted	246±45	219±30	258±51	218±50
S 3	Rafted + HT Rejuvenation	112±21	109±23	124±23	107±24
S 4	Rafted + HT Rejuvenation + Rafted	221±37	188±32	241±47	186±35

Table 6.3 The rafting parameter of four different heat treated samples

Sample No	Heat Treatments	Rafting Parameter	
		Heads	Gauge Lengths
S 1	As-received	0.57	0.59
S 2	Rafted	1.87	1.82
S 3	Rafted + Rejuvenation	0.73	0.78
S 4	Rafted + Rejuvenation + Rafted	2.79	2.71

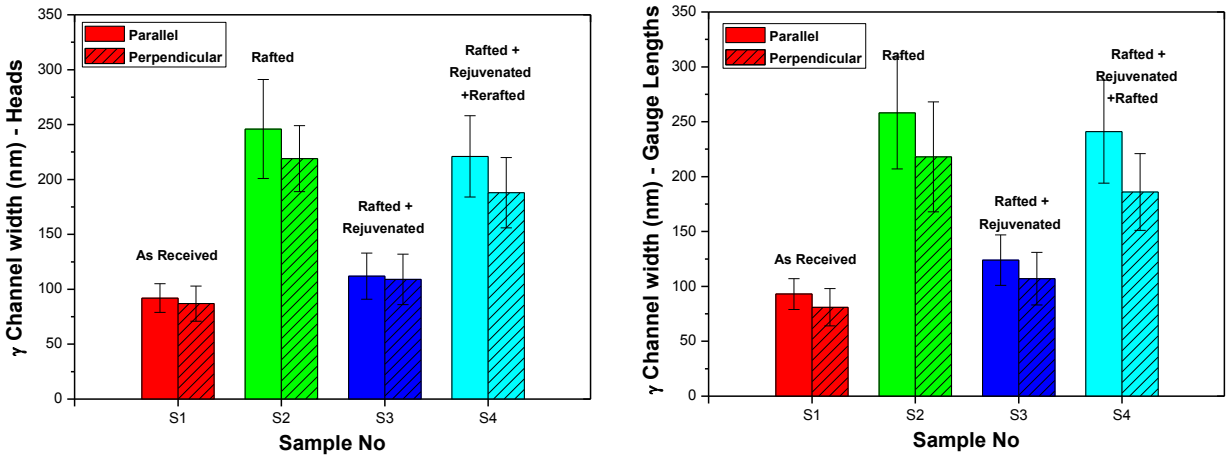

(a) Head Portions **(b) Gauge Length Portions**

Figure 6.7. Channel width measurements of the γ channels of both (a) heads and (b) gauge lengths (right) for the four different heat treated short term creep samples measured in parallel and perpendicular directions.

6.2.3 TEM microstructural examination

In this section the results of TEM microstructural investigation will be presented and discussed. The purpose of this investigation was to examine the presence of the tertiary γ′ precipitates and their effects on the dislocations. Figure 6.8 shows the TEM images of four short term creep tested samples from gauge length. The TEM results were consistent with SEM investigations. S1 and S3 have an even distribution of cuboidal γ ′ particles (measuring 0.5 to 1.0 μm), with a channel width of less than 100 nm. For S2, a number of short rafts were formed in random orientations with relatively larger channels (>200 nm). The channels in S4 are slighter larger than S2, since it has been undergone two degradation treatments. The degradation causes an increase in the length of γ′ rafts by reducing their thickness, resulting in an increase of γ channel width. Tertiary γ′ precipitates were found in samples S2, S3 and S4, which would act as barriers to block the movement of dislocations. In S2, the tertiary γ′ precipitates are relatively large at ~100-200 nm, whereas those formed in S4 are considerably

smaller (~20 nm). Dislocations were also observed in S2 and S4, where they were mainly present in the γ channels, especially near the edge of the secondary γ′ particles. These results are consistent with earlier research [11-14]. A small amount of tertiary γ′ precipitates were also found in S3, which has good agreement with the SEM results. Moreover, the higher magnification images of S3 and S4 show that the dislocations within the γ channels may interact with the tertiary γ′ precipitates, indicating that the tertiary γ′ precipitates have a beneficial effect on the mechanical performance by inhibiting movement of dislocations, even within wider γ channels.

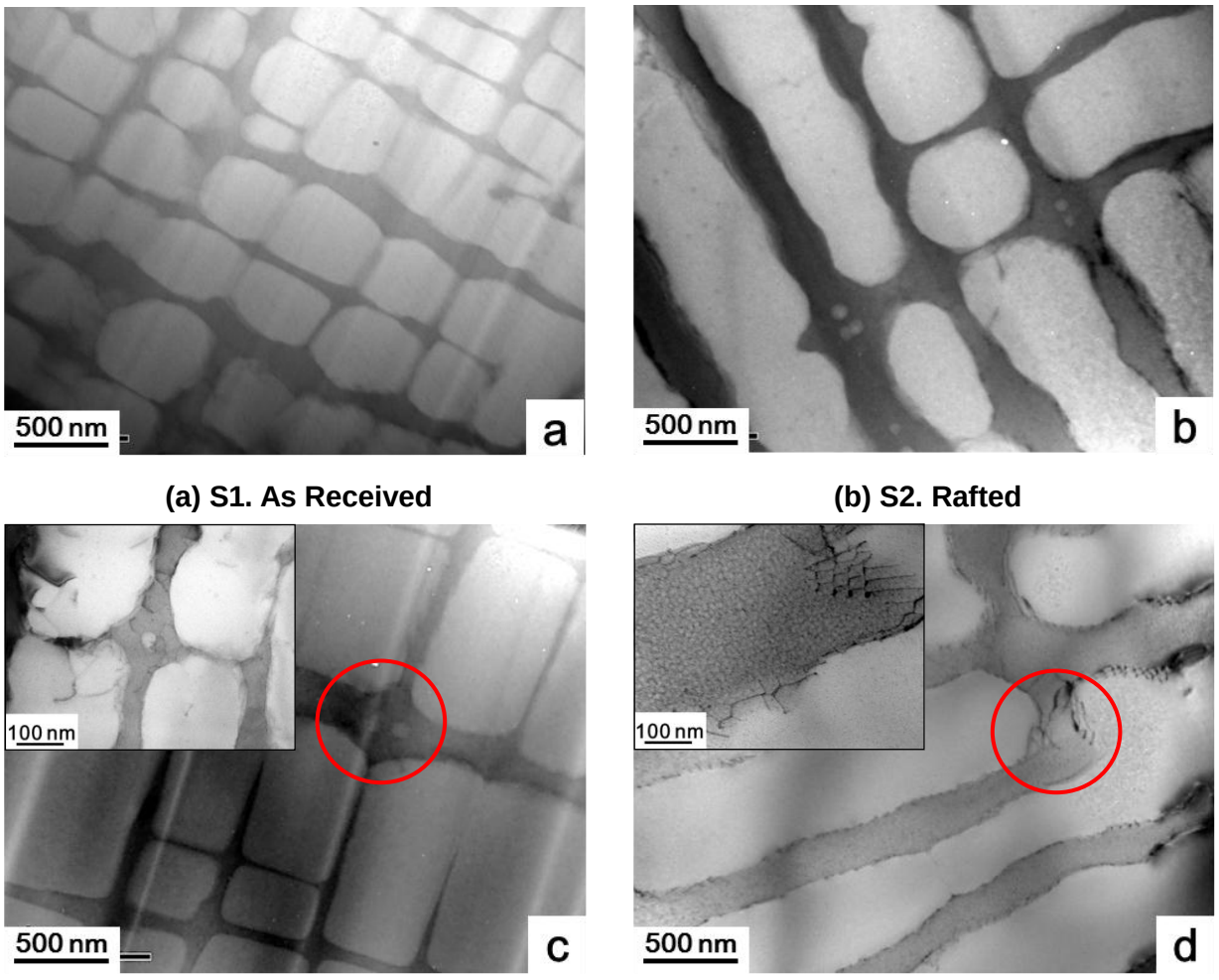

(a) S1. As Received **(b) S2. Rafted**

(c) S3. Rafted + HT Rejuvenation **(d) S4. Rafted + HT Rejuvenation+ Rafted**

Figure 6.8. TEM images of the gauge length of the short term creep samples after four different heat treatment conditions, showing tertiary γ′ precipitates and their effects on the dislocations.

6.2.4 Summary

The microstructural evolution of four short term creep samples after high temperature degradation and rejuvenation has been examined. The microstructural evolution of these four creep samples can be illustrated by the schematic diagrams, see Figure 6.9. The results suggest that degradation increases the size, spacing and rafting parameter of the secondary γ′ precipitates, which in turn makes the γ channel broader and causes a reduction in the measured area fraction of secondary γ′ particles. Moreover, it was observed that the presence of tertiary γ′ precipitates in the γ channels may have a beneficial effect on the mechanical properties. The difference between the rejuvenated sample and the as-received sample indicates that although the rejuvenation can restore the microstructure on a superficial level, it cannot fully restore it to the virgin condition and any residual segregation, stress and misfit between γ/γ′ that may remain after rejuvenation appears to promote the rafting during further degradation, resulting in a fast degradation in mechanical properties.

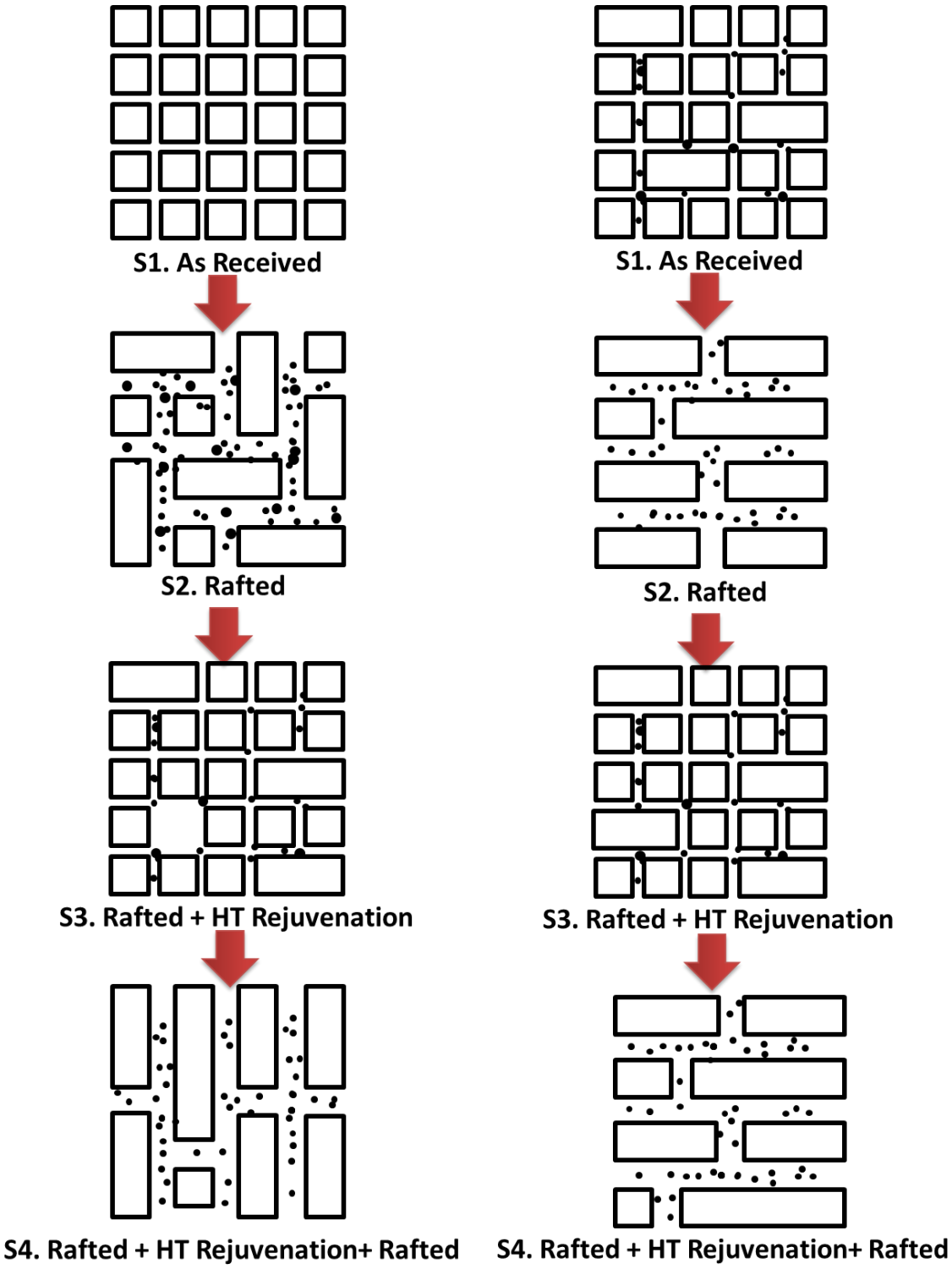

(a) No Stress **(b) With Stress**

Figure 6.9. Schematic diagrams of the microstructural evolution of short term creep samples after four different heat treatment conditions.

6.3 Long Term Creep

The long term creep tests were carried out at 982°C and 167 MPa. These test conditions were based on the creep test performed by Svoboda and Lukas [7] based on a virgin sample which failed after a test time of around 1000 hours; a time short enough to perform tests within the required timeframe but long enough to be a meaningful indicator of longer term creep behaviour. The creep rupture life and creep curves of the samples are shown in Table 6.4 and Figure 6.9. The results have similar trends to the short term creep tests. The rejuvenated (S3) and as-received (S1) samples exhibit longer creep rupture life than the degraded samples. S1 demonstrates a creep life of 1141 hours with a strain of 25.5%, which is in a good agreement with that reported in the literature for virgin CMSX-4 [1]. However, the measured creep life for S3 is about 1174 hours with a strain of 24.8%, which has a very similar creep rupture life and strain to S1. S2 and S4 show a considerably shorter creep life of 804 and 780 hours respectively. Although, the creep rupture lives of S2 and S4 are almost the same, the strain of S4 (35.4%) is much higher than S2 (22.5%). This may result from heat treatments, since S4 had undergone two degradations, which as shown previously can cause a considerably more degraded microstructure hence and reduced mechanical performance.

Table 6.4 Long term creep results of four different heat treated samples performed at 982°C and 167 MPa

Sample No	Heat Treatments	Creep Life (hours)	Strain (%)
S 1	As Received	1141	25.5
S 2	Rafted	807	22.5
S 3	Rafted + Rejuvenated	1174	24.8
S 4	Rafted + Rejuvenated + Rafted	780	35.4

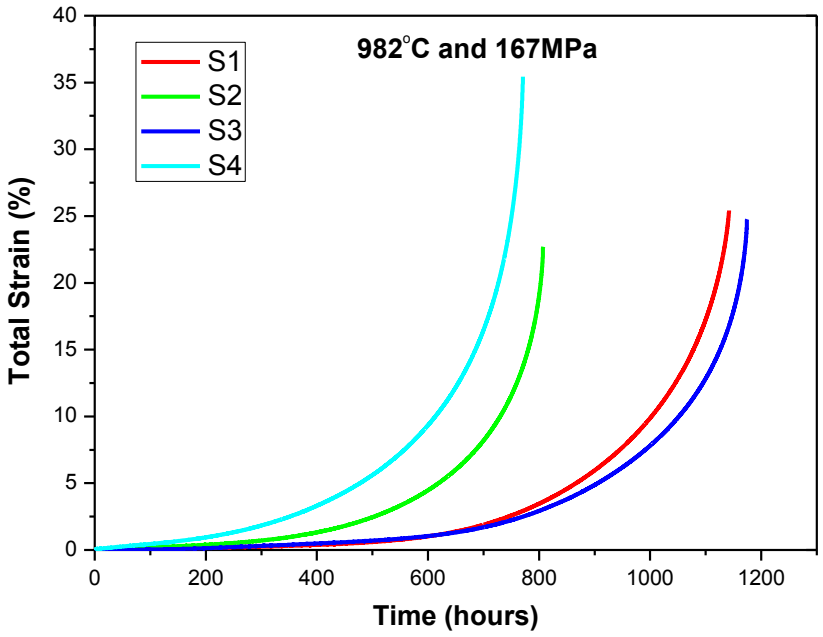

Figure 6.10. Long term creep curves of CMSX-4 samples after four different heat treated conditions: (a) S1. as received, (b) S2. rafted, (c) S3. rafted + HT rejuvenation, and (d) S4. rafted + HT rejuvenation+ rafted.

6.3.1 SEM examination of long term creep samples

In this section, the microstructural examination of four long term creep tested samples will be presented, followed by the quantitative measurements such as area fraction of secondary γ′ particles, γ channel width and rafting parameter. Both the heads and gauge lengths portions of the tested samples were investigated to evaluate the performance of the rejuvenation in relation to microstructural recovery, combined with the examination of the long term creep behaviour. The big difference between the short term and long term creep is that the latter was held at a temperature close to the applied degradation temperature. Therefore, long-time exposure at that condition will cause significant changes to occur within microstructure during the test.

6.3.1.1 Heads

Figure 6.10 illustrates the microstructure of the head portions of the long term creep tested samples. The microstructures are very similar to the short term creep samples, although a more degraded structure was observed, especially for S1 and S3. The microstructure of S1 and S3 are distributed by cuboidal and elongated γ′ particles with a size of ~ 0.5 to 1.0 μm. A number of coarsened γ′ particles and γ′ rafts can also be observed within the microstructure, with a much wider γ cannel width (>100 nm). The extent of the rafts is greater than those of short term creep samples, since these samples have been exposure to a higher temperature and a longer time, causing a greater degree of coarsening and rafting. Degradation not only increases the size of secondary γ′ particles but also raises the degree of rafting. The microstructure of S2 and S4 exhibited a mixture of cuboidal, short and long γ′ rafts with an increased γ channel width (~250 nm). The rafts in S2 are relatively short with random orientations, whilst the rafts in S4 are much longer with a more aligned orientation. The increased extent of rafting in S4 suggests that the microstructure is much more degraded than S2, which is consistent with the results of the short term creep tested samples. These results indicate that a long exposure this temperature has not caused a significant effect on the microstructure of head portions.

Figure 6.11 presents the high magnification images showing the γ channels and tertiary γ′ precipitates of the four long term creep tested samples. The rafted samples have much wider γ channels in both parallel and perpendicular directions. It is interesting to note that tertiary γ′ precipitates were present in all the samples, including the as-received (S1) sample, which is conflict with origin of the tertiary γ′ precipitates discussed in previously. This is because the longer time exposure at that temperature causes significant chemical diffusion and segregation. With fast cooling, the residual concentration of Al and Ti in the γ

channels causes formation of tertiary γ′ precipitates within them. However, the amount of tertiary γ′ precipitates was much less in S1 and S3. This may suggest that the chemical segregation obtained within these samples is much less than within degraded samples, which results in less residual Al and Ti in the channels and thus a lower amount of tertiary γ′ precipitates. These results indicate that the formation of tertiary γ′ precipitates is not from long term aging at high temperature, but more commonly obtained from cooling. More evidence will be given in the next Chapter.

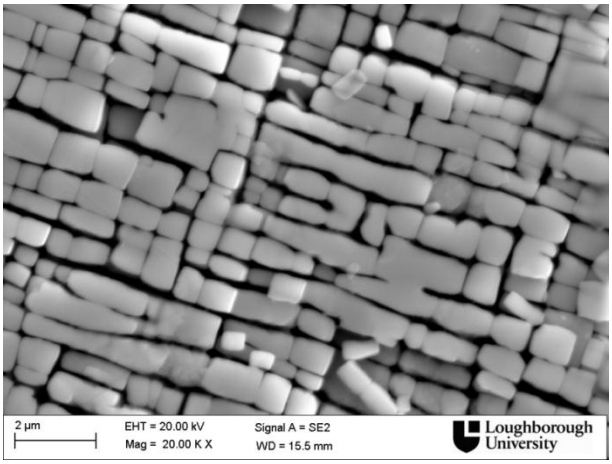

(a) S1. As Received

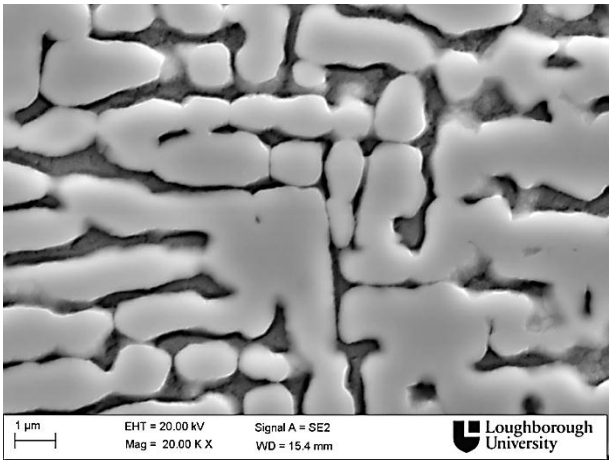

(b) S2. Rafted

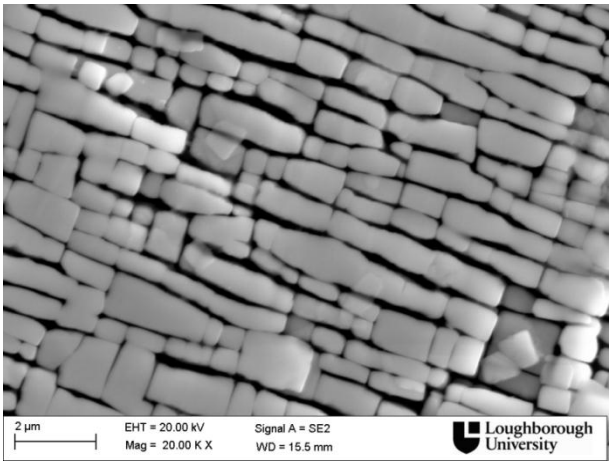

(c) S3. Rafted + HT Rejuvenation

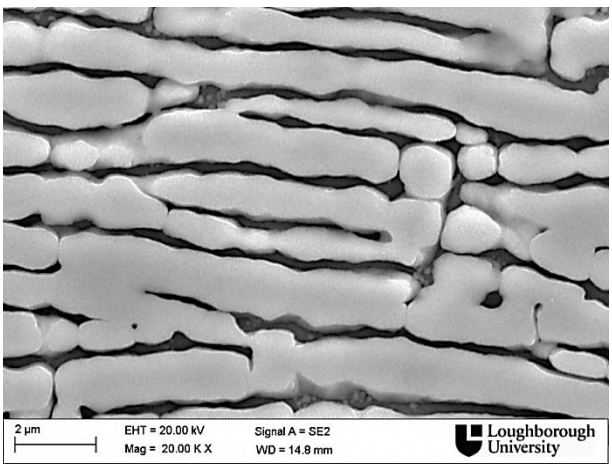

(d) S4. Rafted + HT Rejuvenation+ Rafted

Figure 6.11. The low magnification SEM images of the head portions of the long term creep samples after four different heat treatment conditions, showing distribution and morphology of γ/γ′.

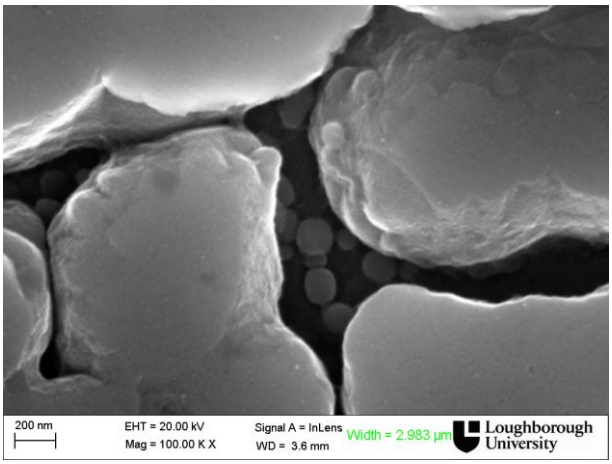

(a) S1. As Received

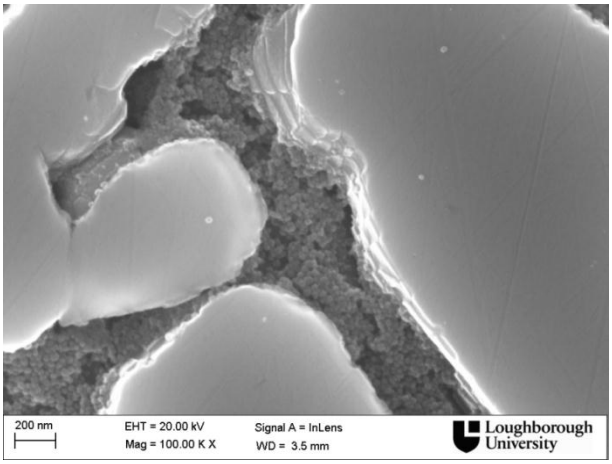

(b) S2. Rafted

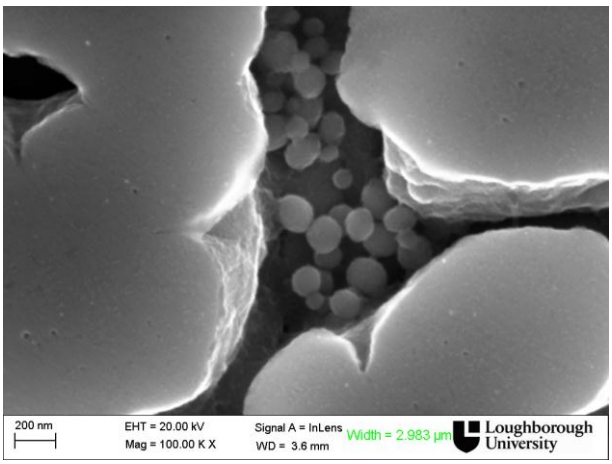

(c) S3. Rafted + HT Rejuvenation

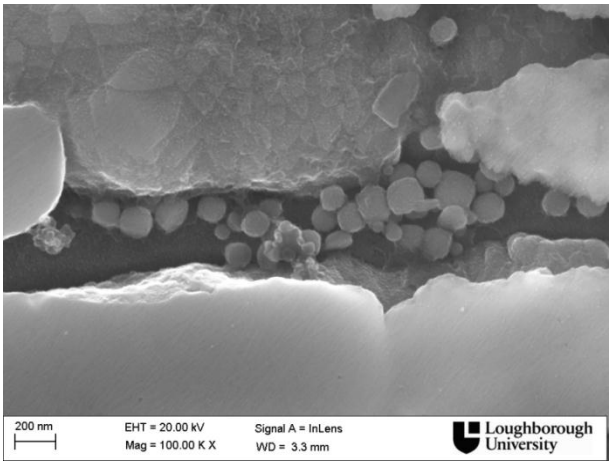

(d) S4. Rafted + HT Rejuvenation+ Rafted

Figure 6.12. The high magnification SEM images of the head portions of the long term creep samples after four different heat treatment conditions, showing γ channels and tertiary γ′ precipitates.

6.3.1.2 Gauge Length

Figure 6.12 shows the microstructure of the gauge length portions after the applied long term creep tests. Unlike the short term creep tested samples, the microstructure of gauge lengths shows significant difference when compared to head portions. This is because rafting is a stress-assisted diffusion controlled process. The longer time exposure has a significant influence on the microstructure of the stressed gauge length portions. In Figure 6.12, the

microstructures of S1 and S3 are no longer dominated by cuboidal γ′ particles, instead, γ′ rafts with a cross-linked structure were observed. These microstructures not only raise the degree of rafting, but also increase the size of γ channels in these samples. In other words, the microstructure of S1 and S3 are more degraded than the head portions. The cross-linked γ′ rafts may not be as beneficial for the mechanical properties as cuboidal γ′ particles, since the size of γ channel and degree of rafting has increased. However, with the help of cross-linked structure, it still provides a significant barrier to the movement of dislocations and improves the creep resistance of the material. This is why S1 and S3 have longer creep rupture life than the degraded samples. The microstructures of S2 and S4 are very similar to the short term creep samples, exhibiting long rafts with much wider γ channels (>250 nm). However, due to two degradations, S4 has a more continuously rafted structure than S2. The presence of the greater extent of rafting and wider channels within the microstructure in S4, reduces its barrier to the dislocation motion and results a relatively shorter creep rupture life than S2.

Figure 6.13 presents the high magnification images showing the γ channels and tertiary γ′ precipitates of the long term creep tested samples. The γ channels in S1 and S3 are much wider than those observed within the head portions, as caused by the influence of the applied stress. The sizes of the channels have doubled from the head to the gauge length. The influence of applied stress has also caused γ channel growth within the degraded samples, increasing their size from ~220 to ~300 nm. The larger channels not only reduce the area fraction of secondary γ′ particles but also decrease its mechanical performance. The detailed γ channel width measurements are shown in the next section. Similar to the head portions, tertiary γ′ precipitates were found in all samples, including the as-received sample. The size of tertiary γ′ precipitates were very small (< 50nm).

The presence of a large amount of tertiary γ′ precipitates results from residual Al and Ti present within the channel due to fast cooling, which later caused a formation of tertiary γ′ precipitates.

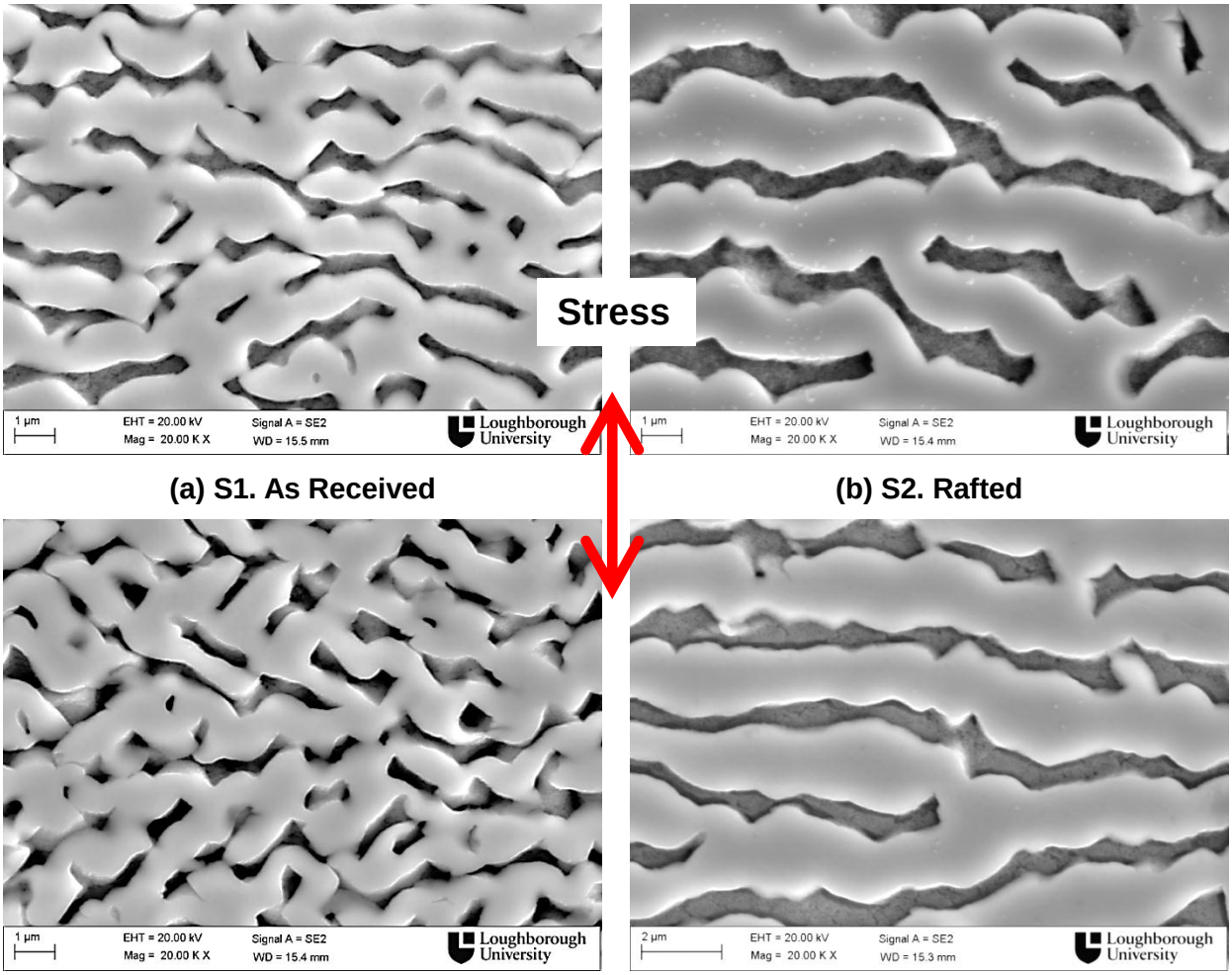

(a) S1. As Received **(b) S2. Rafted**

(c) S3. Rafted + HT Rejuvenation **(d) S4. Rafted + HT Rejuvenation+ Rafted**

Figure 6.13. The low magnification SEM images of the gauge length portions of the long term creep samples after four different heat treatment conditions, showing distribution and morphology of γ/γ′.

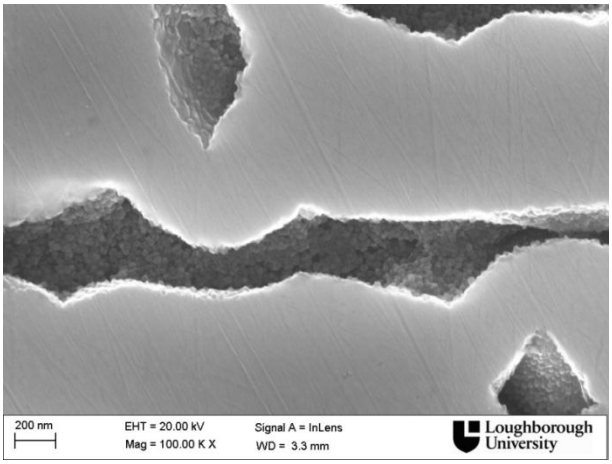

(a) S1. As Received

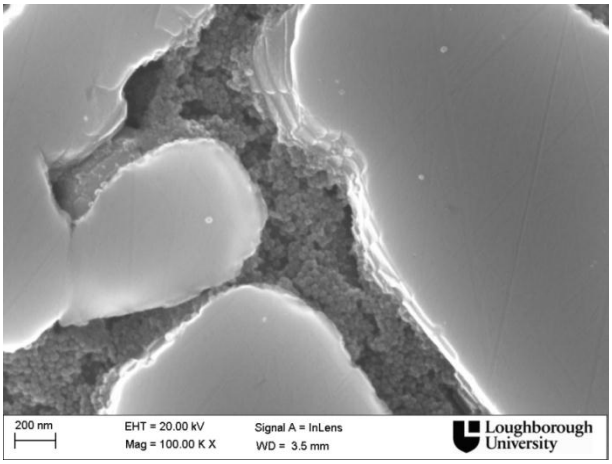

(b) S2. Rafted

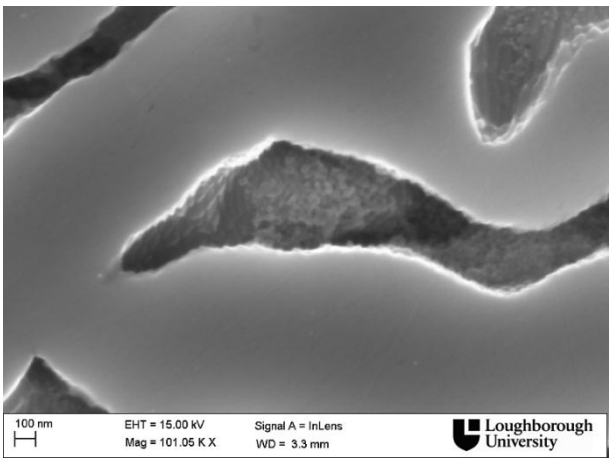

(c) S3. Rafted + HT Rejuvenation

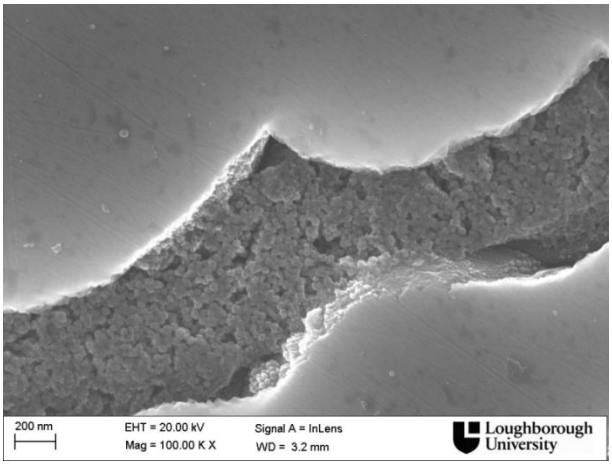

(d) S4. Rafted + HT Rejuvenation+ Rafted

Figure 6.14. The high magnification SEM images of the gauge length portions of the long term creep samples after four different heat treatment conditions, showing γ channels and tertiary γ′ precipitates.

6.3.2 Quantification of area fraction of secondary γ′, γ channel widths and rafting parameter

In order to further examine the microstructures obtained in the previous section, image analysis was carried out to quantify the area fraction of secondary γ′, γ channel widths and rafting parameter using image analysis software. Figure 6.14 illustrates the results of the area fractions of the secondary γ′ for both the heads and gauge lengths of the samples. The area fractions of the head portions are slighter larger than the gauge length portions, since rafting was enhanced by the applied stress, which resulting in an increase in γ channel width and a reduction of the area fraction of secondary γ′. According to the long term creep rupture life and area fraction results, creep rupture life increases with the area fraction. This is because, in single crystal Ni-based superalloys, the high level of rupture strength and creep resistance results from the high volume fraction of γ′ contained within the alloy. The area fraction of S1 and S3 is much higher than the degraded samples, which results a higher creep resistance and longer creep rupture life than the degraded samples. Since S2 and S4 has similar area fraction, their creep rupture lives are very close to each other.

The γ channel widths is another important factor that has been measured with the results displayed in Table 6.5 and Figure 6.15. It is interesting to note that γ channels in the gauge length portions of S1 and S3 are much wider than those in the head portions. This is because rafting was accelerated by the applied stress at that temperature causing a significant microstructural degradation in the gauge length portions of S1 and S3 after long time exposure. Take the parallel channel width for example: the channel has massively increased from the head (100 nm) to the gauge length (223 nm) in S1 and S3. These channel widths are larger than the critical value (180 nm), resulting in a reduced barrier for

dislocations [55-57]. However, as observed in SEM images, the secondary γ′ particles were formed in a cross-linked structure, which provides a much greater barrier effect than the individual rafts, like S2 and S4, and improves the creep performance of these samples. The channel width of S2 and S4 has also increased its size after long term exposure during creep tests. The parallel channel width of S2 has increased from 220 nm to 287 nm and the channel width of S4 has increased from 234 nm to 328 nm. The channel width and creep rupture life indicate that the shorter creep rupture life of S4 results from the wider channels obtained within the microstructure.

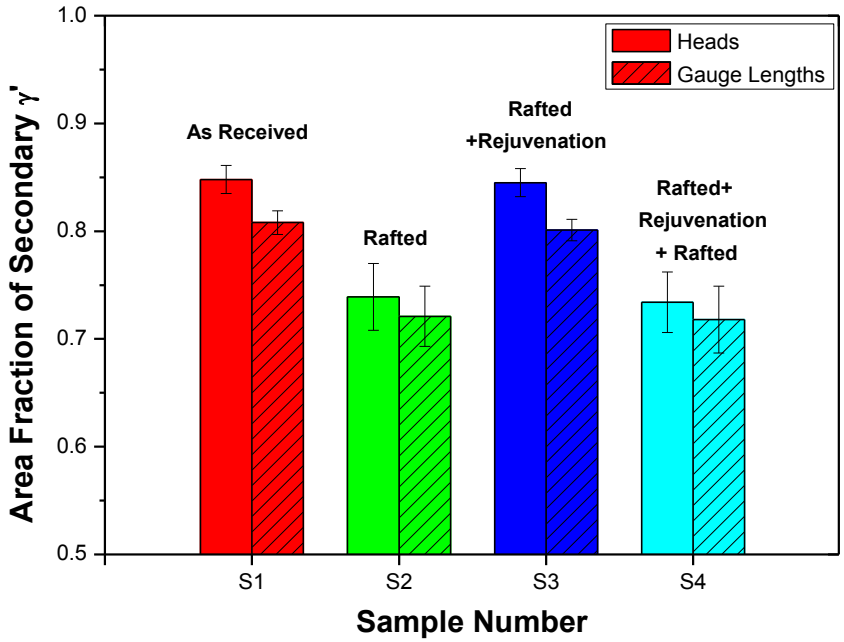

Figure 6.15. The area fractions of secondary γ′ particles from the four different heat treatment conditions for both heads and gauge lengths of the long term creep specimen

Table 6.5 γ channel width measurements of the four different treated samples

Sample No	Heat Treatments	γ Channel Width (nm)			
		Heads		Gauge Lengths	
		//	⊥	//	⊥
S 1	As-received	98±14	90±15	223±39	214±40
S 2	Rafted	220±38	208±33	287±46	273±35
S 3	Rafted + HT Rejuvenation	115±27	106±22	239±32	220±31
S 4	Rafted + HT Rejuvenation + Rafted	234±32	227±26	328±42	282±34

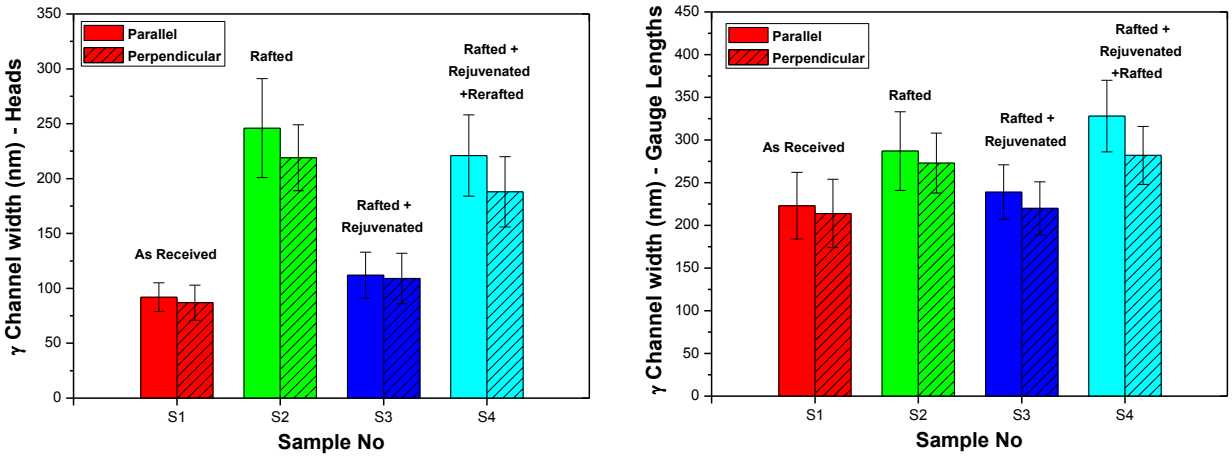

(a) Head Portions **(b) Gauge Length Portions**

Figure 6.16. Channel width measurements of the γ channels of both (a) heads and (b) gauge lengths for the four different heat treated long term creep samples measured in parallel and perpendicular directions using image analysis.

Rafting parameter results are shown in Table 6.6. The rafting parameter of S1 and S3 has significantly increased from the head portions to the gauge length portions, which is consistent with the SEM investigation. The rafting parameter of S1 has increased from 0.90 to 1.70 and 0.92 to 1.74 for S3. The increased degrees of rafting results in a reduction of creep rupture life. However, with the help of cross-linked rafts, the creep rupture life of S1 and S3 are still much higher than the degraded samples. Since the rafting parameter of S4 (2.80) is

much larger than S2 (2.07), less of a barrier to dislocation motion was obtained within the microstructure, resulting in a shorter creep rupture life but a higher strain in S4. The rafting parameter results have a good agreement with the SEM investigation and creep rupture results.

Table 6.6 The rafting parameter of four different heat treated samples

Sample No	Heat Treatments	Rafting Parameter	
		Heads	Gauge Lengths
S 1	As-received	0.90	1.70
S 2	Rafted	2.02	2.07
S 3	Rafted + HT Rejuvenation	0.92	1.74
S 4	Rafted + HT Rejuvenation + Rafted	2.73	2.80

6.3.3 TEM microstructural examination

Within this section the results of the TEM microstructural investigation will be presented and discussed. The purpose of this investigation was not only to observe the presence of tertiary γ′ precipitates within samples, but also to investigate the effect that the morphology of the γ′ rafts, the size of the γ channels and tertiary γ′ precipitates on the dislocations.

Figure 6.16 shows TEM images of the long term creep tested samples from gauge length. The TEM results are in good agreement with the SEM investigation. S1 and S3 show cross-linked γ′ rafts, with relatively larger channels in gauge length portions (>200 nm) when compared to head portions (~100nm). A high density of dislocations was observed in the γ channels, especially near the junction points of γ′ rafts. This is because it is very difficult for

dislocations to cut through γ′ rafts, and, with the help of this cross-linked structure, dislocations were trapped. That is why the γ/γ′ interface has more dislocations observed. In degraded samples (S2 and S4), individual rafts with much wider channels (~300 nm) were observed, which makes dislocations glide through easier than the cross-lined structure and results in a reduction in the creep rupture life. For S4, which has undergone two degradation treatments, more dislocations were observed in the channels than S2. As obtaining larger channels and higher rafting degree within the microstructure, S4 has fewer barriers to dislocation motion, which results a reduction in creep rupture life but an increase of strain.

Tertiary γ′ precipitates with a size of ~ 20-50 nm were found in all the samples, shown in Figure 6.17. This is consistent with the SEM investigation. The presence of tertiary γ′ precipitates could act as barrier to block the movement of dislocations. However, since the channels are too wide, the dislocations can easily glide through even with presence of tertiary γ′ precipitates. This indicates that the morphology of rafts, γ channel width and the degree of rafting play a more important role than the tertiary γ′ precipitates in determining the creep life of the materials.

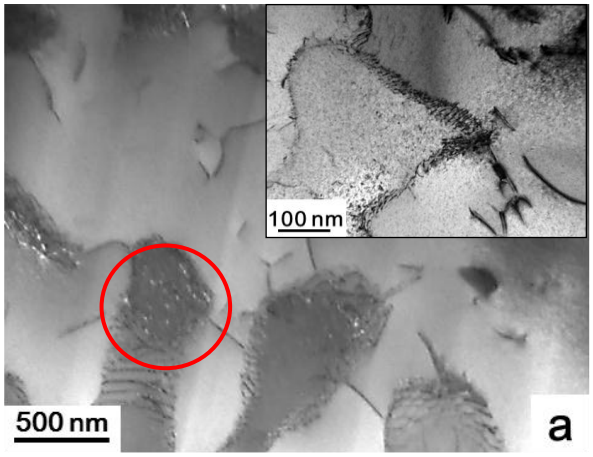

(a) S1. As Received

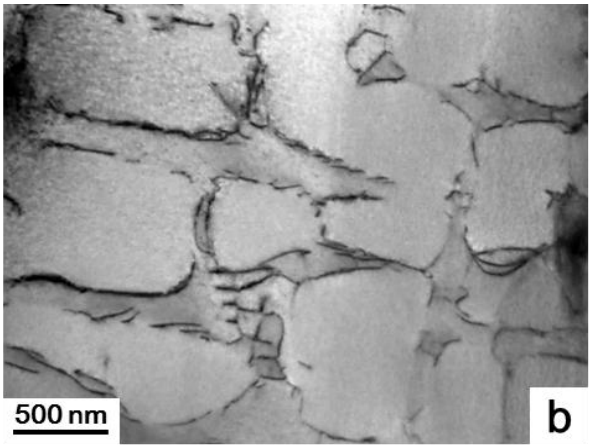

(b) S2. Rafted

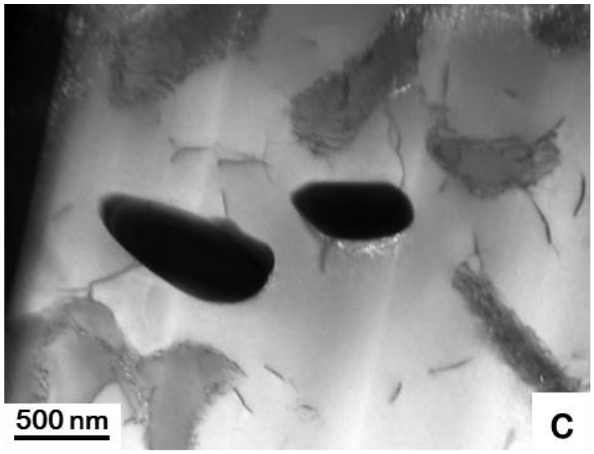

(c) S3. Rafted + HT Rejuvenation

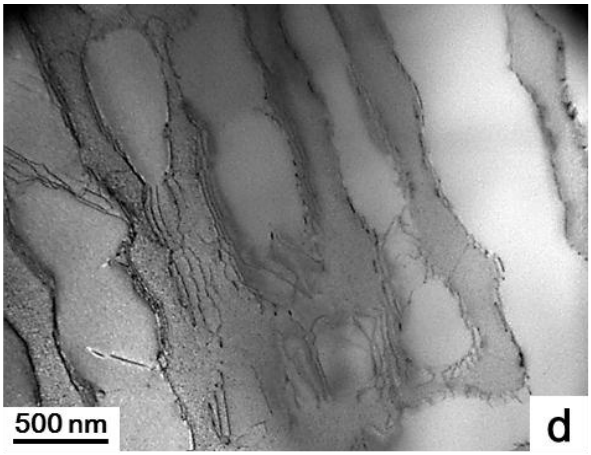

(d) S4. Rafted + HT Rejuvenation+ Rafted

Figure 6.17. The low magnification TEM images of the gauge length portions of the long term creep samples after four different heat treatment conditions, showing distribution and morphology of γ/γ′ and their effects on the dislocations

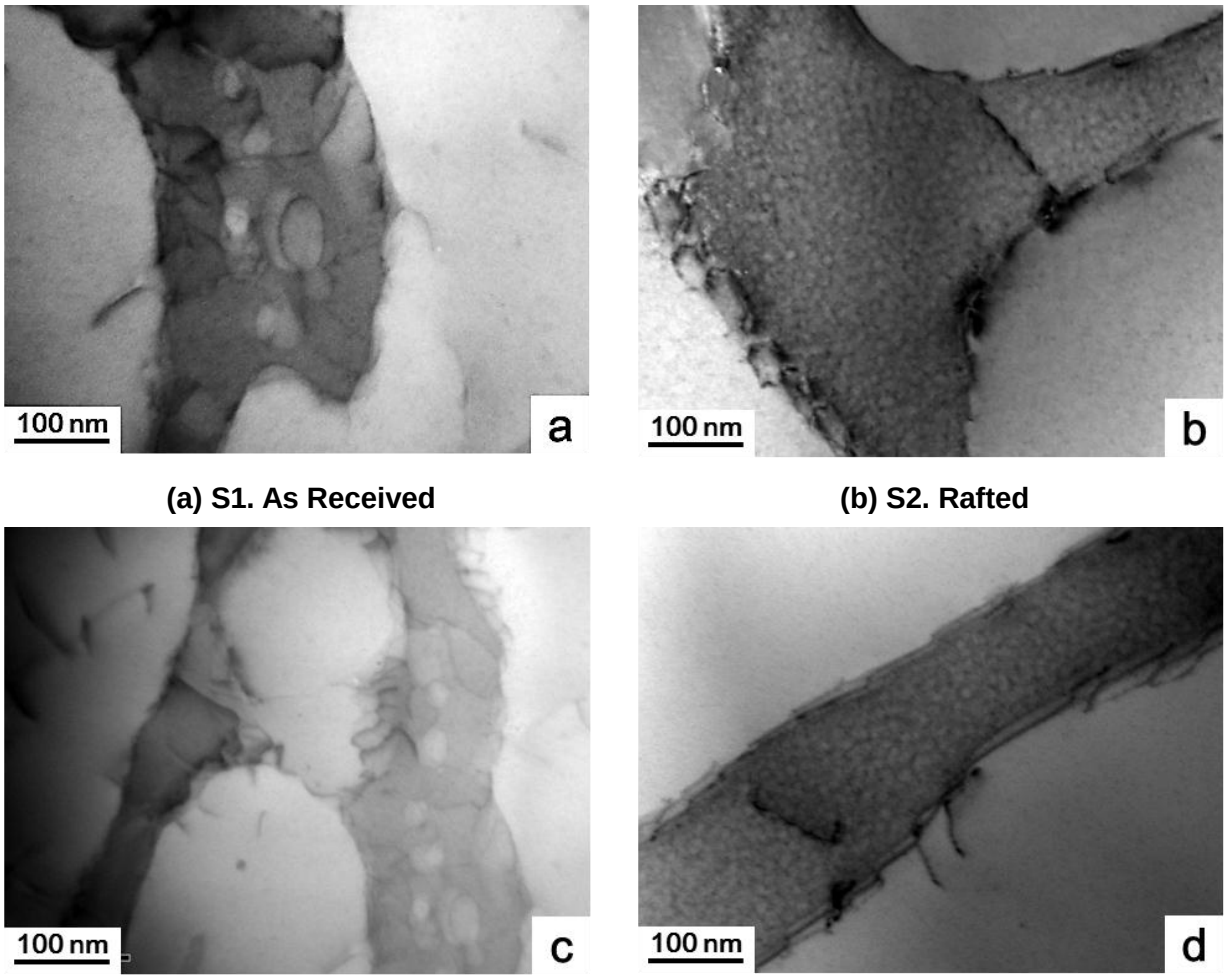

(a) S1. As Received **(b) S2. Rafted**

(c) S3. Rafted + HT Rejuvenation **(d) S4. Rafted + HT Rejuvenation+ Rafted**

Figure 6.18. The high magnification TEM images of the gauge length portions of the long term creep samples after four different heat treatment conditions, showing tertiary γ′ precipitates and their effects on the dislocations.

6.3.4 Summary

The microstructural evolution of these four creep samples can be illustrated by the schematic diagrams, see Figure 6.19. The long-time exposure at testing conditions has a significant influence on the microstructure. However, with the help of cross-linked γ′ rafts, the measured creep rupture life of the as-received and rejuvenated sample is much longer than the degraded samples. It has been

found in this chapter that the morphology and size of the γ channels plays a more important role than tertiary γ′ precipitates.

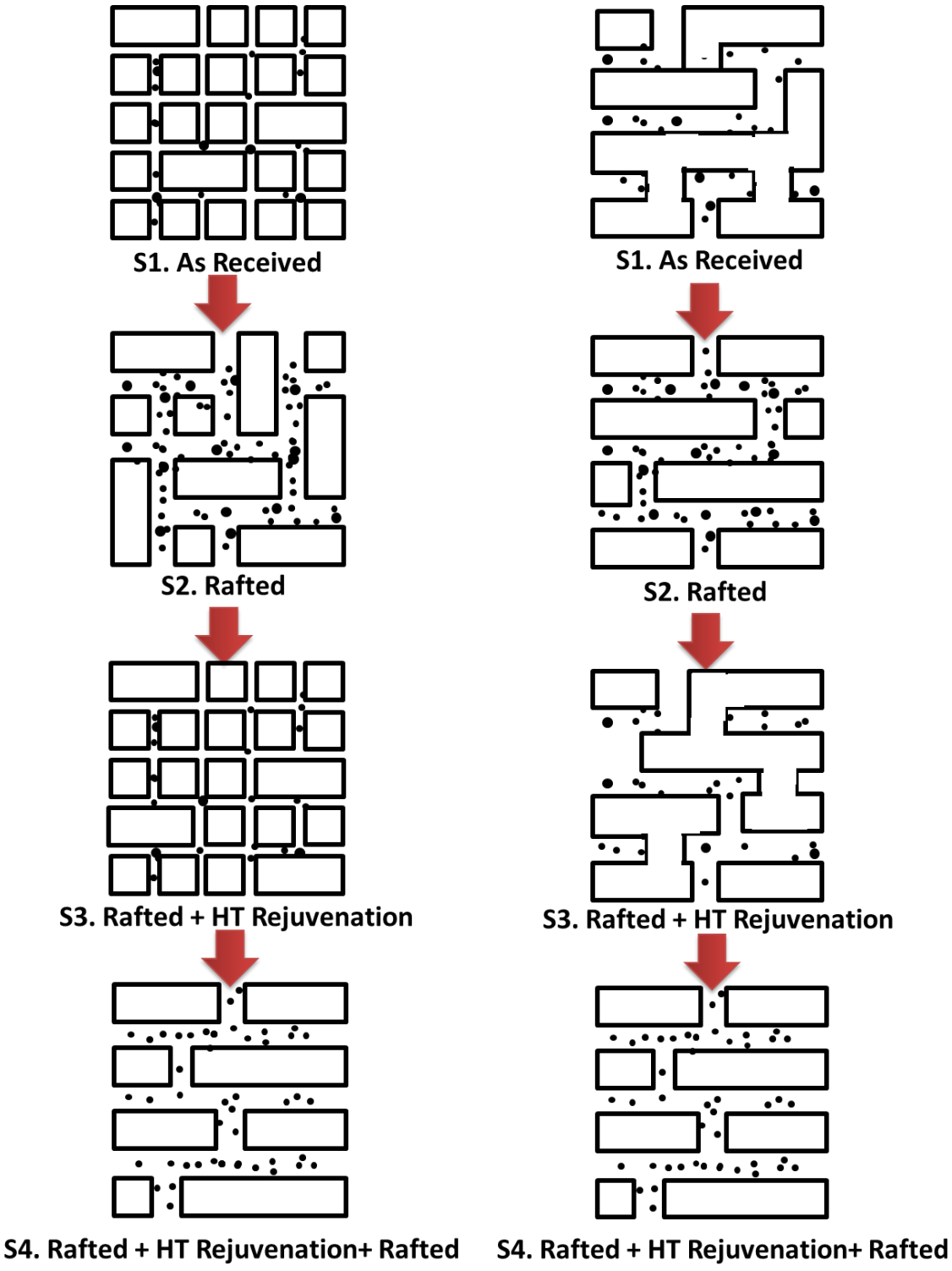

Figure 6.19. Schematic diagrams of the microstructural evolution of long term creep samples after four different heat treatment conditions.

6.4 Conclusions

The microstructural evolution and creep behaviour of CMSX-4 samples before and after high temperature degradation and rejuvenation have been examined. The creep behaviour of the differently heat treated samples results from changes in morphology, area fraction of secondary γ′ particles, γ channel width, rafting parameter and the precipitation of the tertiary γ′ in the channels. The degradation not only increases the size, spacing and rafting parameter of the secondary γ′ particles, which in turn makes the γ channel broader and the degree of rafting higher, but also causes a reduction in the measured area fraction of secondary γ′ particles. Moreover, it was observed that the presence of tertiary γ′ precipitates in the channels has a beneficial effect on the mechanical properties. The increased short term creep rupture life of the rejuvenated sample was contributed to by the presence of a large amount of tertiary γ′ precipitates within the γ channels. However, later research found out that the morphology and size of channels appear to play a more important role than the tertiary γ′ precipitates. The fine distribution of cuboidal γ′ particles with small channels (<120 nm) is the main factor for the longer creep rupture life of these materials at the creep conditions tested here. Although the long term creep sample exhibits long rafts with much broader channels, the cross-linked γ′ particles provides a significant barrier to dislocation motion, resulting in a higher creep rupture life than the degraded samples.

The rejuvenation has recovered the degraded microstructure back to the as-received condition, which shows the same γ′ distribution, size and morphology as the as-received sample. However, the faster degradation of rejuvenated sample when they had undergone a subsequent degradation treatment indicates the rejuvenation has not completely take it back to the as-received condition. The rafting parameter results show that the rejuvenated

sample has a much higher degree of rafting within the microstructure than the as-received sample when they undergone a subsequent degradation treatment. Therefore, any residual segregation, stress and misfit between γ/γ′ left within the rejuvenated sample may promote the γ′ coarsening and rafting in a subsequent degradation and cause a reduction in the mechanical performance.

CHAPTER 7

CHEMICAL SEGREGATION AND MODIFIED REJUVENATION

7.1 Introduction

According to the results given by the previous mechanical tests described in Chapter 5 and 6, the lower temperature refurbishments did not appear helpful in rejuvenating the microstructure of CMSX-4, and in fact, it may be further degraded or damaged by the applied heat treatment. The high temperature rejuvenation heat treatment, however, appears to have successfully restored the microstructure back to its as-received condition, and, in some cases, even improved the mechanical performance of rejuvenated samples over the as-received samples, especially the short term properties. Unfortunately, the underlying microstructural changes which occur during the high temperature rejuvenation are unknown. Moreover, the increased rate of degradation of the rejuvenated samples compared to the as-received during a second rafting heat treatment still remains and is a significant issue for future service performance. In order to address the problems listed above, additional research was conducted which will be discussed in this chapter in order to investigate the mechanisms associated with the rejuvenation heat treatments.

In the first part of this chapter, a chemical segregation investigation of samples before and after high temperature degradation and rejuvenation are presented. The chemical segregation data gave a good understanding of the reasons that

the rejuvenated and as-received samples perform quite differently during the second degradation treatments. The results of mechanical behaviour have been presented and discussed in Chapter 5 and 6. In the second part of this chapter, a modified rejuvenation heat treatment is designed and trialled, followed by microstructure and chemical segregation analysis. The microstructures of CMSX-4 at each step (solution and ageing) of rejuvenation were examined combined with chemical segregation analysis. The microstructures of samples after different modified rejuvenated trials were examined using field emission gun scanning electron microscopy (FEGSEM) with the chemical segregation of all the samples investigated using the energy dispersive x-ray spectroscopy (EDX).

7.2 Chemical Segregation Investigations

In Chapter 5 and 6, the high temperature rejuvenation heat treatment has recovered most of the microstructure to the as-received conditions, but the reason why rejuvenated samples degraded faster than as-received samples during subsequent rafting treatment is still unknown. The possible reasons include: chemical segregation, dislocations and γ/γ′ misfit. The latter two factors are more applicable to situations where rejuvenated blades are used in the stressed condition. However, in the case of the experimental work presented here, both the high temperature degradation and rejuvenations were carried out with no applied stress. Therefore, it is more likely to be related to chemical segregation. As the directional coarsening of the γ′ particles is a diffusion controlled process, it is very dependent on the movement of the alloying elements [1]. The larger the chemical segregation present within the microstructure, the greater the rate of rafting of the γ′ particles potentially is and

may result in a reduction of the mechanical properties.

The degradation caused during rafting, not only alters the microstructure but also causes chemical segregation, which later affects the mechanical performance. The results shown in Chapter 5 and 6 show that the rejuvenation heat treatment recovers most of the microstructure to the as-received conditions, but it is important to examine the chemical segregation levels of these samples after rejuvenation. In order to quantitatively analyse the chemical segregation rate in these samples before and after degradation and rejuvenation, the chemical segregation analysis was applied. Four samples were chosen for this investigation: As-Received (S1), Rafted (S2), Rafted + HT Rejuvenated (S3), Rafted + HT Rejuvenated + Rafted (S4). The microstructures of these four samples are shown in Figure 5.2 and Figure 5.3. The chemical segregation was examined by measuring the chemical difference between the dendritic cores and inter-dendritic regions. Figure 7.1 shows optical microscopy images of these samples showing their structures. The dendritic structures of S1-S4 are very clear and increase in size after the rafting treatment. The hardness indents visible in the images (black square marks) were used to help locate the dendritic core and interdendritic regions after the etching effect was removed through polishing prior to EDX measurements to ensure that accurate chemistries could be obtained without the influence of the etch.

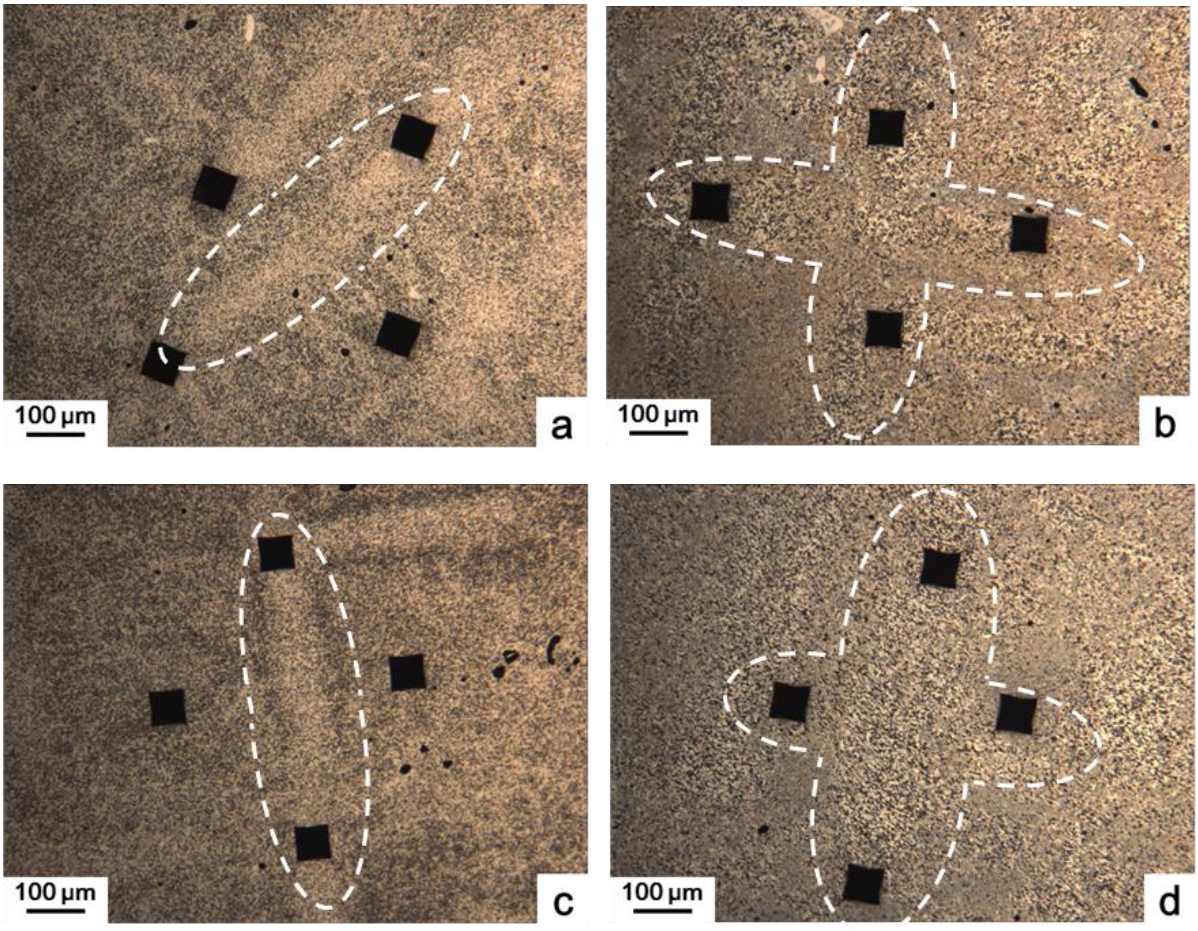

Figure 7.1. Optical microscopy images showing dendrite structures in; (a) S1, as-received, (b) S2, rafted, (c) S3, rafted + HT rejuvenation, and (d) S4, rafted + HT rejuvenation + rafted

Chemical segregation analysis between dendritic core and inter-dendritic regions using EDX is very sensitive to the surface quality and the size of the analysed area. In order to acquire accurate measurements, the following points were under considered:

1. Etching affects the accuracy of measurements since it is used to remove certain phases (in this case, γ phase is removed from the surface), to leave γ′ and other phases in relief.
2. The EDX point analysis has a spatial resolution limitation of approximately 0.5 - 1.0 µm, which is close to the size of the γ′ particles. Therefore, point

analysis results will not accurately present the chemical composition of the analysed area.

To overcome these problems, processes and methods were applied to avoid or reduce their influence on the analysis. The first problem was overcome by using hardness indents to mark the dendritic core and interdendritc regions as shown in Figure 7.1. The etched surface was then removed by re-polishing, leaving a clean surface with the hardness indents making the area for analysis. The second problem was overcome by using area analysis instead of points, which gives an average chemical composition in the analysed area. The size of the area analysis was chosen to be 20X20 μm, which is large enough to avoid the limitation of the spot resolution, but small enough to obtain chemical information within the dendrite core (DC) and inter-dendritic regions (IDR). Figure 7.2 illustrates area analysis measurement locations carried out at the DC and IDR. The chemical composition difference between the DC and IDR was used to represent the chemical segregation within the samples.

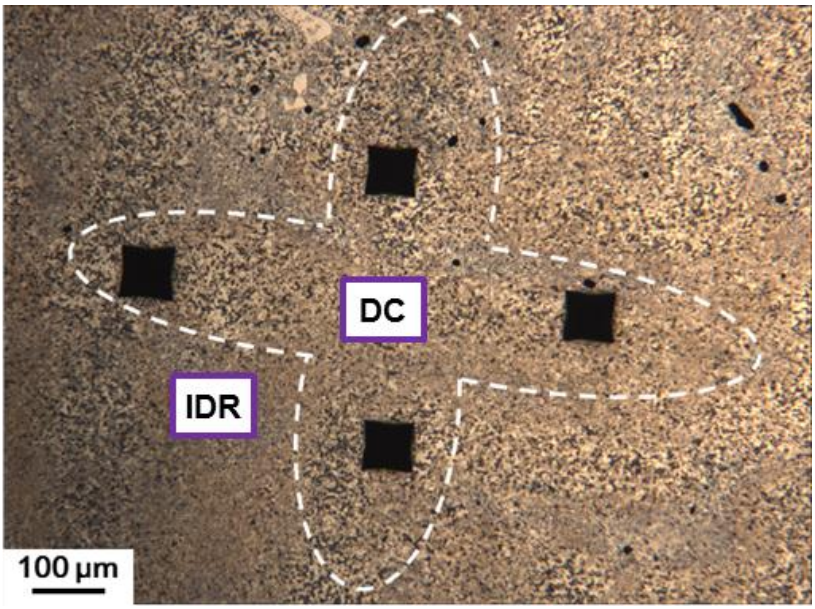

Figure 7.2. A schematic illustration of the location of the EDS area analysis in the dendritic core (DC) and interdendritic region (IDR) with respect to the dendrite structure.

The chemical composition difference results are shown in Figure 7.3. Most of the elements show clear chemical differences between the IDR and DC. Therefore, since the behaviour of Al, Ti, Ta, W and Re were most obvious, the chemical difference of these elements (IDR − DC) was used to represent the chemical segregation trend in this study. It has been found that Al, Ti and Ta are rich in the IDR, but consistently lower in DC (the values are plus), whilst Re and W exhibit contrary trends (the values are minus), which is in good agreement with Karunaratne *et al*. [1]. According to the chemical segregation results, the sequence of the chemical segregation from largest to smallest extent is S4, S2, S3 and S1. The chemical segregation in the as-received sample (S1) is the smallest, presumably because it has not experience any degradation. The result shows that chemical segregation has apparently increased when the sample has undergone a degradation treatment, meaning that the process of degradation not only degrades the microstructure but also causes further chemical segregation, Although, the rejuvenation heat treatment applied here has recovered some segregation as shown in Figure 7.3, e.g. Ti and Ta, it has not fully recovered to the as-received condition, but most of the elements are still closer to the rafted conditions. This residual segregation is due to the slower diffusing elements such as Re and W. According to Karunaratne *et al*. [1], the interdiffusion coefficients of Re and W at the rejuvenation temperature are the slowest, which means the chemical segregation of these elements is very difficult to eliminate with this short term rejuvenation [2-5]. When the HT rejuvenated sample (S3) experiences a further degradation treatment, with the help of the residual chemical segregation, the rafting of the γ′ particles will accelerate and cause a reduction of the mechanical performance. Therefore, according to the results so far, the chemical segregation is the key explanation for the reduction in the performance after the second rafting heat treatment (S4), as the segregation of slowly diffusing elements such as Re and W, is not fully

removed during the short rejuvenation.

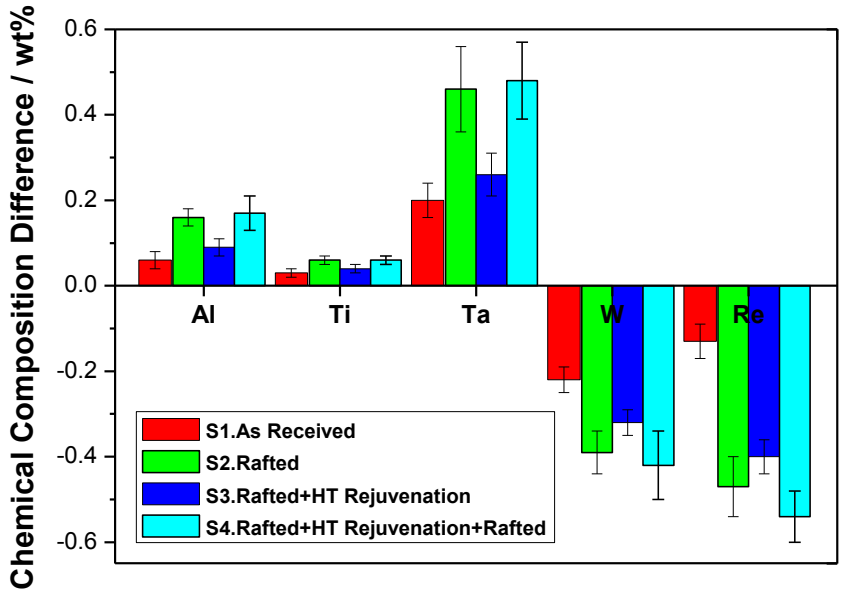

Figure 7.3. Chemical composition difference between dendrite core (DC) and interdendritic regions (IDR) of different heat treated samples.

The results of the chemical segregation investigations of four different heat treated CMSX-4 samples have been presented and discussed in this section. Although the microstructure of the high temperature rejuvenated sample (S3) and as-received (S1) samples are very similar to each other, their chemical segregation results show significant differences. The chemical segregation is a key explanation for the increased rate of the degradation after a second rafting treatment, as the segregation was not removed through the initial rejuvenation and was then enhanced by second degradation process, resulting a faster rafting of γ′ particles and a reduction in mechanical performance. Since the short term rejuvenation has been shown not to fully recover the chemical segregation to the as-received conditions, especially for Re and W, it is possible that an extension in the length of the rejuvenation heat treatment may decrease this

chemical segregation. Consequently, the rejuvenation heat treatment has been modified to extend the heat treatment in time in an attempt to remove any chemical segregation in addition to restoring the microstructure of a rafted sample. The microstructures and chemical segregation after these modified rejuvenations are shown in next section, to determine whether extending the length of rejuvenation could eliminate these detrimental segregation effects, to make a more homogeneous microstructure and chemical distribution and therefore improved long term mechanical properties.

7.3 Modified Rejuvenation

According to the results given in first section of this chapter, the high temperature rejuvenation can restore a rafted microstructure back to the as-received condition. However, the chemical segregation investigation data shows the chemical segregation of rejuvenated samples has not 100% recovered to the as-received condition. The residual chemical segregation was pronounced in the second rafting and caused a reduction of the mechanical performance. Since the slow diffusional rate elements such as Re and W, are not easily eliminated by the short term rejuvenation, a few modified rejuvenations based on the extension of the length of the rejuvenation were carried out. In order to examine the effects of each heat treatment on the microstructure, the high temperature rejuvenation procedure was broken down into a solution heat treatment and two steps of ageings, giving a good understanding of the microstructural evolution of CMSX-4 during the rejuvenation procedure and effects of each treatment on microstructural restoration. The aim of these rejuvenation trials was to find an optimum rejuvenation procedure for the reduction of chemical segregation.

In this section, the results of four different rejuvenation trials are presented and discussed. The name followed by the description of each rejuvenation heat treatment is shown in Table 7.1.

Table 7.1 The name of four different rejuvenation trials

Sample ID	Name of Rejuvenation Trials
RT1	Repeated rejuvenation
RT2	Double holding time rejuvenation
RT3	Five cycles
RT4	Extend the last step of solution to 60 hours

The applied rejuvenation heat treatments are as follows:

1. (RT1) Repeated high temperature rejuvenation heat treatment as described in Table 7.2, in order to act as a control specimen for these experiments. The rejuvenation was separated into steps to examine the microstructural evolution during the solution and two ageing heat treatments.
2. (RT2) Double holding time for each stage of the high temperature solution heat treatment to increase the time available for homogenisation of the microstructure and chemical distribution.
3. (RT3) Five rejuvenation cycles where the solution heat treatment cycle was repeated in its entirety five times.
4. (RT4) Extend the last step (1323°C) of the solution heat treatment, instead of holding 2 hours, it was held for 60 hours to make a more homogeneous microstructure and chemical distribution.

7.3.1 Repeated rejuvenation (RT1)

The high temperature rejuvenation heat treatment was separated into the solution heat treatment and two steps of ageings, giving an indication of the microstructural evolution of the Ni-based superalloy during rejuvenation. The detail of the heat treatment and samples each stage is shown in Table 7.2. These temperatures were chosen based from literature and applied solution treatment used for single crystal Ni-based superalloy [119-124].

Table 7.2 Detail of the modified rejuvenation trial 1 (RT1)

Sample ID	Rejuvenation	
	Solution Heat Treatment	**Ageings**
RT 1	Heat rate 20°C/min ➢ 1283°C for 2 h ➢ 1285°C for 2 h ➢ 1301°C for 2 h ➢ 1309°C for 2 h ➢ 1318°C for 2 h ➢ 1321°C for 2 h ➢ 1323°C for 2 h **RT1-01**	➢ 1140°C for 6 h + Air Cool **RT1-02** ➢ 871°C for 20 h +Air Cool **RT2-03**

The microstructures after the solution heat treatment (RT1-01) and ageing stages (RT1-02, 03) are shown in Figure 7.4. RT1-01 exhibits a uniform distribution of fine diamond shape γ′ particles with a size of ~ 250 nm, as shown in Figure 7.4a. In some regions, spherical and cuboidal γ′ particles were found, but the size of the cuboidal γ′ (250 nm) is much smaller than the normal cuboidal γ′ particles (0.5-1μm) present in Figure 5.2 Chapter 5. The solution heat treatment was designed to dissolve all the degraded γ′ and other phases, such as TCP and carbides, into solution and re-precipitate a uniform distribution of

fine γ′ phases combined with other phases. The solution temperature was gradually increased at each step to further dissolve γ′ and other phases. The new γ′ particles were re-precipitated after cooling since the γ′ phase was more stable at lower temperature. The morphology of the γ′ particles obtained in the microstructure is related to the cooling rate. Spherical γ′ is formed during fast cooling, whilst a cuboidal is more likely from slow cooling. The diamond shape γ′ was formed after a medium cooling, which is consistent with the literature [5].

Figure 7.4b shows the microstructure after the 1st ageing stage (RT1-02), where the diamond shape γ′ particles coarsened and formed cuboidal shape γ′ particles with a size of ~ 0.5 μm. The microstructure was very close to the rejuvenated tensile tested sample (see Figure 5.2), but the edge of these particles appear more rounded than the rejuvenated tensile tested sample. The ageing process not only caused the secondary γ′ particles to grow, but also changed the morphology, which was designed to maintain the excellent mechanical performance. In the literature, the cuboidal γ′ is believed to maintain the maximum mechanical performance of the materials. The purpose of this ageing was to optimise the mechanical properties by producing an even distribution of the cuboidal γ′ particles with a size of ~ 0.5 to 1 μm [1].

Figure 7.4c shows the microstructure of CMSX-4 sample after the 2nd ageing stage, which was carried out 871°C for 20 hours (RT1-03). The microstructure appeared to be exactly the same as the rejuvenated tensile tested sample. The rounded edge of the cuboidal γ′ particles became much sharper after the 2nd ageing. In the literature, the purpose of this ageing stage is not only to stabilise the cuboidal γ′ particles but also to produce additional γ′ particles and other phases such as carbides and borides. In this research, carbides and borides in this alloy are present in only very small quantities and therefore can be ignored.

Therefore, the application of the 2nd ageing is mainly to stabilise the cuboidal γ′ particles. However, when compared to the high magnification images of the microstructure before and after the 2nd step ageing stage, as shown in Figure 7.5, the size of the tertiary γ′ precipitates in the channels has increased. Before 2nd ageing, the size of the tertiary γ′ precipitates was less than 30 nm, whereas after ageing, it has increased to ~50 nm. Therefore, the effect of this ageing is not only to stabilise the cuboidal shape of secondary γ′, but also to increase the size of the tertiary γ′ precipitates in the channels. The presence of tertiary γ′ precipitates in channels is beneficial to the mechanical properties [1].

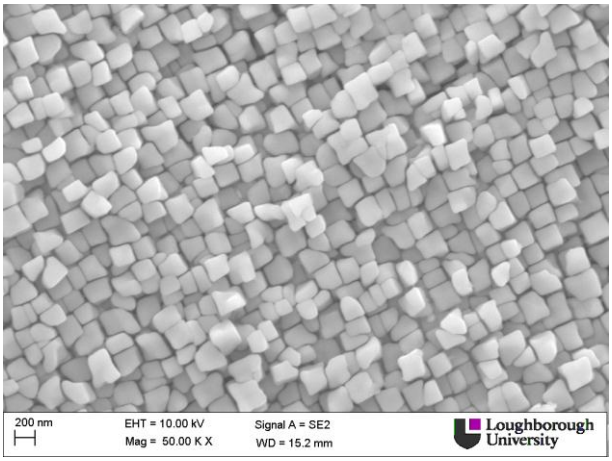

(a) RT1-01

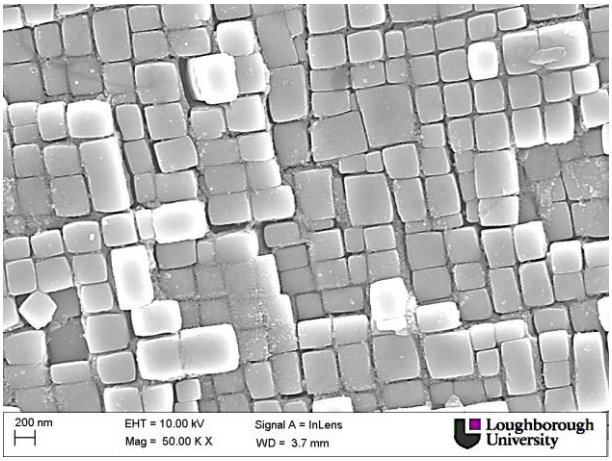

(b) RT1-02

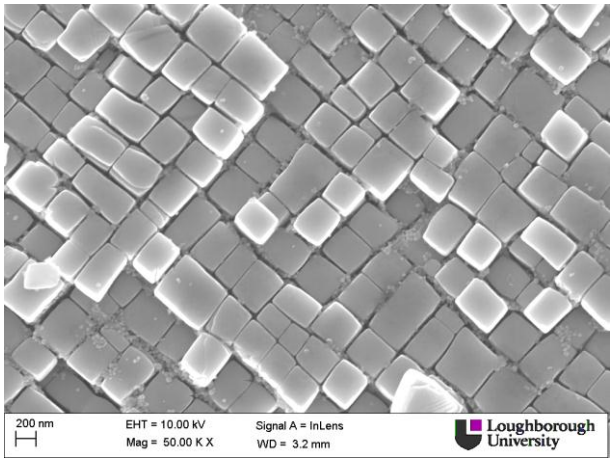

(c) RT2-03

Figure 7.4. SEM images showing microstructure of repeated rejuvenation (RT1) in different stages: (a) after solution heat treatments, (b) after ageing at 1140°C for 6 hours, (c) after ageing at 871°C for 20 hours

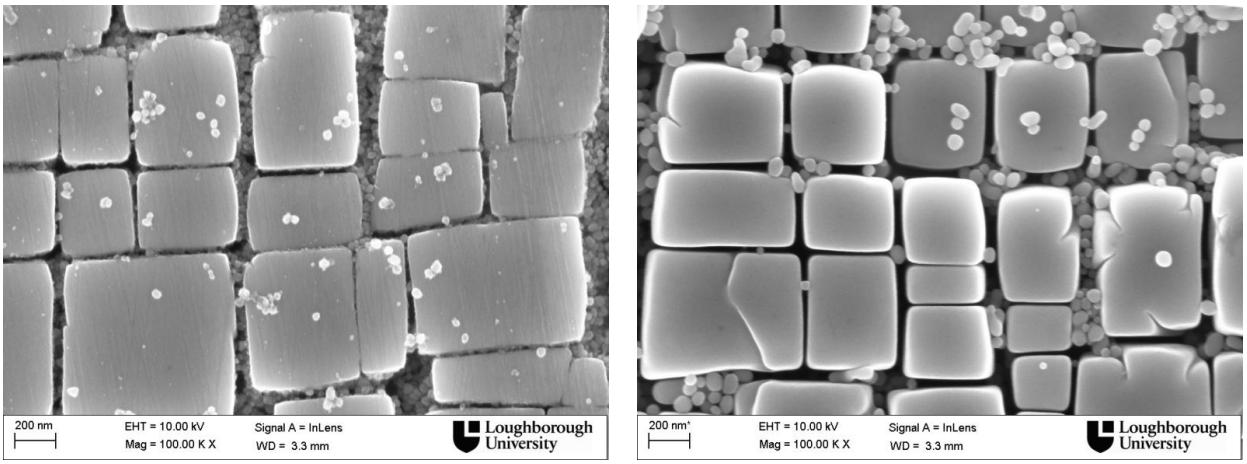

(a) RT1-02 **(b) RT1-03**

Figure 7.5. The high magnification SEM images to show the details of the γ channel and size of tertiary γ′, (a) after ageing at 1140°C for 6 hours, (b) after ageing at 871°C for 20 hours.

In order to further examine the microstructure, the area fraction of secondary γ′, γ channel width and rafting parameter were measured, the results of which are shown in Figure 7.6 and Table 7.3. The area fraction and channel width results of repeated rejuvenation (RT1-03) had a good agreement with the rejuvenated tensile tested sample shown in Figure 5.6 and Figure 5.7. Both microstructures contained an area fraction ~0.86 of secondary γ′ particles, which was very similar to the as-received condition (0.851). The area fraction of secondary γ′ particles was used to represent the volume fraction in this research as noted earlier. The excellent mechanical behaviour of CMSX-4 is attributed to the large volume fraction of γ′ phases present within the microstructure [1]. γ channel width is another important examination factor. The measured channel widths of RT1-03, rejuvenated tensile and as-received samples were ~60 nm in both the parallel and perpendicular directions, which resulted in the same rafting parameter (~0.55) for both rejuvenations. Since these results were the same, the area fraction, channel width and rafting parameter of RT1-03 was used to represent rejuvenated tensile tested sample data in later comparisons. These results suggested that the repeat procedure had reproduced the microstructure

of the high temperature rejuvenation well. In addition, it was very similar to the as-received sample. Tertiary γ′ precipitates were found in rejuvenated samples, which is believed has beneficial effect on the mechanical properties [1].

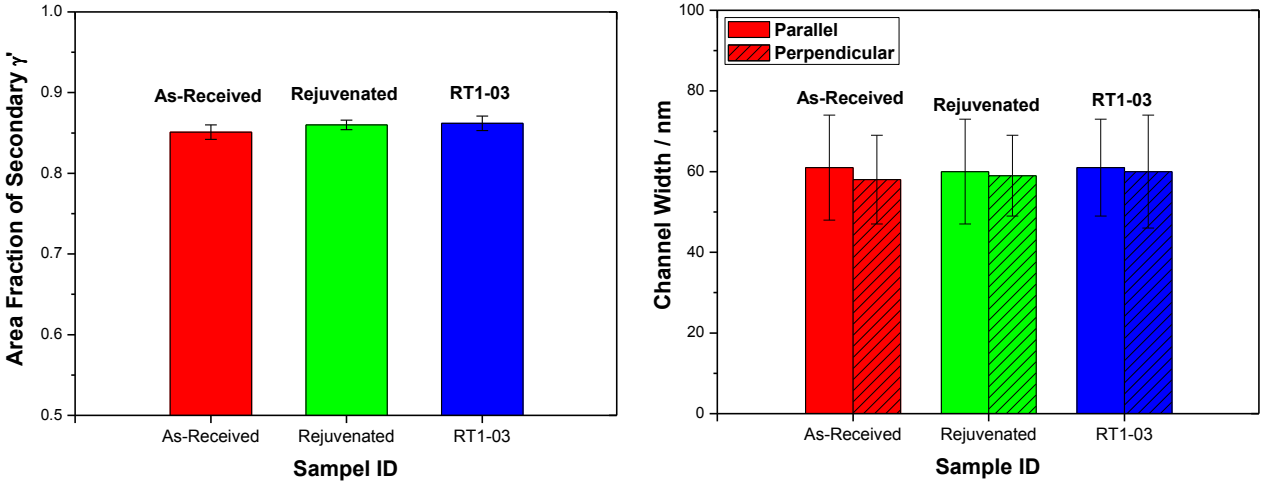

(a) Area Fraction **(b) Channel Width**

Figure 7.6. The microstructural analysis results of RT1-03: (a) area fraction of secondary γ′ particles, (b) γ channel width.

Table 7.3 Channel widths and rafting parameter for rejuvenated samples

Sample No	γ Channel Width / nm		Rafting Parameter
	Parallel	Perpendicular	
As-received	61±13	58±11	0.56
Rejuvenated	60±13	59±10	0.55
RT1-03	61±12	60±14	0.55

The next important factor used to evaluate the rejuvenation procedure is the extent of chemical segregation which exists after the rejuvenation heat treatments. The chemical segregation results are shown in Figure 7.7, where the RT1-03 showed similar results to the rejuvenated tensile tested sample. The rejuvenated samples still had a large chemical difference left between the dendritic core and interdendritic regions, especially for Re and W. These data suggested that the repeat rejuvenation not only reproduced the microstructure, but also obtained the same chemical segregations. Therefore, the chemical segregation data for the repeat rejuvenation (RT1-03) was used to represent the rejuvenated tensile tested sample within this chapter.

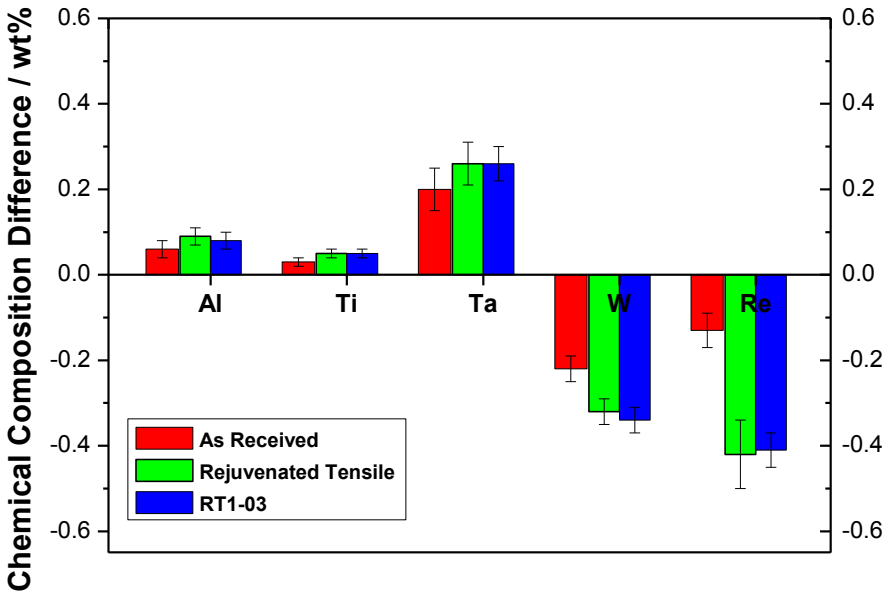

Figure 7.7. Chemical composition difference between dendrite core (DC) and interdendritic regions (IDR) for the repeated rejuvenation (RT1-03) sample

The analysis of each step of the rejuvenation heat treatment gives a good overview of the microstructural evolution of CMSX-4 alloys during the solution and ageing heat treatments applied. According to the results obtained from the repeated rejuvenation, the solution heat treatment is more related to the restoration of the microstructure and recovery of the chemical segregation, whilst the ageing stages play an important role by altering the morphology and coarsening the γ′ particles, in order to maintain the optimum mechanical performance. As the solution heat treatment plays more important role than ageing in recovering chemical segregation, the later rejuvenation trials have focused on modifying the solution heat treatment rather than ageing in this research.

7.3.2 Double holding times rejuvenation (RT2)

As discussed earlier, the modification of the rejuvenation heat treatment has focused on the solution heat treatment rather than the whole procedure. Therefore, the first trial was to extend the holding time of each step in solution heat treatment to 4 hours instead of 2 hours. The microstructure of RT2 has shown in Figure 7.8 and Figure 7.9. At lower magnification, some large gaps or “cracks” were observed in the microstructure, especially near the sample’s edges, as shown in Figure 7.8. At higher magnification, these “cracks” were found to be γ channels with increased widths. These large γ channels will likely be detrimental to the properties, since they provide fewer obstacles for the motion of dislocations through them, which leads to a reduction in mechanical performance.

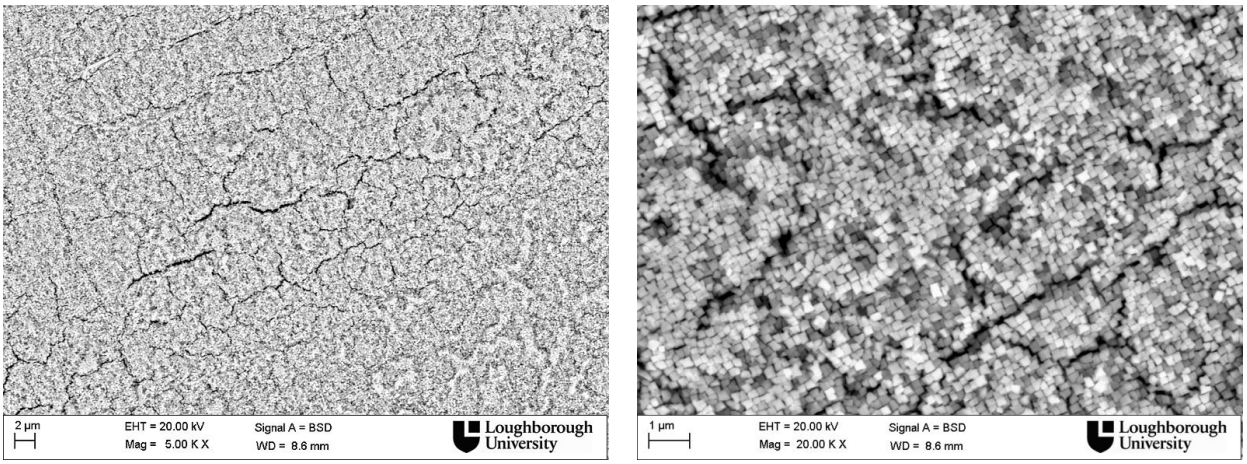

(a) "cracks" **(b) High Mag of "cracks"**

Figure 7.8. SEM images of the sample after double holding time rejuvenation showing. (a) low magnification of "cracks", (b) high magnification of "cracks", which were found to be increased γ channels.

The microstructures of the sample after different heat treatment stages are shown in Figure 7.9. The microstructure was very similar to the microstructure of repeated rejuvenation (RT1). Fine diamond shape γ′ particles were present after solution heat treatment, and they changed morphology to cuboidal and increased in size after ageing. Tertiary γ′ precipitates were found in the channels after ageing. However, there was a difference in the channel width. It has been found that the channel width after the double holding time rejuvenation had increased in size from 60 nm to 115 nm. The detail of channel growth is shown Table 7.4. This microstructure indicates the double holding time rejuvenation may not be an improvement since it does not recover the microstructure to the as-received condition, but instead makes it worse in respect of the channel width. With those wider channels, it is easier for the dislocations to pass through and results in a reduction in mechanical properties [1].

The area fraction of secondary γ′, γ channel width and rafting parameter measurements results are shown in Figure 7.10 and Table 7.4. The area fraction

of secondary γ′ particles of R2-03 (0.850) is same as repeated rejuvenation (0.862) and as-received samples (0.851). However, this small amount reduction in area fraction will not influence the properties. The γ channel width has massively increased from 60 nm to 116 nm in the parallel direction, and from 60 nm to 112 nm in the perpendicular direction. Inside the channels, small spherical tertiary γ′ precipitates with various sizes were observed. Fortunately, most of the secondary γ′ still maintained their cuboidal structure, which leads to a rafting parameter equivalent to the as-received condition of 0.56.

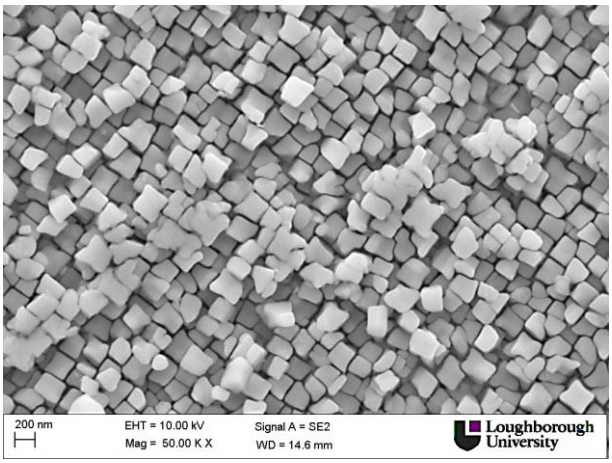

(a) RT2-01

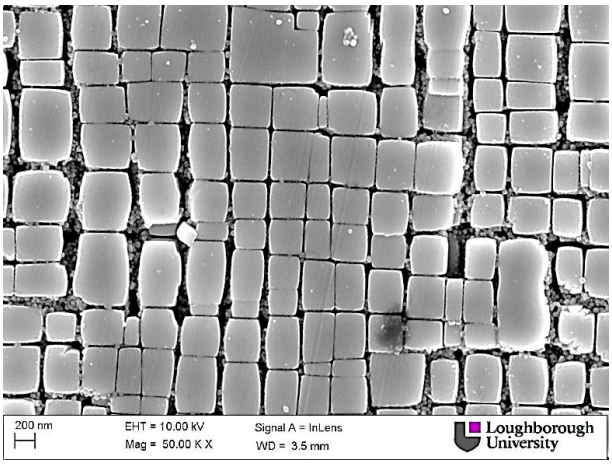

(b) RT2-02

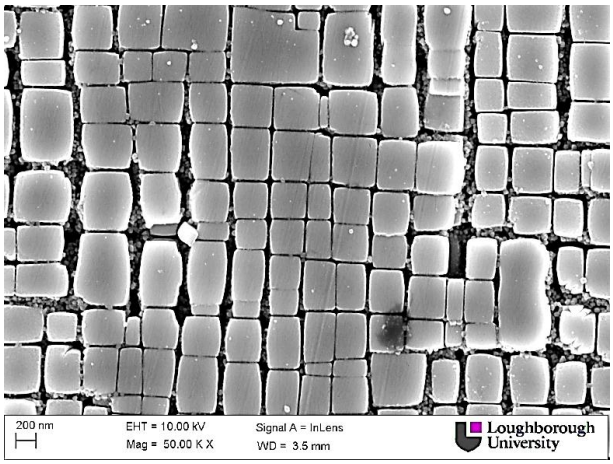

(c) RT2-03

Figure 7.9. SEM images showing microstructure of doubles holding time rejuvenation (RT2) in different stages: (a) after solution heat treatments, (b) after ageing at 1140°C for 6 hours, (c) after ageing at 871°C for 20 hours.

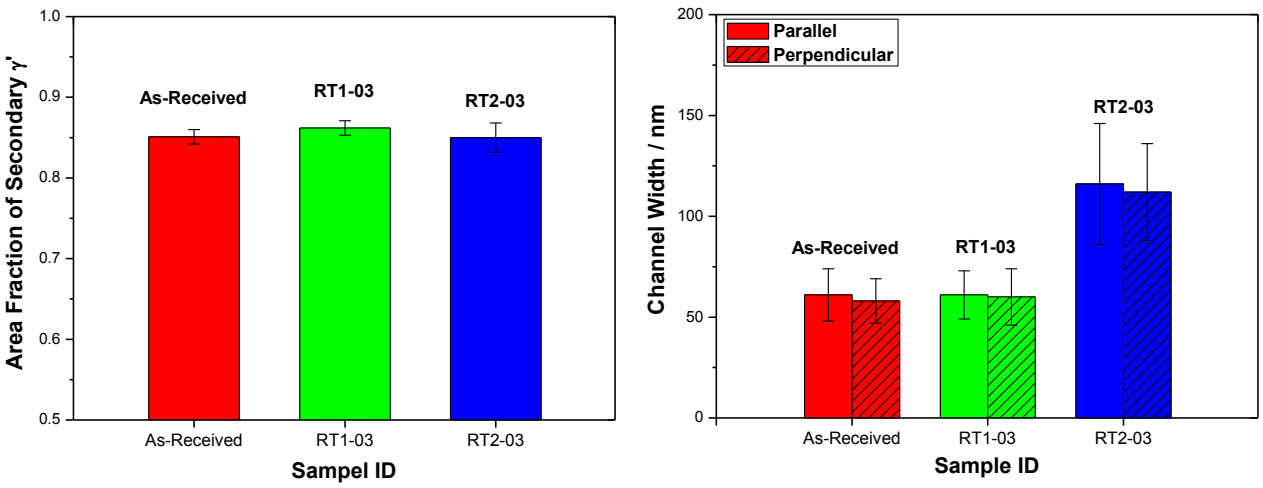

(a) Area Fraction **(b) Channel Width**

Figure 7.10. The microstructural analysis results of RT2-03: (a) area fraction of secondary γ′ particles, (b) γ channel width.

Table 7.4 Channel widths and rafting parameter for rejuvenated samples

Sample No	γ Channel Width / nm		Rafting Parameter
	Parallel	Perpendicular	
As-received	61±13	58±11	0.56
RT1-03	61±12	60±14	0.55
RT2-03	116±30	112±24	0.56

Chemical segregation as another important factor was also examined. The main purpose of the extended solution heat treatment was to reduce chemical segregation by allowing more time for homogenisation. Figure 7.11 shows the chemical difference results between the dendritic core and interdendritic regions, which are used to represent the chemical segregation. The results show a further reduced chemical segregation compared with repeated rejuvenation, especially for the heavy elements W and Re. This suggests that the double

holding time rejuvenation is beneficial to the recovering of chemical segregation. However, the reduction in the chemical segregation is not significant, which still leaves a pronounced difference compared with the as-received condition. This indicates that the doubled holding time of solution heat treatments is not long enough to eliminate the chemical segregation. In conclusion, although the double holding time has reduced some chemical segregation, it did not provide sufficient recovery to produce a chemical distribution equivalent to the as-received condition.

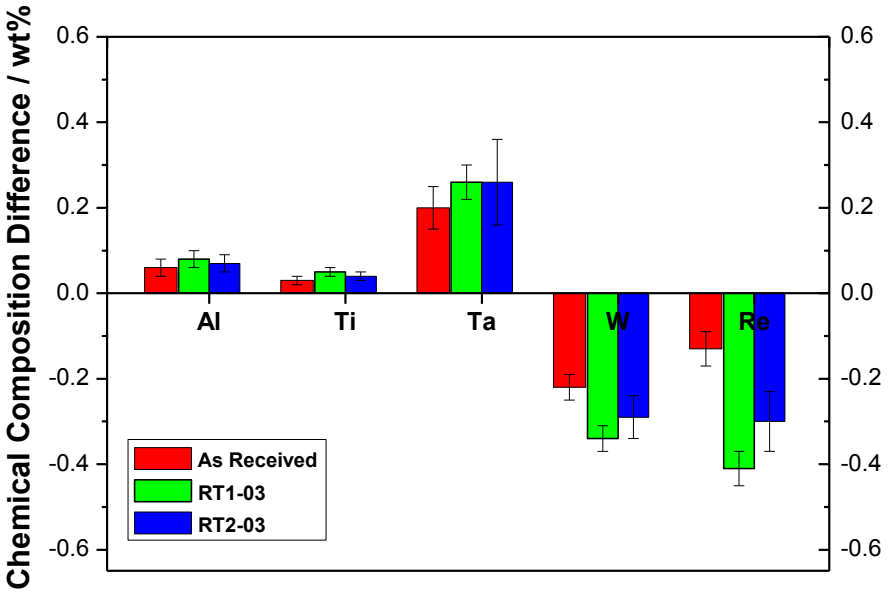

Figure 7.11. Chemical composition difference between dendrite core (DC) and interdendritic regions (IDR) for double holding time rejuvenation (RT2-03) sample

7.3.3 Five cycles (RT3)

The double holding time of solution heat treatment (RT2) reduced level of chemical segregation. However, the reduction was not significant enough, and more importantly it caused the emergence of large γ channels in the

microstructure, which is detrimental for the mechanical performance. The next rejuvenation trial, RT3, was a five cycles rejuvenation heat treatment. It used the exactly same high temperature rejuvenation procedures, but as the name suggests, five solution heat treatment cycles were carried out, before ageing was applied. The purpose of this trial was to examine the influence of the multiple cycles on the microstructure and chemical segregation. Figure 7.12 shows the microstructure of these samples after the different heat treated stages. The microstructure is very similar to that of repeated rejuvenation sample. The biggest difference between the five cycled sample (RT3-03) and repeated rejuvenation (RT1-03) is that in RT3-03, some of the γ′ particles showed a slight tendency to form rafts, where cuboidal γ′ are seen to be joined together. These changes indicated the degree of rafting of this sample was quite different compared with previous rejuvenation. The detailed rafting parameter will be shown in Table 7.5

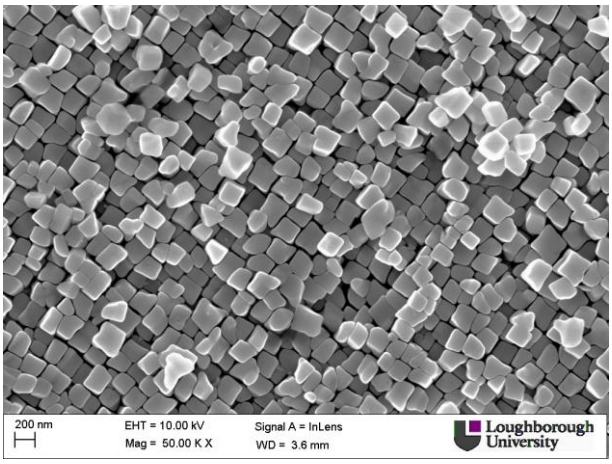

(a) RT3-01

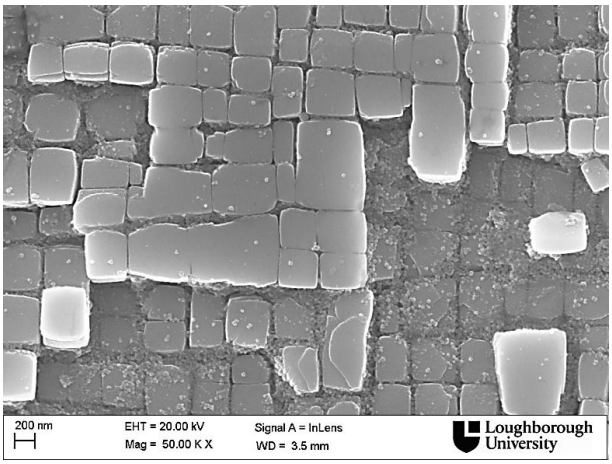

(b) RT03-02

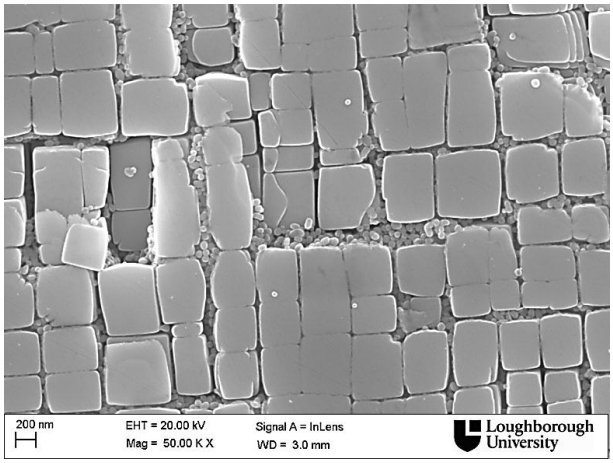

(c) RT03-03

Figure 7.12. SEM images showing microstructure of the five cycled rejuvenation (RT3) in different stages: (a) after solution heat treatments, (b) after ageing at 1140°C for 6 hours, (c) after ageing at 871°C for 20 hours.

The area fraction of secondary γ′, γ channel width and rafting parameter results are shown in Figure 7.13 and Table 7.5. The area fraction of secondary γ′ after RT3-03 was consistent with the repeated rejuvenation, which contained the same area fraction of secondary γ′ particles (0.866). Although the channels were slighter wider than RT1-03 and the as-received samples, they were much smaller than the double holding time rejuvenation. The big difference in the five cycled sample was the rafting parameter. The larger degree of rafting results in a large rafting parameter. For a cuboidal structure, the rafting parameter would be

expected to be close to 0.5. However, the rafting parameter of the RT3-03 sample was 0.65, due to some rafts being present which were formed during rejuvenation. This increased tendency to form rafts may be detrimental to the mechanical properties since it provides less barrier effect on dislocations [1].

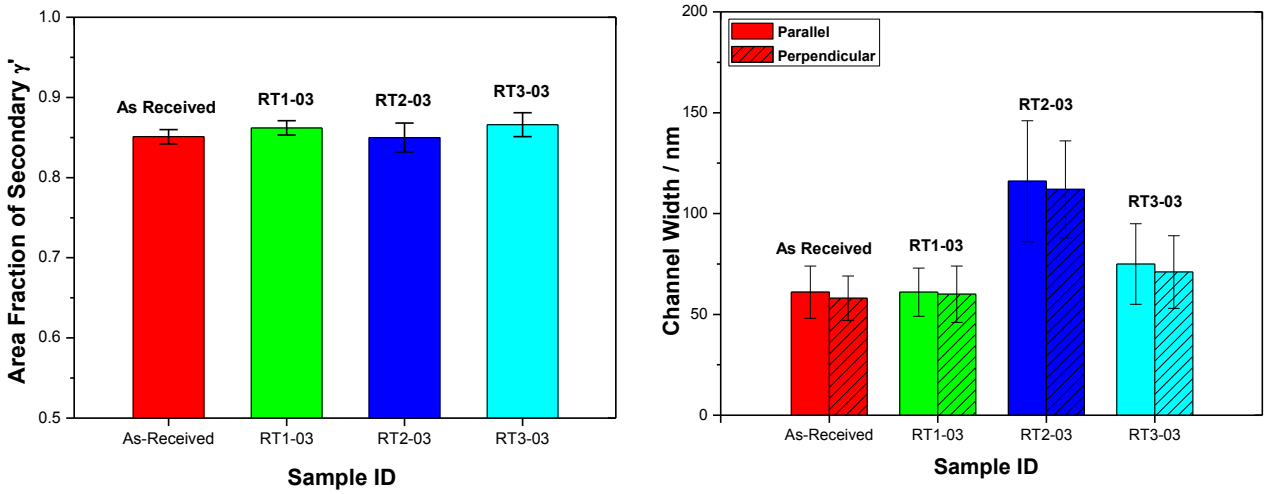

(a) Area Fraction **(b) Channel Width**

Figure 7.13. The microstructural analysis results of RT3-03: (a) area fraction of secondary γ′ particles, (b) γ channel width.

Table 7.5 Channel widths and rafting parameter for rejuvenated samples

Sample No	γ Channel Width / nm		Rafting Parameter
	Parallel	Perpendicular	
As-received	61±13	58±11	0.56
RT1-03	61±12	60±14	0.55
RT2-03	116±30	112±24	0.56
RT3-03	75±20	71±18	0.65

The chemical segregation analysis was also applied for five cycled sample, the result of which is shown in Figure 7.14. The chemical difference of elements between dendritic core and interdendritic regions has further reduced after the five cycle rejuvenation compared with double holding time rejuvenation. With the help of the five cycled rejuvenation, the chemical difference of W and Re is further decreased and is seen to be close to the chemical segregation measured in the as-received condition, particularly for W. This indicates that the five cycle heat treatment can recover more chemical segregation than the double holding time rejuvenation. The microstructural and chemical segregation analysis suggests that the five cycled rejuvenation is better than double holding time rejuvenation. However, the chemical segregation of Re is still pronounced when it is compared to as-received condition, which indicates that the five cycle rejuvenation has not completely reduced the chemical segregation equivalent to as-received condition.

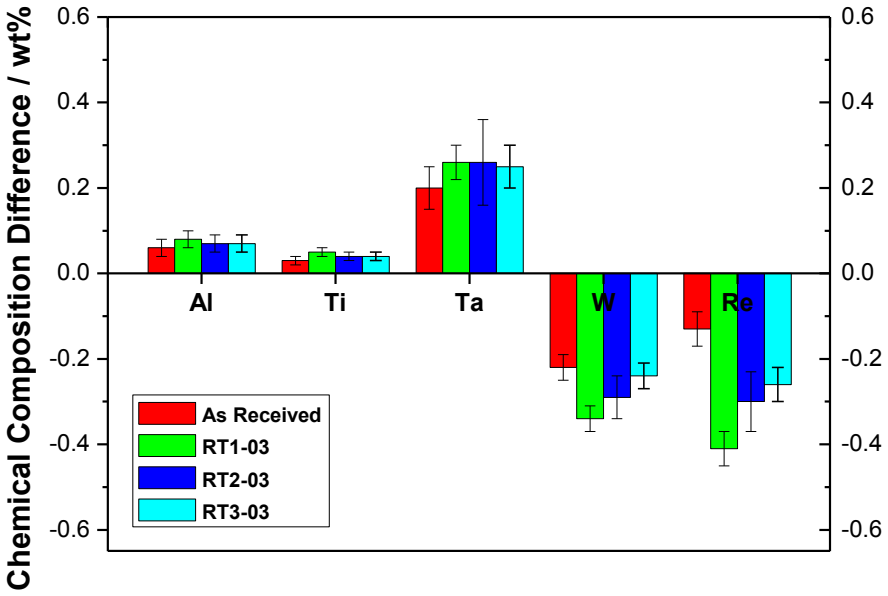

Figure 7.14. Chemical composition difference between dendrite core (DC) and interdendritic regions (IDR) for five cycled rejuvenation (RT3-03) sample

7.3.4 Extend the last step of solution to 60 hours (RT4)

According to some published literature data, the solution heat treatment time for a Ni-based superalloy to achieve reasonable chemical homogeneity is ~48 hours [6]. However, the five cycles rejuvenated sample has a solution heat treatment totallying more than 70 hours, but chemical segregation still remains within the sample. Since homogenisation is a diffusion controlled process, the elements diffuse faster at higher temperatures. In other words, it will much easier to reach chemical homogeneity after the same holding time at higher temperature. Therefore, the final rejuvenation trial was focused on the extension of the last step of solution heat treatment. In this rejuvenation heat treatment, the last step of 1323°C was held for 60 hours, to determine whether the this rejuvenation could eliminate these detrimental chemical segregation effects. However, the use of this temperature presents a significant risk as it is only 20°C below the melting point of CMSX-4 and in some cases less than 7°C below [5]. Therefore, it should be noted that the risk of incipient melting is significant at this temperature.

The microstructure of the sample after a 60 hours solution heat treatment is shown in Figure 7.15. The microstructure was similar to that of the repeated rejuvenation sample (RT1). It contained cuboidal and diamond shape γ′ particles after solution heat treatment (RT4-01), with a size ~250 nm. Very fine tertiary γ′ precipitates with a size of ~ 30 nm were also found after ageing. The same microstructure of RT4-03 and RT1-03 indicates it is a potentially good rejuvenation.

The microstructure of RT4 was further examined using the area fraction of secondary γ′, γ channel width and rafting parameter, the results of which are shown in Figure 7.16 and Table 7.6. The results are very similar to RT1 and

as-received samples. RT4 not only produces a microstructure with an area fraction of secondary γ′ particles (0.85), which is very close to the as-received sample (0.86), but also obtained the same channel size and rafting parameter within the microstructure. The results indicates the 60 hours rejuvenation treatment successfully restores the microstructure back to the as-received conditions, without causing any degraded structure, such as broader channels and higher degree of rafting.

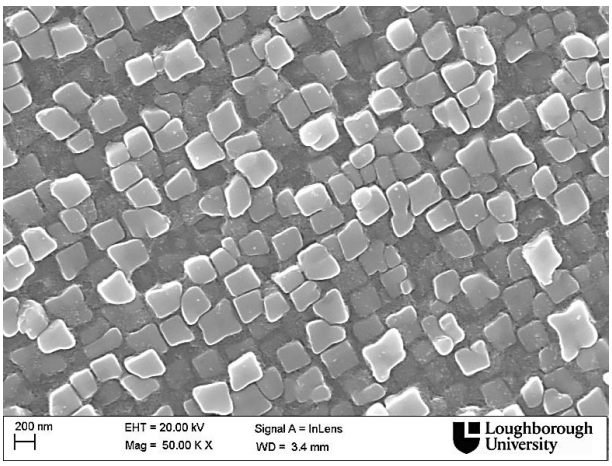

(a) RT4-01

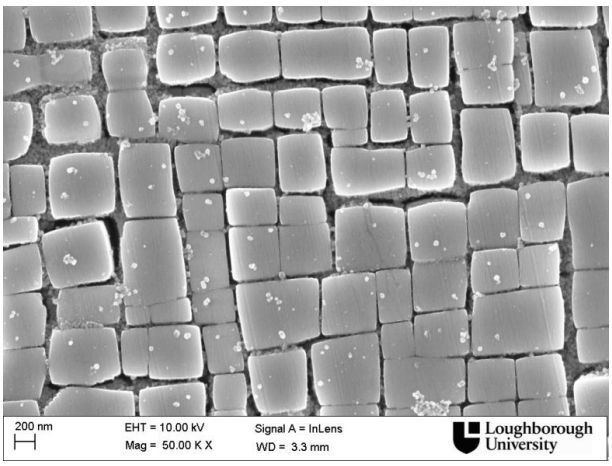

(b) RT4-02

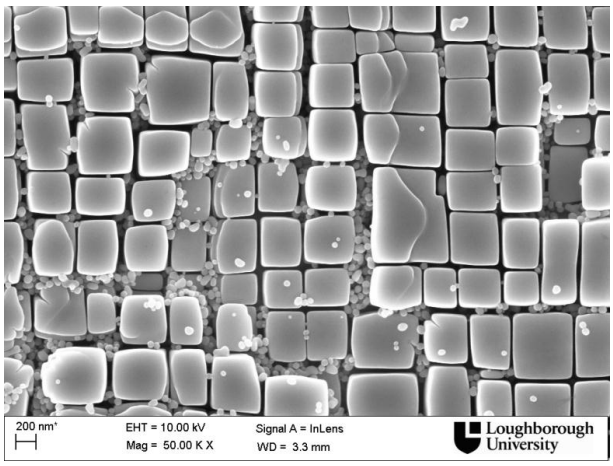

(c) RT4-03

Figure 7.15. SEM images showing microstructure of extend last step of solution to 60 hours rejuvenation (RT4) in different stages: (a) after solution heat treatments, (b) after ageing at 1140°C for 6 hours, (c) after ageing at 871°C for 20 hours.

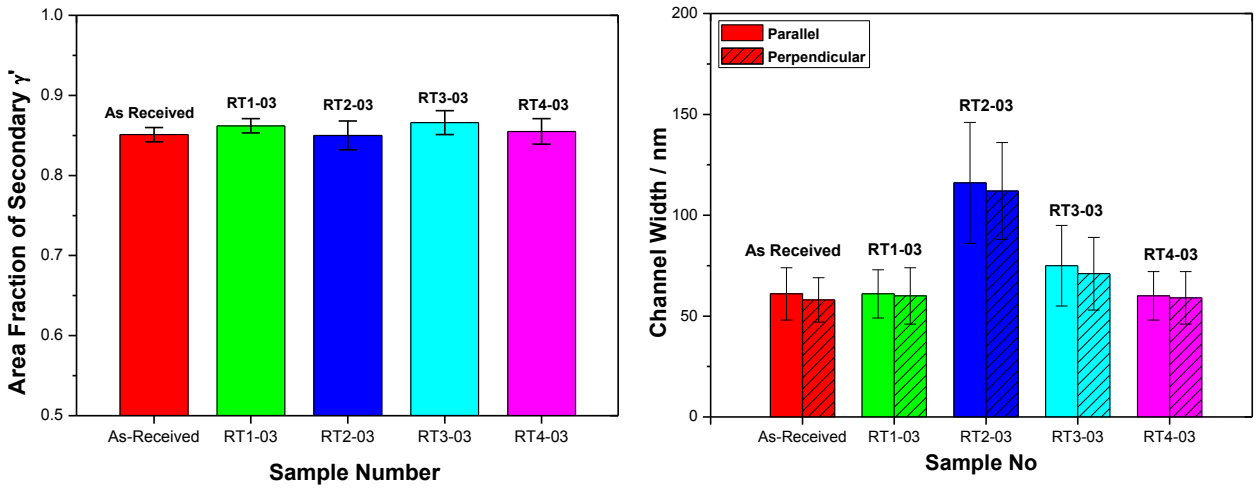

(a) Area Fraction **(b) Channel Width**

Figure 7.16. The microstructural analysis results of RT4-03: (a) area fraction of secondary γ′ particles, (b) γ channel width.

Table 7.6 Channel widths and rafting parameter for rejuvenated samples

Sample No	γ Channel Width / nm		Rafting Parameter
	Parallel	Perpendicular	
As-received	61±13	58±11	0.56
RT1-03	61±12	60±14	0.55
RT2-03	116±30	112±24	0.56
RT3-03	75±20	71±18	0.65
RT4-03	60±12	59±13	0.54

Within the microstructure of RT4 sample, there was no clear dendrite structure observed, the optical image of which is shown in Figure 7.17. This indicated a more homogeneous structure may be obtained in this sample. Therefore, in order to make a comparison of chemical segregation in this sample, 20 EDS area analysis boxes with a size of 20x20 μm were randomly carried out on the

as-received, RT1, RT2, RT3 and RT4, by using the difference between the maximum and minimum chemical composition to represent the inhomogeneity of the samples, as shown in Figure 7.18. The larger the chemical difference, the more chemical inhomogeneity was present within the microstructure. The chemical inhomogeneity was smallest in the as-received sample. For the RT1 sample, there existed a large degree of chemical inhomogeneity which was much greater than as-received conditions, especially for heavy elements, such as W and Re. With the help of the RT2 and RT3, the chemical inhomogeneity had further decreased. RT4 was the best rejuvenation in term of chemical segregation. The measured inhomogeneity has decreased to levels approaching the as-received condition. The microstructure and chemical homogeneity results were very positive for RT4, indicating that an extended last step of solution heat treatment rejuvenation was a good modification suggestion for a rejuvenation heat treatment. How the RT4 sample performs after a second rafting heat treatment and its mechanical behaviour will be presented in the following section.

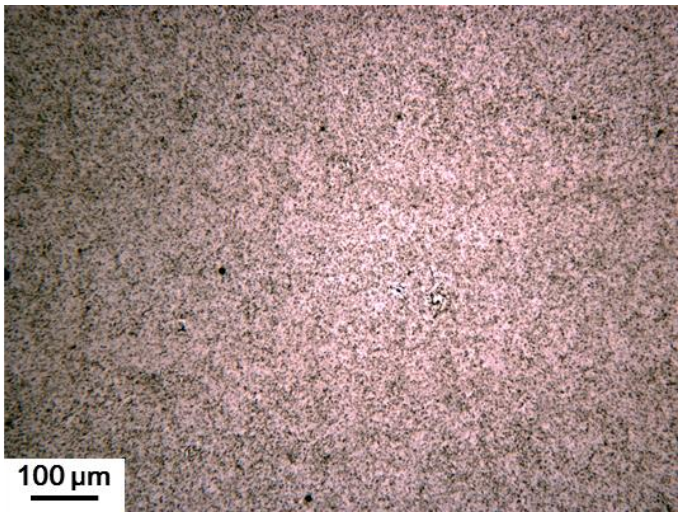

Figure 7.17. Optical microscopy images showing that a dendrite structures was not clearly visible in the RT4-03 sample after extend last step of solution to 60 hour rejuvenation.

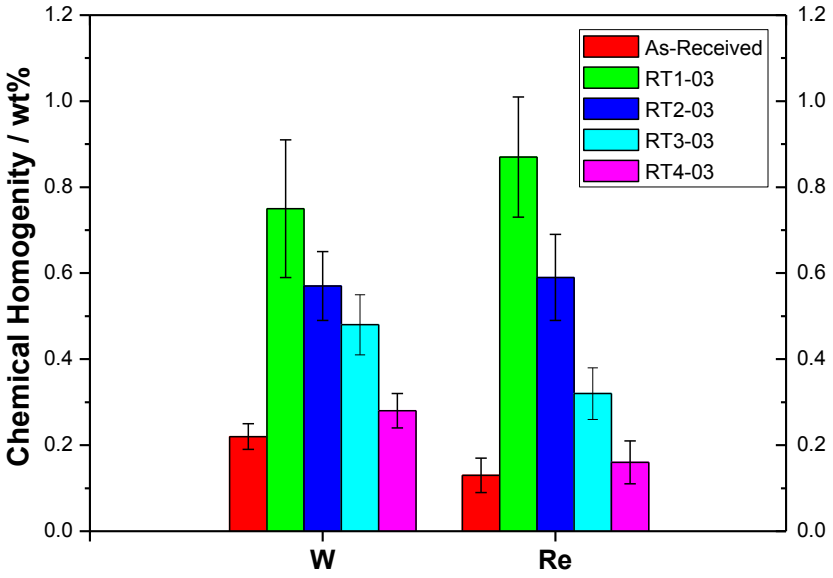

Figure 7.18. Chemical homogeneity of the as-received and four different rejuvenation trials based on 20 randomly selected EDS area analyses

7.3.5 Summary of trialled rejuvenation heat treatments

In this section, four different rejuvenation trials have been described together with microstructural and chemical segregation analysis. The separate rejuvenation treatments provide a good understanding about the microstructural evolution of CMSX-4 in the solution and ageing heat treatments. The solution treatment plays an important role in the recovery of the microstructure and reduction in chemical segregation, whilst the ageing stages are applied to alter the morphology and size of the γ′ particles, by which to maintain the optimum mechanical performance. Therefore, considering the effect of the microstructure and chemical segregation influence, the solution treatment was modified rather than ageing in this study. The microstructural summaries of four rejuvenation trials are shown in Figure 7.20 with their comments shown in Table 7.7.

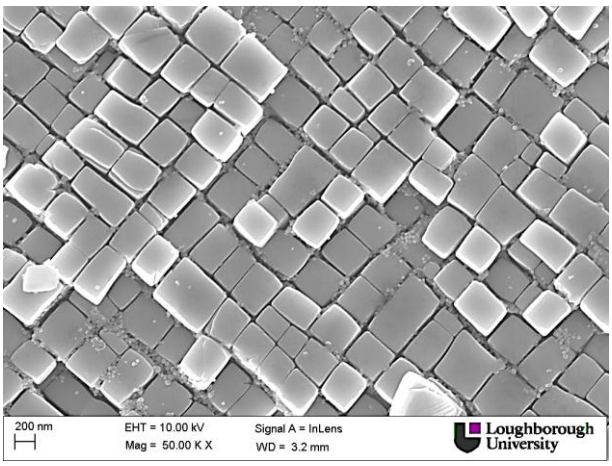

(a) RT1-03

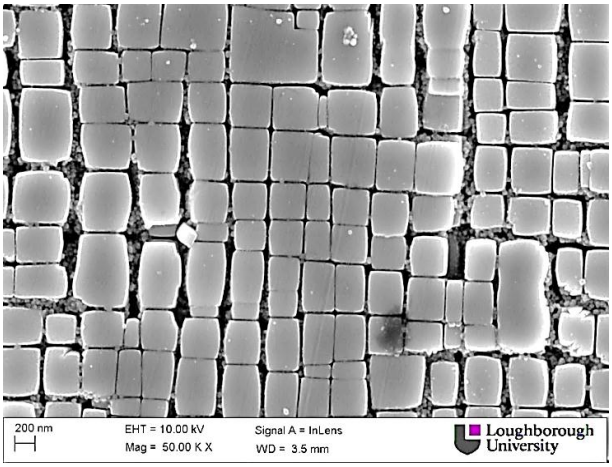

(b) RT2-03

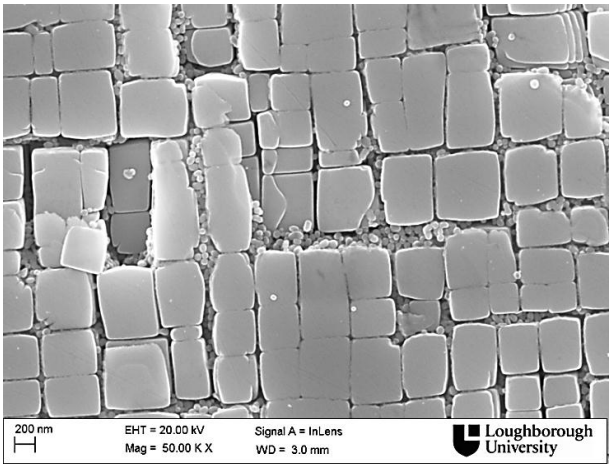

(c) RT3-03

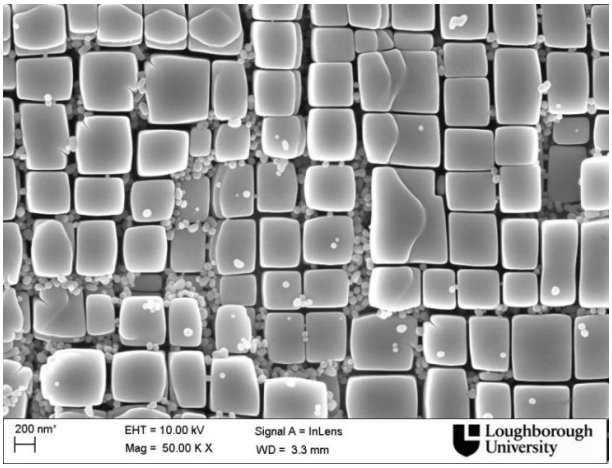

(d) RT4-03

Figure 7.19. SEM images showing microstructures of four different rejuvenation trials: (a)RT1-03 repeated rejuvenation, (b)RT2-03 double holding time (c)RT3-03 five cycled rejuvenation, (d)RT4-03 extend the last step of solution to 60 hours rejuvenation.

Table 7.7 The comments for four different rejuvenation trials

ID	Name of Rejuvenation Trials	Comments
RT1	Repeated rejuvenation	Chemical segregation is not recovered
RT2	Double holding times rejuvenation	Channels are broader
RT3	Five cycles	Rafting Parameter has increased
RT4	Extend the last step of solution to 60 hours	Current best

RT1 has well restored the microstructure back to the as-received condition, however, the chemical segregation result indicates there is still a pronounced difference of some elements presented within the sample. RT2 has reduced the chemical segregation, but the chemical segregation of heavy elements such as W and Re still remained. The biggest problem of RT2 is that the γ channel widths were much broader than RT1, which is detrimental for the mechanical performance [1]. RT3 not only decreased the γ channel width compared RT2, but also further reduced the chemical segregation. However, the rafting parameter was increased by the cycled rejuvenation. The extending last step to 60 hours rejuvenation (RT4) is currently the best rejuvenation based on the microstructure and chemical segregation results. It not only restored the microstructure back to the as-received condition, but also massively reduced the chemical segregation resulting from previous degradation. The mechanical performance of the sample after RT4 is discussed in the following section, to establish whether the reduced chemical segregation will help in the recovery of mechanical performance.

7.4 Mechanical Tests

This section describes long term creep tests which were carried out on samples before and after modified rejuvenation (RT4) heat treatments to compare and evaluate their performance. RT4 is the most promising rejuvenation heat treatment based on the microstructure and chemical segregation reported in section 7.3. Long term creep tests were performed at a temperature of 982°C and a stress of 167 MPa, as detailed in Chapter 3. The creep tests were carried out at two different testing companies, E.ON and EXOVA. In order to ensure that the creep results were comparable, the as-received (S1) sample was tested at

each of the testing companies. Table 7.8 illustrates the long term creep test results for the different heat treated samples. S1 has a creep rupture life of 1178 hours (E.ON) and 1141 (EXOVA), which are both in good agreement with each other and with the literature. The reported creep rupture life for virgin CMSX-4 is about 1000 hours [7]. The similar creep rupture life of the two testing companies shows that the creep data are repeatable and comparable. The creep rupture life of S2 is significantly reduced compared to S1 (807 hour), since it has been degraded through a rafting procedure. The high temperature rejuvenated sample, S3, exhibits a slighter better creep life than the as-received (S1) sample. The modified rejuvenated samples, New S3, shows a creep rupture life of 1174 hours, which is slightly worse than S3 but is the same as S1. These results indicate that the improved chemical segregation does not appear to increase the mechanical properties of the materials under the test conditions used here. However, the creep rupture time for these rejuvenated samples after subsequent rafting heat treatment is virtually the same, 804 hours for S4, and 780 for New S4. The result indicates that the modified rejuvenation (RT4) did not appear to improve the mechanical performance. Therefore, this suggests that the chemical segregation may not influence the mechanical performance of samples under the testing conditions used in this research. However, this test condition is still too short for a long term creep test applied in industry, therefore in order to confirm the performance of these heat treatments, it is suggested that long term creep test should be completed in future. The sample did not contain chemical segregation which may be beneficial for longer term creep behaviour.

Table 7.8 Long term creep tests results of different heat treated samples

Sample No	Heat Treatments	Creep Life (h)	
		E.ON	EXOVA
S1	As-received	1187	1141
S2	Rafted	X	807
S3	Rafted + HT Rejuvenation	1291	
New S3	Rafted + RT4		1174
S4	Rafted + HT Rejuvenation + Rafted	804	
New S4	Rafted + RT4 + Rafted		780

7.5 Summary

In this chapter, the chemical segregation as one of the possible reasons for the faster degradation of rejuvenated samples during subsequent rafting has been examined. The results suggest that although the high temperature rejuvenation does restore the microstructure back to the as-received conditions, the chemical segregation resulting from degradation still remains. The residual chemical segregation was pronounced in the second rafting and caused a reduction of the mechanical performance. This problem was under consideration and therefore four different rejuvenation trials were designed and applied to further reduce the chemical segregation. With the help of analysing the rejuvenation heat treatment after application of the different stages, the best modified rejuvenation RT4 has been developed. RT4 not only restores the microstructure, but also massively recovers chemical segregation, to a level similar to those observed in the as-received condition. Later long term creep tests were applied, the results show that the modified rejuvenation (RT4) has not help to improve the mechanical performance as much as expected under that test condition, which may suggest

that the small chemical segregation present within these samples does not have significant effect on the mechanical properties. However, these results were only based on one test, therefore more mechanical tests should be needed for draw a more convinced conclusion about the influence of chemical segregation on mechanical performance.

CHAPTER 8

REJUVENATION OF AN EX-SERVICE BLADE

8.1 Introduction

According to the results given by the previous mechanical tests and described in Chapter 5 and 6, the high temperature rejuvenation heat treatment performed well in recovering of microstructure and mechanical properties of laboratory cylindrical bar specimens. However, although care was taken to recreate service-like conditions, real industrial gas turbine components are exposed to more aggressive conditions compared with laboratory work. The laboratory bar specimens were simple cylindrical shapes and isothermally aged in a controlled furnace at temperatures and exposure lengths representative of service conditions. Turbine blades have more complex shapes and design, and they experience more aggressive service conditions, and additionally the stress across gas turbine blades are not uniform with aggressive gas environments, which can cause corrosion and oxidation problems during service. Therefore, it necessary to compare controlled laboratory work to a real industrial component after service to help understand how high temperature rejuvenation will work on a large scale industrial service blade. In this chapter, the results of detailed dimensional change measurements of an ex-service blade during rejuvenation will be presented and discussed, followed by microstructural characterisation of the cross-sections from different heights and other features within the blade. Surface deformation caused by rejuvenation heat treatment was also investigated in this chapter.

The blade investigated is a 1st stage high pressure blade from an Alstom GT-26 industrial gas turbine engine used for power generation, which had been service for 24,063 hours. The substrate of the blade was a CMSX-4 single crystal Ni-based superalloy with the nominal chemical composition shown in Table 3.1. The blade was coated with a typical thermal barrier coating (TBC) system, including a NiCoCrAlY bond coat, a service grown thermally grown oxide (TGO) and a ZrO_2 top-coating. The NiCoCrAlY bond coating contained about 30 wt.% Co, 11.5 wt.% Al and 13.0 wt.% Cr. The detail of the coating composition is shown in Table 8.1. The bond coating was applied by low pressure plasma spray (LPPS), with a thickness of ~300 μm. After the coating was applied, this blade underwent a standard heat treatment, which consisted of a hold at 1140°C for 6 hours followed by 870°C for 20 hours, to enhance the initial bonding between with TGO and ceramic top coating [1-2]. In order to determine the viability of rejuvenation heat treatment, it is necessary to determine the dimensional stability of the whole blade during rejuvenation heat treatment. Therefore, after service, the TBC system was removed from the blade and the rejuvenation heat treatment was applied, followed by microstructural characterisation. In order to retain the structure of the blade for rejuvenation, it was not possible to examine the ex-service microstructure. However, since laboratory bar specimens have shown similar microstructural evolution of the γ/γ′ during simulated service conditions, which can be used to represent the microstructure of blade after service. A variety of experimental techniques have been used in the study of the rejuvenated blade. The dimensional change of the blade during rejuvenation was examined using white light scan, by measuring the surface positions of the blade before and after high temperature rejuvenation heat treatment. The microstructures of the blade after rejuvenation were examined using the field emission gun scanning electron microscopy (FEGSEM) and transmission electron microscopy (TEM), followed by the energy dispersive x-ray

spectroscopy (EDX) for chemical analysis.

Table 8.1 The chemical composition of the NiCoCrAlY bond coating

Elements	Al	Co	Cr	Si	Y	Ni
Wt.%	11.5	30.0	13.0	1.2	0.3	44.0

8.2 Dimensional Changes of Blade during Rejuvenation

Alstom's high performing advanced class GT24/GT26 gas turbines deliver the high efficiency, exceptional availability and lower environmental impact due to its excellent design and manufacture [1]. It requires extreme care to ensure that any rejuvenation heat treatment does not produce any dimensional changes beyond design tolerances as these will later affect the whole engine's performance [1, 3, 7]. In this section, the dimensional changes of blade during rejuvenation were examined. Figure 8.1 shows a white light scan image of the ex-service turbine blade before and after high temperature rejuvenation. Before rejuvenation (Figure8.1a), the blade was in excellent condition, although the top tip of the trailing edge was damaged, which was later revealed to be a marker applied by the engine operator to indicate that the blade is to be scrapped. Figure 8.1b illustrates the dimensions of the blade after rejuvenation, where a number of surface deformations are visible, with a number of large protrusions observed on the aerofoil and another found at the top of right hand root, and a few "wrinkles" observed near the root. During the high temperature rejuvenation heat treatment, the blade was laid on its leading edge and root without additional support. The surface deformation may have been caused by large weight of the blade at the rejuvenation heat treatment. Within the exception of these defects, the rest of the blade was in excellent condition. The shape, surface and internal cooling

channels were well preserved. Figure 8.2 shows a dimensional comparison of the blade before and after rejuvenation, indicating that the majority of the blade has dimensional differences of less than 0.4 mm after rejuvenation, except the protrusions, which show ~ 1.0-2.0 mm of dimensional difference. It has been found that the pressure side shows more dimensional changes compared with the suction side since which may be a result of the conditions experienced during service. The root of the aerofoil shows more dimensional changes compared with tip of the blade, although the tip of the aerofoil experienced higher temperature and stress during rejuvenation [87-90]. This is because, the blade was laid down on its leading edge and root during heat treatment, therefore the root of the aerofoil experienced more stress, resulting in more dimensional changes recorded during the white light scan. All of these dimensional changes (except for the major surface protrusions) were about 0.4 mm within the tolerances of the blade for the refurbishment, which suggests that at the temperatures experienced for rejuvenation, the blade is dimensionally stable [7]. However, care must be taken with a support system required for handling these large scale industrial gas turbine blades without imparting additional stresses during the very high temperature exposure of the rejuvenation heat treatment.

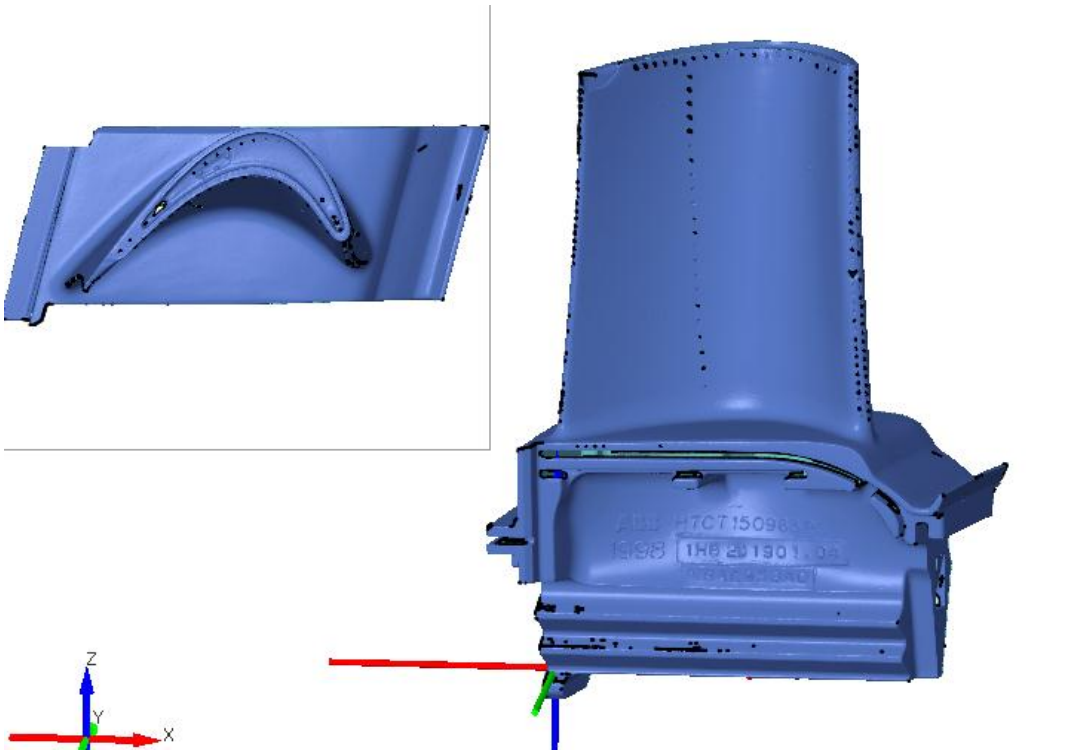

(a)

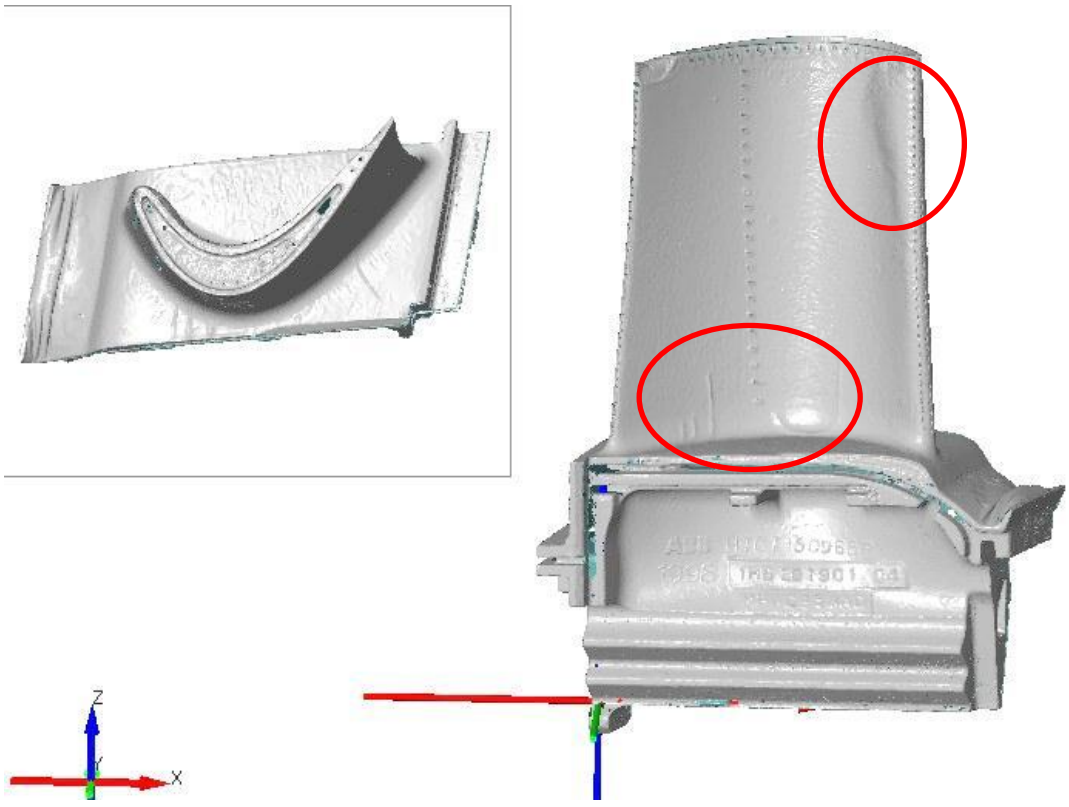

(b)

Figure 8.1. White light scan results of the ex-service gas turbine blade before (a) and after (b) high temperature rejuvenation, showing surface protrusions.

Figure 8.2. Dimensional comparisons of the ex-service run turbine blade before and after high temperature rejuvenation, showing top view, pressure side view and suction side view of the blade.

8.3 Microstructural Examination of Blade's Sections

This section will present and discuss the results of the microstructural investigations carried out on the ex-service blade. In order to examine the impact of the rejuvenation heat treatment on different blade locations, cross-sections were taken at 1/3, 1/2 and 2/3 height of the aerofoil of the blade, defined as sections 2, 4 and 6 respectively and characterisation was carried out at various positions around the aerofoil of the sections, to encompass any microstructural difference between different heights and positions within the blade. Figure 8.3 shows a schematic diagram of where the cross-sections were extracted.

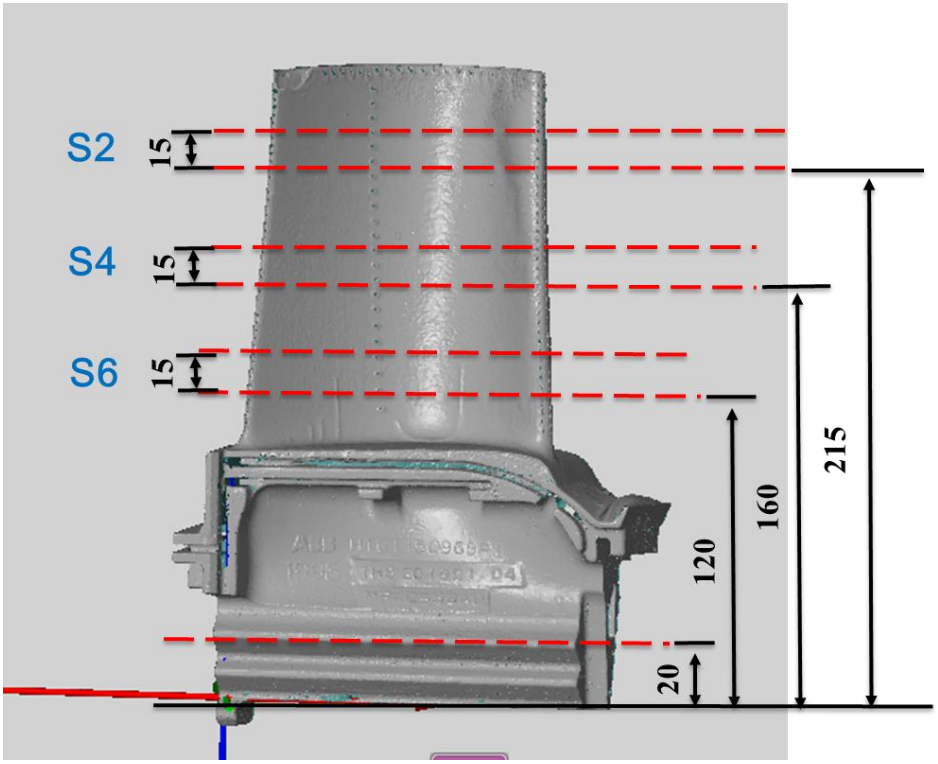

Figure 8.3. Schematic diagram of a service run gas turbine blade, showing the cut cross-portions (section 2, 4 and 6) were extracted (measurement are in mm).

Figure 8.4 shows the overall structure of the coated blade after rejuvenation, which contains three different regions: a surface region probably originating as an effect of the past coating, an oxidation region adjacent to the cooling channels and the γ/γ′ region. Since the blade had a coating in place during service, the external surface of the blade has been affected by the coating which leaves a region ~ 300 μm near the external surface with an altered microstructure. This region contains β (NiAl), small γ′ particles (0.2-0.5 μm) and a few MX particles within the microstructure, shown in Figure 8.4a. Another interesting region was observed near the internal surface of cooling channels within the blade, shown in Figure 8.4b, where Cr_2O_3 and Al_2O_3 oxides were formed. The oxide scale in the surface has a thickness ~ 50 μm, which was caused by long term exposure to the combustion gas working environment

during service. Therefore, this region was named the oxidation region. The region affected by the past coating and the oxidation regions only extend a few hundreds microns from the surface of the blade, and the majority of the blade is still dominated by the γ/γ′ region, where the microstructure shows a uniform distribution of cuboidal γ/γ′ structure with a few MX particles. In this research, the focus has been on the changes in γ/γ′ size, distribution and morphology during rejuvenation. Therefore, in this section, investigations were carried out on the microstructures taken from the centre of γ/γ′ region. The microstructural characterisation of the other two regions will be discussed in the section 8.4.

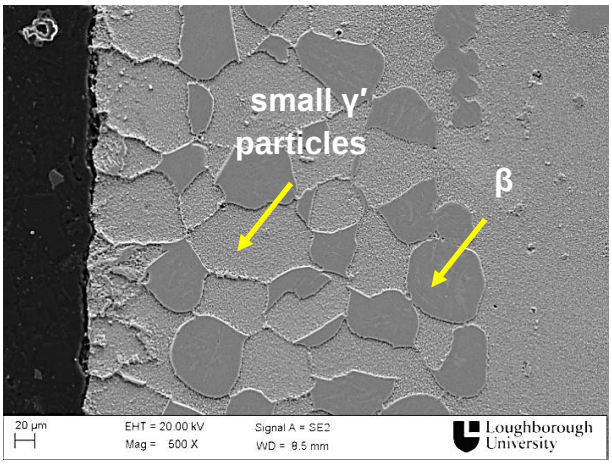

(a) Region affected by past coating

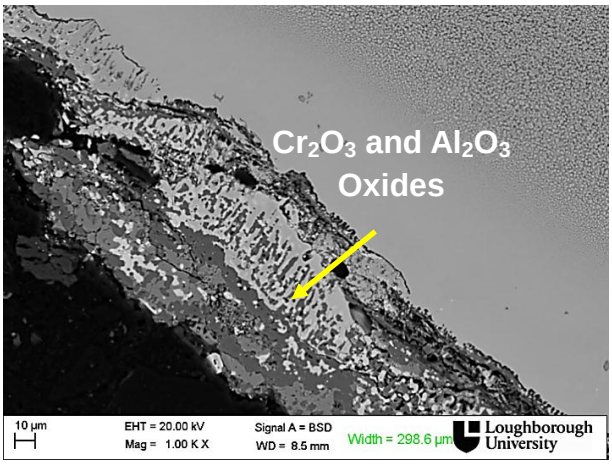

(b) Oxidation region

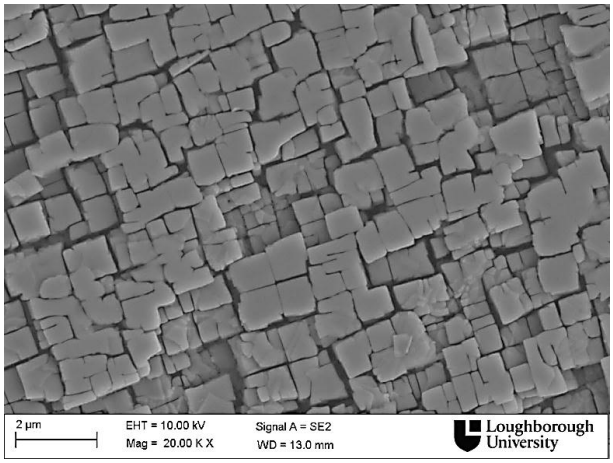

(c) γ/γ′ region

Figure 8.4. SEM images illustrating overall structure of the three different regions in the coated blade after rejuvenation: (a) Region affected by past coating, (b) Oxidation region, (c) γ/γ′ region

Figures 8.5, Figure 8.6 and Figure 8.7 show representative microstructures of the centre area of the γ/γ′ region of blade section 2, 4 and 6, which were taken from 1/3, 1/2 and 2/3 the height of the aerofoil of the blade respectively. The suction side, pressure side, leading edge and trailing edge are shown as labelled. Generally, the microstructures of the different sections are similar to each other. All of them show a uniform distribution of “cuboidal” γ′ particles with a size ~0.5-1.0 μm. However, this “cuboidal” structure is not the same as found in experimental bar specimens. The γ′ particles were found to have curved and star shaped edges. In some regions, “flower” shaped and irregular γ′ particles were also found. The likely reason for this phenomenon is that when the blade experienced a long service run, with non-uniform stress and temperature distribution, this leads to a difference in rafting rate and γ′ orientation in different places within the microstructure and results a different shape, size and distribution of γ′ particles after service. Although high temperature rejuvenation is capable of restoring the degraded microstructure to the original conditions for the laboratory bars, the temperature and stress distribution are different in this large scale industrial blade, which causes a non-uniform recovery and results in a formation of the cuboidal and irregular γ′ particles within the microstructure. Spherical tertiary γ′ precipitates have been found in the channels of all blade locations, with a size ~ 20-30 nm. Typical high magnification images showing the morphology and size of tertiary γ′ in the channels are shown in middle of Figure 8.5, Figure 8.6 and Figure 8.7. The morphology and size of the tertiary γ′ have a good agreement with those observed in cylindrical bar specimens. The similarities in the microstructures of section 2, 4 and 6, indicate the position along the blade’s length has little or no influence on the effectiveness of the rejuvenation heat treatment applied.

In order to examine the effect of the position around the blade aerofoil on the rejuvenation process, different samples were taken from positions around the section and microstructural investigation were carried out on these seven samples, shown in Figure 8.5, Figure 8.6 and Figure 8.7. In each section, the microstructures are similar. However, if the microstructure is examined in more detail, the leading and trailing edges have a more degraded microstructure when compared to the microstructure observed in the centre of the blade. Both of them have an increased amount of star shaped and irregular γ′ particles in the microstructure. This is because the leading and trailing edges experienced more thermal exposure, stress and erosion during service, which causes more degradation and results in a more degraded structure within it. This difference is more pronounced in P7 of section 2, where the large protrusion was caused during high temperature rejuvenation heat treatment. That damage causes a more degraded microstructure within the sample, and results an even increased amount of the irregular secondary γ′ particles and broader channels in the γ/γ′ region. Detailed results are presented from the image analysis, later in this section. However, all of these differences in size and morphology are very small and the generally similar microstructures of these samples indicate that the rejuvenation is not significantly influenced by the aerofoil position within each section.

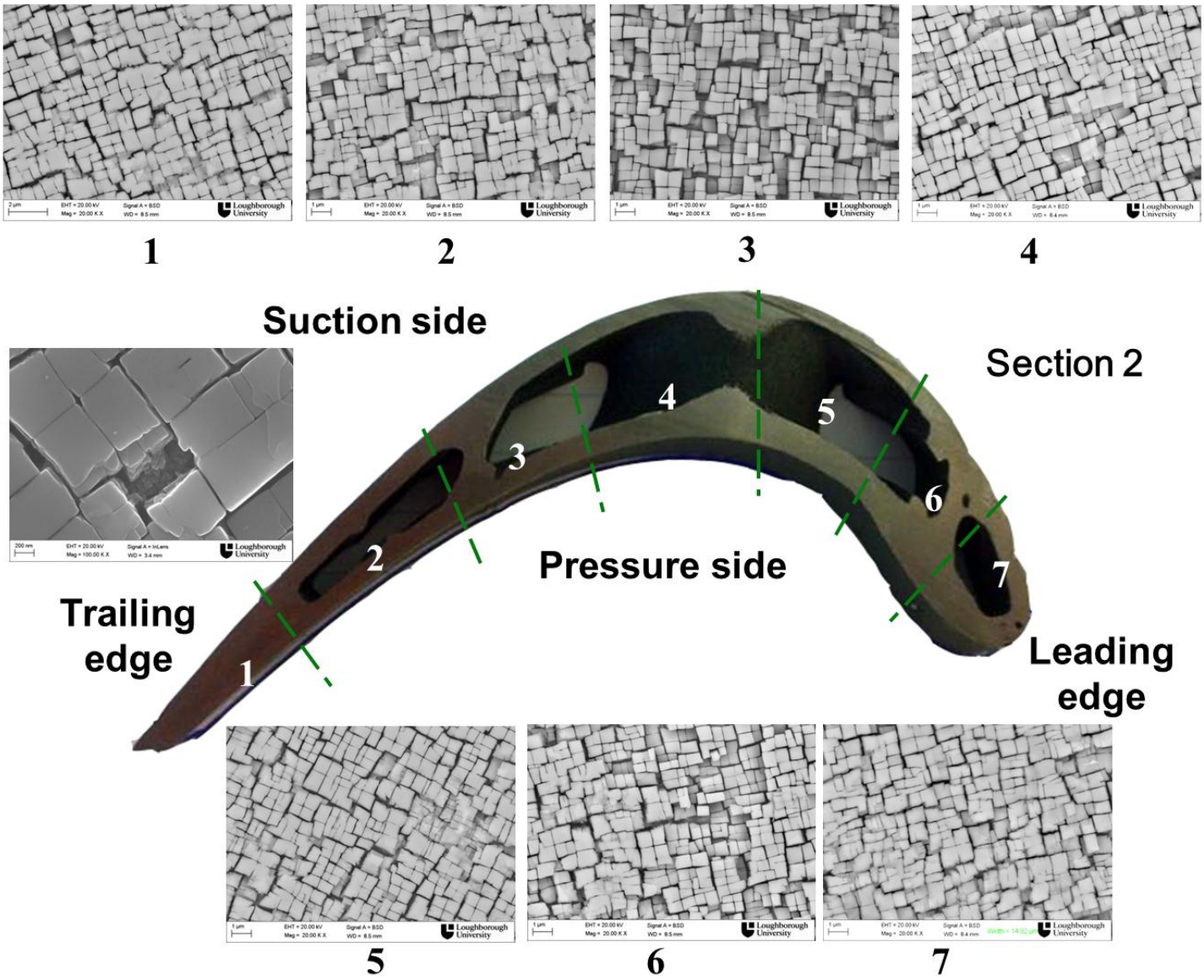

Figure 8.5. SEM images showing the microstructures of centre area of γ/γ′ region for each point taken from the section 2

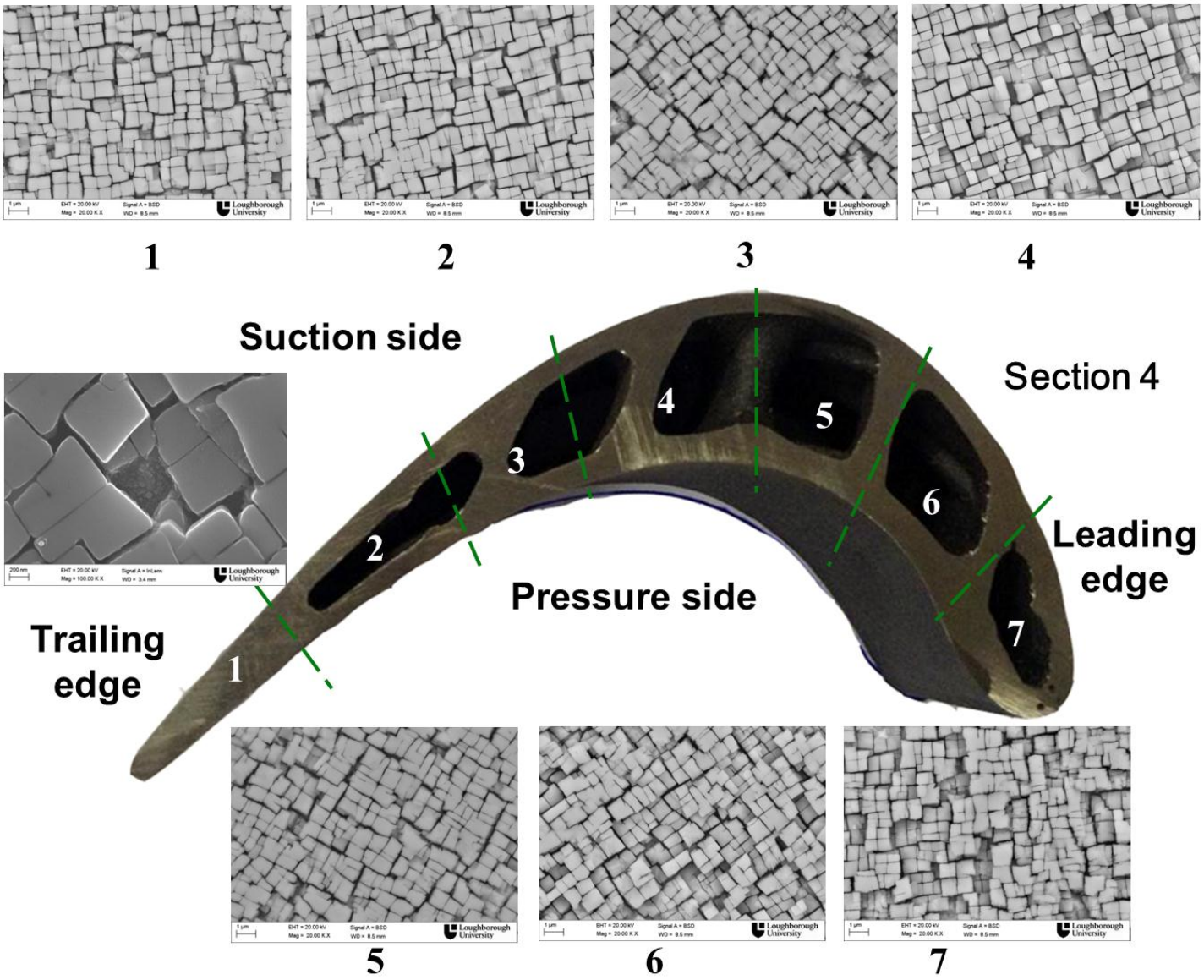

Figure 8.6. SEM images showing the microstructures of centre area of γ/γ′ region for each point taken from the section 4

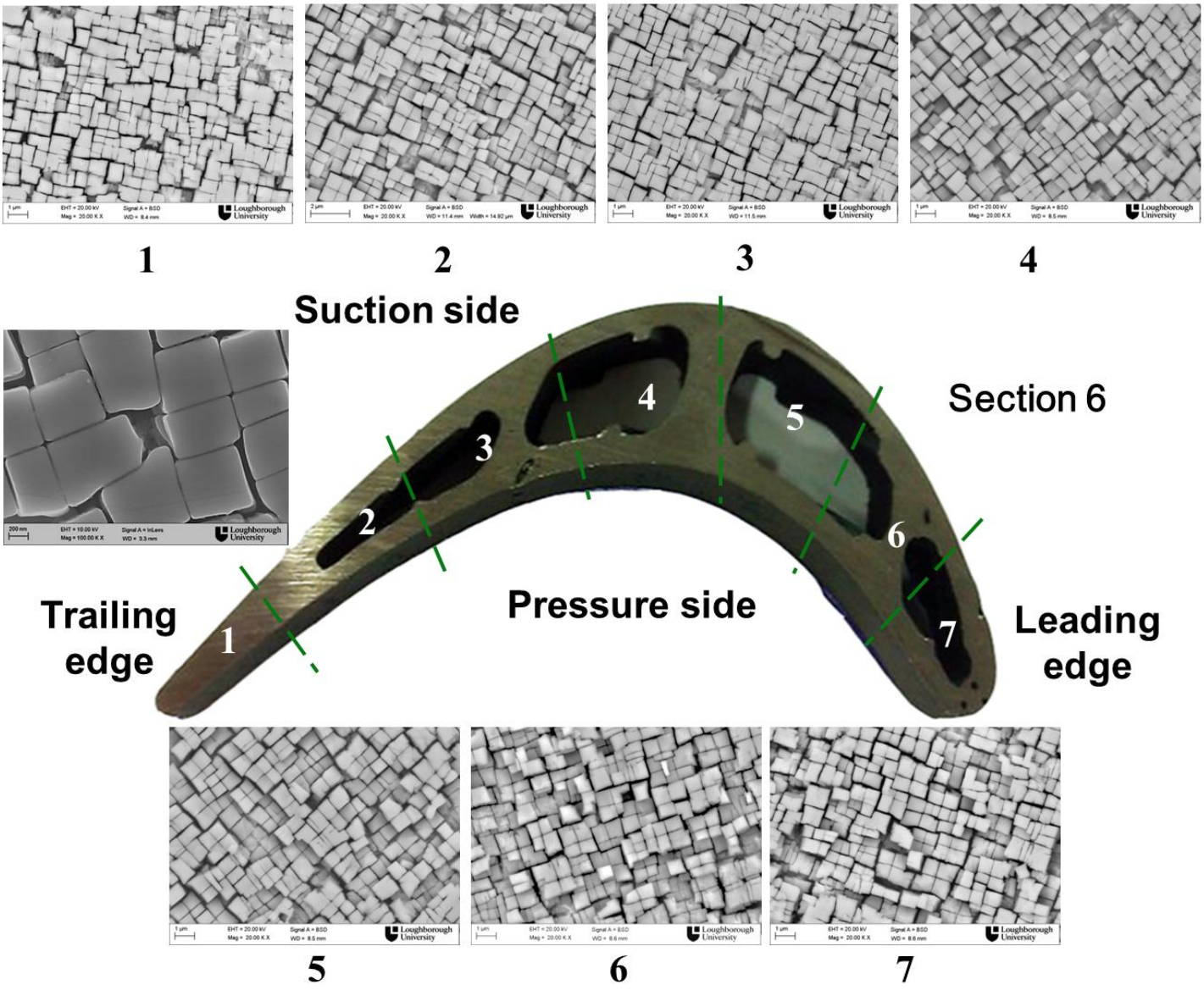

Figure 8.7. SEM images showing the microstructures of centre area of γ/γ′ region for each point taken from the section 6.

Image analysis (area fraction of secondary γ′ particles and γ channel width) was carried out on these samples, to provide a detailed microstructural comparison of the samples after rejuvenation. Figure 8.8 show the area fraction of secondary γ′ particles for blade sections 2, 4 and 6 respectively. In each section, the area fractions of secondary γ′ (from P1 to P7) are very similar to each other. However, when compared in more detail, take section 4 for example, the leading edge (P7) and trailing edge (P1) experienced more degradation during service [7], which results in a slightly lower area fraction of secondary γ′, 0.86 and 0.87 respectively, when compared to middle of the blade, P4 (0.89). The same trend has found in sections 2 and section 6. However, this small difference will not significantly influence the mechanical properties of the blade.

The γ channel width measurements are also shown in Figure 8.8. The γ channels in blade section 2, 4 and 6 are ~ 60 nm in both parallel and perpendicular directions. Again, since the leading and trailing edges have experienced more degradation, the results show a slight increase in the size of the γ channel in the measurements although these are within experimental error. Take the parallel channel of section 4 for example, the channel widths are relatively larger in P7 (65 nm) and P1 (61 nm) when compared to P4 (58 nm).

In summary, the area fractions of secondary γ′ and γ channel width measurement have a good agreement with the microstructural examination. Although the leading and trailing edges have experienced higher temperature and stress, the image analysis results show very similar values to the centre part of the blade, and only a small amount of reduction in area fraction of secondary γ′ particles and slighter broader γ channel width has been found there. The results indicate that the impact of rejuvenation on microstructural recovery has a small dependence on the position and height difference throughout the blade.

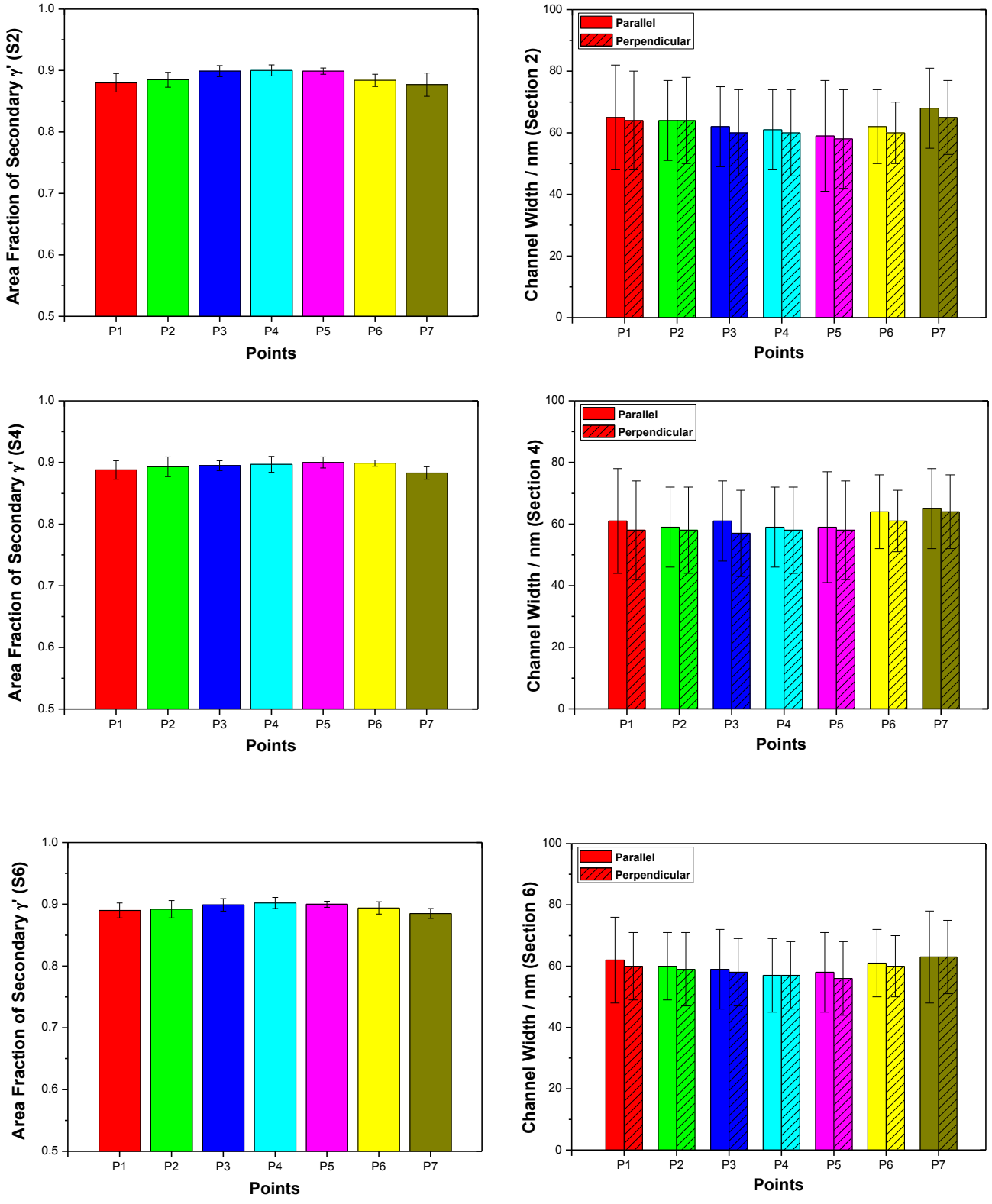

(a) Area Fraction **(b) Channel Width**

Figure 8.8. Image analysis results of blade sections 2, 4 and 6: (a) area fraction, and (b) channel width measurements.

8.4 Comparison of Blade and Bar Specimens

In the previous sections, the results showed a uniform recovery of the blade microstructure, with only a small influence of position and height difference. However, the microstructural differences between rejuvenated laboratory cylindrical bar specimens and the complex industrial turbine blade still require comparison. In order to provide an understanding of these differences, the microstructures of the bar and blade samples after rejuvenation will be compared and discussed in this section, followed by microstructural analysis.

Figure 8.9 shows SEM images of the microstructures of the head portion of the rejuvenated tensile specimen and sections 2, 4, and 6 of the rejuvenated ex-service blade. In order to minimise the influence of the stress and variable temperature, and make a reasonable comparison between blade and bar sample, only the microstructure of the middle parts (P4) of each section are presented for comparison. The results illustrate that microstructures of the blade are still very similar to the microstructure observed in the tensile specimen. They exhibit a uniform distribution of secondary γ′, with a size of 0.5-1.0μm, which is only a minor increase when compared to the tensile specimen, the size of which is ~ 0.5 μm. For the rejuvenated blade, the morphology of the secondary γ′ particles is very close to a cuboidal structure, although some irregular γ′ particles were also observed within the microstructure. The larger secondary γ′ and presence of irregular γ′ particles may result from non-uniform stress and temperature distribution within the blade during service and rejuvenation. However, the secondary γ′ found in the blade has a good agreement with bar specimens both in size and morphology. In high magnification images, shown in Figure 8.10, fine (<30 nm) spherical tertiary γ′ precipitates were found in the γ channels of both the blade and bar specimens after rejuvenation. It is difficult to give quantitative results of the amount of tertiary γ′ within the microstructure,

since they have same appearance as secondary γ′ particles. However, although the presence of these particles is at the expense of secondary γ′, they are beneficial to the mechanical properties [4-6]. These results indicate that the high temperature rejuvenation restores the microstructure back to an excellent condition, no matter the size or complexity of the shape of the specimens used.

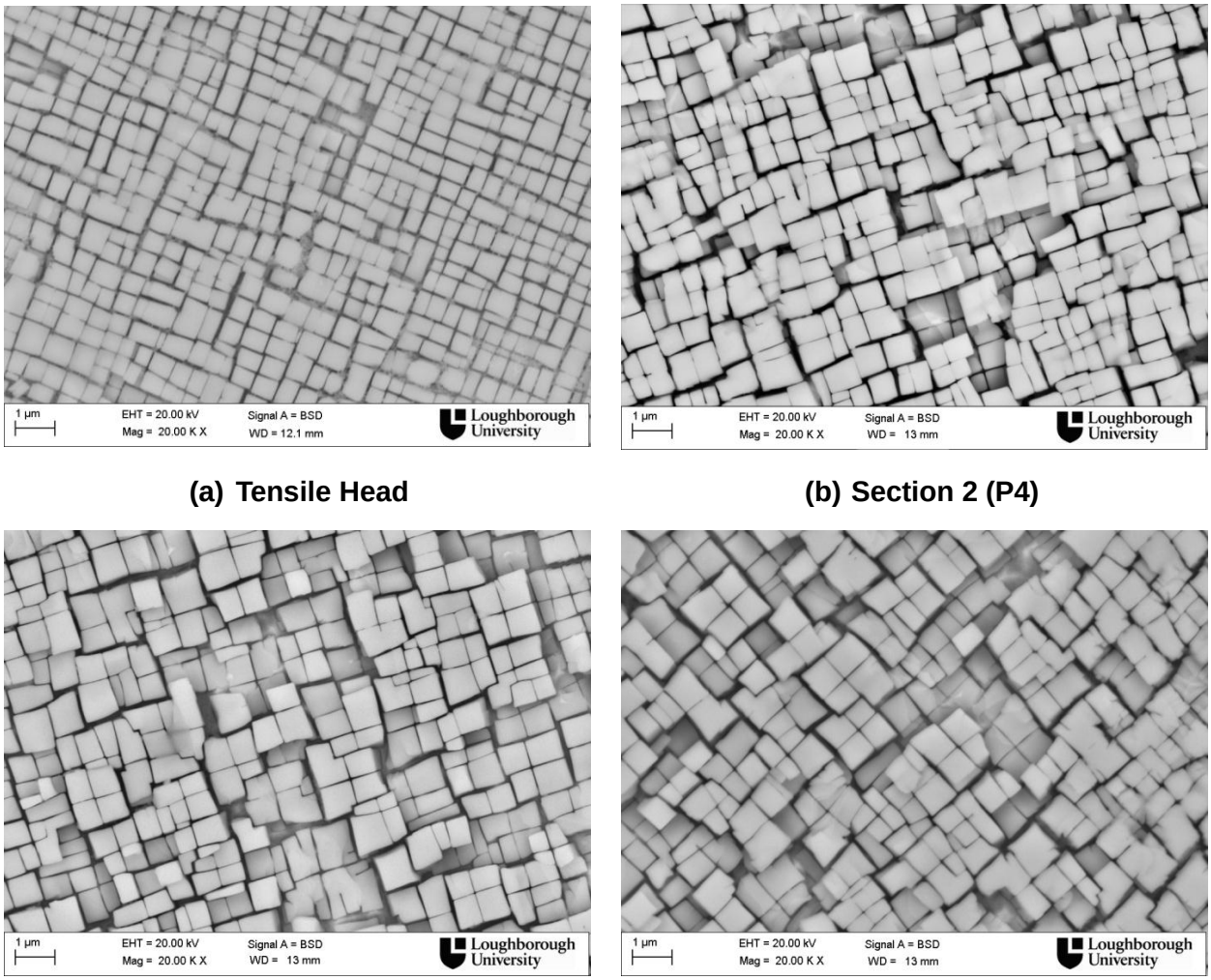

(a) Tensile Head **(b) Section 2 (P4)**

(c) Section 4 (P4) **(d) Section 6 (P4)**

Figure 8.9. Low magnification SEM image showing the microstructure of (a) tensile head and (b-d) blade sections 2, 4 and 6 respectively after same rejuvenation.

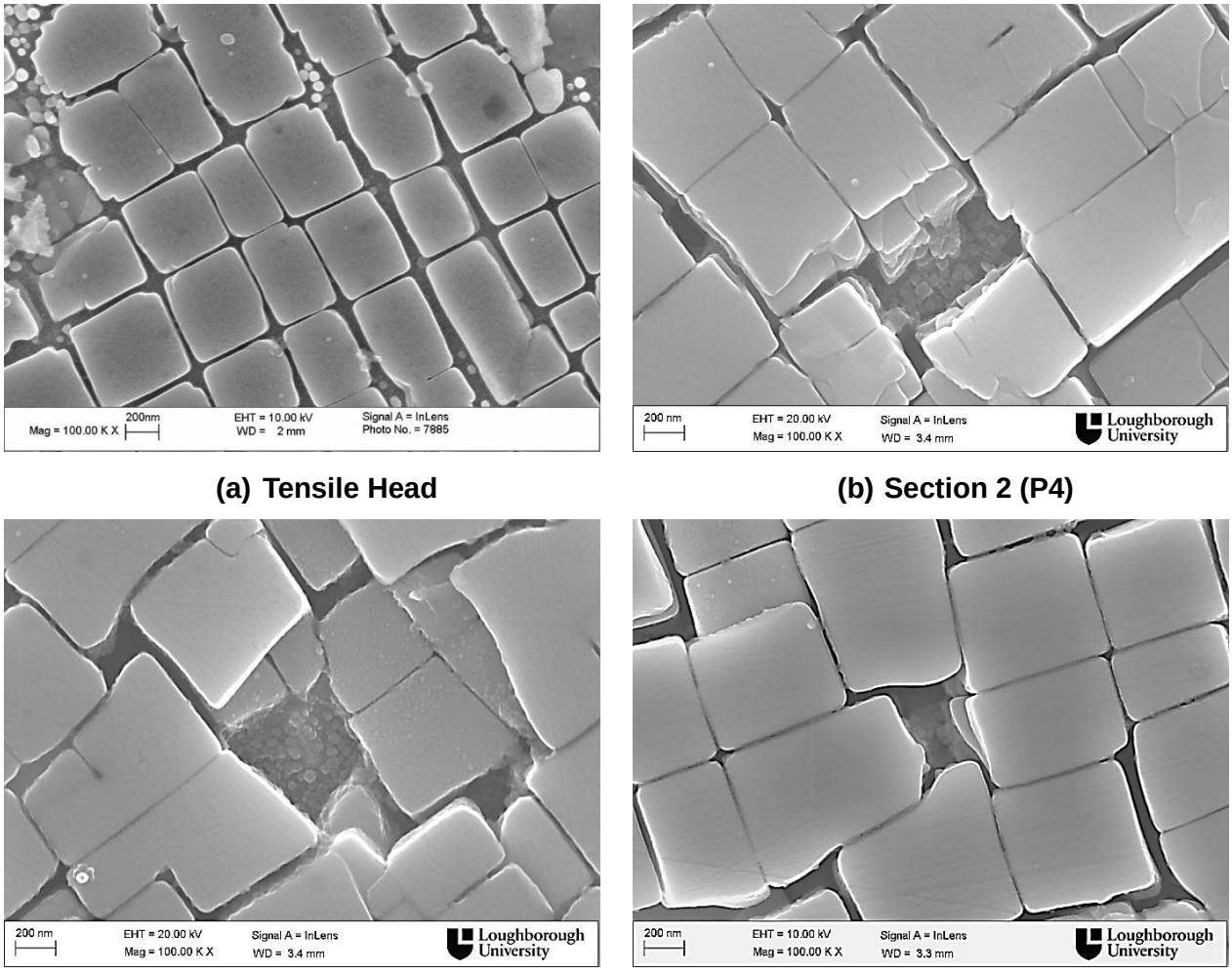

(a) Tensile Head **(b) Section 2 (P4)**

(c) Section 4 (P4) **(d) Section 6 (P4)**

Figure 8.10. High magnification SEM image showing the microstructure of (a) tensile head and (b-d) blade sections 2, 4 and 6 respectively after same rejuvenation.

The microstructures of bar specimens and blade sections were further examined using image analysis, the results of which are shown in Table 8.2. For the blade, the average values of area fraction of secondary γ′ particles and γ channel widths were used for this comparison. In Table 8.2, the head of tensile specimen has an area fraction of secondary γ′ particles of ~ 0.851. However this is probably an effect of the irregularly shaped γ′, which increases the visibility of an underlying layer of γ′. The area fractions of secondary γ′ in the blade have increased relative to the tensile head to 0.879, 0.885, and 0.887 for sections 2, 4

and 6 respectively. However, this 3-4% difference between the bar specimens and blade is unlikely to significantly influence the mechanical performance of the sample. The same comparison was carried out on the γ channel widths, where the head of the tensile specimen is about 60 nm in parallel direction, and 59 nm in the perpendicular direction. These small channels will inhibit the movement of dislocations and make it difficult for the dislocation to pass through the structure, resulting in a higher strength and creep resistance in the material [6]. The channel width for the blade is ~ 61-63 μm in parallel direction and 59-62 in perpendicular directions.

Table 8.2 Image analysis summary of tensile and blade portions

Sample ID	Area Fraction of Secondary γ′	Channel Width (nm)	
		//	⊥
Head of Tensile	0.851±0.009	60±13	59±10
Blade S2	0.879±0.011	63±14	62±13
Blade S4	0.885±0.010	62±13	61±11
Blade S6	0.887±0.011	60±13	60±12

This section provides useful information for a complete comparison of a rejuvenated bar specimens and the rejuvenated blade. The microstructure and microstructural analysis results showed very consistent findings. The similarity between the microstructures suggests that knowledge of the laboratory bar specimens can be directly related to the microstructure of the blade's degradation, rejuvenation and refurbishment.

8.5 Other Blade Features

There were three different regions found in the rejuvenated blade, which were reported in section 8.3, which are areas affected by the past coating, the oxidation region and the bulk γ/γ′ region. The microstructural investigation of the γ/γ′ region has been discussed in detail in the previous section. In this section, the microstructure of the other two regions will be presented and discussed.

8.5.1 Region affected by the past coating

The substrate had been affected by the presence of the coatings through chemical interdiffusion during service, resulting in an affected region with a thickness of ~300 μm on top of the substrate. The microstructure of this affected region is shown in Figure 8.11, which comprises a four phase structure: islands of β (NiAl), γ′(Ni_3Al), γ(Ni) matrix and a number of MX particles. The islands of β phase appear dark-grey when imaged using backscattered electrons. These islands are observed throughout the external surface of this region and exist in various sizes, but most of them are larger than 10 μm, see Figure 8.11c. Chemical analysis of the β phase, shown in Table 8.3, indicates that they contain high concentrations of Al ~16 wt.%, Co ~15 wt.% and Ni ~57 wt.%, which are in close agreement to literature values [4]. In a NiCoCrAlY bond coating system, the β phases are regarded as an Al reservoir, enabling the formation of protective oxide scale at the coating surface [1, 2, 5]. In the matrix, star shaped γ′ particles were finely dispersed with a size of 0.3-0.5 μm throughout this region. The chemical analysis shows they are rich in Ni ~ 56.6 wt.%, Al ~7.0 wt.%, and Co ~14.6 wt.%, which has a close agreement with the chemical composition of γ′ in the γ/γ′ region and the thermodynamic calculations reported in Chapter 4, but with a higher Co concentration, which results from the diffusion of Co from the

bond coating towards substrate. Near the β phase, some large blocky γ′ particles were observed associated with the β phase, which are eutectic (primary) γ′. The microstructure indicates that the large eutectic γ′ are decomposing and tending to form smaller (secondary) γ′ particles, shown in Figure 8.11b and Figure 8.11c. In Figure 8.11c, the edge of island β particles has the same appearance as the star γ′ particles. The chemical analysis shows they contain high concentration of Ni, Ta and Al, which has a good agreement with γ′ in the matrix. The chemical composition, shown in Table 8.3, suggests there is no difference between eutectic γ′, star shaped γ′ and γ′ on β-particle edges.

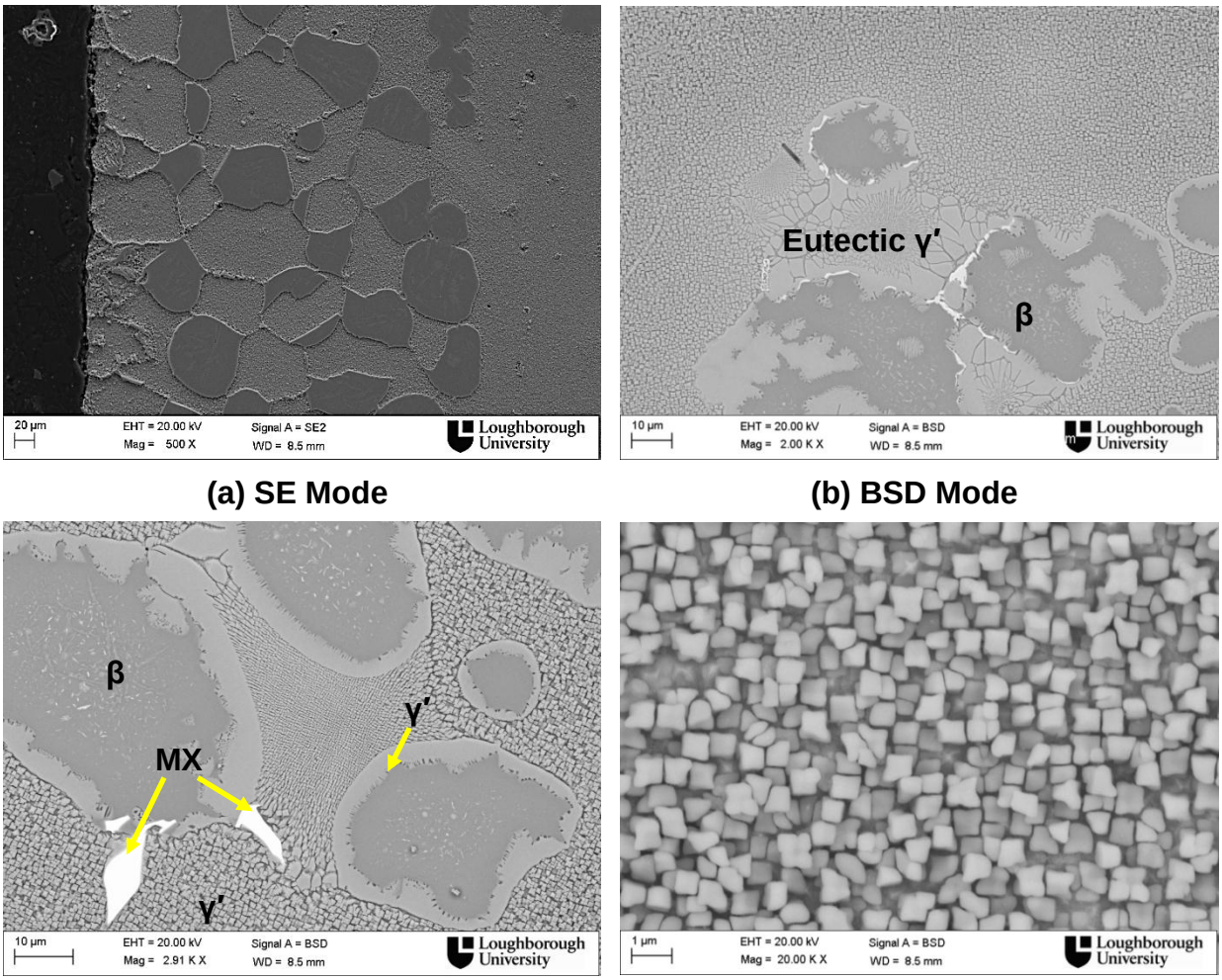

(a) SE Mode **(b) BSD Mode**

(c) β, γ′ and MX **(d) γ′ particles**

Figure 8.11. SEM image of the region affcted by the past coating, (a) SE mode, (b)BSD mode, (c) size and morphology of β, γ′ and MX carbides and (d) high magnification of γ′ particles

The decomposition of the eutectic γ′ into secondary γ′ indicates that this region has locally melted during the rejuvenation heat treatment. The presence of the large amount of β phase indicates that the Al concentration was high in this region due to the interdiffusion of Al from the coating system. Therefore, one possible reason for this phenomenon is that the enrichment of Al in this region locally reduces the melting temperature of this region and results in local melting and formation of β phase in this region [6]. In order to confirm this assumption, the Al sensitivity of the melting temperature of CMSX-4 was calculated using an MTDATA isopleth, where the concentration of Al started from the nominal substrate composition (5.7 wt.%) and ended at the concentration of the previously applied coating (11.5 wt.%), the expense of Ni. The isopleth plot is shown in Figure 8.12, where it can be see that the melting temperature or solution temperature is about 1380°C for the nominal substrate Al concentration.

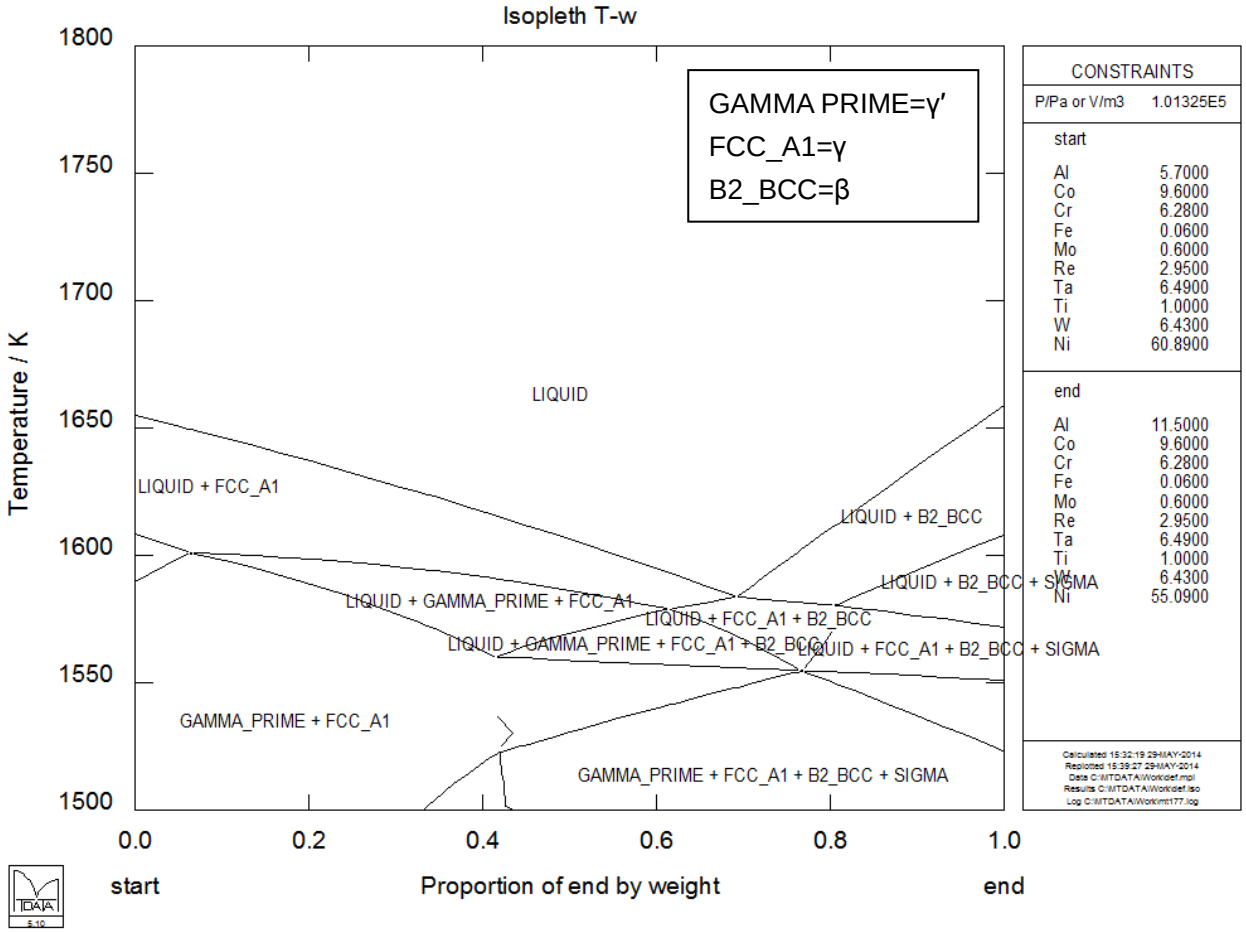

Figure 8.12. Phase diagram of the Ni-alloy with Al concentration increasin g from 5.7 wt.% to 11.5 wt.% by MTDATA Isopleth Calculations, showing Liquid, β, γ′, γ and some TCP phases.

The melting temperature of the system decreases with increasing Al concentration and the liquid and γ phases are formed. The minimum melting temperature is predicted to be 1309°C at a concentration of 9.5 wt.% Al. When the Al concentration further increases, the β phase starts to form and the melting temperature is predicted to increase. The melting temperature is at its maximum of 1400°C when the Al concentration reaches the composition of the bond coating. However, over the majority of the chemical ranges studied, the melting temperature is predicted to be below the rejuvenation heat treatment temperature applied to the blade. This result indicates that the melting temperature is very sensitive to the Al concentration and the Al rich layer formed

through interdiffusion from the coating reduces the melting temperature of top surface of substrate, which later leads to dimensional changes of the surface and causes the formation of β rich microstructure within the surface. Therefore, for a coated industrial ex-service blade, an additional removal process of the Al rich layer from the surface of substrate is required, in order to avoid melting and dimensional changes of the blade.

Large, light particles within average size of 2-3 μm were observed throughout the whole of the sample in Figure 8.11. Most of them were found together with β phase within the surface region of the blade. The bright appearance of these particles suggests they contain heavier chemical elements. Chemical analysis of these particles found them to be rich in Ta and Ni with approximately 78 wt.% and 3 wt.% respectively. The detailed chemical composition of these particles is shown in Table 8.3. The chemical composition of these particles indicates that they are MC carbides [11-15]. MC carbides are known to form in the molten state and therefore are invariably “frozen” in the microstructure. It has been reported that MC carbides with a high Ta content do not break down easily during solution heat treatment [11-15]. This is consistent with thermodynamic equilibrium calculations, showing the MC is stable until the temperature goes to 1400°C, see Figure 4.1. The MC carbides were further confirmed by TEM chemical analysis and diffraction, the result of which is shown in Figure 8.13. The literature and diffraction pattern show the MC is face-close packed structure. Selected area diffraction and EDX analysis enabled the identification of the MC as the MC particles was observed to have a lattice parameter of a_0= c_0=4.43 Å, which is consistent with literature data (a_0=4.45 Å) [6-7].

The MC particles, which were found everywhere within the blade, had a chemical composition which indicated that the M was Ta, Ti and Hf. The

presence of Ti and Hf indicates that they may be a result of outward diffusion from the substrate into coating. However, results shown in Chapter 4 have indicated that the 0.0022 wt.% carbon present within the substrate alloy does not allow the formation of MC or $M_{23}C_6$ carbides in the bulk of the blade. Therefore, it is possible that carbon was introduced into the system during the coating processes. In order to confirm the source of carbon, the MC distribution of three different regions was examined using image analysis, where MC was used to represent the carbon concentration, since MC carbides are stable once when they formed and would not decompose during service and rejuvenation [6]. Table 8.4 shows the area fraction of MC taken from 15 randomly collected images taken from three different regions of the rejuvenated blade. The results show that the amount of MC within the microstructure is highest (3.9%) at the outer region of the blade and decreases to 3.2% at the γ/γ' region and further decreased to 1.0 % at oxidation region. The decrease of MC from external surface to the internal surface indicates that the carbon was introduced into the blade during the coating processes. In order to avoid formation of MC carbides, a vacuum or clean environment may be required during coating application.

Table 8.3 Chemical compositions of points from the blade

Point	C	Al	Ti	Cr	Co	Ni	Mo	Ta	W	Hf
Star γ′	--	7.04	1.38	3..88	13.55	57.39	0.30	13.43	3.03	0.0
Eutectic γ′	--	7.12	1.19	4.24	14.75	57.05	0.18	12.59	2.88	0.00
β	--	15.94	0.67	5.55	14.56	56.55	0.15	4.62	1.96	0.00
γ′ on β edge	--	7.06	1.15	4.24	14.72	56.31	0.48	12.21	3.83	0.0
MC	8.41	--	4.59	0.65	1.09	2.93	--	70.37	--	11.96
MC in TEM	2.41	--	6.33	0.43	--	0.29	0.11	89.22	1.2	0.0

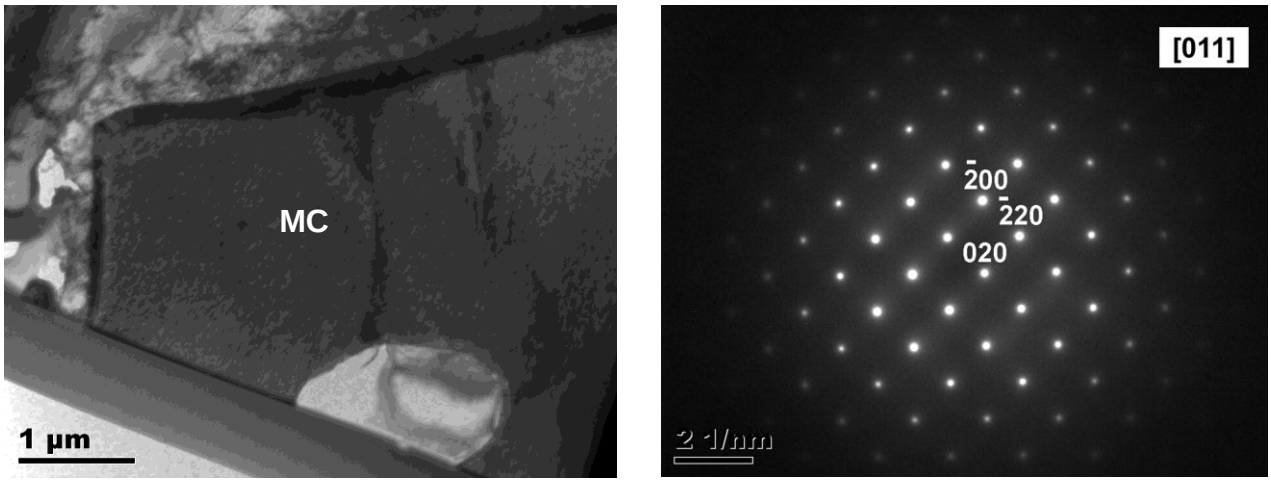

(a) Bright Filed **(b) Diffraction Pattern**

Figure 8.13. TEM image showing (a) bright filed image of MC carbides, (b) the diffraction patten of MC carbides.

Table 8.4 MC carbides distribution in three different regions of the blade

Region affected by the past coating	γ/γ' region	Oxidation region
3.9	3.2	1.0

8.5.2 Oxidation regions

The microstructure of the internal surface adjacent to the cooling channels of the ex-service blade is illustrated in Figure 8.14. A needle-like oxide layer was observed with a thickness ~ 50 μm. This oxide layer was formed due to oxidation and corrosion within the combustion gas during the working environment. Chemical mapping (Figure 8.15) indicates that the oxide consists of Al and Cr rich oxides in the layer. The presence of Al_2O_3 and/or Cr_2O_3 on the top of the substrate prevents further oxidation and corrosion by providing a protective layer on the substrate. Star shaped γ′ particles were precipitated and increased gradually in size from the near internal surface towards the centre of the blade. These particles have grown into a cuboidal or close to cuboidal structure in the

γ/γ′ region with a size ~ 0.2-0.5 μm. In between the oxide layer and these star-shaped γ′ particles, some dark grey particles were observed near the oxide layer, see Figure 8.14. The chemical analysis showed that they contain high concentrations of Ti ~56 wt.% and Hf ~12 wt.%. The detailed chemical composition is shown in Table 8.5. Due to the high proportion of Ti, Hf and the presence of N, these particles were identified as MN nitrides, which are TiN and HfN. These nitrides were further identified by TEM. The microstructure and diffraction are shown in Figure 8.16, where the diffraction pattern of these nitrides has the same face-close cubic (FCC) structure as the matrix. The calculated lattice parameter of these particles is a_0=4.31Å, which has a close agreement with the literature data, a_0=4.24 Å [138]. However, there is normally no nitrogen contained within the substrate or the coatings. Therefore, it is very possible that nitrogen was introduced into the system during the service. The high concentration of nitrogen in the combustion gas and the location of the nitride formed, suggests that these nitrides may be formed by the reaction of Hf and Ti with nitrogen of the combustion gas at high temperature working environment.

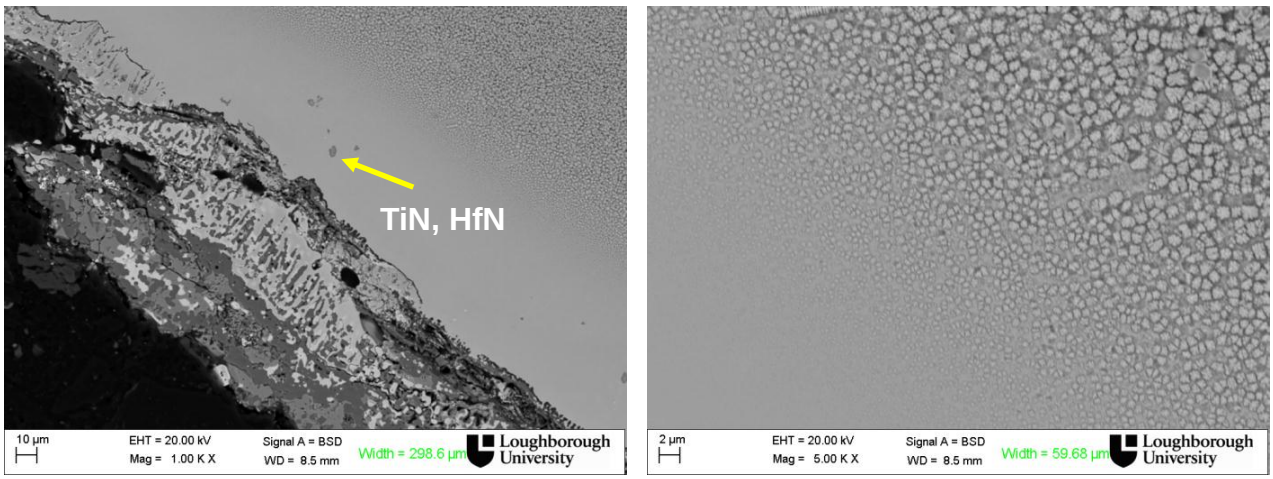

(a) Oxide Layers and MX Nitrides **(b) Star Shape γ′**

Figure 8.14. SEM images showing (a) oxide layers and MX nitrides, (b)star shape γ′ increased in size from internal surface towards centre of the blade

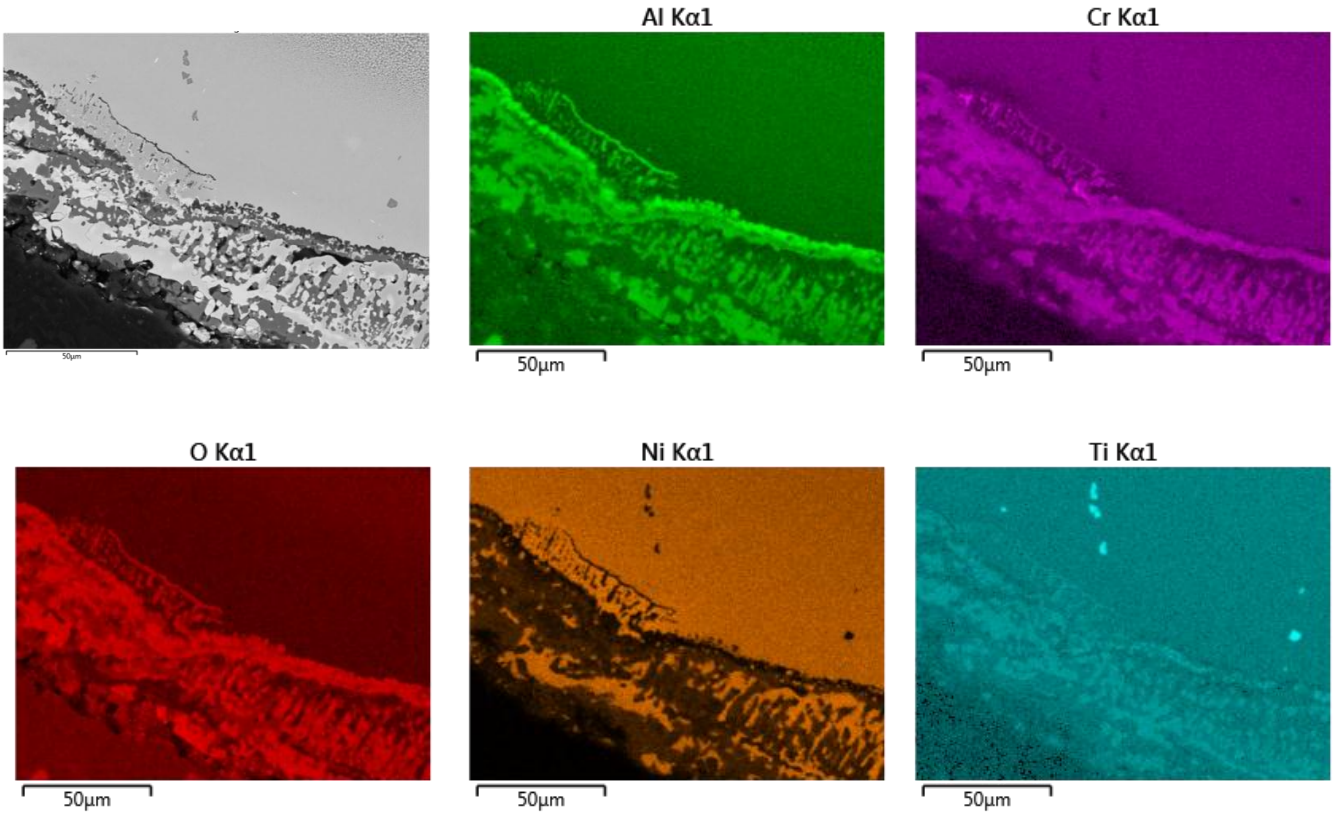

Figure 8.15. SEM EDX mapping showing the chemical distribution of elements in the oxidation region.

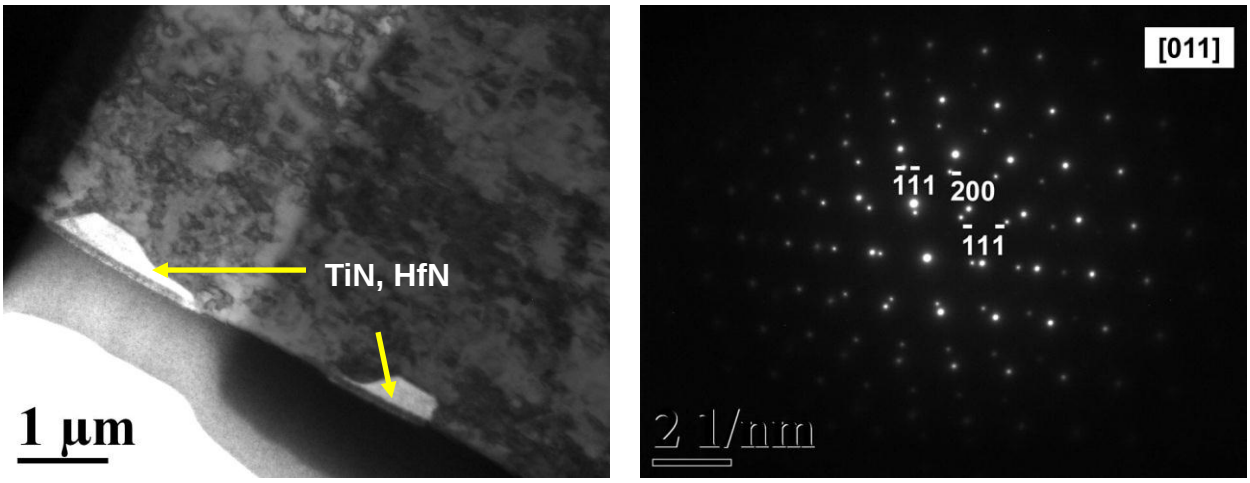

(a) Bright Filed **(b) Diffraction Pattern**

Figure 8.16. TEM images showing (a) bright feild image of MX nitrides, (b) the diffraction patten of MN nitrides combined with matrix, showing the same FCC structure.

Table 8.5 Chemical Composition of the MN found in oxidation region / wt%

Point	N	Al	Ti	Cr	Co	Ni	Hf	Ta	W	Re
MN (SEM no N)	--	0.84	67.61	0.78	1.15	7.92	13.92	6.91	0.27	0.61
MN (SEM with N)	17.07	0.66	56.19	0.63	0.96	6.62	11.69	5.48	0.21	0.47
MN (TEM with N)	17.87	--	66.51	0.44	0.21	0.70	7.02	6.73	0.52	--

8.6 Surface Deformation

As shown in 8.2 section of this chapter, some surface deformations have been observed in rejuvenated blade. The dimensional examination shows there is a 1-2 mm difference for the protruded region before and after rejuvenation, and 0.3-0.4 mm for the “wrinkles”, which were later found to be cracks. The microstructural investigation of these places was carried out, to provide a good understanding of the microstructure evolution of the melted part of the coated blade after rejuvenation.

8.6.1 Protruded Region

Figure 8.17 shows the microstructure of the protruded region in the section 2 of the blade, where a few voids were formed near the external surface. In the high magnification image (Figure 8.17b) most of the unfilled voids have a size of ~ 50-100 μm, with small number of measuring ~ 200 μm. The voids were surrounded by β particles. At the bottom of the voids, some cuboidal γ′ of various sizes were observed, from 0.5 to 3.0 μm. The rest of the microstructure is the same as in the surface region. These voids are quite different to the casting porosity found in the bar specimens, which measure only 10-20 μm and they are spherical in

shape. These voids are evidence of local melting at the surface region of blade during rejuvenation heat treatment.

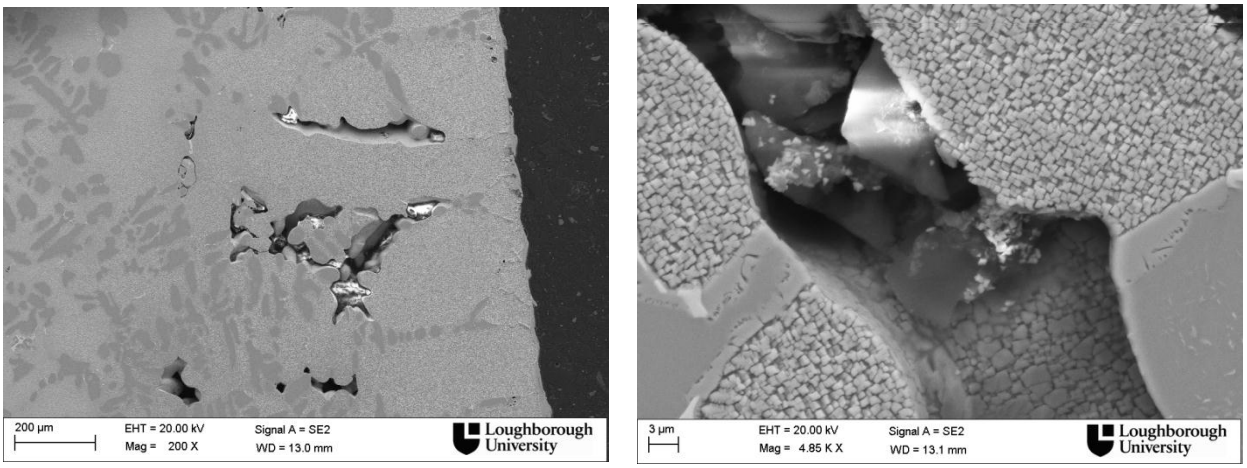

(a) Low Mag **(b) High Mag**

Figure 8.17. SEM images showing (a) low magnification of protruded region, (b) high magnification image showing the detail of the voids at protruded region in section 2 of the blade.

8.6.2 Cracks

Figure 8.18 shows the microstructure of the “wrinkles” taken from the pressure side of section 6 of the blade. Where it was found that these “wrinkles” were cracks, the length of the crack in section 6 is ~ 300 µm in length and a few microns in width. The cracks were only found within the pressure side of the root of the aerofoil. The cracks can either result from the service or rejuvenation heat treatment. These cracks became visible during white light scanning after the rejuvenation heat treatment, since this location experienced a high stress concentration during rejuvenation due to weight of the blade whilst it was laying down within the furnace. However, cracks were only found near the surface of the pressure side of the aerofoil root, where stress was concentrated during rejuvenation heat treatment. According to the location of the cracks and their size, it is likely that cracks were formed during rejuvenation heat treatment.

Usually, service introduced cracks in blade were more often formed at the tip of the aerofoil rather than root, with a much increased crack size (a few mm in length) [115].

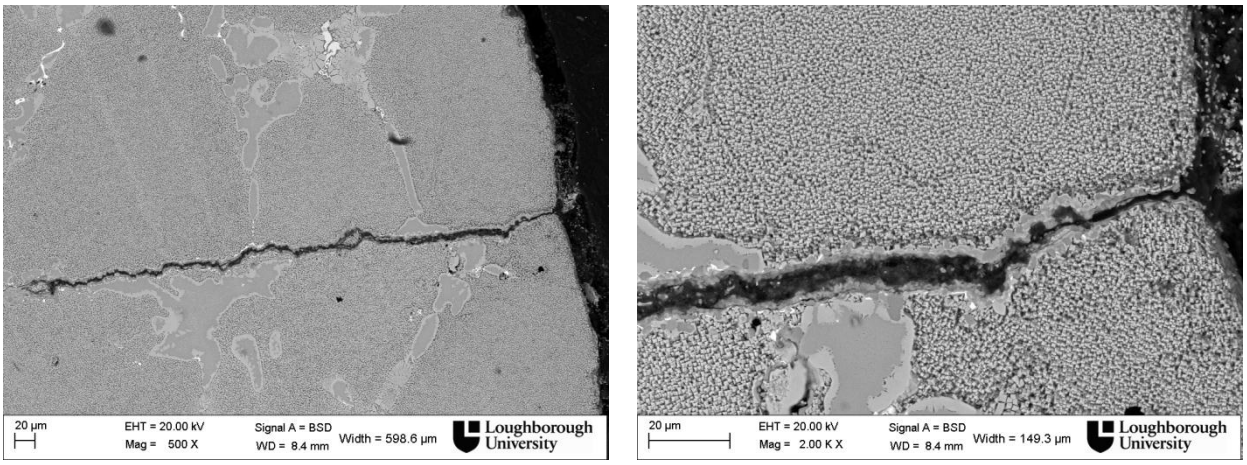

(a) Low Mag **(b) High Mag**

Figure 8.18. SEM images showing (a) low magnification of the crack, (b) high magnification image showing the detail of the crack in section 6 of the blade.

8.7 Summary

In this section, the results of the dimensional changes and microstructural investigation of the coated industrial ex-service blade after rejuvenation has been presented and discussed, followed by a microstructural comparison with laboratory bar specimens. The microstructures of surface region and oxidised internal region were also examined in this chapter, with some interesting features observed in relation to surface deformation.

The dimensional stability of the blade before and after rejuvenation heat treatment has been examined. Ignoring the surface deformation caused by the heat treatment, the remainder of the blade has successfully achieved the dimensional stability with maximum dimensional changes of less than 0.4 mm.

Microstructural comparisons of the positions in a number of turbine blade cross-sections show very consistent findings when compared to experimental bar specimens. Although the pressure and temperature acting on the blade during service is different in different heights and positions, the majority of substrate has restored its microstructure close to a pre-service condition after rejuvenation heat treatment.

Although the high temperature rejuvenation heat treatment can restore the microstructure of the blade back to an acceptable condition, care must be taken during handling of a large industrial ex-service blade, since small mechanical stress whilst at high temperature may cause permanent damage to the blade. One thing that must be emphasised is that rejuvenation can only be applied to blade without permanent physical damage. Once cracks or defects are formed within the blade, this damage is irreversible, and could cause failure of components. Therefore, X-ray scanning is required for examination to determine whether there any cracks and/or defects inside the blade before microstructural rejuvenation is attempted.

CHAPTER 9

CONCLUSIONS AND FURTHER WORK

9.1 Conclusions

The conclusions which arise from the various investigations carried out in this research are discussed as follows, which refer to the thermodynamic calculations and general microstructure, tensile and creep tests and their microstructural analysis, chemical segregation investigation and modified rejuvenation, and rejuvenation of an ex-service blade.

Thermodynamic predictions show a good agreement with the experimental observations: the phases, amounts and their chemical compositions are consistent with the microstructural investigation results carried out on the standard CMSX-4 material after heat treatments at different temperatures.

The resulting mechanical properties (tensile and creep) developed in CMSX-4 after high temperature degradation and rejuvenation, result from changes in morphology and area fraction of secondary γ′ particles, γ channel width, rafting parameter and the precipitation of the tertiary γ′ in the channels. The degradation not only increases the size, spacing and rafting parameter of the secondary γ′ particles, which in turn makes the γ channel broader and the degree of rafting higher, but also causes a reduction in the measured area fraction of secondary γ′ particles. The presence of tertiary γ′ precipitates in the channel has a beneficial effect on the mechanical properties if the channels are small. The rejuvenation

procedure used here restores the rafted microstructure to a microstructure which is apparently equivalent to the as-received structure. However, the faster degradation of rejuvenated samples during a subsequent degradation treatment still remains. The low temperature refurbishment does not appear to be helpful in rejuvenating the microstructure of CMSX-4 and, in fact, care must be taken to ensure that the process does not further degrade the materials.

Chemical segregation as one of the most likely reasons for the faster degradation rate of rejuvenated CMSX-4 has been examined in Chapter 7. The results suggest that although the high temperature rejuvenation does restore the microstructure to the as-received conditions, the chemical segregation resulting from degradation still remains, which was enhanced by a second degradation and causes a reduction in the mechanical performance of the materials. This problem was solved by the modification of rejuvenation heat treatment. However, long term creep test results show that a modified rejuvenation (RT4) does not help to improve the mechanical performance, which suggests that at the test conditions used here, the small chemical segregation present within these samples does not have significant effect on the mechanical properties. However, these results were only based on one test, therefore more mechanical tests should be needed for draw a more convinced conclusion about the influence of chemical segregation on mechanical performance.

The microstructural investigation results show that the microstructures from different locations of a rejuvenated ex-service blade are the same and are consistent with the microstructures obtained from bar specimens. The dimensional comparison of the blade before and after rejuvenation suggests the rejuvenation heat treatment has very little influence on the dimensional stability of the complex shape industrial gas turbine blade. These results indicate that the

rejuvenation heat treatment can well restore an ex-service blade to its pre-service condition without having a significant influence on the dimensional stability. However, care must be taken for handling large-scale industrial ex-service blades and an in-furnace support system is required during rejuvenation heat treatment, since small changes at high temperature may cause permanent damage on the blade and limits its further applications. Whether the rejuvenation heat treatment has a similar effect on the mechanical properties of an ex-service blade compared to the bar samples examined requires further investigation.

9.2 Further Work

In this thesis, the microstructural evolution of the CMSX-4 during high temperature degradation and rejuvenation has been examined, together with changes in mechanical performance. Moreover, chemical segregation as one of the possible underlying mechanisms of a faster degradation rate of rejuvenated sample has been investigated. Finally, an application of the rejuvenation on an ex-service industrial blade has been examined and evaluated. However, there are some areas which require further work. Areas for suggested further work are as follows.

According to long term creep test results carried out within this project, a conclusion could be drawn that chemical segregation has little influence on the mechanical performance of the materials. However, these tests are too short-term compared with real service conditions, which did not show significant differences between the degraded sample and rejuvenated sample after a subsequent degradation. Therefore, a longer creep test, around 10,000 hours at

the same temperature but with a much lower applied stress is preferred for further research. This would provide a further indication of the influence of the chemical segregation on the mechanical performance of materials. On the other hand, if chemical segregation has apparently no influence on the faster degradation of rejuvenated samples, the dislocations and the misfit between γ/γ′ as two other possible candidates for the mechanism should be further investigated. These could provide more information about the underlying mechanism of the difference between rejuvenated and as-received samples, and help to develop a more efficient rejuvenation heat treatment in future.

A large portion of the research has been concerned with the microstructural investigation of an ex-service blade after rejuvenation. However, as only one blade from industry was available here, therefore no comparison of the blade before and after rejuvenation was made. Moreover, the influence of long time exposure under service conditions on a coated blade has not been studied. Therefore, a microstructural investigation of an ex-service coated blade after similar exposure time and conditions should be carried out. This should provide very useful information about the microstructural evolution of the MCrAlY coated blade during service and rejuvenation, which assists the life prediction of the coated materials as blading applications for the power plant application.

In respect of thermodynamic and diffusion modelling results, it has been shown that the model prediction data in this project are in good agreement with the experimental observations. Unfortunately, these models have not been applied to the coated ex-service blade. Use of these models could provide a complete prediction of the evolution of phase with time and temperature of the MCrAlY coated blade during service and rejuvenation. These thermodynamic and diffusion modelling results can then link with the experimental work shown in

Chapter 8, to help the life prediction of the coated industrial blade in service conditions and provide information to enhance coating systems for service components in the turbine engine for power generation applications in future.

References

[1] R. C. Reed, *The superalloys: fundamentals and applications*. London: Cambridge University Press, 2006.

[2] C. T. Sims, N. S. Stoloff, and W. C. Hagel, *Superalloys II*. New York: Wiley-Interscience, 1987.

[3] H. K. D. H. Bhadeshia, “Nickel based superalloys,” 2003. [Online]. Available: http://www.msm.cam.ac.uk/phase-trans/2003/Superalloys/superalloys.html. [Accessed: 12-Sep-2010].

[4] R. Bowman, “Superalloys: a primer and history,” 2000. [Online]. Available: http://www.tms.org/meetings/specialty/superalloys2000/superalloyshistory.html. [Accessed: 12-Sep-2010].

[5] M. Durand-Charre, *The microstructure of superalloys*. Paris: CRC press, 1998.

[6] A. James, “Review of rejuvenation process for nickel base superalloys,” *Mater. Sci. Technol.*, vol. 17, no. 5, pp. 481–486, May 2001.

[7] C. Degnan, “Refurbishment and life extension of gas turbine blading fabricated from CMSX-4 single crystal Ni-based superalloy,” E.ON New Build & Technology Internal Report, 2010.

[8] M. . Acharya and G. . Fuchs, “The effect of long-term thermal exposures on the microstructure and properties of CMSX-10 single crystal Ni-base superalloys,” *Mater. Sci. Eng. A*, vol. 381, no. 1–2, pp. 143–153, Sep. 2004.

[9] M. J. Donachie, *Superalloys: a technical guide*. New York: ASM international, 2002.

[10] T. M. Pollock, N. Rene, and S. Tin, “Nickel-based superalloys for advanced turbine engines: chemistry, microstructure and properties,” *J. Propuls. Power*, vol. 22, no. 2, pp. 361–374, Mar. 2006.

[11] T. Niki, K. Ogawa, and T. Shoji, “Segregation of alloying elements of directionally solidified nickel based superalloy CM247LC during creep degradation process,” *Key Eng. Mater.*, vol. 353–358, pp. 537–540, 2007.

[12] M. McLean, *Directionally solidified materials for high temperature service*. London: Maney Publishing, 1988.

[13] S. Tin and T. M. M. Pollock, “Phase instabilities and carbon additions in single-crystal nickel-base superalloys,” *Mater. Sci. Eng. A*, vol. 348, no. 1–2, pp. 111–121, May 2003.

[14] P. Caron, “High γ’ solvus new generation nickel-Based superalloys for single crystal turbine blade applications,” in *Proceeding of Superalloys 2000, (Editors:T.M.Pollock et al.)*, Pennsylvania, pp. 737–746, 2000.

[15] G.L.Erickson, “The Development and application of CMSX-10,” in *Proceeding of Superalloys 1996, (Editors R.D. Kissinger et al.,)*, Pennsylvania, pp. 35–44, 1996.

[16] J. J. Moverare, A. Sato, M. Hasselqvist, F. Karlsson, and R. C. Reed, “A new single crystal superalloy for power generation applications,” in *Proceeding of Superalloys 2004, (Editors K. A. Green et al.,)*, Pennsylvania, pp. 245–257, 2004.

[17] S. Walston, A. Cetel, R. MacKay, K. O’hara, D. Duhl, and R. Dreshfield, “Joint development of a fourth generation single crystal superalloy,” in *Proceeding of Superalloys 2004, (Editors K. A. Green et al.,),* Pennsylvania, pp. 15–24, 2004.

[18] J. X. Zhang, T. Murakumo, Y. Koizumi, T. Kobayashi, and H. Harada, “Slip geometry of dislocations related to cutting of the γ′ phase in a new generation single-crystal superalloy,” *Acta Mater.*, vol. 51, no. 17, pp. 5073–5081, Oct. 2003.

[19] A. Sato, H. Harada, A. Yeh, T. Yokokawa, and J. X. Zhang, “A 5th generation SC superalloy with balanced high temperature properties and processability,” in *Proceeding of Superalloys 2008, (Editors R. C. Reed et al.,)*, Pennsylvania, pp. 131–138, 2008.

[20] J. Li and R. P. Wahi, “Investigation of γ/γ′ lattice mismatch in the polycrystalline nickel-base superalloy IN738LC: Influence of heat treatment and creep deformation,” *Acta Metall. Mater.*, vol. 43, no. 2, pp. 507–517, Feb. 1995.

[21] K. Y. Cheng, C. Y. Jo, D. H. Kim, T. Jin, and Z. Q. Hu, “Influence of local chemical segregation on the γ′ directional coarsening behavior in single crystal superalloy CMSX-4,” *Mater. Charact.*, vol. 60, no. 3, pp. 210–218, Mar. 2009.

[22] R. a. MacKay and M. V. Nathal, “γ’coarsening in high volume fraction nickel-base alloys,” *Acta Metall. Mater.*, vol. 38, no. 6, pp. 993–1005, Jun. 1990.

[23] R. G. G. M.V. Nathal, R.A. Mackay, “Temperature dependence of γ-γ’ lattice mismatch in nickel-base superalloys,” *Mater. Sci. Enginnering*, vol. 75, pp. 195–205, 1985.

[24] M. F.-K. R. Völkla, Corresponding author contact information, U. Glatzelb, “Measurement of the lattice misfit in the single crystal nickel based superalloys CMSX-4, SRR99 and SC16 by convergent beam electron diffraction,” *Acta Mater.*, vol. 46, no. 12, pp. 4395–4404, 1998.

[25] J. Zhang, J. Wang, H. Harada, and Y. Koizumi, “The effect of lattice misfit on the dislocation motion in superalloys during high-temperature low-stress creep,” *Acta Mater.*, vol. 53, no. 17, pp. 4623–4633, Oct. 2005.

[26] S. Tin, T. M. Pollock, and W. T. King, “Influence of Carbon Additions on the Phase Stability of As-Solidified High Refractory Content Ni-Base Superalloys,” *Mater. Sci. Enginnering A*, vol. 345, pp. 111–121, 2000.

[27] C.-N. Wei, H.-Y. Bor, and L. Chang, “The effects of carbon content on the microstructure and elevated temperature tensile strength of a nickel-base superalloy,” *Mater. Sci. Eng. A*, vol. 527, no. 16–17, pp. 3741–3747, Jun. 2010.

[28] K. A. Al-Jarba and G. E. Fuchs, “Effect of carbon additions on the as-cast microstructure and defect formation of a single crystal Ni-based superalloy,” *Mater. Sci. Eng. A*, vol. 373, no. 1, pp. 255–267, 2004.

[29] S. Tin, T. M. Pollock, and W. Murphy, “Stabilization of thermosolutal convective instabilities in Ni-based single-crystal superalloys: Carbon additions and freckle formation,” *Metall. Mater. Trans. A*, vol. 32, no. 7, pp. 1743–1753, 2001.

[30] A. K. Koul and G. H. Cessincer, “On the mechanism of serrated grain boundary formation in Ni-based superalloys,” *Acta Metall.*, vol. 31, no. 7, pp. 1061–1069, 1982.

[31] G. Lvov, V. I. Levit, and M. J. Kaufman, “Mechanism of primary MC carbide decomposition in Ni-base superalloys,” *Metall. Mater. Trans. A*, vol. 35, no. 6, pp. 1669–1679, 2004.

[32] L. R. Liu, T. Jin, N. R. Zhao, X. F. Sun, H. R. Guan, and Z. Q. Hu, “Formation of carbides and their effects on stress rupture of a Ni-base single crystal superalloy,” *Mater. Sci. Eng. A*, vol. 361, no. 1–2, pp. 191–197, Nov. 2003.

[33] C. M. F. Rae, M. S. Hook, and R. C. Reed, “The effect of TCP morphology on the development of aluminide coated superalloys,” *Mater. Sci. Eng. A*, vol. 396, no. 1, pp. 231–239, 2005.

[34] R. A. Hobbs, L. Zhang, C. M. F. Rae, and S. Tin, “Mechanisms of topologically close-packed phase suppression in an experimental ruthenium-bearing single-crystal nickel-base superalloy at 1100 C,” *Metall. Mater. Trans. A*, vol. 39, no. 5, pp. 1014–1025, 2008.

[35] C. M. F. Rae, M. S. A. Karunaratne, C. J. Small, R. W. Broomfield, C. N. Jones, and R. C. Reed, “Topologically close packed phases in an experimental rhenium-containing single crystal superalloy,” in *Proceeding of Superalloys 2000, (Editors:T.M.Pollock et al.),* Pennsylvania, pp. 767–776, 2000.

[36] C. M. F. Rae and R. C. Reed, “The precipitation of topologically close-packed phases in rhenium-containing superalloys,” *Acta Mater.*, vol. 49, no. 19, pp. 4113–4125, 2001.

[37] S. H. Mousavi Anijdan and A. Bahrami, “A new method in prediction of TCP phases formation in superalloys,” *Mater. Sci. Eng. A*, vol. 396, no. 1, pp. 138–142, 2005.

[38] V. Vaithyanathan and L. Q. Chen, “Coarsening of ordered intermetallic precipitates with coherency stress,” *Acta Mater.*, vol. 50, no. 16, pp. 4061–4073, 2002.

[39] S. Zhao, X. Xie, G. D. Smith, and S. J. Patel, “Gamma prime coarsening and age-hardening behaviors in a new nickel base superalloy,” *Mater. Lett.*, vol. 58, no. 11, pp. 1784–1787, Apr. 2004.

[40] S. M. C. J. K. Tien, “The effect of uniaxial stress on the periodic morphology of coherent gamma prime precipitates in nickel-base superalloy crystals,” *Metall. Mater. Trans. A*, vol. 2, no. 1, pp. 215–219, 1971.

[41] R. A. Stevens and P. E. J. Flewitt, “The effects of γ′ precipitate coarsening during isothermal aging and creep of the nickel-base superalloy IN-738,” *Mater. Sci. Eng.*, vol. 37, no. 3, pp. 237–247, 1979.

[42] J. W. Martin, “Coarsening of γ′-precipitates in single-crystal superalloy SRR 99,” *Mater. Sci. Technol.*, vol. 2, no. 6, pp. 543–546, 1986.

[43] A. M. Ges, “Coarsening behaviour of a Ni-base superalloy under different heat treatment conditions,” *Mater. Sci. Eng. A*, vol. 458, no. 1–2, pp. 96–100, Jun. 2007.

[44] J. Z. Zhu, T. Wang, A. J. Ardell, S. H. Zhou, Z. K. Liu, and L. Q. Chen, “Three-dimensional phase-field simulations of coarsening kinetics of γ’particles in binary Ni–Al alloys,” *Acta Mater.*, vol. 52, no. 9, pp. 2837–2845, 2004.

[45] M. V Nathal and L. J. Ebert, “Gamma prime shape changes during creep of a nickel-base superalloy,” *Scr. Metall.*, vol. 17, no. 9, pp. 1151–1154, 1983.

[46] A. Baldan, “Review progress in Ostwald ripening theories and their applications to nickel-base superalloys Part I: Ostwald ripening theories,” *J. Mater. Sci.*, vol. 37, no. 11, pp. 2171–2202, 2002.

[47] L. R. Liu, T. Jin, N. R. Zhao, Z. H. Wang, X. F. Sun, H. R. Guan, and Z. Q. Hu, “Microstructural evolution of a single crystal nickel-base superalloy during thermal exposure,” *Mater. Lett.*, vol. 57, no. 29, pp. 4540–4546, Nov. 2003.

[48] A. Baldan, “Review Progress in Ostwald ripening theories and their applications to the γ′-precipitates in nickel-base superalloys Part II Nickel-base superalloys,” *J. Mater. Sci.*, vol. 37, no. 11, pp. 2171–2202, 2002.

[49] M. Kamaraj, “Rafting in single crystal nickel-base superalloys – An overview,” *Sadhana*, vol. 28, no. 1–2, pp. 115–128, 2003.

[50] N. Matan, D. C. Cox, C. M. F. Rae, and R. C. Reed, “On the kinetics of rafting in CMSX-4 superalloy single crystals,” *Acta Mater.*, vol. 47, no. 7, pp. 2031–2045, May 1999.

[51] N. Matan, D. C. C. Cox, C. M. F. M. F. Rae, R. C. C. Reed, and M. A. Rist, “Creep of CMSX-4 superalloy single crystals: effects of rafting at high temperature,” *Acta Mater.*, vol. 47, no. 12, pp. 3367–3381, May 1999.

[52] W. Chen and J. P. Immarigeon, “Thickening behaviour of γ′ precipitates in nickel base superalloys during rafting,” *Scr. Mater.*, vol. 39, no. 2, pp. 167–174, 1998.

[53] M. Kamaraj, “Rafting in single crystal nickel-base superalloys—An overview,” *Sadhana*, vol. 28, no. 1–2, pp. 115–128, 2003.

[54] A. S. Argon, “Directional coarsening in nickel-base single crystals with high volume fractions of coherent precipitates,” *Acta Metall. Mater.*, vol. 42, no. 6, pp. 1859–1874, 1994.

[55] M. Kamaraj, C. Mayr, M. Kolbe, and G. Eggeler, “On the influence of stress state on rafting in the single crystal superalloy CMSX-6 under conditions of high temperature and low stress creep,” *Scr. Mater.*, vol. 38, no. 4, pp. 589–594, 1998.

[56] T. Ichitsubo, D. Koumoto, M. Hirao, K. Tanaka, M. Osawa, T. Yokokawa, and H. Harada, “Rafting mechanism for Ni-base superalloy under external stress: elastic or elastic–plastic phenomena,” *Acta Mater.*, vol. 51, no. 14, pp. 4863–4869, Aug. 2003.

[57] R. C. Reed, D. C. Cox, and C. M. F. Rae, “Kinetics of rafting in a single crystal superalloy: effects of residual microsegregation,” *Mater. Sci. Technol.*, vol. 23, no. 8, pp. 893–902, Aug. 2007.

[58] W. B. R Viswanathan, “Materials for ultrasupercritical coal power plants—Boiler materials: Part 1,” *J. Mater. Eng. Perform.*, vol. 10, no. 1, pp. 81–95, 2001.

[59] A. Epishin, T. Link, U. Brückner, B. Fedelich, and P. Portella, “Effects of segregation in nickel-base superalloys: dendritic stresses,” in *Proceeding of Superalloys 2004, (Editors K. A. Green et al.,)*, Pennsylvania, pp. 537–543, 2004.

[60] H. Klingelhöffer, A. Epishin, T. Link, B. Fedelich, and P. D. Portella, “Creep damage of single-crystal nickel base superalloys: mechanisms and effect on low cycle fatigue,” *Mater. High Temp.*, vol. 27, no. 1, pp. 53–59, 2010.

[61] A. Epishin, T. Link, U. Brückner, B. Fedelich, and P. Portella, “Segregation in single-crystal Nickel-base superalloys,” *Defect Diffus. Forum*, vol. 309, no. 1, pp. 121–126, 2011.

[62] L. Shui, T. Jin, S. Tian, and Z. Hu, “Influence of precipitate morphology on tensile creep of a single crystal nickel-base superalloy,” *Mater. Sci. Eng. A*, vol. 454–455, no. 72, pp. 461–466, Apr. 2007.

[63] V. Sass, U. Glatzel, and M. Feller-Kniepmeier, “Anisotropic creep properties of the nickel-base superalloy CMSX-4,” *Acta Mater.*, vol. 44, no. 5, pp. 1967–1977, May 1996.

[64] J. Safari and S. Nategh, “Microstructure evolution and its influence on deformation mechanisms during high temperature creep of a nickel base superalloy,” *Mater. Sci. Eng. A*, vol. 499, no. 1–2, pp. 445–453, Jan. 2009.

[65] F. Tancret, H. K. D. H. Bhadeshia, D. J. C. MacKay, T. Sourmail, M. a. Yescas, R. W. Evans, C. McAleese, L. Singh, and T. Smeeton, “Design of a creep resistant nickel base superalloy for power plant applications: Part 3 - Experimental results,” *Mater. Sci. Technol.*, vol. 19, no. 3, pp. 296–302, Mar. 2003.

[66] T. Sugui, Z. Huihua, Z. Jinghua, Y. Hongcai, X. Yongbo, and H. Zhuangqi, “Formation and role of dislocation networks during high temperature creep of a single crystal nickel–base superalloy,” *Mater. Sci. Eng. A*, vol. 279, no. 1–2, pp. 160–165, Feb. 2000.

[67] a. . Hopgood and J. . Martin, “The creep behaviour of a Nickel-based single-crystal superalloy,” *Mater. Sci. Eng.*, vol. 82, pp. 27–36, Sep. 1986.

[68] D. W. MacLachlan and D. M. Knowles, “Creep-behavior modeling of the single-crystal superalloy CMSX-4,” *Metall. Mater. Trans. A*, vol. 31, no. 5, pp. 1401–1411, May 2000.

[69] P. Caron and T. Khan, “Improvement of creep strength in a nickel-base single-crystal superalloy by heat treatment,” *Mater. Sci. Eng.*, vol. 61, no. 2, pp. 173–184, Nov. 1983.

[70] M. Feller-Kniepmeier and T. Kuttner, “[011] Creep in a single crystal nickel base superalloy at 1033K,” *Acta Metall. Mater.*, vol. 42, no. 9, pp. 3167–3174, 1994.

[71] R. Völkl, U. Glatzel, and M. Feller-Kniepmeier, “Analysis of matrix and interfacial dislocations in the nickel base superalloy CMSX-4 after creep in [1̄11] direction,” *Scr. Metall. Mater.*, vol. 31, no. 11, pp. 1481–1486, 1994.

[72] K. Serin, G. Göbenli, and G. Eggeler, “On the influence of stress state, stress level and temperature on γ-channel widening in the single crystal superalloy CMSX-4,” *Mater. Sci. Eng. A*, vol. 387–389, pp. 133–137, Dec. 2004.

[73] Z. Peng, U. Glatzel, T. Link, and M. Feller-Kniepmeier, “Change of phase morpholigies during creep of CMSX-4 at 1253K,” *Scr. Mater.*, vol. 34, no. 2, pp. 221–226, 1996.

[74] A. Epishin, T. Link, M. Nazmy, M. Staubli, and G. Nolze, “Microstructural degradation of cmsx-4: kinetics and effect on mechanical properties,” in *Proceeding of Superalloys 2008, (Editors R. C. Reed et al.,)*, Pennsylvania, pp. 725–731, 2008.

[75] M. V Nathal and R. A. MacKay, “The stability of lamellar γ-γ′ structures,” *Mater. Sci. Eng.*, vol. 85, pp. 127–138, 1987.

[76] J. Yu, X. Sun, N. Zhao, T. Jin, H. Guan, and Z. Hu, “Effect of heat treatment on microstructure and stress rupture life of DD32 single crystal Ni-base superalloy,” *Mater. Sci. Eng. A*, vol. 460–461, pp. 420–427, Jul. 2007.

[77] T. Grosdidier, a Hazotte, and a Simon, “Precipitation and dissolution processes in γ/γ′ single crystal nickel-based superalloys,” *Mater. Sci. Eng. A*, vol. 256, no. 1–2, pp. 183–196, Nov. 1998.

[78] J. Safari and S. Nategh, “On the heat treatment of Rene-80 nickel-base superalloy,” *J. Mater. Process. Technol.*, vol. 176, no. 1–3, pp. 240–250, Jun. 2006.

[79] B. Reppich, P. Schepp, and G. Wehner, “Some new aspects concerning particle hardening mechanisms in γ’precipitating nickel-base alloys—II. Experiments,” *Acta Metall.*, vol. 30, no. 1, pp. 95–104, 1982.

[80] B. F. Dyson, “Modeling the effects of damage and microstructural evolution on the creep behavior of engineering alloys,” *J. Energy Mater. Technol.*, vol. 122, no. 3, pp. 273–278, 2000.

[81] M. E. Kassner and T. A. Hayes, “Creep cavitation in metals,” *Int. J. Plast.*, vol. 19, no. 10, pp. 1715–1748, 2003.

[82] N. D’Souza, R. Beanland, C. Hayward, and H. B. Dong, “Accuracy of composition measurement using X-ray spectroscopy in precipitate-strengthened alloys: application to Ni-base superalloys,” *Acta Mater.*, vol. 59, no. 3, pp. 1003–1013, Feb. 2011.

[83] B. A. Lerch and S. D. Antolovich, “Fatigue crack propagation behavior of a single crystalline superalloy,” *Metall. Trans. A*, vol. 21, no. 8, pp. 2169–2177, 1990.

[84] D. W. MacLachlan and D. M. Knowles, “Fatigue behaviour and lifing of two single crystal superalloys,” *Fatigue Fract. Eng. Mater. Struct.*, vol. 24, pp. 503–521, 2001.

[85] M. Ott and H. Mughrabi, “Dependence of the high-temperature low-cycle fatigue behaviour of the monocrystalline nickel-base superalloys CMSX-4 and CMSX-6 on the γ/γ′-morphology,” *Mater. Sci. Eng. A*, vol. 272, no. 1, pp. 24–30, 1999.

[86] A. Costa, E. Poggio, E. Vacchieri, and S. Corcoruto, “On the TMF behaviour of a 1 st and 2 nd generation single crystal Ni Based superalloy with and without NiCoCrAlY + Re coatings,” in *Proceeding of 8th International Charles Parsons Turbine Conference*, 2011, pp. 121–128, 2011.

[87] J. Hou, B. J. Wicks, and R. a Antoniou, “An investigation of fatigue failures of turbine blades in a gas turbine engine by mechanical analysis,” *Eng. Fail. Anal.*, vol. 9, no. 2, pp. 201–211, Apr. 2002.

[88] T. Coppola, S. Riscifuli, O. Tassa, and G. Pasquero, “Thermomechanical fatigue behavior of bare and coated CMSX-4,” *J. Eng. Gas Turbines Power*, vol. 132, no. 1, pp. 101–106, 2009.

[89] T. J. Carter, “Common failures in gas turbine blades,” *Eng. Fail. Anal.*, vol. 12, no. 2, pp. 237–247, Apr. 2005.

[90] Z. Mazur, a. Luna-Ramírez, J. a. Juárez-Islas, and a. Campos-Amezcua, “Failure analysis of a gas turbine blade made of Inconel 738LC alloy,” *Eng. Fail. Anal.*, vol. 12, no. 3, pp. 474–486, Jun. 2005.

[91] A. Jung and A. Schnell, “Thermo-mechanical fatigue behaviour of coatings for industrial gas turbines,” Alstom Internal Report, Switzerland, 2005.

[92] H. H. and T. Y. T.Hino, T.Kobayashi, Y.Koizumi, “Development of a new single crystal superalloy for industrial gas turbines,” in *Proceeding of Superalloys 2000, (Editors:T.M.Pollock et al.)*, Pennsylvania, pp. 1–8, 2000.

[93] K. Harris, G. L. Erickson, and S. L. Sikkenga, “Develop of the rhenium containing superalloy CMSX-4 and CM186LC for single crystal blade and directionally solidified vane application in advanced turbine engine,” in *Proceeding of Superalloys 1992, (Editors S.D. Antolovich et al.,)*, Pennsylvania, pp. 297–306, 1992.

[94] K. S. Chan, N. S. Cheruvu, and G. R. Leverant, “Coating life prediction for combustion turbine blades,” *J. Eng. Gas Turbines Power*, vol. 121, no. 3, pp. 484–488, 1999.

[95] G. Marahleh, A. R. I. Kheder, and H. F. Hamad, “Creep life prediction of service-exposed turbine blades,” *Mater. Sci. Eng. A*, vol. 433, no. 1, pp. 305–309, 2006.

[96] Cannon-Muskegon Corporation, “CMSX-4.” [Online]. Available: http://www.c-mgroup.com/spec_sheets/CMSX_4.htm. [Accessed: 10-Sep-2010].

[97] C.-M. Group, “C-M Group Alloy Index,” 2004. [Online]. Available: http://www.c-mgroup.com/vacuum_melt_index/nickel_base_sx.htm. [Accessed: 10-Sep-2010].

[98] J. Chang, Y. Yun, C. Choi, and J. Kim, “Development of microstructure and mechanical properties of a Ni-base single-crystal superalloy by hot-isostatic pressing,” *J. Mater. Eng. Perform.*, vol. 12, no. 4, pp. 420–425, 2003.

[99] Y. Matsuoka, Y. Aoki, K. Matsumoto, A. Satou, T. Suzuki, K. Chikugo, and K. Murakami, “The formation of SRZ on a fourth generation single crystal superalloy applied with aluminide coating,” in *Proceeding of Superalloys 2004, (Editors K. A. Green et al.,)*, Pennsylvania, pp. 637–642, 2004.

[100] R. A. Miller, “Current status of thermal barrier coatings—an overview,” *Surf. Coatings Technol.*, vol. 30, no. 1, pp. 1–11, 1987.

[101] P. Krukovsky, K. Tadlya, A. Rybnikov, N. Mozhajskaya, I. Krukov, and V. Kolarik, “Life time analysis of MCrAlY coatings for industrial gas turbine blades (calculational and experimental approach),” in *Gas Turbine*, 2010, pp. 325–346, 2010.

[102] M. J. J. Pomeroy, “Coatings for gas turbine materials and long term stability issues,” *Mater. Des.*, vol. 26, no. 3, pp. 223–231, May 2005.

[103] A. G. Evans, D. R. Mumm, J. W. Hutchinson, and G. H. Meier, “Mechanisms controlling the durability of thermal barrier coatings,” *Prog. Mater. Sci.*, vol. 46, no. 5, pp. 505–553, 2001.

[104] M. Konter and M. Thumann, “Materials and manufacturing of advanced industrial gas turbine components,” *J. Mater. Process. Technol.*, vol. 117, no. 3, pp. 386–390, Nov. 2001.

[105] P. W. Schilke, A. D. Foster, and J. J. Pepe, “Advanced gas turbine materials and coatings,” General Electric Company, Internal Report, New York, 1995.

[106] N. P. Padture, M. Gell, and E. H. Jordan, “Thermal barrier coatings for gas-turbine engine applications,” *Science (80-.).*, vol. 296, no. 5566, pp. 280–284, 2002.

[107] A. Rybnikov, P. Krukovsky, V. Kolarik, K. Tadlya, N. Mojaiskaya, I. Kryukov, and M. Juez-Lorenzo, “Lifetime prediction for gas turbine blades MCrAlY coatings,” *Microsc. Microanal.*, vol. 10, no. S02, pp. 66–67, Aug. 2004.

[108] V. Srinivasan, N. S. Cheruvu, T. J. Carr, and C. M. O'rien, "Degradation of MCrAlY Coating and substrate superalloy during long term thermal exposure," *Mater. Manuf. Process*, vol. 10, no. 5, pp. 955–969, 1995.

[109] M. S. A. Karunaratne, I. Di Martino, S. L. Ogden, D. L. Oates, and R. C. Thomson, "Modeling of microstructural evolution in an MCrAlY overlay coating on different superalloy substrates," *Metall. Mater. Trans. A*, vol. 43, no. 2, pp. 774–788, 2012.

[110] N. Czech, F. Schmitz, and W. Stamm, "Improvement of MCrAlY coatings by addition of rhenium," *Surf. Coatings Technol.*, vol. 68, pp. 17–21, 1994.

[111] E. Inclusions, D. I. E. Modulierte, and D. I. E. Elastische, "On the modulated structure of aged Ni-Al alloys," *Acta Metall.*, vol. 14, no. 10, pp. 1295–1309, 1966.

[112] M. S. A. Karunaratne, S. L. Ogden, S. D. Kenny, and R. C. Thomson, "A multicomponent diffusion model for prediction of microstructural evolution in coated Ni based superalloy systems," *Mater. Sci. Technol.*, vol. 25, no. 2, pp. 287–299, 2009.

[113] E. Poursaeidi, M. Aieneravaie, and M. R. Mohammadi, "Failure analysis of a second stage blade in a gas turbine engine," *Eng. Fail. Anal.*, vol. 15, no. 8, pp. 1111–1129, Dec. 2008.

[114] M. Attarian, R. Khoshmanesh, S. Nategh, and P. Davami, "Microstructural evaluation and fracture mechanisms of failed IN-738LC gas turbine blades," *Case Stud. Eng. Fail. Anal.*, vol. 1, no. 2, pp. 85–94, Apr. 2013.

[115] J. a. Daleo, K. a. Ellison, and D. H. Boone, "Metallurgical considerations for life assessment and the safe refurbishment and requalification of gas turbine blades," *J. Eng. gas turbines power*, vol. 124, no. 3, pp. 571–579, 2002.

[116] S. Pahlavanyali, M. Wood, and G. Marchant, "Microstructural evolutions of IN738LC during multiple reheat treatment and aging," *Int. Heat Treat. Surf. Eng.*, vol. 10, no. 1, pp. 132–139, 2012.

[117] P. L. and J. L. A.K. Koul, J-P. Immarigeon, R. Castillo, "Rejuvenation of service-exposed IN 738 turbine blades," in *Proceeding of Superalloys 1988, (Editors S.Reichman et al.,)*, Pennsylvania, pp. 755–764, 1998.

[118] Z. Yao, C. C. Degnan, M. A. E. Jepson, and R. C. Thomson, "Microstructural Evolution in a Ni-based Superalloy High Temperature Degradation and Rejuvenation," *Mater. Sci. Technol.*, vol. 29, no. 7, pp. 775–780, 2013.

[119] A. Baldan, “Rejuvenation procedures to recover creep properties of nickel-base superalloys by heat treatment and hot isostatic pressing techniques,” *J. Mater. Sci.*, vol. 26, no. 13, pp. 3409–3421, 1991.

[120] R. B. Girdwood and R. W. Evans, “Recovery of creep properties of the nickel-base superalloy nimonic 105,” *Int. J. Press. Vessel. Pip.*, vol. 66, no. 1–3, pp. 141–153, Jan. 1996.

[121] G. E. Fuchs, “Solution heat treatment response of a third generation single crystal Ni-base superalloy,” *Mater. Sci. Eng. A*, vol. 300, no. 1–2, pp. 52–60, Feb. 2001.

[122] P. Caron and T. Khan, “Evolution of Ni-based superalloys for single crystal gas turbine blade applications,” *Aerosp. Sci. Technol.*, vol. 3, no. 8, pp. 513–523, Dec. 1999.

[123] E. Lvova and D. Norsworthy, “Influence of service-induced microstructural changes on the aging kinetics of rejuvenated Ni-Based superalloy gas turbine blades,” *J. Mater. Eng. Perform.*, vol. 10, no. June, pp. 299–312, 2001.

[124] A. Baldan, “Effects of carbides and cavitation on the Monkman-Grant ductility of a nickel-base superalloy,” *J. Mater. Sci. Lett.*, vol. 11, no. 19, pp. 1315–1318, 1992.

[125] J. N. Greenwood, D. R. Miller, and J. W. Suiter, “Intergranular cavitation in stressed metals,” *Acta Metall.*, vol. 2, no. 2, pp. 250–258, 1954.

[126] R. T. Ratcliffe and G. W. Greenwood, “The mechanism of cavitation in magnesium during creep,” *Philos. Mag.*, vol. 12, no. 115, pp. 59–69, 1965.

[127] ASTM, “E8/E8M standard test methods for tension testing of metallic materials 1,” *Annu. B. ASTM Stand. 4*, pp. 1–27, 2010.

[128] ASTM, “E139 standard test methods for conducting creep , creep-rupture , and stress-rupture tests of metallic materials 1,” *Annu. B. ASTM Stand. 4*, pp. 1–14, 2014.

[129] J. Goldstein, D. E. Newbury, D. C. Joy, C. E. Lyman, P. Echlin, E. Lifshin, L. Sawyer, and J. R. Michael, *Scanning electron microscopy and X-ray microanalysis*. Springer, 2003.

[130] M. Ignat, J.-Y. Buffiere, and J. M. Chaix, “Microstructures induced by a stress gradient in a nickel-based superalloy,” *Acta Metall. Mater.*, vol. 41, no. 3, pp. 855–862, Mar. 1993.

[131] D. B. Williams and C. B. Carter, *The transmission electron microscope*. Springer, 1996.

[132] L. Reimer and H. Kohl, *Transmission electron microscopy: physics of image formation*, vol. 36. Springer, 2008.

[133] L. A. Giannuzzi and F. A. Stevie, *Introduction to focused ion beams: instrumentation, theory, techniques and practice*. Springer, 2005.

[134] L. A. Giannuzzi and F. A. Stevie, “A review of focused ion beam milling techniques for TEM specimen preparation,” *Micron*, vol. 30, no. 3, pp. 197–204, 1999.

[135] D. A. Wollman, K. D. Irwin, G. C. Hilton, and L. L. Dulcie, “High resolution, energy dispersive microcalorimeter spectrometer for X ray microanalysis,” *J. Microsc.*, vol. 188, no. 3, pp. 196–223, 1997.

[136] R. H. Davies, A. T. Dinsdale, J. A. Gisby, J. A. J. Robinson, and S. M. Martin, “MTDATA-thermodynamic and phase equilibrium software from the national physical laboratory,” *Calphad*, vol. 26, no. 2, pp. 229–271, 2002.

[137] R. H. Davies, A. T. Dinsdale, T. G. Chart, T. I. Barry, and M. H. Rand, “Application of MTDATA to the Modeling of Multicomponent Equilibria,” in *Materials Chemistry at High Temperatures*, Springer, 1990, pp. 251–262.

[138] F. Alexandre, “Modelling the optimum grain size on the low cycle fatigue life of a Ni based superalloy in the presence of two possible crack initiation sites,” *Scr. Mater.*, vol. 50, no. 1, pp. 25–30, Jan. 2004.